ISTANBUL TECHNICAL UNIVERSITY ★ GRADUATE SCHOOL

SIMULATION AND CIRCUIT DESIGN OF AN INVERTER DRIVER WITH SENSORLESS FIELD ORIENTED CONTROL FOR A PMSM USED IN COMPRESSOR

M.Sc. THESIS

Tolga ODABAŞI

Department of Electrical Engineering

Electrical Engineering Programme

FEBRUARY 2022

ISTANBUL TECHNICAL UNIVERSITY ★ GRADUATE SCHOOL

SIMULATION AND CIRCUIT DESIGN OF AN INVERTER DRIVER WITH SENSORLESS FIELD ORIENTED CONTROL FOR A PMSM USED IN COMPRESSOR

M.Sc. THESIS

Tolga ODABAŞI
504171045

Department of Electrical Engineering

Electrical Engineering Programme

Thesis Advisor: Prof. Dr. Lale Tükenmez ERGENE

FEBRUARY 2022

ISTANBUL TEKNİK ÜNİVERSİTESİ ★ LİSANSÜSTÜ EĞİTİM ENSTİTÜSÜ

PMSM KULLANILAN KOMPRESÖR İÇİN VE ALGILAYICISIZ ALAN YÖNLENDİRMELİ KONTROL KULLANILAN EVRİCİ SÜRÜCÜNÜN BENZETİM VE DEVRE TASARIMI

YÜKSEK LİSANS TEZİ

Tolga ODABAŞI
504171045

Elektrik Mühendisliği Bölümü

Elektrik Mühendisliği Programı

Tez Danışmanı: Prof. Dr. Lale Tükenmez ERGENE

ŞUBAT 2022

Tolga Odabaşı, a M.Sc. student of İTU Graduate School student ID 504171045, successfully defended the thesis entitled “SIMULATION AND CIRCUIT DESIGN OF AN INVERTER DRIVER WITH SENSORLESS FIELD ORIENTED CONTROL FOR A PMSM USED IN COMPRESSOR”, which he prepared after fulfilling the requirements specified in the associated legislations, before the jury whose signatures are below.

Thesis Advisor :	**Prof. Dr. Lale Tükenmez ERGENE** Istanbul Technical University	.....
Jury Members :	**Assoc. Prof. Dr. Murat YILMAZ** Istanbul Technical University	.....
	Prof. Dr. Mehmet Timur AYDEMİR Kadir Has University	.....

Date of Submission : 14 January 2022
Date of Defence : 07 February 2022

Dedicated to my family,

FOREWORD

First of all, I would like to thank Prof. Dr Lale Tükenmez Ergene for her precious support and guidance during the preparation of this thesis.
I would like to thank Research Assistant Alper Tap for valuable assistance.
Another thank is to Reha Özgür Şimşek for helping in the coding side.
And also, I would like to thank Arçelik A.Ş. Power Electronics Laboratory for providing me components and test equipment for the thesis.
Finally, the biggest thank is to my family for supporting me all my life.

December 2021

Tolga ODABAŞI
(Electrical Engineer)

TABLE OF CONTENTS

Page

ABBREVIATIONS

AC : Alternating Current
ADC : Analog to Digital Converter
Back-EMF : Back Electromotive Force
BLDC : Brushless Direct Current
CISC : Complex Instruction Set Computing
CM : Common Mode
CPLD : Complex Programmable Logic Device
d AXIS : Direct Axis
DC : Direct Current
DM : Differential Mode
DSP : Digital Signal Processor
DTC : Direct Torque Control
EFK : Extended Kalman Filter
EFT : Electrical Fast Transient
EMC : Electromagnetic Compatibility
EMI : Electromagnetic Interference
ESR : Equivalent Series Resistance
FEM : Finite Elements Method
FOC : Field Oriented Control
HP : Horse Power
I2C : Inter-Integrated Circuit
IC : Integrated Circuit
IGBT : Insulated Gate Bipolar Transistor
I2C : Inter-Integrated Circuit
IM : Induction Motor
IPM : Intelligent Power Module
LDO : Low Dropout
LED : Light Emitting Diode
LPF : Low Pass Filter
LVIC : Low Voltage Integrated Circuit

MANN **:** Multiple Artificial Neural Networks

MCU **:** Microcontroller Unit

MOSFET **:** Metal Oxide Semiconductor Field Effect Transistor

MPC **:** Model Predictive Control

NTC **:** Negative Temperature Coefficient

OP-AMP **:** Operational Amplifier

PCB **:** Printed Circuit Board

PF **:** Power Factor

PFC **:** Power Factor Correction

PI **:** Proportional Integral

PM **:** Permanent Magnet

PMSM **:** Permanent Magnet Synchronous Motor

PWM **:** Pulse Width Modulation

q AXIS **:** Quadrature Axis

SMD **:** Surface Mount Device

SMO **:** Sliding Mode Observer

SMPS **:** Switch Mode Power Supply

SPI **:** Serial Peripheral Interface

SRAM **:** Static Random-Access Memory

SPWM **:** Sinusoidal Pulse Width Modulation

SVM **:** Space Vector Modulation

SVPWM **:** Space Vector Pulse Width Modulation

THD **:** Total Harmonic Distortion

UART **:** Universal Asynchronous Receiver Transmitter

USART **:** Universal Synchronous Asynchronous Receiver Transmitter

V/F **:** Voltage/Frequency

VSI **:** Voltage Source Inverter

WNN **:** Wavelet Neural Network

SYMBOLS

$\boldsymbol{\Phi}$	**:** flux
ϕ_v	**:** angular displacement referred to the rotor
$\boldsymbol{\theta_{ev}}$	**:** phase angle of the stator voltage
$\boldsymbol{\theta_{offset}}$	**:** offset angle
$\boldsymbol{\theta_r}$	**:** displacement of the rotor
$\boldsymbol{\theta_{r\_correct}}$	**:** corrected displacement of the rotor
$(\boldsymbol{\theta_r})_n$	**:** previous value of the displacement of the rotor
$(\boldsymbol{\theta_r})_{n-1}$	**:** amplification factor for desired speed range
$\boldsymbol{\mu_0}$	**:** permeability of free space
$\boldsymbol{\mu_r}$	**:** relative permeability of the steel laminations
$\boldsymbol{\omega_r}$	**:** angular velocity of the rotor
$\boldsymbol{\mu_{rec}}$	**:** relative magnetic permeability of the recoil line
$\boldsymbol{\gamma_{rel}}$	**:** relative angle
$\boldsymbol{\lambda}$	**:** flux linkage
$\boldsymbol{\lambda_{0s}}$	**:** zero component of the flux linkage
$\boldsymbol{\lambda_{abcs}}$	**:** matrix of the stator flux linkages
$\boldsymbol{\lambda_{ds}^r}$	**:** direct component of the flux linkage referred to the rotor
$\boldsymbol{\lambda_m'}$	**:** flux linkage of the permanent magnet
$\boldsymbol{\lambda_m'^r}$	**:** magnitude of the flux linkage of the permanent magnet referred to the rotor
$\boldsymbol{\lambda_{qd0s}^r}$	**:** matrix of the stator flux linkages referred to the rotor
$\boldsymbol{\lambda_{qs}^r}$	**:** quadrature component of the flux linkage referred to the rotor
$\boldsymbol{B_{damp}}$	**:** damping coefficient of the rotational system
$\boldsymbol{B_m}$	**:** magnetic flux density
$\boldsymbol{B_{rem}}$	**:** residual flux density
$\boldsymbol{C_{bus}}$	**:** capacitance of the DC bus capacitor
$\boldsymbol{cos\,\varphi}$	**:** power factor of the motor
$\boldsymbol{C_y}$	**:** value of the Y capacitor
$\boldsymbol{e_{as}}$	**:** alfa component of the Back-EMF voltage

$e_{\beta s}$: beta component of the Back-EMF voltage

$\widetilde{E}_a$: phasor of the Back-EMF volatge

f : grid frequency

$f_{switching}$: switching frequency

F : MMF

H_c : coercive force

H_m : magnetic field intensity

i_{as} : alfa component of the stator current

$i_{\beta s}$: beta component of the stator current

i_{0s} : zero component of the stator current

i_{0s}^r : zero component of the stator current referred to the rotor

i_{as} : phase a current of the stator

i_{abcs} : matrix of the stator currents

i_{bs} : phase b current of the stator

i_{cs} : phase c current of the stator

i_{ds} : direct component of the stator current

i_{ds}^r : direct component of the stator current referred to the rotor

$i_{ds\_flux\_weak}$: calculated reference current for flux weakening

i_{qd0s}^r : matrix of the stator currents referred to the rotor

i_{qs} : quadrature component of the stator current

i_{qs}^r : quadrature component of the stator current referred to the rotor

$i_{qs\_ref\_max}$: maximum reference current of the quadrature axis

i_{s_max} : maximum allowable stator current

I : current in the coil

I_{ds}^r : direct component of the stator current referred to the rotor in steady state

$I_{IGBT\_ave\_half}$: average current of IGBT over half period

I_{qs}^r : quadrature component of the stator current referred to the rotor in steady state

I_{phase_peak} : peak of the motor phase current

I_{rated} : rated RMS current

$I_{rev\_ave\_half}$: average peak current of the reverse recovery over half period

$\tilde{I}_{as}$: phasor of the stator current

J : total inertia of the rotor and a connected load

k : product coefficient

K : amplification factor for desired speed range

K_c : Back-EMF constant

ℓ : length of the flux line

ℓ_g : air gap length

ℓ_m : thickness of the magnet

L : inductance

L_{2s} : second harmonic of stator inductance

L_{ds} : direct component of the stator inductance

$L_{leakage}$: leakage current

L_{ls} : leakage inductance of the stator

L_{md} : direct component of the stator magnetizing inductance

L_{mq} : quadrature component of the stator magnetizing inductance

L_{qs} : quadrature component of the stator inductance

L_s : matrix of the stator inductances

m : number of the accumulated value of the angular velocity of the rotor

m_{index} : modulation index

n : exponent coefficient

n_{freq} : frequency coefficient

n_{temp} : temperature coefficient

N : number of turns

r_s : resistance of the stator

p : derivative sign

P : pole number of the rotor

P_{loss_bridge} : power loss of the bridge diode

$P_{loss\_cond\_diode}$: conduction power loss on the diode

$P_{loss\_cond\_IGBT}$: conduction power loss on the IGBT

$P_{loss\_cond\_inv}$: conduction power loss on the inverter

$P_{loss\_cond\_pack}$: conduction power loss on the package

P_{loss_ntc} : power loss of the NTC

$P_{loss\_off\_diode}$: turn-off diode loss

$P_{loss\_off\_IGBT}$: turn-off IGBT loss

$P_{loss\_on\_IGBT}$: turn-on IGBT loss

$P_{loss\_sw\_inv}$: switching power loss on the inverter

$P_{loss\_sw\_pack}$: switching loss in package

$P_{loss\_tot\_inv}$: total power loss on the inverter

$P_{loss\_tot\_pack}$: total power loss on the package

P_{input_max} : maximum input power

r_d : dynamic diode resistance

r_{IGBT} : dynamic IGBT resistance

$\mathfrak{R}$: reluctance

R_{cs_bridge} : case to the heatsink thermal resistance of the bridge diode

R_{cs_IPM} : case to the heatsink thermal resistance of the IPM

$\mathfrak{R}_d$: direct component of the reluctance

R_{jc_bridge} : junction to case thermal resistance of the bridge diode

R_{jc_IPM} : junction to case thermal resistance of the IPM

R_{ntc} : NTC resistance

R_{sa} : sink to the ambient thermal resistance of the heatsink

$\mathfrak{R}_q$: quadrature component of the reluctance

$t_{c(off)}$: turn-off time

$t_{c(on)}$: turn-on time

t_{rr} : reverse recovery time

T_0 : on time for $\overrightarrow{V_0}$

T_1 : on time for $\overrightarrow{V_1}$

T_2 : on time for $\overrightarrow{V_2}$

T_a : ambient temperature

T_{c_bridge} : case temperature of the bridge diode

T_{c_IPM} : case temperature of the IPM

T_e : electromagnetic torque

T_{j_bridge} : junction temperature of the bridge diode

T_{j_IPM} : junction temperature of the IPM

T_L : load torque

T_s : sampling period of PWM

T_{sink} : heatsink temperature

v_{0s} : zero component of a stator voltage referred to a rotor

v_{abcs} : matrix of the stator voltages

v_{as} : stator voltage of a phase

v_{bs} : stator voltage of b phase

v_{cs} : stator voltage of c phase

V_{d0} : V_d that is found by tangenting to the operation point

v_{ds}^{r} : direct component of the stator voltage referred to a rotor

v_{qd0s}^{r} : matrix of the stator voltages referred to the rotor

v_{qs}^{r} : quadrature component of the stator voltage referred to a rotor

v_s : magnitude of the stator voltage

V_{bemf} : Back-EMF voltage

$V_{\alpha s}$: alfa component of the stator voltage

$V_{\beta s}$: beta component of the stator voltage

$\overrightarrow{V_0}$: null vector

$\overrightarrow{V_1}$: vector of V_1

$\overrightarrow{V_2}$: vector of V_2

$\widetilde{V}_{as}$: phasor of the stator voltage

V_{CE0} : V_{CE} that is found by tangenting to the operation point

V_{DC} : DC bus voltage

V_{ds} : direct component of the stator voltage

V_{ds}^{r} : direct component of the stator voltage referred to the rotor in steady state

V_f : forward voltage

V_{input} : input RMS voltage

V_{p-p_ripple} : peak to peak voltage ripple of the rectified side

V_{input_peak} : peak voltage of the input

V_{qs} : quadrature component of the stator voltage

V_{qs}^{r} : quadrature component of the stator voltage referred to the rotor in steady state

V_{qs_ref} : reference voltage of the quadrature axis

$\overrightarrow{V_{ref}}$: reference vector

V_{s_max} : maximum allowable stator voltage

W_{pm} : energy in coupling field due to the presence of the permanent magnet

LIST OF TABLES

Page

LIST OF FIGURES

Page

SIMULATION AND CIRCUIT DESIGN OF A INVERTER DRIVER WITH SENSORLESS FIELD ORIENTED CONTROL FOR A PMSM USED IN COMPRESSOR

SUMMARY

The main purpose of this thesis is to design an inverter board with a sensorless field oriented control algorithm and to drive a PMSM with a compressor system using this inverter board. Simulation of the board is also evaluated. The measurements are taken and some comparisons are made. Finally, the measurements are interpreted and studies are carried out to improve some points. Simulation and verification of the inverter board are studied in detail before starting to the design. Summary of the study is given step by step as follows.

The first attempts of design of a permanent magnet synchronous motor with low quality hard magnetic materials were attributed in 19^{th} century. Magnets with high energy density began to be used in motors around the 1950s and usage of these types of motors has started to accelerate due to developments in material science. The removal of the brush system in a motor structure has reduced maintenance and caused a motor to be designed more compact with high energy density. Nowadays, permanent magnet synchronous motors have become indispensable for many usage areas such as industry, white goods, transportation, military and so on due to their high reliability and high-power density.

With the appearance of switching power transistors and silicon-controlled rectifiers, the mechanical commutator driving system was replaced by an inverter-based driving system in late 1950s. Various inverter topologies have been designed such as flying capacitor multilevel inverter and diode clamped multilevel inverter. As semiconductor technology improves dramatically, wide bandgap switches such as SiC and GaN have become popular especially in driving systems because of their high efficiency.

As a result of PMSM and hardware technology developments, motor control theory has also developed. Six-step control which is also called as trapezoidal control is preferred in inverter systems at the early works. In this control theory, ratio of voltage and frequency is kept as a constant at each rotor speed. In addition to that, this is also called a scalar control technique due to the absence of vector information of voltages. Hall sensors are used to determine rotor position for a commutation time. Six-step control can cause torque ripple and also the dynamic response of six-step control can be insufficient for critical loads. In order to enhance the dynamic performance of systems, field oriented control was developed. This is a vector control and the main purpose of the theory is to keep magnetic fluxes of rotor and stator perpendicular to each other at every position of the rotor. So, the torque value is maximum in this condition. In order to do that, torque and flux components of the stator currents are derived and torque component is aimed to be maximized. Some matrix transformations such as Clarke and Park are needed for these calculations. In sensorless field oriented control, the rotor position is determined by observing the BEMF signal in the stator winding rather than using hall sensors. Inverter system with sensorless field oriented

control has a wide usage area such as industry, white goods, transportation, military and so on. Quiter and smoother operation of a PMSM is enabled by this control technique.

In this thesis, literature review is presented in the first chapter. Development stages of a PMSM, inverter systems and control methods that are from 1962 to nowadays are reviewed. Gradual enhancement of efficiency and smooth control techniques are observed in the literature.

In the second chapter, permanent magnets are reviewed. Properties of soft and hard permanent magnets, graphs and equations are given in this section. With the development of materials science, more efficient permanent magnets are produced.

In the third chapter, PMSMs are introduced. History, definition and usage area of this motor are given. Finally, types of a PMSM which are surface mounted, surface insert, interior, spoke and line start are studied. It has been observed that each motor type is suitable for different usage areas. For instance, some of them are convenient for high-speed operation and some of them have higher power density than other types.

A dynamic model of a PMSM is presented in the fourth chapter. Electrical model and its equations such as transformations of rotor and stator reference frame, inductance, flux linkage, voltage, current and torque of a PMSM are given in detail. Main equations are utilized in the coding stage of a PMSM driver board.

In the fifth chapter, field oriented control is explained in detail. Six-step control method is also considered for the comparison. The advantage of the control method on dynamic performance is mentioned. A diagram of a space vector modulation for an inverter system are shown with the transformation equations and related graphs are given. BEMF based sensorless algorithm that is used in the thesis is explained at last. All sequences of control diagrams are implemented to the algorithm in a PMSM driver board.

Hardware design is given in the sixth chapter. Main hardware block diagram of the inverter board is constructed at first. Design stage of the inverter board is summarized as follow. X and Y type capacitors, common mode and differential mode inductors are placed due to the EMC regulation. Differential mode inductor is also used as a harmonic filter at the same time. In addition to these components, some protection components such as fuse and varistor are placed. A negative temperature coefficient resistor (NTC) is used to limit the inrush currents. This NTC is bypassed via a relay after the electrolytic bus capacitor is charged in order to terminate power loss on NTC. The bleeding resistor is for discharging X capacitor after the plugging out. The second part is the rectification circuit. This circuit includes bridge diode and electrolytic bus capacitor. The grid voltage is rectified and smoothed in this stage. 15V voltage is generated by the SMPS circuit. This voltage is used for driving the gate of the power module and feeding the linear regulator. Buck converter was preferred as a converter topology. Linear regulator which is also called LDO generates 5V voltage. Microcontroller, Op-Amp and other related components are fed by this voltage. Currents through shunt resistors are sensed with the Op-Amp circuit and sent to the microcontroller. The voltage on shunt resistors is amplified with a predetermined gain value. And also offset voltage is added to this amplified value in order to sense negative voltage on the shunt resistor. This 2.5V offset voltage is generated with a buffer circuit. The inverter stage is the heart of the driver board. An intelligent power module which is called IPM is preferred as a switch type. This module includes six switches and their gate drivers. In addition to that, it has short circuit and temperature

protections. Sensorless field oriented control is executed with an algorithm embedded in the microcontroller. Six PWM signals are generated regarding current feedbacks coming from Op-Amp in the microcontroller. The speed of a rotor is also determined by the reading frequency of a square wave signal coming from a speed reference circuit. There is anolog or software protection feature on driver board such as over-current, over-voltage, over-temperature and so on.

Schematic and PCB designs are implemented in Altium Designer software. Double layer and FR4 type PCB is used for the driver board. PCB size is 155mmx150mm. After the PCB design, ten pieces of PCB are printed and assembling of two inverter board were carried out.

Simulation of the driver board is run in PSIM simulation software in the seventh chapter. Hardware and control blocks are constructed. Phase currents are extracted with the sensors in simulation. On the other hand, in a real driver board, the sensorless algorithm is run. The simulation contains three different rotor speeds that are 1300 rpm, 2000 rpm and 3000 rpm. Phase currents and actual rotor speed are taken from the simulation.

Sensorless field oriented control is run in the motor control software and shown in the eighth chapter. This software contains classical function of field oriented control such as Clarke and Park transforms. In addition to that, there are special functions such as DC bus ripple elimination. BEMF observer is implemented for sensorless algorithm.

In the nineth chapter, the inverter board is run with a compressor setup on the bench. Several measurements are taken from the inverter board such as phase current, bus voltage, PWM signals and so on. Speed references are remained the same with simulation to compare.

Finally, simulation and real application are compared in terms of algorithm and waveforms in the tenth chapter. Some differences are observed and interpreted. On the algorithm side, simulation has field oriented control with the sensors. At starting condition, there is also a maximum torque algorithm. In a real application, sensorless field oriented control is implemented with the aligning, open loop and closed loop stages. Finally, after interpreting the measurements, studies are carried out to improve total harmonic distortion of the phase current, and the way for possible future studies is opened.

PMSM KULLANILAN KOMPRESÖR UYGULAMASI İÇİN ALGILAYICISIZ ALAN YÖNLENDİRMELİ KONTROLLÜ EVİRİCİ SÜRÜCÜ DEVRESİNİN BENZETİM VE TASARIMI

ÖZET

Tezin amacı algılayıcısız alan yönlendirmeli evirici sürücü devresinin tasarım, benzetim ve gerçeklemesini yaparak içinde daimi mıknatıslı senkron motor (PMSM) bulunan kompresör sistemini sürmektir. Bu bağlamda sürücü devrenin tasarımı ve benzetimi gerçekleştirilmiştir. Devre tasarımı gerçeklenerek kontrol algoritması evirici kartına gömülmüştür. Sürücü kartı kompresör sistemi üzerinde çalıştırılarak ölçümler alınmış ve benzetim ile karşılaştırmalar yapılmıştır. En sonunda da ölçümler yorumlanarak bazı noktaların iyileşmesine yönelik gelecekte yapılması olası çalışmalar belirtilmiştir. Tasarım, simülasyon ve gerçeklemeden önce, detaylı bir literatür araştırması yapılmıştır. Tez çalışmasının özeti aşağıdaki adım adım verilmiştir.

Düşük kaliteli daimi mıknatısların kullanıldığı ilk daimi mıknatıslı senkron motor tasarım çalışmaları 19. yüzyıla dayanmaktadır. Malzeme biliminin gelişmesi ile birlikte 1950'li yıllarda yüksek enerjili daimi mıknatısların kullanıldığı motorların kullanımı artmıştır. Fırça kollektör sisteminin olmadığı bu motor türü ile bakım masrafları azalmış, basit ve yüksek enerji yoğunluklu tasarımlarının önü açılmıştır. Günümüzde bu motorlar endüstri, beyaz eşya, taşıma, askeri gibi birçok sektörde güvenilirliği ve yüksek enerji yoğunluğu nedeniyle vazgeçilmez bir konuma gelmiştir.

1950'lerin sonlarına doğru, güç transistörlerinin ve silikon kontrollü doğrultucuların ortaya çıkmasıyla birlikte, mekanik komütatörlü sürücü sistemlerinin yerini, evirici tabanlı sürücü sistemleri almaya başlamıştır. Uçan kapasiteli çok seviyeli evirici, diyot kesimli çok seviyeli evirici gibi farklı evirici topolojileri ortaya çıkmıştır. Yarıiletken teknolojisinin hızlı bir şekilde gelişmesi ile birlikte SiC ve GaN gibi geniş bant aralıklı anahtarların sürücü sistemlerinde kullanılmaya başlanması, yüksek verimler elde edilmesini sağlamıştır.

PMSM ve donanım teknolojileri gelişirken diğer yandan motor kontrol teorileri de gelişmiştir. Önceleri, altı adım kontrolü, diğer bir adı ile trapez kontrol, evirici sistemlerinde tercih ediliyordu. Bu kontrol yönteminde, gerilim ve frekans oranı her rotor hızında sabit tutulmaktadır. Ayrıca, gerilim vektör bilgilerinin olmamasından dolayı, bu kontrole 'skaler kontrol' de denilmektedir. Komütasyon zamanı için rotor pozisyonu belirlemede, Hall algılayıcıları kullanılmaktadır. Altı adım kontrol; moment dalgalanmasına neden olmakla birlikte, kontrol yönteminin dinamik performansı kritik yükler için yetersiz kalmaktadır. Dinamik performansı daha iyi hale getirmek için alan yönlendirmeli kontrol geliştirilmiştir. Bu bir vektör kontrolüdür ve amaç, rotor ve stator manyetik akılarını rotorun her pozisyonu için birbirlerine 90° derecede tutmaktır. Bu durumda moment değeri maksimum olur. Bunu yapmak için, stator akımının moment ve akı bileşenleri birbirinden ayrılır ve moment bileşeni maksimum seviyede tutulmaya çalışılır. Bu hesaplamalarda, Clarke ve Park gibi bazı dönüşüm matrisleri kullanılmaktadır. Algılayıcısız alan yönlendirmeli kontrolde, rotor pozisyon

kestirimi, Hall algılayıcısı kullanmak yerine, stator sargılarındaki zıt elektromotor kuvvet (BEMF) sinyalini gözlemleyerek elde edilir. Algılayıcısız alan yönlendirmeli evirici sistemler, endüstri, beyaz eşya, ulaşım, askeri gibi geniş bir kullanım alanı vardır. Sessiz ve daha yumuşak motor kontrolünü mümkün kılar.

Bu tezin ilk bölümünde literatür taraması gerçekleştirilmiştir. PMSM, evirici sistemleri ve kontrol yöntemlerinin 1962'den günümüze kadar olan gelişim süreci araştırılmıştır. Literatürde, verim ve yumuşak kontrol ile ilgili sürekli bir gelişim olduğu gözlemlenmiştir.

İkinci bölümde ise de kalıcı mıknatıslar ile ilgili araştırma yapılmıştır. Yumuşak ve sert kalıcı mıknatısların özellikleri, grafikler ve denklemler verilmiştir. Malzeme biliminin gelişmesi ile birlikte daha verimli kalıcı mıknatısların üretildiği görülmüştür.

PMSM ile ilgili araştırma üçüncü bölümde verilmiştir. Tarihi, çalışma ilkesi ve kullanım alanlarından bahsedilmiştir. Yüzey mıknatıslı, gömülü, spoke, ve şebeke kalkışlı PMSM türleri ile ilgili araştırma yapılmıştır. Her bir motor tipi farklı kullanım alanı için uygundur. Örnek olarak bazı tipler yüksek hızlı çalışma için uygunken, bazı tipler ise yüksek güç yoğunluğu gerektiren uygulamalar için daha uygundur.

Dördüncü bölümde ise dinamik kontrol ele alınmış ve elektriksel model verilmiştir. PMSM için rotor ve stator referans çerçeve dönüşümleri, indüktans, halkalanma akısı, gerilim, akım ve moment denklemleri detaylı bir şekilde verildi. Ana denklemler, PMSM sürücü devresinin yazılım kısmında kullanılmıştır.

Alan yönlendirmeli kontrol beşinci bölümde ele alınmıştır. Diğer bir kontrol yöntemi olan altı adım kontrol de karşılaştırma için verilmiştir. Kontrol yönteminin dinamik performans üzerindeki pozitif etkisinden bahsedilmiştir. Evirici sisteminde kullanılan uzay vektör modülasyonu, denklem ve ilgili grafikler sunulmuştur. Sonunda da tezde kullanılan BEMF tabanlı algılayıcısız kontrol algoritması verilmiştir. Tüm bu kontrol akışı evirici algoritmasına daha sonra uyumlu hale getirilmiştir.

Altıncı bölümde ise donanım tasarımı bütünüyle ele alabilmek adına, öncelikle eviricinin ana donanım blok şeması çıkarılmıştır. Bu şemaya göre ilk bölüm elektromanyetik uyumluluk (EMC) filtre devresidir. X ve Y tipi kondansatörler, ortak ve fark modu indüktörleri EMC regülasyonu için eklenmiştir. Fark modu indüktörü aynı zamanda harmonik filtre işlevi de görmektedir. Bunların yanı sıra, sigorta ve varistör gibi koruma bileşenleri de devreye eklenmiştir. Negatif sıcaklık katsayılı direnç (NTC) de kartın ilk enerjilendirilmesi sırasında oluşacak ani hücum (inrush) akımını limitlemek için konulmuştur. Elektrolitik kondansatör şarj oldıktan sonra NTC röle vasıtası ile kısa devre edilerek NTC üzerinde oluşacak kayıp engellenmiştir. Enerjinin kesilmesinden sonra X kondansatörünü boşaltmak için de boşaltım direnci kullanılmıştır. İkinci donanım bölümü ise doğrultma devresidir. Köprü diyodu ve elektrolitik bara kondansatörü içeren devre şebeke geriliminin doğrultulmasını sağlamıştır. 15V gerilimi anahtarlamalı güç kaynağı (SMPS) devresi ile oluşturulmuştur. Bu gerilim ile güç modülünün kapı işaretlerinin ve doğrusal regülatörün beslemesi sağlanır. Alçaltıcı çevirici topoloji olarak tercih edilmiştir. 5V gerilim ise doğrusal regülatör diğer adı ile de LDO vasıtası ile üretilir. Mikro denetleyici, Op-Amp ve diğer bileşenler bu gerilim ile beslenmektedir. Şönt dirençleri üzerinden akım geçmesi ile oluşan gerilim, önceden belirlenen kazanç ile çarpılarak Op-Amp vasıtası ile mikro denetleyiciye gönderilir. Offset gerilimi de bu gerilime eklenerek şönt üzerinde oluşacak negatif gerilimlerin okunması sağlanır. 2.5V değerindeki bu gerilim tampon devresi ile üretilmiştir. Evirici bölümü sürücü sistemin en önemli bileşenidir. Bu kısımda akıllı güç modülü olan akıllı güç modülü (IPM)

anahtar tipi olarak tercih edilmiştir. Altı anahtar ve onların sürücülerini içerir. Bunlara ek olarak da modül, kısa devre ve sıcaklık korumalarını içerir. Algılayıcız alan yönlendirmeli kontrol mikro denetleyici içine gömülü olan algoritma ile koşturulur. Altı adet darbe genişlik modülasyonu (PWM) işareti Op-Amplardan mikro denetleyiciye gelen akım geribeslemesi doğrultusunda üretilir. Rotor hızı, hız referans devresinden gelen kare dalganın frekansı okunarak karar verilir. Devre üzerinde analog ve yazılımsal olarak aşırı akım, aşırı gerilim ve aşırı sıcaklık gibi korumalar mevcuttur.

Şematik ve PCB tasarımı Altium Designer programı kullanılarak gerçekleştirilmiş ve yedinci bölümde verilmiştir. Sürücü kartı için FR4 tipi ve çift katlı PCB kullanılmıştır. PCB 155x150mm boyutundadır. Şematik ve devre sonra on adet PCB basılmış ve bunlardan iki adedinin dizgisi gerçekleştirilmiştir.

Yedinci bölümde ise sürücü kartın PSIM yazılımı ile benzetim çalışmaları verilmiştir. Donanım ve kontrol blokları oluşturulmuştur. Faz akımı algılayıcı kullanılarak algılanmıştır. Gerçek uygulamada ise algılayıcısız algoritma adapte edilmiştir. Simülasyon, 1300 rpm, 2000 rpm ve 3000 rpm hızları için gerçekleştirilmiştir. Simülasyonda, faz akımları ve gerçek rotor hızı incelenmiştir.

Algılayıcısız alan yönlendirmeli kontrol algoritmasının evirici kartına gömülme çalışmaları sekizinci bölümde yer almaktadır. Yazılım, Clarke ve Park dönüşümleri gibi klasik fonksiyonlar içermekle birlikte DA bara dalgalanması etkisini azaltma fonksiyonu gibi özel fonksiyonlar da içermektedir. BEMF gözleyicisi yardımıyla, faz akımları kullanılarak rotor pozisyonu belirlenir.

Dokuzuncu bölümde ise, evirici kartı kompresör kullanılarak test düzeneğinde çalıştırılmıştır. Faz akımı, bara gerilimi, PWM işareti gibi birçok ölçüm alınmıştır. Hız referans değeri de benzetimlerdekine karşılaştırma yapabilmek için aynı tutulmuştur.

Son bölüm olan onuncu bölümde ise, benzetim ve gerçek sistem algoritma ve ölçüm sonuçları karşılaştırılmıştır. Bazı farklılıklar gözlemlenmiş ve bunlar da yorumlanmıştır. Algoritma olarak düşünülürse, benzetimde algılayıcı kullanılarak alan yönlendirmeli kontrol yapılmıştır. Başlangıç durumunda ise maksimum moment algoritması vardır. Gerçek uygulamada ise algılayıcısız olarak alan yönlendirmeli kontrol yapılmıştır ve hizalama, açık çevrim ve kapalı çevrim gibi bölgelere sahiptir. Gerçek kompresör sisteminin sistem dinamiğinden dolayı modellenmesinin zor olduğu görülmüştür. En sonunda da ölçümler yorumlanarak akım harmonik bozunumunun iyileşmesine yönelik çalışmalar yapılarak gelecekte yapılacak olası çalışmaların önü açıldı.

1. INTRODUCTION

1.1 Purpose of the Thesis

The purpose of this thesis is to design an inverter board with a sensorless field oriented control (FOC) algorithm and drive a PMSM with a compressor system using this inverter board. Model of the board is simulated and realized. Finally, measurements are taken, and some comparisons are made. The background of the subject is studied in detail to acquire the design inputs for the inverter board before starting to design, simulate and verify the inverter board.

1.2 Litereture Review

Cahill and Adkins (1962) implemented the first prototype of a PMSM by modifying an induction motor. The cage rotor of an induction motor (IM) was replaced by permanent magnets. They conducted the performance analysis and obtained the mathematical modelling for a PMSM. The permanent magnets of these motors were inserted into the rotor and the surface of the rotor was covered with the rotor cage. Because of the existence of the permanent magnet, reluctance torque which has the opposite magnitude concerning a wound rotor synchronous motor was arisen [1].

Slemon (1971) analyzed a PMSM in terms of electromagnetic perspective and derived equations [2].

Rahman (1979) analyzed a PMSM that had a cage rotor structure. This motor was operating at a fixed grid frequency which is 60 Hz. A steady state-analysis of a PMSM was accomplished in this study [3].

Richter (1979) analyzed the power density limitation of a PMSM. He used rare-earth cobalt in the rotor as a permanent magnet in a PMSM [4].

Honsinger (1980) analyzed a PMSM performance considering effect of iron loss. The startup condition of a PMSM with load was studied dealing with the effect of a permanent magnet and cage torque. Components of sub-synchronous torque were

analyzed with detailed explanations. Performance analysis of single-phase PMSM was obtained in terms of starting and steady state operations [5].

Miller (1981) observed transient torque characteristics in starting condition. Different rotor designs were handled while doing it. He analyzed the synchronization of the rotor and revealed the criteria's of that condition [6].

Rahman, Little and Dash (1981) analyzed starting characteristics of a PMSM. d, q axis equations were used in a PMSM model with damper windings. Considering the saturation effect on the q axis, they designed a PMSM. It was pointed out that, usage of cage structure in rotor increases the probability of saturation because of rotor induced currents [7].

Slemon and Gumaste (1981) made a steady state analysis of a PMSM which was fed with voltage and current source inverter [8].

Weschta (1982) investigated the effect of various motor designs on the performance of the driving systems. Back EMF and current patterns were taken into account in order to achieve constant output power. To get maximum performance, the motor inductance value was calculated at the optimum point [9].

Pfaff, Weschta and Wick (1982) analyzed a PMSM and offered new design techniques in order to decrease rippled torque value. The volume of permanent magnets was recalculated for best performance. To get fast response for different load conditions of a PMSM, a low moment of inertia was aimed to implement [10].

Takeda, Morimoto and Hirasi (1983) made a field analysis of a PMSM using lumped and distributed parameters of a PMSM [11].

Binns and Wong (1984) used the finite elements method (FEM) in order to analyze motor performance. They conducted FEM analysis with various motor designs [12].

E. Richter, T.J.E. Miller and T.W. Neumann (1984) compared an induction motor and a PMSM in terms of efficiency and power factor. A PMSM was confirmed as the best choice for both topics. The possibility of replacing an induction motor with a PMSM and economic recovery of this implementation were also investigated [13].

Chalmers, Hamed and Baines (1985) offered to get magnetic circuit parameters of a PMSM with a systematic approach. They aimed to predict the steady state characteristics of a PMSM [14].

Neumann and Tompkins (1985) pointed out the effect of changing parameters for the performance of a PMSM. They were analyzed the effect of usage of different magnetic materials and their combinations such as NbFeB magnets in a PMSM [15].

Enjeti, Lindsay and Rashid (1985) derived a PMSM model based on dynamic characteristics with no damper windings. In this study, a linear d-q transformation circuit model for a surface mounted PMSM was used [16].

Lajoie-Mazenc, Villaneuva and Hector (1985) conducted a detailed study on the drive performance of inverter systems. They investigated complementary switching and loss modulation in the inverter system of a PMSM. In this study, damper windings were not used; therefore, synchronous motor torque was only torque for a PMSM at starting condition [17].

Rahman and Osheiba (1986) studied self-starting characteristics of a PMSM in the situation of variable parameters [18].

Sebastian, Slemon and Rahman (1986) studied a flux weakening of inverter driven a PMSM in order to operate a PMSM above its rated speeds. They investigated operating limits when applying flux weakening to a PMSM [19].

Pillay and R. Krishnan (1987) proposed a complete model in order to simulate, control and analyze a whole drive system based on vector controlled PMSM. In this system, the state-space model of a PMSM was used. Real-time models of the system which included speed controller, switching patterns of inverter and vector control flow diagram were offered [20].

Krause, Nucera, Krefta and Waynczuk (1987) obtained admittance matrixes and phasor diagrams of a PMSM and analyzed the performance of the motor. They investigated 180^o phase-controlled voltage inverter and derived torque and voltage equations of a PMSM [21].

Pillay and Krishnan (1987) handled a PMSM and a BLDC motor and compared motors each others in terms of different characteristics [22].

Bose (1987) proposed a complete control strategy for 70 HP internal a PMSM. Vector control was used to produce constant torque; whereas, square wave currents were applied to a PMSM in order to get constant power from a motor [23].

Demerdash, Hijazi and Arkadan (1988) gave the computing technique of winding inductance of a PMSM [24].

Hijazi and Demerdash (1988) analyzed a PMSM with damper winding considering current density distributions and space harmonics [25].

Pillay and R. Krishnan (1988) designed a microprocessor-based speed controller. Z-transform was used in the digital modelling. Analog circuitry and digital speed controller were combined and different sampling rates were tried in this study [26].

Colby (1988) classified inverted driven a PMSM considering power electronics circuit design, motor design, current and commutation control and main motor control approach. He also compared a BLDC motor and a PMSM in terms of power density, torque per unit current, speed range, feedback devices, inverter rating, cogging torque, ripple torque and parameter sensitivity. Braking capacity, losses and thermal characteristics of these motors were also handled [27].

Schiferl and Lipo (1988) analyzed the power capability of the machine considering the effect of the d-q reactance and open-circuit voltage of a PMSM by using a lossless equivalent circuit. This study also contained enhancement of speed, torque and power capability of a PMSM [28].

Zeid (1998) designed an interior PMSM driver based on FOC, In control strategies, the outer control loop was used as a speed control loop; whereas, an inner loop was used to control direct (d) and quadrature (q) axis current using a PI controller. High-speed DSP was used as a controller [29].

Bolognani, Oboe ve Ziglitto (1999) designed a sensorless interior PMSM driver to get a wide flux-weakening region. An Extended Kalman Filter was used to estimate rotor angular speed and position in this study [30].

Jin, Yong, Goo (2001) proposed an adaptive speed controller for a PMSM using FOC. It was aimed to minimize required motor parameters using FOC. The control algorithm has been simplified. A simple current controller with three-level comparators was also proposed [31].

Hwang, Kim, Kim, Baek (2001) studied an optimization method using the multiple responses optimization. Factor decision, design of experiment, regression analysis, response surface design, optimization process, and capability analysis were steps of optimization. Acoustic noise and power consumption were aimed to reduce with this study [32].

Perera, Petersen, Blaabjerg, Thøgersen (2003) implemented sensorless V/f control method for pump and fan applications. The negative effect of the absence of damper winding in certain applied frequency was aimed to eliminate in wide operation range with this study [33].

Sun, Shi, Wang, Wang (2005) proposed a digitized servo control system for a PMSM based radar driven system. DSP and CPLD were used to control the system. A SVPWM was a switching technique for FOC in this study [34].

Jiang, Zhang, Liang, Liu (2005) designed a digital servo system using MC56F8357. DC bus ripple compensation, digital PI regulating with correction of the integral term and AntiHunt Processing control strategies were included in a FOC strategy [35].

Zhou, Li, Yang and Yan (2007) proposed the sliding model speed observer in order to estimate rotor angular speed and position reliably in both high and low-speed applications. Required low pass filter and shaft encoder was eliminated using this sensorless FOC method [36].

Song, Liu, and Luo (2008) studied FOC for a PMSM based on HIL simulation. A mathematical model was constructed considering iron losses. 3.7 KVA VSI and 8-poles 1KW PMSM were used in the design. MATLAB/Simulink is used for programming the real-time control module [37].

Simanek, Novak, Cerny and Dolecek (2008) analyzed control algorithm for a PMSM which was used in the light rail vehicles. A wide operation range was aimed for traction application with FOC based algorithm. Experiments were conducted with a 58 kW PMSM prototype [38].

Zhang and Feng (2008) studied on speed and position estimation for a PMSM using EKF based sensorless FOC. Different types of covariance matrixes were observed in order to get higher dynamic performance. The effect of changing of motor parameters was also investigated for optimum performance [39].

Accetta, Cirrincione, Pucci and Vitale (2009) proposed a signal injection method to detect machine saliency. Motor position and speed were obtained using a difference of axis inductances. Both rotating and pulsating voltage carrier injection methods by a neural adaptive band filter were taken into account to determine optimum performance solution [40].

El-Sousy (2010) designed a new robust motion-control system based on a hybrid H∞-based wavelet neural network (WNN) position tracking controller for a PMSM. Usage of both WNN and H∞ together enhanced the performance of a PMSM in terms of robustness and overcoming the uncertainties of the servo drive [41].

Rahimi, Abbaszadeh and Radan (2010) developed a new algorithm that was based on Fourier analysis. It was aimed to reduce torque ripple and current harmonics using a simple harmonic computation method for surface mounted PMSM with FOC. Non-sinusoidal currents were injected into a PMSM in order to reduce torque ripple which was caused by non-sinusoidal back electromotive force [42].

Kangkang, Jianqiu, Minggao, Jing and Yan (2011) studied performances of plug braking and regenerative braking of a PMSM. Maximum braking torque, braking torque ripple and the feedback power of braking energy have been taken into account in performance analysis. Six step commutation and FOC techniques were compared to each other for performance [43].

T. Wang, Y. Guo J. Zhu, Y. Zhang (2012) analyzed a PMSM with different control methods which were FOC, DTC and MPC. The steady state performances under a range of sampling frequency of each method were simulated. Sampling frequencies were applied between 1.5 kHz and 20 kHz. Results were compared and torque ripple was reduced for all control methods when sampling frequency increased [44].

Wang, Li, and Xu (2014) proposed a new model to enhance starting performance of a PMSM. In the classical model, a PMSM had been driven with the V/f control method until reaching a certain speed because the BEMF estimation method for sensorless control had a drawback in the low-speed regions. A position open loop constant current (I-F) method was developed instead of the V/f control method. Torque current feedback control method was applied in I/f until switching to BEMF-based sensorless FOC [45].

Savadkoohi, Khaburi, and Sadr (2015) introduced a new switching method for inverters. In the classical switching method, MOSFET or IGBT in inverters had been switched in constant frequency and this had caused narrow-band harmonics. Acoustic noises and EMI had been generated because of narrow-band harmonics. With proposed random-switching PWM techniques, this narrow band harmonics in the current spectrum were spread over all current spectrum. Classical and proposed switching patterns were compared and this spread of harmonic content reduced acoustic noises and EMI [46].

Kung and Risfendra (2016) proposed to combine the I/f startup method and EKF based sensorless FOC for PMSM. Initial rotor position and PMSM parameters were not needed in the I/f control method and I/f was appropriate for low-speed regions; whereas, in medium and high-speed regions, EKF based sensorless FOC was suitable. By using two control methods together, control of a PMSM in a wide speed range has become possible [47].

Tau and Tzou (2017) designed a mixed dq-control method for a sensorless PMSM drive in order to increase the input power factor. In this study, a very small film capacitor was used as a DC bus capacitor instead of using a bulky traditional

electrolytic capacitor. Although using film capacitor in DC bus increased torque ripple, this electrolytic capacitor-less design was more suitable for applications with large-inertia load such as fan and pump systems. Inverter input current was controlled with dq currents in order to overlap with the phase voltage so the power factor was increased [48].

Li, Zhang, Hang, Ding, Liu and Wang (2018) compared MPC and FOC control strategies for a PMSM in order to observe the dynamic performance of the motor. Both continuous and discrete-time analyses were used for these two control methods. In terms of overshoot, peak and stable time of speed and torque, MPC gave better dynamic performance than FOC [49].

Chethan and Kumaran (2019) compared sinusoidal pulse width modulation (SPWM) and space vector pulse width modulation (SVPWM) in voltage source inverter (VSI) drive for PMSM with the field oriented control. Driver was analyzed in MATLAB/Simulink tool under the different speed conditions. According to analysis, SVPWM enables to drive PMSM with less voltage and current harmonic distortion. In addition to that, speed response under torque variation is also enhanced in SVPWM [50].

Nicola, Nicola and Duta (2020) designed sensorless control method for PMSM where Multiple Artificial Neural Networks (MANN) is utilized in the speed controller. Sliding Mode Observer (SMO) is also used in order to determine rotor speed. Load torque observer is implemented and variation of load torque is tracked and divided into sub intervals. Reference current values are generated for each interval by PI controllers and saved as a vector. These vectors are used to train Multiple Artificial Neural Networks. This control method is compared with classical field oriented control in simulation. Higher performance is acquired under variation of the load torque [51].

Zuluaga, Riba and Garcia (2021) studied on the estimation of PMSM electromagnetic parameters by implementing a new method. In classical method, the finite elements method (FEM) is generally used to extract the motor parameter. However, this new method is based on analyzing the motor at the full operation range and acquiring motor parameters as a function of the load condition by considering dq electrical model. The differential power factor which is caused by harmonic distortion is considered on parameter estimation. Geometry information of a motor, knowing the rotor position and sensors are not needed for implementation of the method. The method was tested by using two PMSM and consistent and accurate results were acquired [52].

Tian, Molinas, An, Zhou and Wei (2022) constructed a new sensorless field oriented control algorithm for five phase PMSM that operate under single phase IGBT failure. The theory is based on utilizing freewheeling current that flows in the failed phase. BEMF value is estimated and position/speed information is determined by using second order generalized integrator with a frequency-locked loop. This method is proven both theoretically and experimentally at the mid and high speeds under internal and external disturbances [53].

2. PERMANENT MAGNETS

Magnetic materials are basically classified into two types which are soft magnetic materials and the hard magnetic materials. Soft magnetic materials can be magnetized and demagnetized easily unlike the hard magnetic materials [54]. Permanent magnets (PM) are considered as hard magnetic materials that can strongly keep their magnetized states after the magnetization process.

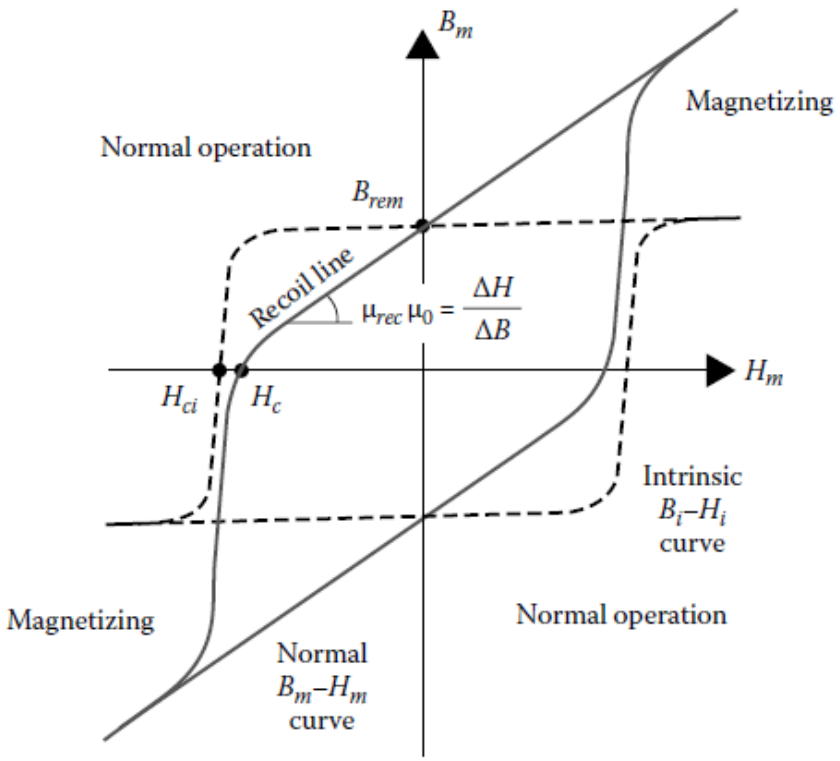

Figure 2.1: Hard magnetic material hysteresis loop and characteristic parameters [54].

The hard magnetic materials have a very large magnetic hysteresis loop as given in Figure 2.1. Quadrant I or III are the magnetizing area of the PMs; whereas, quadrant II or IV are the operation areas of the PMs. Dashed lines represent intrinsic hysteresis loop and a solid line represent normal hysteresis loop in Figure 2.1. Magnetic flux which is produced by the PM materials is represented in the intrinsic curve and the total magnetic flux which is the combination of the air and the PM is represented in

the normal curve. The residual flux density *(B_r)* and the coercive force *(H_c)* are two significant parameters of PMs. The residual flux density is the flux density of the PM while there is no external magnetizing field. The coercive force is the minimum value of an external opposite magnetic field in order to demagnetize the PM. The recoil line is the operation area of the PM. The operation area in the recoil line depends on load condition. As load increases, the operation point goes to the H_c due to increasing of stator current. The differential relative magnetic permeability of the recoil line is labelled μ_{rec} and is slightly higher than unity. Equation (2.1) can be used to determine the recoil line:

$$B_m = B_r + \mu_{rec}\mu_0 H_m \tag{2.1}$$

B_m : magnetic flux density [T]
B_r : residual flux density [T]
μ_{rec} : relative magnetic permeability of the recoil line
μ_0 : permeability of free space [H/m]
H_m : magnetic field intensity [A/m]

The PM energy product can be found by multiplying B_m and H_m. The PM is demagnetized by the external system if the operation point moves from B_r to H_c. On the other hand, the PM is magnetized by the external system if the operation point moves from H_c to B_r. These magnetizing and demagnetizing processes are reversible if the operating point remains on the recoil line. If the demagnetizing field goes beyond H_{ci}, which is called an intrinsic coercive field, the PM materials lose all their magnetic properties and there is needed to implement a new magnetizing process. In every PMSM, $H_{ci} > H_c$ is always met [55].

Table 2.1: Main properties of some hard magnetic materials [54].

	B_r (T)	H_c (kA/m)	Curie T (°C)	Operating T_{max} (°C)	Density (kg/m3)	$\{B_m H_m\}$max (kJ/m^3)
Ferrite	0.38	250	450	300	4800	30
AlNiCo	1.20	50	860	540	7300	45
SmCo	0.85	570	775	250	8300	140
NdFeB	1.15	880	310	180	7450	260

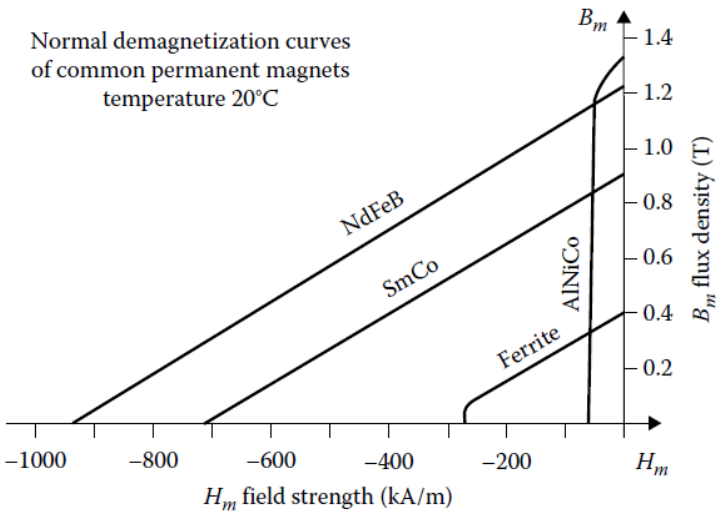

Figure 2.2: Demagnetization curves of PM materials [54].

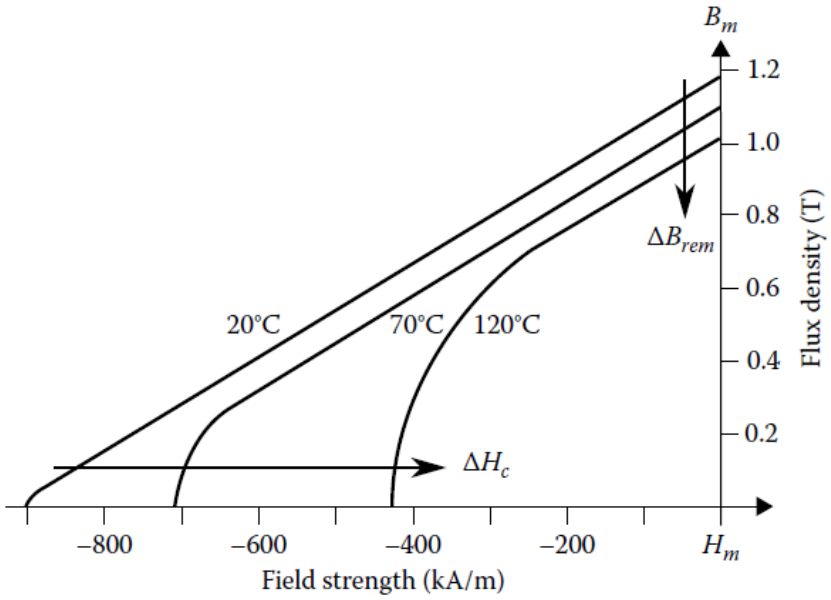

Figure 2.3: Effect of temperature on PM demagnetization curve [54].

3. PMSM TYPES

The first design attempts of a PMSM were made around the 19th century. Very low quality hard magnetic materials were used such as steel and tungsten. AlNiCo was invented in 1932 and it was used in excitation in small power DC commutator motor. With the production of high energy density PM, dc machines with a PM field excitation have been started to develop in 1950s. The use of a PM in the production of a magnetic field instead of conventional excitation winding has made the electrical machines more compact. Slip rings and brush assembly disappeared as using a PM in rotor structure. With the removal of the brush system, the amount of maintenance has been reduced by 90 percent. With the appearance of switching power transistors and silicon-controlled rectifiers, the mechanical commutator driving system was replaced by an inverter-based driving system in the later part of 1950s. The development of a PM materials and switching devices had a considerable effect on the development of a PMSM and brushless DC machines. The armature of the DC machine need not be on the rotor if electronic control is used instead of a mechanical commutator. Better cooling and reaching high voltage can be achieved if the stator is used as the armature of the machine. Because stator has more clearance space for thermal dissipation and insulation.

There are many advantages of using a PMSM. There are no excitation losses due to the absence of the field winding. Hence, the efficiency of the motor is increased. A PMSM has higher power and torque density if compared with other types of motor. Higher dynamic performance is obtained. Higher flux density is generated in the air gap thanks to PM materials. Comparing PMSM and PM commutator motor with the same output power, a PMSM can be produced with a smaller volume of about 40..50% than a PM commutator motor [56].

A PMSM can be produced in a wide power range from a few milliwatts to megawatts. A PMSM is frequently encountered in many fields. Some application areas and subtitles of these areas are as follows.

- Industry

- ✓ Robots, servo drives, pumps, fans, blowers, compressors

- Public life
  - ✓ air conditioning, automatic teller machine, barcode scanner at the supermarket
- Domestic life
  - ✓ Refrigerators, dishwasher, washing machine, vacuum cleaners, cellular phone
- Office equipment
  - ✓ Printers, scanners, computers, photocopies
- Transportation
  - ✓ Elevators, light railways, electric cars, electric ships, electric aircraft
- Military
  - ✓ Tanks, radar systems, submarines, rockets

Electrical motors in a vehicle shown in Figure 3.1 can be given as an example of the usage area of a PMSM.

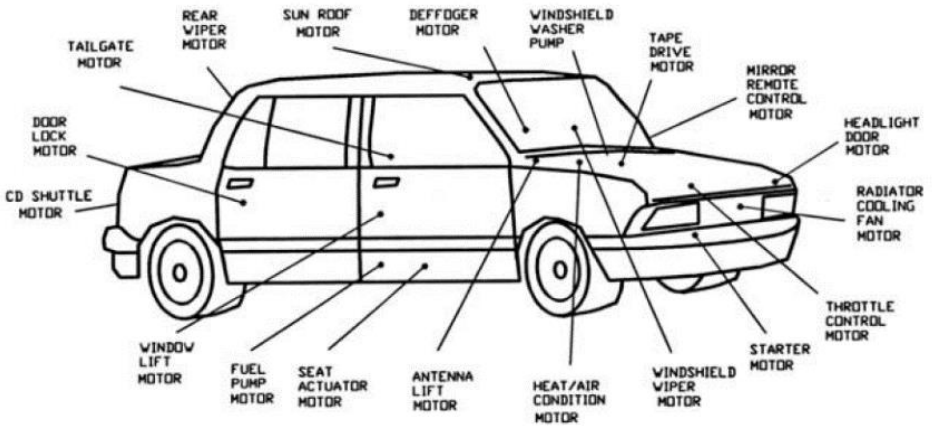

Figure 3.1: PMSMs in a vehicle [57].

A PMSM can be basically classified into two categories based on the direction of field flux. If the flux direction is along the radius of the machine, this is called as a radial field motor. Whereas if the flux direction is parallel to the rotor shaft, this is also called as an axial field motor. The use of radial field PMSM is more common. However, the axial field PMSM has higher power density and acceleration capacity than the radial field PMSM and this type of machine is used in specific high performance applications.

The placement of PM in the rotor defines the type of the motor. Surface mounted PMSM with a radial field is more preferable in high power applications. Interior PMSM is frequently used in high speed applications. Regardless of the placement of the PM in a rotor structure, the operating principle of the motors is the same. Placement of the PM basically causes direct (d) and quadrature (q) axes inductance values to be different. The direct axis is defined as a rotor magnetic axis. This axis is parallel with a magnetic field of a rotor. Direct inductance is the inductance value measured when the flux of the permanent magnet and the stator flux are aligned. On the other hand, quadrature inductance is the inductance value measured at the intersection of stator and rotor flux by 90°. Inductance can be found as using equation (3.1).

$$L = \frac{\lambda}{I} = \frac{N\Phi}{I} = \frac{NF}{I\Re} = \frac{NNI}{I\Re} = \frac{N^2}{\Re} = \frac{\mu_o \mu_r N^2 A}{l} \tag{3.1}$$

L : inductance [H]

λ : flux linkage [Wb]

I : current in the coil [A]

N : number of turns

Φ : flux [Wb]

F : MMF [A.t]

$\Re$: reluctance [A.t/Wb]

μ_o : permeability of free space [H/m]

μ_r : relative permeability of the ferromagnetic material

ℓ : length of the flux line [m]

A : area of the cross-section [m^2]

Reluctance can be also found as using equation (3.2).

$$\Re = \frac{\ell}{\mu_o \mu_r A} \tag{3.2}$$

$\Re$: reluctance [A.t/Wb]

ℓ : length of the flux line [m]

μ_o : permeability of free space [H/m]

μ_r : relative permeability of the ferromagnetic material

A : area of the cross-section [m^2]

If only the air gap and magnet reluctance are taken into account and reluctance of the iron is ignored, the ratio of the direct axis and quadrature axis reluctance are basically calculated as using equation (3.3).

$$\frac{\Re_d}{\Re_q} = \frac{\ell_g + \ell_m}{\ell_g} \tag{3.3}$$

$\Re_d$: direct component of the reluctance [A.t/Wb]

$\Re_q$: quadrature component of the reluctance [A.t/Wb]

ℓ_g : air gap length [m]

ℓ_m : thickness of the magnet [m]

Magnet thickness is much bigger than the air gap in a PMSM. It is obviously seen in equation (3.3) that the direct axis reluctance is always bigger than the quadrature axis reluctance. If it is needed to say that differently, the effective air gap of the direct axis is multiple times that of the effective air gap of the quadrature axis. As a result of that, considering equation (3.3), inequality (3.4) can be found:

$$L_{qs} > L_{ds} \tag{3.4}$$

L_{qs} : quadrature component of the stator inductance [H]

L_{ds} : direct component of the stator inductance [H]

Although the quadrature axis inductance is always greater than the direct axis inductance in PMSM, there is the opposite situation in a wound rotor salient synchronous motor. In this motor, there is embedded excitation winding in rotor slots. This winding is aligned with the direct axis. There is a uniform and small air gap between the direct axis and stator. On the other hand, the quadrature axis has non-uniform and big air gap. This difference causes the quadrature axis inductance to be much smaller than the direct axis inductance, unlike a PMSM.

3.1 Surface Mounted PMSM

Surface mounted PMSM is shown in Figure 3.2. Magnets are mounted on the outer surface of the rotor in this type of motor. The magnetic flux of magnets directly penetrates through the air gap without facing rotor lamination. Therefore, air gap has a high flux density. On the other hand, lower structural integrity and mechanical robustness can be counted as the drawbacks of this type of motor. Magnets are exposed to external mechanical influences. Besides, magnets face the danger of being demagnetized.

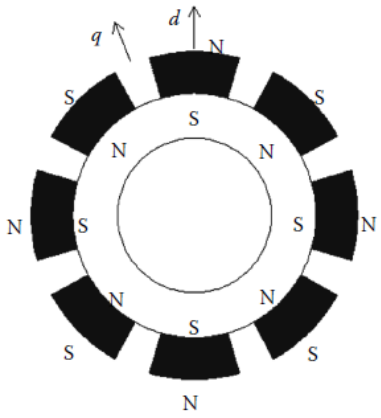

Figure 3.2: Surface mounted PMSM [57].

Surface mounted PMSM is not used in high speed applications, greater than 3000 rpm, due to mechanical weakness of placement of magnets. However, surface mounted PMSM with a small rotor diameter can be used in some special high speed applications. In order to prevent from demagnetizing action of armature reaction and centrifugal forces, an external and high conductivity nonferromagnetic cylinder can be placed on the outer surface of the rotor. This structure also provides asynchronous starting torque to the motor as if used a damper winding. There is a small difference in the reluctance value of the direct and quadrature axis due to the placement of magnets. Approximately less than 10% difference is observed in direct and quadrature axis inductance values.

3.2 Surface Insert PMSM

Surface insert PMSM is shown in Figure 3.3.

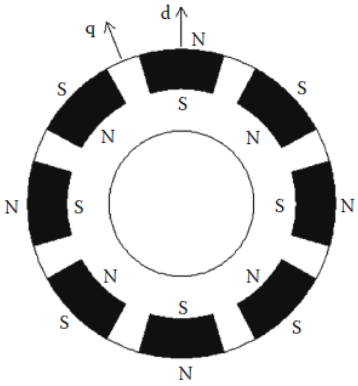

Figure 3.3: Surface insert PMSM [57].

Magnets are embedded on the outer surface of the rotor in surface mounted PMSM. This structure enables to construct the uniform cylindrical surface of the rotor. Nevertheless, structural integrity and mechanical robustness are enhanced if compared with surface mounted PMSM. The ratio between the quadrature and direct axes inductances can reach to between 2…2.5 in surface insert PMSM. EMF induced by the PM in surface insert PMSM is lower than surface mounted PMSM.

3.3 Interior PMSM

Interior PMSM is shown in Figure 3.4.

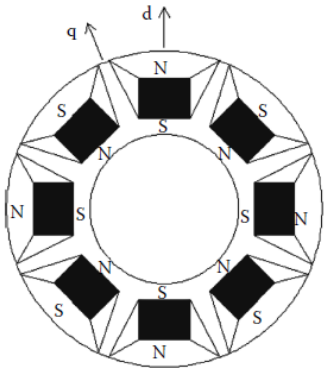

Figure 3.4: Interior PMSM [57].

Magnets are placed inside of rotor lamination with different placement patterns. This type of a motor has excellent structural integrity and mechanical robustness characteristics if compared with the other two types of a motor. The magnets in this motor are more protected against centrifugal force. This feature makes this motor preferable for high-speed applications. These motors have a higher production difficulty. The ratio between the quadrature and direct axes inductances can be up to

three and in addition to that, this ratio can reach much higher for some special interior PM rotor structures. As seen in Figure 3.4, air gap is generated between each two adjacent magnets by removing some steel laminations. It is aimed to prevent the magnetic flux from dispersing from the rotor surface to adjacent magnets as soon as possible. This air isolation is called as a flux barrier. It enables more magnetic flux to reach to stator windings; therefore, mutual flux linkages between stator and rotor are increased. Flux barriers also provide to reduce the weight of the rotor and accordingly reduce rotor inertia. This feature makes this motor suitable for higher acceleration and higher speed applications. The position of magnets is circumferential and perpendicular to the rotor. This arrangement makes the motor large volume and costly. In addition to that, this type of a motor is not applicable for applications that need high energy density. Low-cost ferrite magnets are generally preferred for this placement of magnets. Using this configuration, the total cross-sectional area of magnets is increased if compared surface mounted PMSM. This provides more air gap flux density in the motor. Higher efficiency and small stator currents can be achieved. Briefly, the higher airgap flux density is provided with the drawback of higher rotor volume.

Flux in the rotor lamination does not change with time both surface and interior PMSM. This stable flux value in the rotor causes zero eddy current and hysteresis losses. However, in the real world, there is some flux fluctuation in the rotor due to variation of reluctance caused by stator slots and teeth; therefore, it leads to some core losses which can be ignored in some situations.

3.4 Spoke PMSM

Spoke PMSM is shown in Figure 3.5.

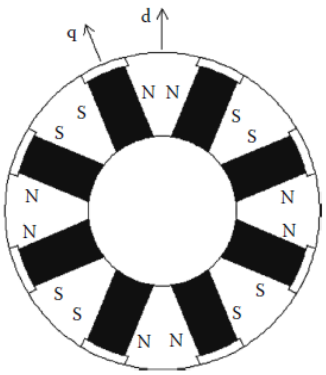

Figure 3.5: Spoke PMSM [57].

PMs are embedded in deep slots and placed circumferentially in the rotor. This arrangement increases the distance between the shaft and the surface of the rotor. Quadrature axis inductance is higher than direct axis inductance in this type of the motor. Cage winding in the rotor pole shoes can be used to provide asynchronous starting torque to the motor. Distance of laminated of iron placed between neighbouring magnets has a significant parameter for design. A nonferromagnetic shaft is most preferable in the applications. As seen Figure 3.6, if the ferromagnetic shaft is used, most of the magnetic flux goes to the shaft and a small part of the flux crosses the air gap and reaches the stator. This unused flux leads to a loss of efficiency. Either a nonferromagnetic shaft or sleeve between a ferromagnetic shaft and rotor core can be used in order to canalize the magnetic flux to the stator.

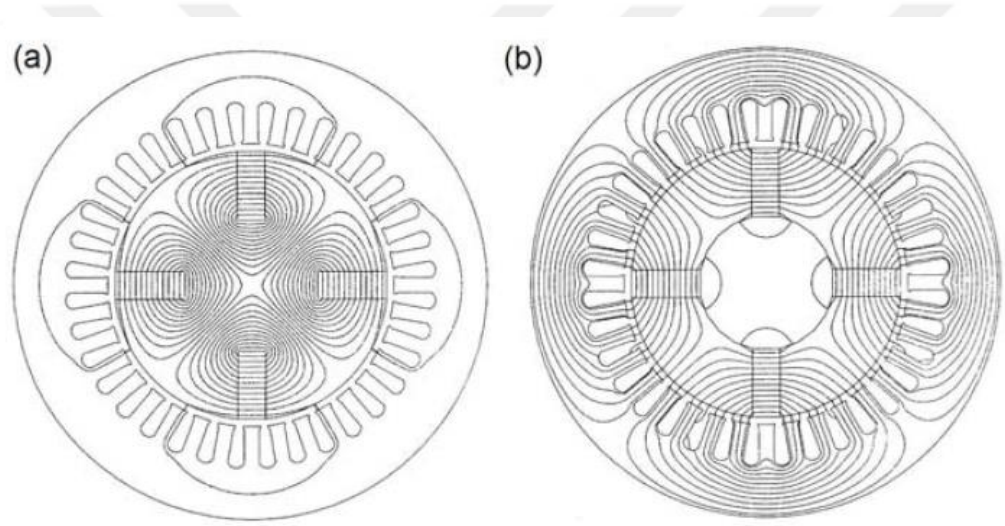

Figure 3.6: Magnetic flux distribution in the cross-section of a spoke PMSM (a) rotor with ferromagnetic shaft (b) rotor with nonferromagnetic shaft [57].

3.5 Line Start PMSM

For constant speed application, line start PMSM can be used. It presents higher efficiency and higher power factor if compared to induction and wound rotor synchronous motor. Line start PMSM has a squirrel cage structure which is called damper winding in order to contribute initial torque for a motor. Voltage is induced in the squirrel cage until reaching synchronous speed. At that speed, there is no induced voltage as well as current in the cage structure; therefore, there is no torque production supplied by the squirrel cage in synchronous speed. This structure also provides natural damping for the oscillations under transient conditions without speed feedback. If the speed tends to lose synchronization, the slip of the rotor takes a nonzero value and

voltage is induced in the squirrel cage. Generated torque accelerates the rotor and the speed of the rotor reaches synchronous speed again.

For variable speed applications, there is no need to use damper winding. Required current for starting and running conditions is supplied by an inverter. Not using the damping winding increases the efficiency of a motor due to the absence of the induced current loss. However, current and position feedback are needed for control of the inverter.

Line start PMSM can be preferable in order to increase the security of the system. For normal conditions, the motor is driven by the inverter; however, in case of failure, the inverter is bypassed and the motor is connected to the grid system and driven by constant frequency thanks to damper winding [56]. Characteristics of a line start PMSM is shown in Figure 3.7.

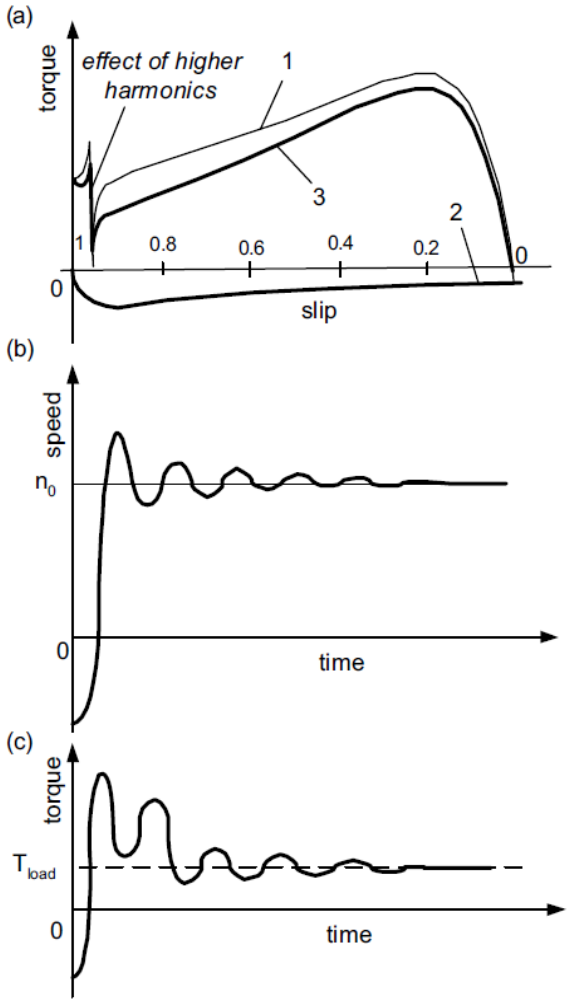

Figure 3.7: Characteristics of a line start PMSM (a) steady state torque–slip characteristic 1: asynchronous torque 2: braking torque produced by PMs 3: resultant torque (b) speed–time characteristic (c) torque–time characteristic [56].

4. DYNAMIC MODEL OF A PMSM

A two-pole and three-phase PMSM is given Figure 4.1. Stator windings are connected as wye and there is a PM in the rotor structure. Stator windings are displaced at 120°. Each winding has N_s equivalent turns and resistance r_s so all three winding are the same. The stator windings will be considered to be distributed as sinusoidal in the analysis.

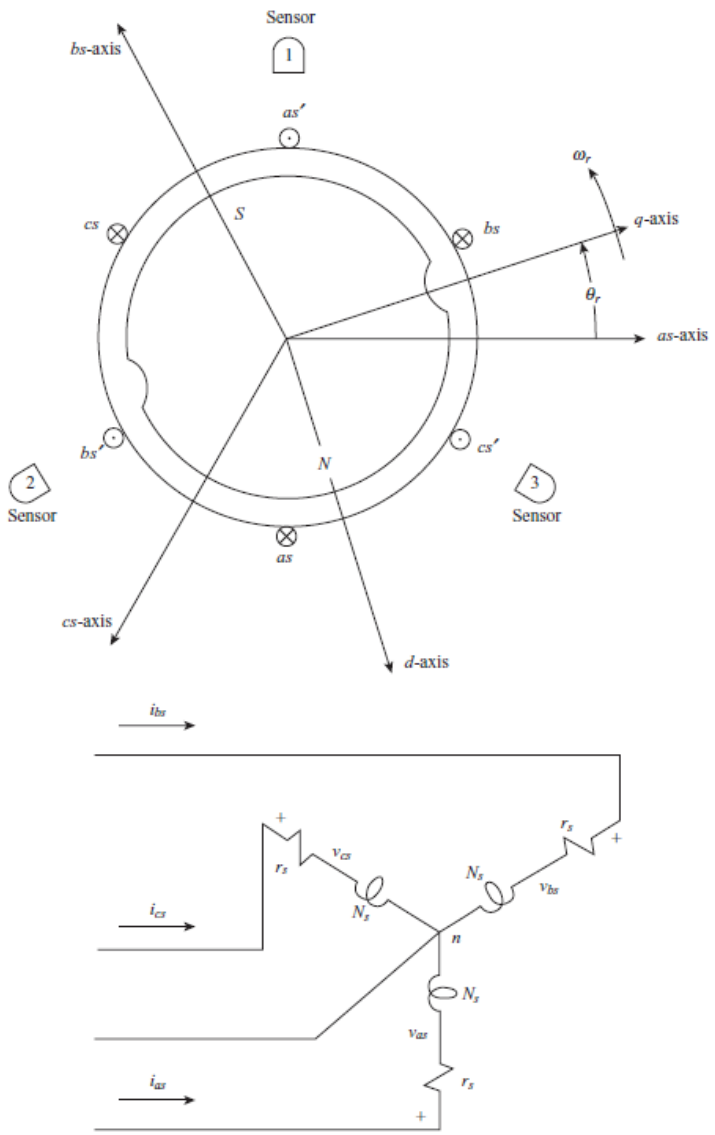

Figure 4.1: Two-pole, three-phase permanent-magnet AC machine [58].

The voltage equations of a PMSM are written as,

$$\boldsymbol{v}_{abcs} = \boldsymbol{r}_s \boldsymbol{i}_{abcs} + p\boldsymbol{\lambda}_{abcs} \tag{4.1}$$

$\boldsymbol{v}_{abcs}$: matrix of the stator voltages [V]

$\boldsymbol{r}_s$: matrix of the stator resistances [Ohm]

$\boldsymbol{i}_{abcs}$: matrix of the stator currents [A]

p : derivative operator

$\boldsymbol{\lambda}_{abcs}$: matrix of the stator flux linkages [Wb.t]

Where,

$$(\boldsymbol{f}_{abcs})^T = [f_{as} \quad f_{as} \quad f_{as}] \tag{4.2}$$

$$\boldsymbol{r}_s = diag[r_s \quad r_s \quad r_s] \tag{4.3}$$

The flux linkages are given as,

$$\boldsymbol{\lambda}_{abcs} = \boldsymbol{L}_s \boldsymbol{i}_{abcs} + \boldsymbol{\lambda}'_m \tag{4.4}$$

$\boldsymbol{\lambda_{abcs}}$: matrix of the stator flux linkages [Wb]

$\boldsymbol{L_s}$: matrix of the stator inductances [H]

$\boldsymbol{i_{abcs}}$: matrix of the stator currents [A]

$\boldsymbol{\lambda'_m}$: flux linkage of the permanent magnet [Wb]

Mutual leakage terms are neglected and $\boldsymbol{L}_s$ is given as,

$$\boldsymbol{L_s} = \begin{bmatrix} L_{ls} + L_A + L_B cos2\theta_r & -\frac{1}{2}L_A + L_B cos2\left(\theta_r - \frac{\pi}{3}\right) & -\frac{1}{2}L_A + L_B cos2\left(\theta_r + \frac{\pi}{3}\right) \\ -\frac{1}{2}L_A + L_B cos2\left(\theta_r - \frac{\pi}{3}\right) & L_{ls} + L_A + L_B cos2\left(\theta_r - \frac{2\pi}{3}\right) & -\frac{1}{2}L_A + L_B cos2(\theta_r + \pi) \\ -\frac{1}{2}L_A + L_B cos2\left(\theta_r + \frac{\pi}{3}\right) & -\frac{1}{2}L_A + L_B cos2\left(\theta_r + \frac{\pi}{3}\right) & L_{ls} + L_A + L_B cos2\left(\theta_r - \frac{2\pi}{3}\right) \end{bmatrix} \tag{4.5}$$

$\boldsymbol{L_s}$: matrix of the stator inductances [H]

L_{ls} : leakage inductance of the stator [H]

θ_r : displacement of the rotor [rad]

The flux linkage $\boldsymbol{\lambda}'_m$ is written as,

$$\boldsymbol{\lambda}'_{\boldsymbol{m}} = \lambda'_m \begin{bmatrix} sin\theta_r \\ sin\left(\theta_r - \frac{2\pi}{3}\right) \\ sin\left(\theta_r + \frac{2\pi}{3}\right) \end{bmatrix} \tag{4.6}$$

$\boldsymbol{\lambda}'_m$: flux linkage of permanent magnet [Wb]

λ'_m : magnitude of flux linkage of permanent magnet

λ'_m is the amplitude of the flux linkages which are generated by a permanent magnets as seen from thee stator windings. Therefore, $p\lambda_{abcs}$ are the open circuit voltage which are induced in the stator windings. Damper windings are also neglected in the calculations. Induced voltages in stator windings are assumed as constant amplitude sinusoidal voltages [59].

Electromagnetic torque is expressed as,

$$T_e = \left(\frac{P}{2}\right)\frac{\partial W_c}{\partial \theta_r} \tag{4.7}$$

T_e : electromagnetic torque [Nm]

P : pole number of the rotor

θ_r : displacement of the rotor [rad]

Where,

$$W_c = \frac{1}{2}\boldsymbol{i}^{\boldsymbol{T}}_{\boldsymbol{abcs}}\boldsymbol{L_s}\,\boldsymbol{i_{abcs}} + \boldsymbol{i}^{\boldsymbol{T}}_{\boldsymbol{abcs}}\boldsymbol{\lambda}'_{\boldsymbol{m}} + \boldsymbol{W_{pm}} \tag{4.8}$$

$\boldsymbol{i_{abcs}}$: matrix of the stator currents [A]

$\boldsymbol{L_s}$: matrix of the stator inductances [H]

$\boldsymbol{\lambda}'_{\boldsymbol{m}}$: flux linkage of the permanent magnet [Wb]

$\boldsymbol{W_{pm}}$: energy in coupling field due to presence of the permanent magnet [J]

Substituting equation (4.8) into (4.7) and neglecting any change in $W_{pm}$with rotor position, the electromagnetic torque can be written as,

$$T_e = \left(\frac{P}{2}\right)\left\{\frac{L_{md} - L_{mq}}{3}\left[\left(i_{as}^2 - \frac{1}{2}i_{bs}^2 - \frac{1}{2}i_{cs}^2 - i_{as}i_{bs} - i_{as}i_{cs} + 2i_{bs}i_{cs}\right) sin2\theta_r + \frac{\sqrt{3}}{2}\left(i_{bs}^2 - i_{cs}^2 - 2i_{as}i_{bs} + 2i_{as}i_{cs}\right)cos2\theta_r\right] + \lambda'_m\left[\left(i_{as} - \frac{1}{2}i_{bs} - \frac{1}{2}i_{cs}\right)cos\theta_r + \frac{\sqrt{3}}{2}(i_{bs} - i_{cs})sin\theta_r\right]\right\} \quad (4.9)$$

T_e : electromagnetic torque [Nm]

P : pole number of the rotor

L_{md} : direct component of the stator magnetizing inductance [H]

L_{mq} : quadrature component of the stator magnetizing inductance [H]

i_{as} : phase a current of the stator [A]

i_{bs} : phase b current of the stator [A]

i_{cs} : phase c current of the stator [A]

θ_r : displacement of the rotor [rad]

λ'_m : magnitude of the flux linkage of the permanent magnet [Wb]

Where,

$$L_{mq} = \frac{3}{2}(L_A + L_B) \quad (4.10)$$

$$L_{md} = \frac{3}{2}(L_A - L_B) \quad (4.11)$$

L_{mq} : quadrature component of the stator magnetizing inductance [H]

L_{md} : direct component of the stator magnetizing inductance [H]

Torque equation may be arranged using speed as,

$$T_e = J\left(\frac{2}{P}\right)p\omega_r + B_{damp}\left(\frac{2}{P}\right)\omega_r + T_L \quad (4.12)$$

T_e : electromagnetic torque [Nm]

J : total inertia of the rotor and a connected load [kg.m^2]

P : pole number of the rotor

p : derivative operator

ω_r : angular velocity of the rotor [rad/s]

B_{damp} : damping coefficient of the rotational system [Nm.s/rad]

T_L : load torque [Nm]

Load torque T_L is positive for motor action and damping coefficient B_{damp} is often neglected due to its small value.

The voltage equations can be written in rotor reference frame by taking $\omega = \omega_r$.

$$\boldsymbol{v}_{\boldsymbol{qd0s}}^{\boldsymbol{r}} = \boldsymbol{r}_{\boldsymbol{s}}\boldsymbol{i}_{\boldsymbol{qd0s}}^{\boldsymbol{r}} + \omega_r\boldsymbol{\lambda}_{\boldsymbol{qd0s}}^{\boldsymbol{r}} + p\boldsymbol{\lambda}_{\boldsymbol{qd0s}}^{\boldsymbol{r}} \tag{4.13}$$

$\boldsymbol{v}_{\boldsymbol{qd0s}}^{\boldsymbol{r}}$: matrix of the stator voltages referred to the rotor [V]

$\boldsymbol{r}_s$: matrix of the stator resistances [Ohm]

$\boldsymbol{i}_{\boldsymbol{qd0s}}^{\boldsymbol{r}}$: matrix of the stator currents referred to the rotor [A]

ω_r : angular velocity of the rotor [rad/s]

$\boldsymbol{\lambda}_{\boldsymbol{qd0s}}^{\boldsymbol{r}}$: matrix of the stator flux linkages referred to the rotor [Wb]

p : derivative operator

Where,

$$(\boldsymbol{\lambda}_{dqs}^{r})^T = [\lambda_{ds}^{r} \quad -\lambda_{qs}^{r} \quad 0] \tag{4.14}$$

$$\boldsymbol{\lambda}_{qd0s}^{r} = \begin{bmatrix} L_{ls}+L_{mq} & 0 & 0 \\ 0 & L_{ls}+L_{md} & 0 \\ 0 & 0 & L_{ls} \end{bmatrix} \begin{bmatrix} i_{qs}^{r} \\ i_{ds}^{r} \\ i_{0s}^{r} \end{bmatrix} + \boldsymbol{\lambda}_{m}^{\prime r} \begin{bmatrix} 0 \\ 1 \\ 0 \end{bmatrix} \tag{4.15}$$

$\boldsymbol{\lambda}_{\boldsymbol{qd0s}}^{\boldsymbol{r}}$: matrix of the stator flux linkages referred to the rotor [Wb]

L_{ls} : leakage inductance of the stator [H]

L_{mq} : quadrature component of the stator magnetizing inductance [H]

L_{md} : direct component of the stator magnetizing inductance [H]

i_{qs}^{r} : quadrature component of the stator current referred to the rotor [A]

i_{ds}^{r} : direct component of the stator current referred to the rotor [A]

i_{0s}^{r} : zero component of the stator current referred to the rotor [A]

$\boldsymbol{\lambda}_{m}^{\prime r}$: magnitude of the flux linkage of the permanent magnet referred to the rotor [Wb]

The voltage equation for each axis can be obtained as,

$$v_{qs}^{r} = r_s i_{qs}^{r} + \omega_r \lambda_{ds}^{r} + p\lambda_{qs}^{r} \tag{4.16}$$

$$v_{ds}^{r} = r_s i_{ds}^{r} - \omega_r \lambda_{qs}^{r} + p\lambda_{ds}^{r} \tag{4.17}$$

$$v_{0s} = r_s i_{0s} + p\lambda_{0s} \tag{4.18}$$

v_{qs}^{r} : quadrature component of the stator current voltage referred to a rotor [V]

r_s : resistance of the stator [Ohm]

i_{qs}^{r} : quadrature component of the stator current referred to the rotor [A]

ω_r : angular velocity of the rotor [rad/s]

λ_{ds}^{r} : direct component of the flux linkage referred to the rotor [Wb]

p : derivative operator

λ_{qs}^{r} : quadrature component of the flux linkage referred to the rotor [Wb]

v_{ds}^{r} : direct component of the stator current voltage referred to a rotor [V]

i_{ds}^{r} : direct component of the stator current referred to the rotor [A]

v_{0s} : zero component of a stator voltage referred to a rotor [V]

i_{0s} : zero component of the stator current referred to the rotor [A]

λ_{0s} : zero component of the flux linkage [Wb]

Where,

$$\lambda_{qs}^{r} = L_{qs} i_{qs}^{r} \tag{4.19}$$

$$\lambda_{ds}^{r} = L_{ds} i_{ds}^{r} + \lambda_{m}^{\prime r} \tag{4.20}$$

$$\lambda_{0s} = L_{ls} i_{0s} \tag{4.21}$$

λ_{qs}^{r} : quadrature component of the flux linkage referred to the rotor [Wb]

L_{qs} : quadrature component of the stator inductance [H]

i_{qs}^{r} : quadrature component of the stator current referred to the rotor [A]

λ_{ds}^{r} : direct component of the flux linkage referred to the rotor [Wb]

L_{ds} : direct component of the stator inductance [H]

i_{ds}^{r} : direct component of the stator current referred to the rotor [A]

$\lambda_{m}^{\prime r}$: flux linkage of permanent magnet referred to the rotor [Wb]

λ_{0s} : zero component of the flux linkage [Wb]

L_{ls} : leakage inductance of the stator [H]

i_{0s} : zero component of the stator current [A]

Where,

$$L_{qs} = L_{ls} + L_{mq} \tag{4.22}$$

$$L_{ds} = L_{ls} + L_{md} \tag{4.23}$$

L_{qs} : quadrature component of the stator inductance [H]

L_{ls} : leakage inductance of the stator [H]

L_{mq} : quadrature component of the stator magnatizing inductance [H]

L_{ds} : direct component of the stator inductance [H]

L_{md} : direct component of the stator magnatizing inductance [H]

Equations (4.19), (4.20) and (4.21) are substituted into equations (4.16), (4.17) and (4.18) by considering $p\lambda_{m}^{\prime r}$, the voltage equations can be arranged as,

$$v_{qs}^{r} = \left(r_s + pL_{qs}\right)i_{qs}^{r} + \omega_r L_{ds} i_{ds}^{r} + \omega_r \lambda_{m}^{\prime r} \tag{4.24}$$

$$v_{ds}^{r} = (r_s + pL_{ds})i_{ds}^{r} - \omega_r L_{qs} i_{qs}^{r} \tag{4.25}$$

$$v_{0s} = (r_s + pL_{ls})i_{0s} \tag{4.26}$$

v_{qs}^{r} : quadrature component of the stator voltage referred to a rotor [V]

r_s : resistance of the stator [Ohm]

p : derivative operator

L_{qs} : quadrature component of the stator inductance [H]

i_{qs}^r : quadrature component of the stator current referred to the rotor [A]

ω_r : angular velocity of the rotor [rad/s]

L_{ds} : direct component of the stator inductance [H]

i_{ds}^r : direct component of the stator current referred to the rotor [A]

$\lambda_m'^r$: flux linkage of the permanent magnet referred to the rotor [Wb]

v_{ds}^r : direct component of the stator voltage referred to the rotor [V]

v_{0s} : zero component of the stator current voltage [V]

i_{0s} : zero component of the stator current [A]

Input power of a PMSM can be expressed by using direct and quadrature axis current as,

$$T_e\left(\frac{2}{P}\right)\omega_r = \frac{3}{2}\left(v_{qs}^r i_{qs}^r + v_{ds}^r i_{ds}^r + 2v_{0s}i_{0s}\right) \tag{4.27}$$

T_e : electromagnetic torque [Nm]

P : pair of the rotor

ω_r : angular velocity of the rotor [rad/s]

vv_{qs}^r : quadrature component of the stator voltage referred to the rotor [V]

i_{qs}^r : quadrature component of the stator current referred to the rotor [A]

v_{ds}^r : direct component of the stator voltage referred to the rotor [V]

i_{ds}^r : direct component of the stator current referred to the rotor [A]

v_{0s} : zero component of the stator voltage referred to the rotor [V]

i_{0s} : zero component of the stator current referred to the rotor [A]

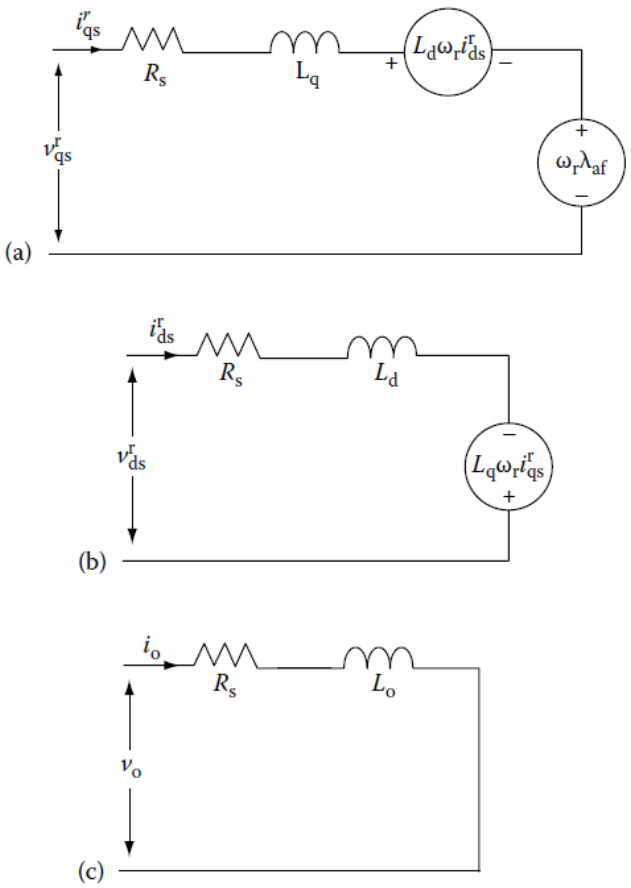

Figure 4.2: a) Stator q-axis equivalent circuit b) Stator d-axis equivalent circuit c) Zero sequence equivalent circuit [57].

If the equations (4.24), (4.25) and (4.26) are substituted into equation (4.27), another form of the input power can be obtained as,

$$T_e\left(\frac{2}{P}\right)\omega_r = \frac{3}{2}r_s\left(i_{qs}^{r\,2} + i_{ds}^{r\,2} + 2i_{0s}^{\,2}\right) + \frac{3}{2}\left(\lambda_{ds}^r i_{qs}^r - \lambda_{qs}^r i_{ds}^r\right)\omega_r + \frac{3}{2}\left(i_{qs}^r p\lambda_{qs}^r + i_{ds}^r p\lambda_{ds}^r + 2i_{0s}p\lambda_{0s}\right)\left(i_{qs}^r p\lambda_{qs}^r + i_{ds}^r p\lambda_{ds}^r + 2i_{0s}p\lambda_{0s}\right) \quad (4.28)$$

T_e : electromagnetic torque [Nm]

P : pole number of the rotor

ω_r : angular velocity of the rotor [rad/s]

r_s : resistance of the stator [Ohm]

i_{qs}^r : quadrature component of the stator current referred to the rotor [A]

i_{ds}^r : direct component of the stator current referred to the rotor [A]

i_{0s} : zero component of the stator current referred to the rotor [A]

λ_{ds}^{r} : direct component of the flux linkage referred to the rotor [Wb]

λ_{qs}^{r} : quadrature component of the flux linkage referred to the rotor [Wb]

ω_r : angular velocity of the rotor [rad/s]

p : derivative operator

λ_{0s} : direct component of the flux linkage [Wb]

Ohmic power loss in the stator windings is presented in the first term on the right-hand side of the equation (4.28). The change of stored energy is also presented in the last term on the right-hand side. Electromagnetic torque can be obtained by equating the coefficient w_r as,

$$T_e = \left(\frac{3}{2}\right)\left(\frac{P}{2}\right)\left(\lambda_{ds}^{r} i_{qs}^{r} - \lambda_{qs}^{r} i_{ds}^{r}\right) \tag{4.29}$$

T_e : electromagnetic torque [Nm]

P : pole number of the rotor

λ_{ds}^{r} : direct component of the flux linkage referred to the rotor [Wb]

i_{qs}^{r} : quadrature component of the stator current referred to the rotor [A]

λ_{qs}^{r} : quadrature component of the flux linkage referred to the rotor [Wb]

i_{ds}^{r} : direct component of the stator current referred to the rotor [A]

If the equations (4.19) and (4.20) are substituted into equation (4.29), another form of the electromagnetic torque can be expressed as,

$$T_e = \left(\frac{3}{2}\right)\left(\frac{P}{2}\right)\left(\lambda_{m}^{\prime r} i_{qs}^{r} + \left(L_{ds} - L_{qs}\right) i_{qs}^{r} i_{ds}^{r}\right) \tag{4.30}$$

T_e : electromagnetic torque [Nm]

P : pole number of the rotor

$\lambda_{m}^{\prime r}$: flux linkage of permanent magnet referred to the rotor [Wb]

i_{qs}^{r} : quadrature component of the stator current referred to the rotor [A]

L_{ds} : direct component of the stator inductance [H]

L_{qs} : quadrature component of the stator inductance [H]

i_{ds}^{r} : direct component of the stator current referred to the rotor [A] [60]

The sign of the electromagnetic torque is positive for motor operation.
Angular rotor speed is calculated as,

$$\frac{d\theta_r}{dt} = \omega_r \tag{4.31}$$

θ_r : displacement of the rotor [rad]

ω_r : angular velocity of the rotor [rad/s]

Angular rotor position can be found by integrating equation (4.31). However, θ_r is obtained in different ways instead of using this equation in order to simplify the calculation. Hall sensor, a position observer or encoder are commonly used practically for the calculation of the angular rotor position. The applied stator voltages are assumed as sinusoidal as a step in finding the rotor position.

$$v_{as} = \sqrt{2} v_s cos\theta_{ev} \tag{4.32}$$

$$v_{bs} = \sqrt{2} v_s cos\left(\theta_{ev} - \frac{2\pi}{3}\right) \tag{4.33}$$

$$V_{cs} = \sqrt{2} v_s cos\left(\theta_{ev} + \frac{2\pi}{3}\right) \tag{4.34}$$

v_{as} : stator voltage of a phase [V]

v_{bs} : stator voltage of b phase [V]

v_{cs} : stator voltage of c phase [V]

v_s : magnitude of the stator voltage [V]

θ_{ev} : phase angle of the stator voltage [rad]

The stator voltages are controlled with the inverter in order to satisfy equation (4.35).

$$\theta_{ev} = \theta_r + \phi_v \tag{4.35}$$

θ_{ev} : phase angle of the stator voltage [rad]

θ_r : displacement of the rotor [rad]

ϕ_v : angular displacement referred to the rotor [rad]

If it is assumed that equations (4.32), (4.33) and (4.34) have only fundamental components and all harmonic contents which are caused by switching are ignored, the stator voltage referred to rotor reference can be written as,

$$v_{qs}^r = \sqrt{2} v_s cos\phi_v \tag{4.36}$$

$$v_{ds}^r = -\sqrt{2} v_s sin\phi_v \tag{4.37}$$

v_{qs}^r : quadrature component of the stator voltage referred to the rotor [V]

v_{ds}^r : direct component of the stator voltage referred to the rotor [V]

v_s : magnitude of the stator voltage [V]

ϕ_v : angular displacement referred to the rotor [rad]

Sinusoidal stator voltages can be expressed for steady state with balanced operation as,

$$V_{qs}^r = r_s I_{qs}^r + \omega_r L_{ds} I_{ds}^r + \omega_r \lambda_m^{\prime r} \tag{4.38}$$

$$V_{ds}^r = r_s I_{ds}^r - \omega_r L_{qs} I_{qs}^r \tag{4.39}$$

V_{qs}^r : quadrature component of the stator voltage referred to the rotor in steady state [V]

r_s : resistance of the stator [Ohm]

I_{qs}^r : quadrature component of the stator current referred to the rotor in steady state [A]

ω_r : angular velocity of the rotor [rad/s]

L_{ds} : direct component of the stator inductance [H]

I_{ds}^{r} : direct component of the stator current referred to the rotor in steady state [A]

$\lambda_{m}^{\prime r}$: flux linkage of the permanent magnet referred to the rotor [Wb.turns]

V_{ds}^{r} : direct component of the stator voltage referred to the rotor in steady state [V]

L_{qs} : quadrature component of the stator inductance [H]

Steady state parameters which are constant are indicated with uppercase letters. If the demagnetization effect is ignored, $\lambda_{m}^{\prime r}$ can be treated as a constant value. In light of this information, the steady state torque can be written as,

$$T_e = \left(\frac{3}{2}\right)\left(\frac{P}{2}\right)\left[\lambda_{m}^{\prime r} I_{qs}^{r} + \left(L_{ds} - L_{qs}\right) I_{qs}^{r} I_{ds}^{r}\right] \tag{4.40}$$

T_e : electromagnetic torque [Nm]

P : pole number of the rotor

$\lambda_{m}^{\prime r}$: flux linkage of the permanent magnet referred to the rotor [Wb]

I_{qs}^{r} : quadrature component of the stator current referred to the rotor in steady state [A]

L_{ds} : direct component of the stator inductance [H]

L_{qs} : quadrature component of the stator inductance [H]

I_{ds}^{r} : direct component of the stator current referred to the rotor in steady state [A]

The angular displacement between the peak value of the fundamental component of V_{as} and quadrature axis fixed in the rotor is denoted with ϕ_v that is the constant value. The phasor voltage equations can be obtained by referencing the phasor to quadrature axis which is assumed positive real axis of the stationary phasor diagram. Phasor $\tilde{V}_{as}$ can be expressed as,

$$\tilde{V}_{as} = V_s e^{j\phi_v} = V_s cos\phi_v + jV_s sin\phi_v \tag{4.41}$$

$\tilde{V}_{as}$: phasor of the stator voltage [V]

V_s : magnitude of the stator voltage in steady state [V]

ϕ_v : angular displacement referred to the rotor [rad]

If equations (4.38) and (4.39) are combined with equation (4.41), equation (4.42) is obtained as,

$$\sqrt{2}\tilde{V}_{as} = V_{qs}^{r} - jV_{ds}^{r} \tag{4.42}$$

$\tilde{V}_{as}$: phasor of the stator voltage [V]

V_{qs}^{r} : quadrature component of the stator voltage referred to the rotor in steady state [V]

V_{ds}^{r} : direct component of the stator voltage referred to the rotor in steady state [V]

Similar equation can be established for currents as,

$$\sqrt{2}\tilde{I}_{as} = I_{qs}^{r} - jI_{ds}^{r} \tag{4.43}$$

$\tilde{I}_{as}$: phasor of the stator current [A]

I_{qs}^{r} : quadrature component of the stator current referred to the rotor in steady state [A]

I_{ds}^{r} : direct component of the stator current referred to the rotor in steady state [A]

If voltage and current equations are arranged, the phasor voltage can be expressed as,

$$\tilde{V}_{as} = \left(r_s + j\omega_r L_{qs}\right)\tilde{I}_{as} + \tilde{E}_a \tag{4.44}$$

$\tilde{V}_{as}$: phasor of the stator voltage [V]

r_s : resistance of the stator [Ohm]

ω_r : angular velocity of the rotor [rad/s]

L_{qs} : direct component of the stator inductance [H]

$\tilde{I}_{as}$: phasor of the stator current [A]

$\tilde{E}_a$: phasor of the BEMF volatge [V]

Where,

$$\tilde{E}_a = \frac{1}{\sqrt{2}}\left[\omega_r\left(L_{ds} - L_{qs}\right)I_{ds}^r + \omega_r\lambda_m'^r\right]e^{j0} \tag{4.45}$$

$\tilde{E}_a$: phasor of the BEMF volatge [V]

ω_r : angular velocity of the rotor [rad/s]

L_{ds} : direct component of the stator inductance [H]

L_{qs} : quadrature component of the stator inductance [H]

I_{ds}^r : direct component of the stator current referred to the rotor in steady state [A]

$\lambda_m'^r$: flux linkage of the permanent magnet referred to the rotor [Wb.t]

$\tilde{E}_a$ is placed in the real axis for a PM [58].

5. FIELD ORIENTED CONTROL (FOC)

The Field Oriented Control (FOC) method is generally used in sensitive motor drives such as compressors, pumps, fans etc. Sensorless FOC which is used in BLDC or PMSM driving decreases overall system cost. Because sensors and their wiring harnesses are eliminated. Sensors may have manufacturing problems and they may be affected by magnetic field or sunlight. Besides cost efficiency, FOC reduces problems caused by using sensors and increases system reliability. On the other, FOC has a significant contribution to the energy efficiency of a motor. Efficiency can be raised up to 95% by using FOC. The dynamic response of a motor is enhanced with FOC. Heat dissipation is kept at a minimum value in this technique. Provided sinusoidal current shape with FOC generates less rippled torque and represents the quiet operation to consumers [61].

In the FOC theory, one of the fluxes which can be rotor, stator or airgap is taken as a reference frame corcerning all other parameters. The main purpose of FOC is to decouple torque and flux components of the stator current. By extracting these two components from the stator current, a complex three-phase motor is transformed DC motor with separate excitation. This means the torque is generated by the armature current and the flux is generated by the excitation current. The control of a PMSM is aimed to get easier by transforming a PMSM into a DC motor with FOC. Rotor flux will be taken as a reference frame for a PMSM. The air gap flux has a smooth shape and BEMF is sinusoidal for a PMSM. Direct axis current is considered as a reference frame for surface mounted PMSM and a reference direct axis current which can be thought of as armature reaction flux is set to zero. The sum of the stator and the rotor flux linkage generate the airgap flux. The permanent magnets generate rotor flux linkage and stator currents generate stator flux linkage in a PMSM. The stator flux linkages are not generated in the airgap below the rated speed which means the direct axis current is set to zero and the air gap flux is equal to the rotor flux linkage. Above the rated speed, the direct axis current is set to a negative value in order to generate opposite stator flux linkage to the rotor flux linkage so the airgap flux is weakened.

Six step commutation is preferred as the traditional control technique for a BLDC motor drives. This method causes torque ripple in a motor. Hall sensors are placed in a motor with 60° or 120° each other. They generate six exact position regions on the rotor side. In every region, only two windings are energized until the rotor reaches the next region. Electronic commutation is carried out considering the output of hall sensors. On the other hand, in the sensorless FOC technique, the rotor position is determined by observing the Back-EMF signal in the stator winding. Six step control which is also called as trapezoidal control is not an applicable to device that has a dynamically changing load such as a washing machine. In every cycle, load varies spontaneously and the dynamic response of six step control is insufficient in this type of load. FOC has an excellent dynamic response and this feature makes FOC one of the most suitable methods for these kinds of load [62].

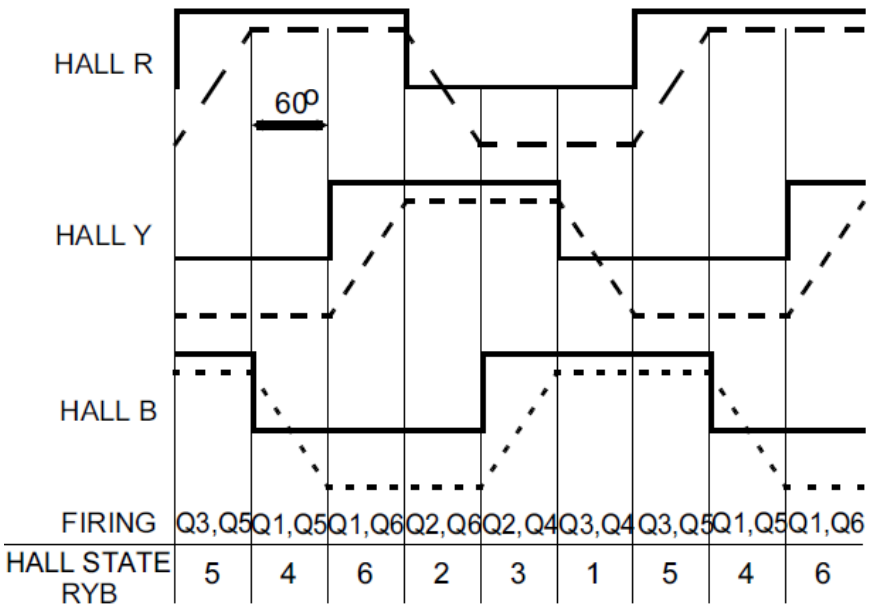

Figure 5.1: Six step commutation diagram [63].

Before summarizing PMSM equations, some assumptions must be made. The stator winding is connected as wye connection. If the delta connection is used, the connection must be converted to the wye. Secondly, the magnetic saturation of lamination is neglected in order to reduce the complexity of the equation and reach the results easier. Lastly, eddy current and hysteresis losses are also neglected due to the above reasons. Voltage and flux linkage equation of a PMSM are summarized as below:

$$\boldsymbol{V}_{abcs} = \boldsymbol{r}_s \boldsymbol{i}_{abcs} + p\boldsymbol{\lambda}_{abcs} \tag{5.1}$$

$\boldsymbol{v_{abcs}}$: matrix of the stator voltages [V]

$\boldsymbol{r_s}$: matrix of the stator resistance [Ohm]

$\boldsymbol{i_{abcs}}$: matrix of the stator currents [A]

$\boldsymbol{p}$: derivative operator

$\boldsymbol{\lambda_{abcs}}$: matrix of the stator flux linkages [Wb.t]

$$\boldsymbol{\lambda}_{\text{abcs}} = \begin{bmatrix} L_{ls} + L_{ms} & -\frac{L_{ms}}{2} & -\frac{L_{ms}}{2} \\ -\frac{L_{ms}}{2} & L_{ls} + L_{ms} & -\frac{L_{ms}}{2} \\ -\frac{L_{ms}}{2} & -\frac{L_{ms}}{2} & L_{ls} + L_{ms} \end{bmatrix} \mathbf{i}_{\text{abcs}} + \begin{bmatrix} \sin\theta_r \\ \sin\left(\theta_r - \frac{2\pi}{3}\right) \\ \sin\left(\theta_r + \frac{2\pi}{3}\right) \end{bmatrix} \lambda'_m \qquad (5.2)$$

λ_{abcs} : matrix of the stator flux linkages [Wb.t]

L_{ls} : stator leakage inductance [H]

L_{ms} : magnetizing inductance of the stator [H]

i_{abcs} : matrix of the stator currents [A]

θ_r : displacement of the rotor [rad]

λ'_m : magnitude of the flux linkage of the permanent magnet [Wb.t] [64].

As seen in equation (5.2), stator flux linkages are mutually coupled and dependent on the rotor position. As will be explained in detail in the following section, the stator values can be divided into two components rotating synchronously with the rotor by ninety degrees apart. The direct ‘d’ axis is aligned with the rotor flux and the quadrature ‘q’ axis leads at 90 degrees. Voltage and flux equations corcerning direct and quadrature axis are written as

$$v_{qs} = r_s i_{qs} + \frac{d\lambda_{qs}}{dt} + \omega_r \lambda_{ds} \qquad (5.3)$$

$$v_{ds} = r_s i_{ds} + \frac{d\lambda_{ds}}{dt} - \omega_r \lambda_{qs} \qquad (5.4)$$

$$\lambda_{qs} = L_{qs} i_{qs} \qquad (5.5)$$

$$\lambda_{ds} = L_{ds} i_{ds} + \boldsymbol{\lambda}'_m \tag{5.6}$$

v_{qs} : quadrature component of the stator voltage [V]

r_s : resistance of the stator [Ohm]

i_{qs} : quadrature component of the stator current [A]

λ_{qs} : quadrature component of the flux linkage [Wb.t]

ω_r : angular velocity of the rotor [rad/s]

λ_{ds} : direct component of the flux linkage [Wb.t]

v_{ds} : direct component of the stator voltage [V]

i_{ds} : direct component of the stator current [A]

$\boldsymbol{\lambda}'_m$: flux linkage of the permanent magnet [Wb.t]

Inductances of d and q axis are the same for surface mounted PMSM and inductances can be written as,

$$L_s = L_{qs} = L_{ds} = L_{ls} = \frac{3L_{ms}}{2} \tag{5.7}$$

L_s : inductance of the stator [H]

L_{qs} : quadrature component of the stator inductance [H]

L_{ds} : direct component of the stator inductance [H]

L_{ls} : leakage inductance of the stator [H]

L_{ms} : magnetizing inductance of the stator [H]

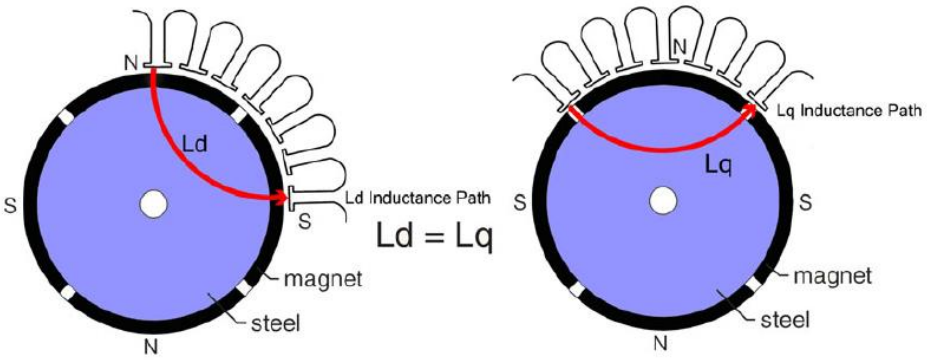

Figure 5.2: Surface mounted PMSM structure [65].

On the other hand, interior PMSM has salient magnetic properties; therefore, these two axis inductances are not equal to each other. Inductance values can be expressed as,

$$L_{qs} = L_{ls} + \frac{3(L_{ms} + L_{2s})}{2} \tag{5.8}$$

$$L_{ds} = L_{ls} + \frac{3(L_{ms} - L_{2s})}{2} \tag{5.9}$$

L_{qs} : quadrature component of a stator inductance [H]

L_{ls} : leakage inductance of the stator [H]

L_{ms} : magnetizing inductance of the stator [H]

L_{2s} : second harmonic of stator inductance [H]

L_{ds} : direct component of a stator inductance [H]

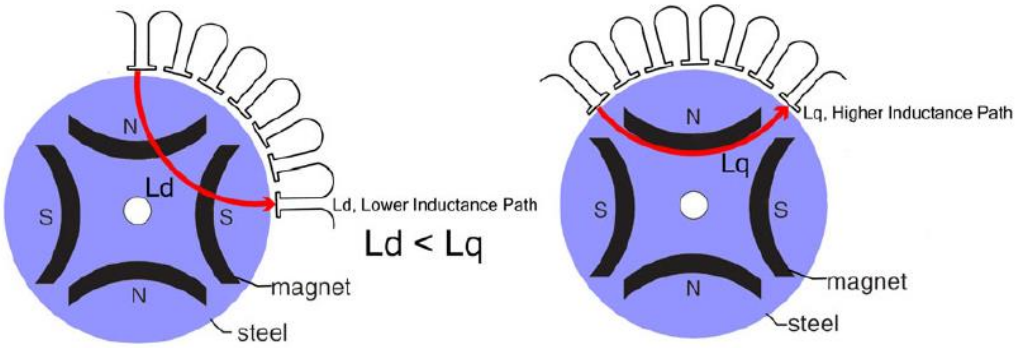

Figure 5.3: Interior PMSM structure [65].

Electromagnetic torque equation of surface mounted PMSM is given as,

$$\begin{aligned} T_e &= \left(\frac{3}{2}\right)\left(\frac{P}{2}\right)\left(\lambda_{ds} i_{qs} - \lambda_{qs} i_{ds}\right) \\ &= \left(\frac{3}{2}\right)\left(\frac{P}{2}\right)\left(L_s i_{ds} i_{qs} + \lambda'_m i_{qs} - L_s i_{qs} i_{ds}\right) \end{aligned} \tag{5.10}$$

$$T_e = \left(\frac{3}{2}\right)\left(\frac{P}{2}\right)\left(\lambda'_m i_{qs}\right) \tag{5.11}$$

T_e : electromagnetic torque [Nm]

P : pole number of the rotor

λ_{ds} : direct component of the flux linkage [Wb.t]

i_{qs} : quadrature component of a stator current [A]

λ_{qs} : quadrature component of the flux linkage [Wb.t]

i_{ds} : direct component of a stator current [A]

L_s : inductance of the stator [H]

λ'_m : flux linkage of the permanent magnet [Wb.t]

As seen in equation (5.11), generated torque is only and linearly dependent on i_{qs} current for surface mounted PMSM. i_{ds} current has no contribution to torque generation in this type of a motor. The electromagnetic torque equation of interior PMSM is expressed as

$$T_e = \left(\frac{3}{2}\right)\left(\frac{P}{2}\right)\left(\lambda_{ds}i_{qs} - \lambda_{qs}i_{ds}\right) = \left(\frac{3}{2}\right)\left(\frac{P}{2}\right)\left(L_s i_{ds} i_{qs} + \lambda'_m i_{qs} - L_s i_{qs} i_{ds}\right) \tag{5.12}$$

$$T_e = \left(\frac{3}{2}\right)\left(\frac{P}{2}\right)\left(\lambda'_m i_{qs}\right) + \left(\frac{3}{2}\right)\left(\frac{P}{2}\right)(L_{ds} - L_{qs}) i_{qs} i_{ds} \tag{5.13}$$

T_e : electromagnetic torque [Nm]

P : pole number of the rotor

λ_{ds} : direct component of the flux linkage [Wb.t]

i_{qs} : quadrature component of a stator current [A]

λ_{qs} : quadrature component of the flux linkage [Wb.t]

i_{ds} : direct component of a stator current [A]

L_s : inductance of the stator [H]

λ'_m : flux linkage of the permanent magnet [Wb.t]

Unlike surface mounted PMSM, in the above equation, there are two terms on the right side of the equation. The first term indicates permanent magnet excitation torque which is similar to the electromagnetic torque equation of surface mounted PMSM. The second term expresses the reluctance torque. Because interior PMSM has saliency in the rotor so inductance values of the quadrature and direct axis are not the same and

typically $L_d < L_q$. As seen, not just i_{qs} contributes torque generation and i_{ds} also generates torque in interior PMSM.

FOC is also called as the vector control. Briefly, this control method contains coordinate transformation processes, PI controllers, speed and position estimation and space vector modulation that are given in Figure 5.4 [66].

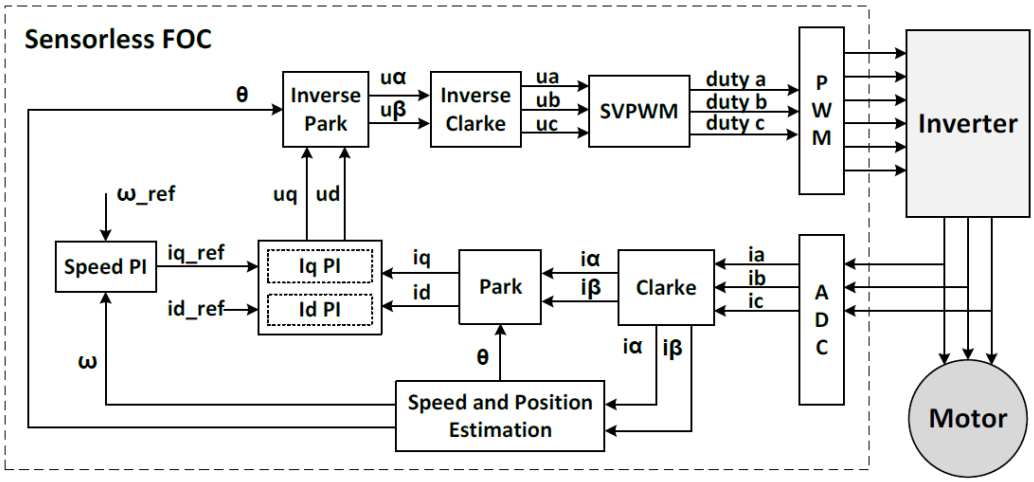

Figure 5.4: Sensorless FOC control block diagram [67].

In Figure 5.5, a basic hardware block diagram of the sensorless FOC system is shown. The main parts of a hardware system are a microcontroller unit (MCU), inverter stage, a PMSM, current sampling circuit and communication interface. The power and the signal circuits can be designed to be on the same board or as a separate modular system.

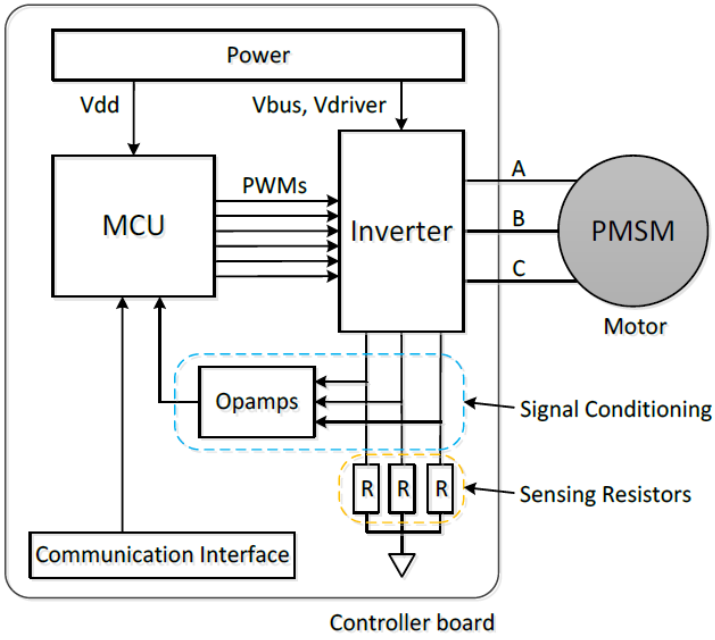

Figure 5.5: Overview of a typical sensorless FOC system [67].

In Figure 5.6, the basic topology of three-phase full bridge inverter is shown. The power system of the inverter consists of six N channel MOSFETs. Required gate signals which are space vector modulation in this thesis for six MOSFETs are generated by MCU and these signals are transferred to the gates via MOSFET gate driver. Each phase of a motor is connected between high side and low side MOSFETs in the same leg. The shunt resistors for current measurement are placed between low side MOSFETs and the ground. IGBT is generally used in high power motor drive applications instead of MOSFET. Fast diodes are connected to each MOSFET in order to allow reverse current coming from a PMSM. V_{bus} is supplied by rectified grid voltage or separated DC power sources. In some motor driver applications, a boost converter is placed between V_{bus} and rectified grid voltage. With a boost converter, the power factor can reach up to 99.9% and efficiency is increased.

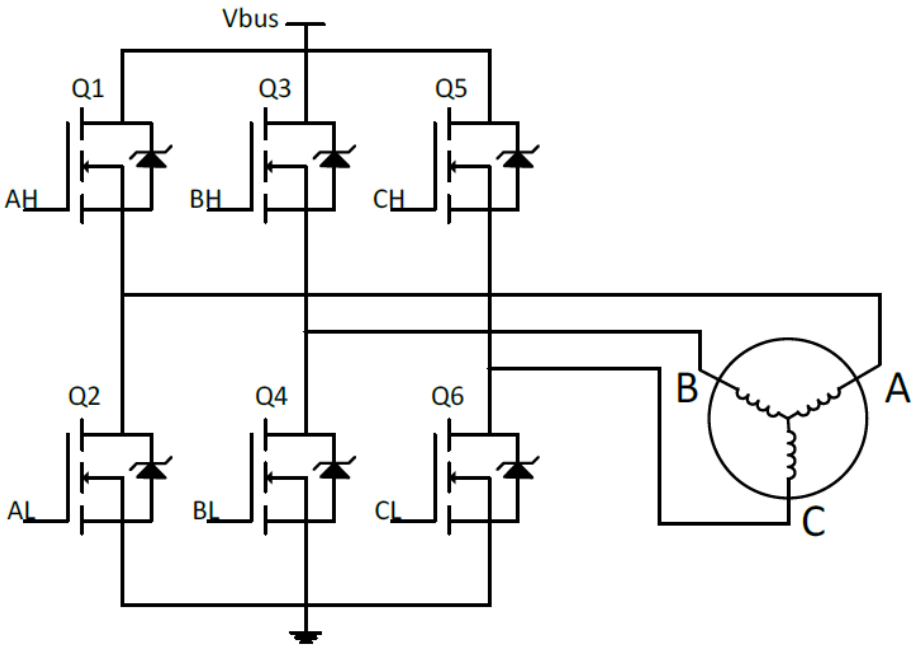

Figure 5.6: Inverter block [67].

The stator currents are measured via the shunt resistors in order to start the coordinate transformation processes. The shunt resistors are typically in the order of milliohms. The resistors must have tolerance of at least 1% or lower. Measured current values on the shunt resistors are amplified by the operational amplifier and sent to a microcontroller. Only i_{as} and i_{bs} are used for calculations in order to decrease sensor quantity and as well as reduce the total cost. Because instantaneous sum of three stator currents are zero and i_{cs} current is easily extracted by using the below formula,

$$i_{as} + i_{bs} + i_{cs} = 0 \tag{5.14}$$

i_{as} : phase a current of the stator[A]

i_{bs} : phase b current of the stator [A]

i_{cs} : phase c current of the stator [A]

In some applications, instead of three shunt resistors in each phase, the single resistor is used where the phases combine and go to earth connection. In this case, the measurement should be taken as considering time intervals where three-phase currents belong to.

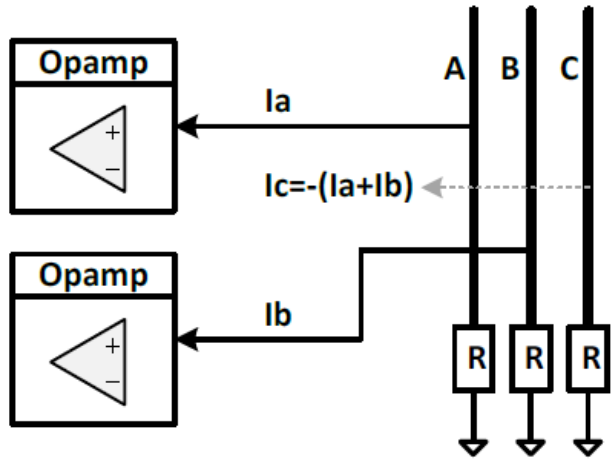

Figure 5.7: Dual shunt current sampling [67].

The coordinate transformation process starts with the Clarke Transform. Calculated i_{cs} phase current, and measured i_{as} and i_{bs} phase currents are converted to $i_{\alpha s}$ and $i_{\beta s}$ currents which are perpendicular to each other and these currents are as viewed from the perspective of the stator. In other words, $i_{\alpha s}$ and $i_{\beta s}$ currents have a stationary reference. Calculations of $i_{\alpha s}$ and $i_{\beta s}$ currents are given below,

$$i_{as} + i_{bs} + i_{cs} = 0 \tag{5.15}$$

$$i_{\alpha s} = i_{as} \tag{5.16}$$

$$i_{\beta s} = \frac{i_{as} + 2i_{bs}}{\sqrt{3}} \tag{5.17}$$

i_{as} : phase a current of the stator [A]

i_{bs} : phase b current of the stator [A]

i_{cs} : phase c current of the stator [A]

$i_{\alpha s}$: alfa component of the stator current [A]

$i_{\beta s}$: beta component of the stator current [A]

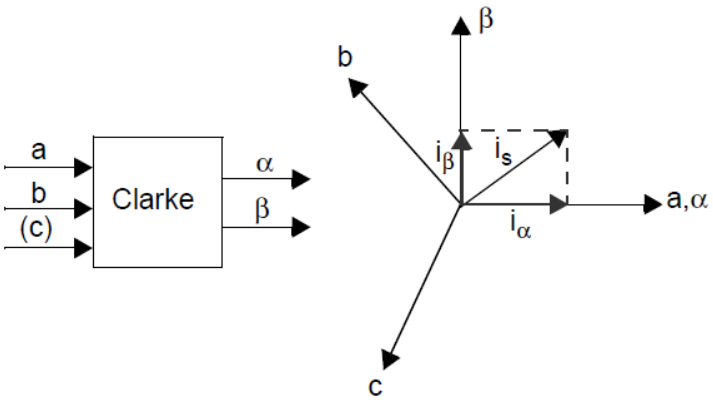

Figure 5.8: Clarke Transformation [62].

Two-axis orthogonal system with the axis called αβ is obtained after performing the Clarke Transform. These stationary currents are transformed to another two-axis system which is rotating with the rotor flux. This process is called as the Park Transform and i_{ds} and i_{qs} currents at rotating reference frame are obtained. Equations related to the Park Transform are written below,

$$i_{ds} = i_{\alpha s}\, cos\, \theta_r + i_{\beta s}\, sin\, \theta_r \tag{5.18}$$

$$i_{qs} = -i_{\alpha s}\, sin\, \theta_r + i_{\beta s}\, cos\, \theta_r \tag{5.19}$$

i_{ds} : direct component of the stator current [A]

i_{qs} : quadrature component of the stator current [A]

$i_{\alpha s}$: alfa component of the stator current [A]

$i_{\beta s}$: beta component of the stator current [A]

θ_r : displacement of the rotor [rad]

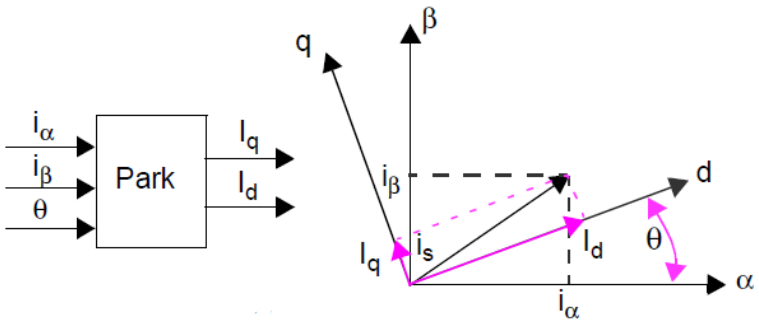

Figure 5.9: Park transformation [62].

After these two transformations, three PI loops are used to control three variables independently. Rotor speed, i_{ds} which is used to control the rotor flux and i_{qs} that is used to control the torque have a different PI controllers. A PMSM is controlled as if a separated excited DC motor is controlled. PI controllers generate an error signal for speed, flux and torque in a closed loop to achieve that the desired system response is generated rapidly. Coefficients of PI controllers can be adjusted empirically considering desired system response. The proportional term (P) multiplies the error signal by P gain. Dynamic system response and overshoot increases, the overall error decreases by using the proportional term. As an error goes to zero, the proportional term loses its impact and a small steady state error remains. To get rid of this error, the integral term (I) is used. Small steady state error accumulates into a large error value over time. This accumulated error signal is multiplied by I gain factor; therefore, steady state error is zero when the integral term is used. The derivative term (D) is not used in the motor control algorithm generally. Because the derivative term could generate an excessive error signal when there is high-frequency noise. This cause sudden change in the PWM duty cycle and excessive current tend to flow in a motor so over current error signal could be received. In some cases, the integral term causes saturation in the output parameters. When this happens, any increasing integrated error signal does not affect the output. In order to eliminate this phenomenon, an integral windup is included in the PI controller.

After the PI controller section, two voltage vectors based on the rotating dq axis are obtained. In order to obtain three-phase motor voltage, inverse transformations are needed. Two-axis rotating V_q and V_d voltages are transformed to two-axis stationary $V_{\alpha s}$ and $V_{\beta s}$ voltages. This process is known as the Inverse Park Transform. Related calculation about the Inverse Park Transform is given as,

$$V_{\alpha s} = V_{ds} * cos\,\theta_r - V_{qs} * sin\,\theta_r \quad (5.20)$$

$$V_{\beta s} = V_{ds} * sin\,\theta_r + V_{qs} * cos\,\theta_r \quad (5.21)$$

V_{ds} : direct component of the stator voltage [V]

V_{qs} : quadrature component of the stator voltage [V]

$V_{\alpha s}$: alfa component of the stator voltage [V]

$V_{\beta s}$: beta component of the stator voltage [V]

θ_r : displacement of the rotor [rad]

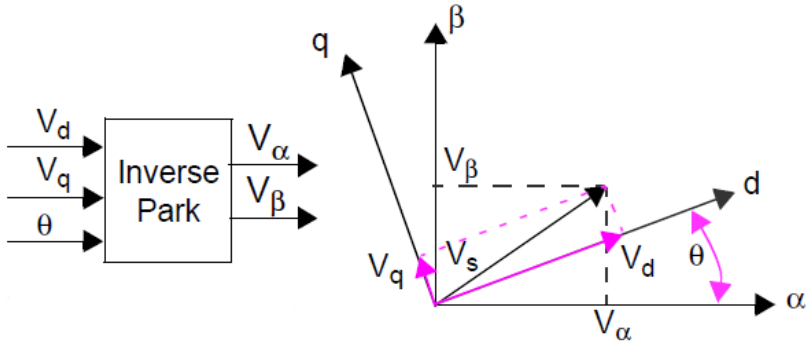

Figure 5.10: Inverse Park transformation [62].

After obtaining stationary two axes V_α and V_β voltages, stationary three-axis V_{r1}, V_{r2} and V_{r3} reference stator voltage is calculated by using Inverse Clarke Transform. Equations for calculations are expressed as,

$$V_{r1} = V_{\beta s} \quad (5.22)$$

$$V_{r2} = \frac{-V_{\beta s} + \sqrt{3} * V_{\alpha s}}{2} \quad (5.23)$$

$$V_{r3} = \frac{-V_{\beta s} - \sqrt{3} * V_{\alpha s}}{2} \quad (5.24)$$

V_{r1} : reference stator voltage of a phase [V]

V_{r2} : reference stator voltage of b phase [V]

V_{r3} : reference stator voltage of c phase [V]

$V_{\alpha s}$: alfa component of the stator voltage [V]

$V_{\beta s}$: beta component of the stator voltage [V]

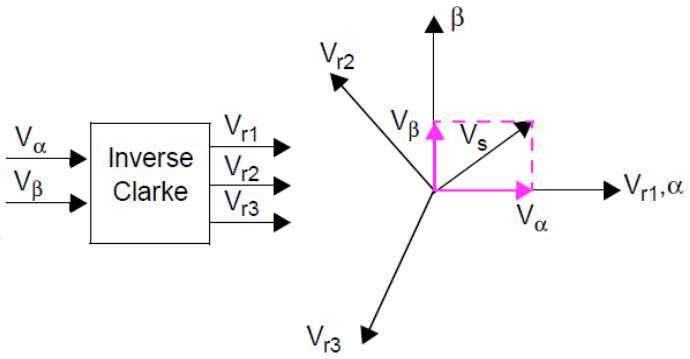

Figure 5.11: Inverse Clarke transformation [62].

Finally, PWM signals for the inverter are generated to get three phase stator voltage. In space vector modulation, calculations of PWM are based on a few simple equations. A special scheme is used to switch power transistors in order to generate sinusoidal currents in the stator windings. Phases of a motor can be connected to either the positive bus or the negative bus. High side and low side transistors in the same leg cannot be fired at the same time. Because excessive current flows in this leg and the transistors and driver system may be damaged. Therefore, there are eight switching combinations for the power transistors. In two switching patterns which are 0(1.1.1) and 0(0.0.0), all three windings are connected either to the positive bus or the negative bus; hence, there are no voltages across the phases. These states are called as the null states. If the remaining six states that are U_0(1.0.0), U_{60}(1.1.0), U_{120}(0.1.0), U_{180}(0.1.1), U_{240}(0.0.1) and U_{300}(1.0.1) can be represented as vectors with 60° rotation between each state, space vector modulation (SVM) star is obtained as Figure 5.12 [68].

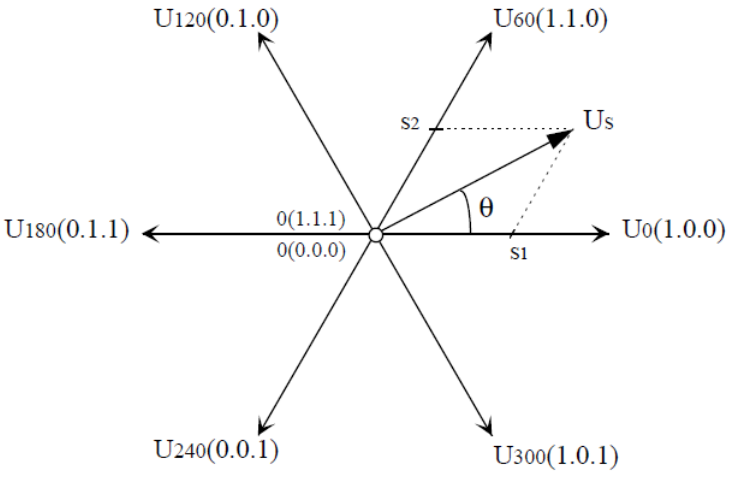

Figure 5.12: Voltage space vectors [69].

SVM enables to express any desired vector in terms of the sum of components belonging to two adjacent space vectors. $\overrightarrow{V_{ref}}$ is desired reference vector in Figure 5.13. This vector is placed between $\overrightarrow{V_1}$ and $\overrightarrow{V_2}$ in sector A. This means vector $\overrightarrow{V_{ref}}$ can be expressed using $\overrightarrow{V_1}$ and $\overrightarrow{V_2}$. In addition to that, null vector $\overrightarrow{V_0}$ is also needed in the calculation. PWM duty cycles of each transistor are computed as below,

$$T_s = T_1 + T_2 + T_0 \tag{5.25}$$

Where,

T_s : sampling period of PWM

T_1 : on time for $\overrightarrow{V_1}$

T_2 : on time for $\overrightarrow{V_2}$

T_0 : on time for $\overrightarrow{V_0}$

$$\overrightarrow{V_{ref}} * T_s = \overrightarrow{V_1} * T_1 + \overrightarrow{V_2} * T_2 + \overrightarrow{V_0} * T_0 \tag{5.26}$$

$$\overrightarrow{V_0} * T_0 = 0 \tag{5.27}$$

So,

$$\overrightarrow{V_{ref}} = \frac{T_1}{T_s} * \overrightarrow{V_1} + \frac{T_2}{T_s} * \overrightarrow{V_2} \tag{5.28}$$

$\overrightarrow{V_{ref}}$: reference vector

T_s : sampling period of PWM

$\overrightarrow{V_1}$: vector of V_1

T_1 : on time for $\overrightarrow{V_1}$

$\overrightarrow{V_2}$: vector of V_2

T_2 : on time for $\overrightarrow{V_2}$

$\overrightarrow{V_0}$: null vector

T_0 : on time for $\overrightarrow{V_0}$

Considering the complex numbers in polar coordinate, PWMs on time of a SVM are expressed as,

$$T_1 = \frac{\sqrt{3} * T_s * V_{ref}}{V_{DC}} sin\left(\frac{\pi}{3} - \gamma_{rel}\right) \tag{5.29}$$

$$T_2 = \frac{\sqrt{3} * T_s * V_{ref}}{V_{DC}} sin(\gamma_{rel}) \tag{5.30}$$

$$T_0 = T_s + T_1 + T_2 \tag{5.31}$$

T_1 : on time for $\overrightarrow{V_1}$

T_s : sampling period of PWM

V_{ref} : magnitude of the reference vector

V_{DC} : DC bus voltage

γ_{rel} : relative angle

T_2 : on time for $\overrightarrow{V_2}$

T_0 : on time for $\overrightarrow{V_0}$

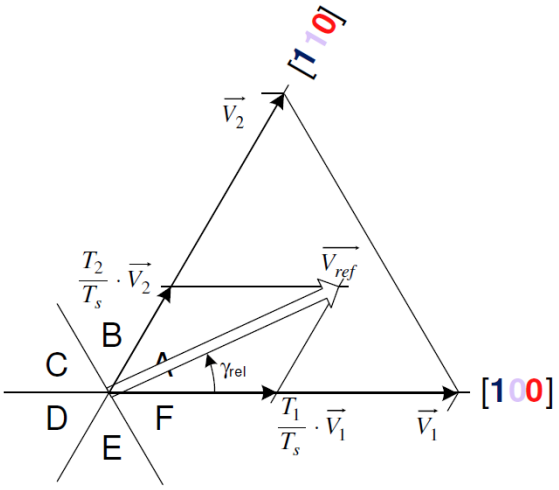

Figure 5.13: Reference vector diagram [67].

As shown in Figure 5.14, the PWM period is expressed as T_{PWM}, the vector T_1 is output for $\frac{T_1}{T_{PWM}}$ and the vector T_1 is output for $\frac{T_2}{T_{PWM}}$. During the remaining time, the null vector T_0 is output. There is a symmetry with respect to the centre of the period.

Generally, centre aligned PWM is used in the motor drive systems. Two pulses in line to line are generated each period with the centre aligned mode. Using this method, the effective frequency value is doubled and the ripple current is reduced while not increasing the switching losses in the power devices; therefore, this type of PWM generates less current harmonic than edge-aligned PWM. Two PWM signals in the same leg of the inverter are complementary to each other. Dead time should be inserted to the period for the same leg in order to prevent the leg from the short circuit [70]. PWM frequency determines the cycle period of FOC. This period is increased or decreased by adjusting PWM frequency. A shorter control period of s system has two significant advantages. First of all, the motor can be driven at a higher speed. This feature can be desirable in high-speed applications. Secondly, decreasing period allows a motor to respond better to load changes. This feature can be useful for applications with sudden load changes such as a washing machine.

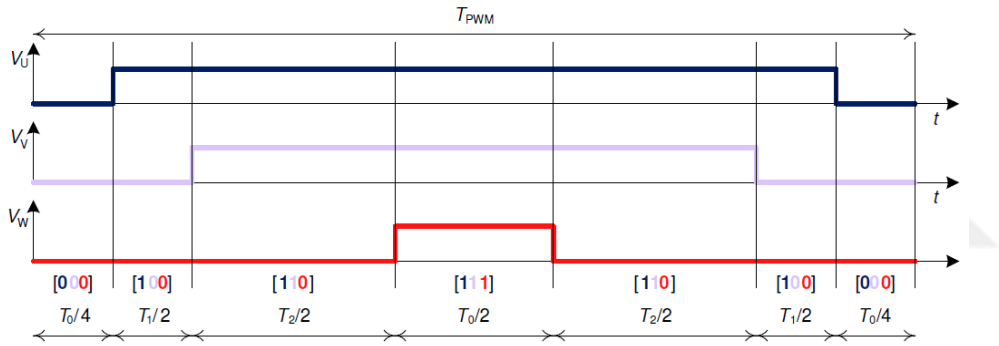

Figure 5.14: PWM pattern of a seven-segment switching sequence [61].

With the SVM, six voltage states and two null states are generated in the stator windings. There are all switching combinations of the power transistors and phase to neutral voltages of each phase in Table 5.1.

Table 5.1: SVM inverter states [62].

Phase C	Phase B	Phase A	V_{ab}	V_{bc}	V_{ca}	V_{ds}	V_{qs}	Vector
0	0	0	0	0	0	0	0	U(000)
0	0	1	V_{DC}	0	$-V_{DC}$	$2/3V_{DC}$	0	U_0
0	1	1	0	V_{DC}	$-V_{DC}$	$1/3V_{DC}$	$1/3V_{DC}$	U_{60}
0	1	0	$-V_{DC}$	V_{DC}	0	$-1/3V_{DC}$	$1/3V_{DC}$	U_{120}
1	1	0	$-V_{DC}$	0	V_{DC}	$-2/3V_{DC}$	0	U_{180}
1	0	0	0	$-V_{DC}$	V_{DC}	$-1/3V_{DC}$	$-1/3V_{DC}$	U_{240}
1	0	1	V_{DC}	$-V_{DC}$	0	$1/3V_{DC}$	$-1/3V_{DC}$	U_{300}
1	1	1	0	0	0	0	0	U(111)

The maximum output voltage based on the space vector theory is $\frac{2}{\sqrt{3}} = 1.155$ times as large as the conventional sinusoidal modulation. It causes higher torque at high speed and higher efficiency. 3rd harmonic injection is seen for each phase. The line to ground voltages for each phase are shown Figure 5.15.

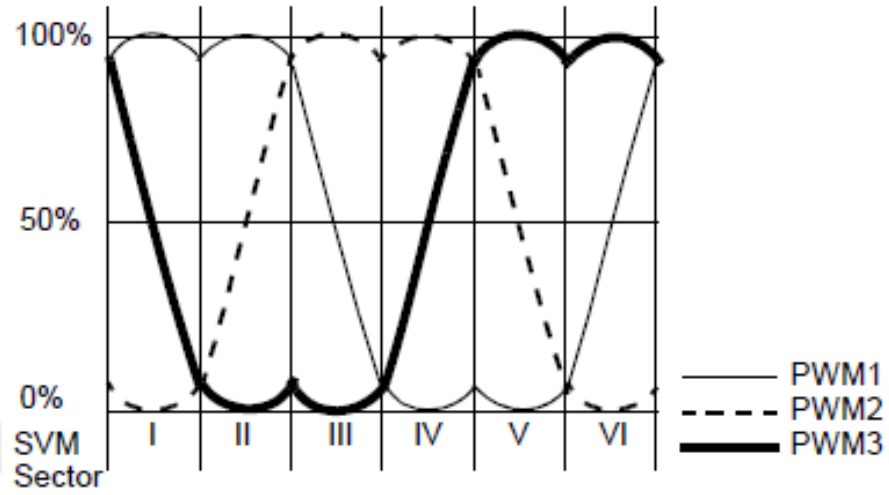

Figure 5.15: The line to ground voltages using space vector modulation [71].

Although the line to ground voltages don't have a pure sinusoidal shape, the resulting line to line voltages in the motor phases are sinusoidal and shown in Figure 5.16.

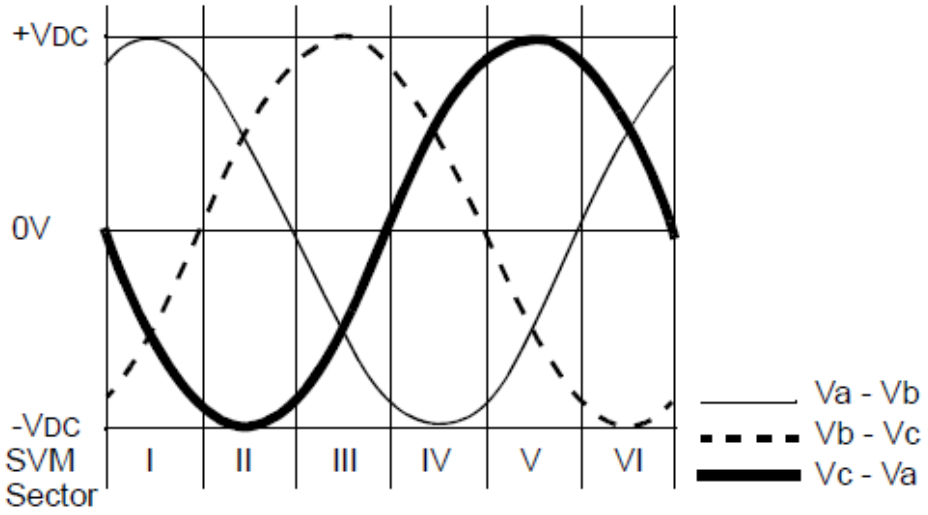

Figure 5.16: The line-to-line voltages using space vector modulation [71].

All transformations used in the FOC technique are shown in Figure 5.17. Three phase currents are converted to two phase rotating reference frame currents. The PI controller compares these two currents with reference currents and rotating reference frame

currents are converted to three-phase currents again. Finally, three phase SVPWM signals are generated according to the current transformation.

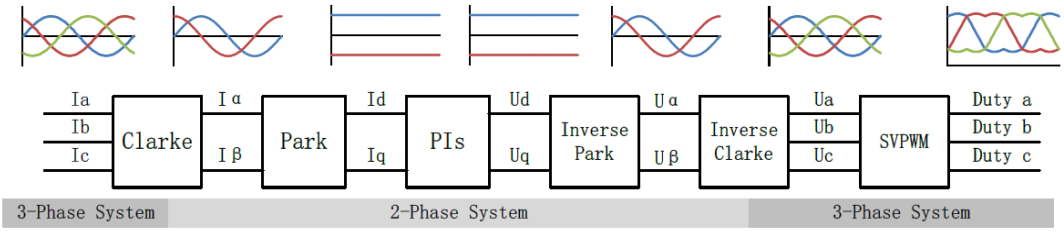

Figure 5.17: Sensorless FOC calculation flow [67].

Determining the position and the speed of a motor is one of the most significant sections for FOC. The rotor position angle θ_r which is between the rotor flux linkage and α axis is used in Park Transform. Information of the rotor position can be obtained from physical sensors. Hall effect sensors, optical encoders and resolvers are the most used physical sensors in applications. Determination of the position and speed is developed as sensorless due to reducing system cost and required maintenance. In sensorless FOC, the position and the speed of a motor are calculated by using back electromagnetive force (Back-EMF). In Figure 5.18, e_α and e_β components of EMF that are used in the calculation are shown. The algorithm that is used to determine the position and the speed.

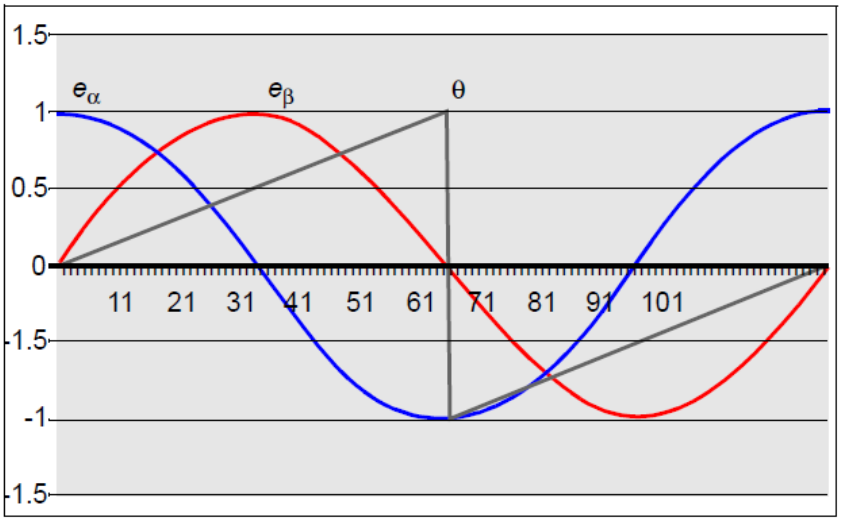

Figure 5.18: Back-EMF and theta relationship [62].

The rotor position is calculated in every PWM period with interrupt service routine using below basic equations,

$$e_{\alpha s} = V_{\alpha s} - r_s i_{\alpha s} - L_s \frac{di_{\alpha s}}{di_t} \tag{5.32}$$

$$e_{\beta s} = V_{\beta s} - R_s i_{\beta s} - L_s \frac{di_{\beta s}}{di_t} \text{ [11]} \tag{5.33}$$

$e_{\alpha s}$: alfa component of the Back-EMF voltage [V]

$V_{\alpha s}$: alfa component of the stator voltage [V]

r_s : resistance of the stator [Ohm]

$i_{\alpha s}$: alfa component of the stator current [A]

L_s : inductance of the stator [H]

$e_{\beta s}$: beta component of the Back-EMF voltage [V]

$V_{\beta s}$: beta component of the stator voltage [V]

$i_{\beta s}$: beta component of the stator current [A]

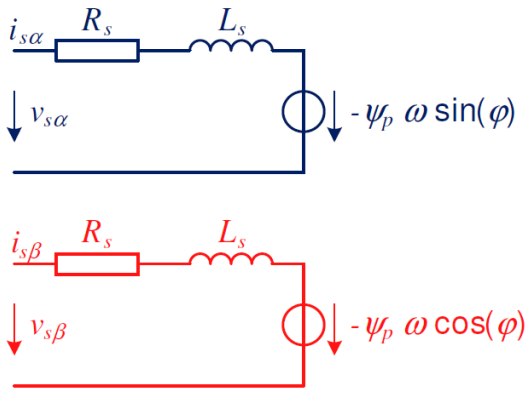

Figure 5.19: Equivalent circuit of α-β frame [61].

And $e_{\alpha s}$ and $e_{\beta s}$ values can be also shown as,

$$e_{\alpha s} = -\lambda'_m * \omega_r * sin\,\theta_r \tag{5.34}$$

$$e_{\beta s} = \lambda'_m * \omega_r * cos\,\theta_r \tag{5.35}$$

So,

$$\theta_r = arctan \frac{-e_{\alpha s}}{e_{\beta s}} \tag{5.36}$$

$e_{\alpha s}$: alfa component of the Back-EMF voltage [V]

λ'_m : magnitude of the flux linkage of the permanent magnet [Wb.turns]

ω_r : angular velocity of the rotor [rad/s]

θ_r : displacement of the rotor [rad]

$e_{\beta s}$: beta component of the Back-EMF voltage [V]

Signal is filtered by first-order low pass filter (LPF). The smoother signal is taken via LPF. Because of using the filter in the calculation of the rotor position, the little phase delay is seen in the rotor angle if compared to the real rotor position. In order to eliminate delay, an offset angle value is added to the calculated angle.

$$\theta_{r\_correct} = \theta_r + \theta_{offset} \tag{5.37}$$

$\theta_{r\_correct}$: corrected displacement of the rotor [rad]

θ_r : displacement of the rotor [rad]

θ_{offset} : offset angle [rad]

θ_{offset} value depends on the rate of change of theta in other words, depends on the rotor speed. Before calculating $\theta_{r\_correct}$, the speed of the motor must be calculated. Uncompensated theta (θ_r) is a main parameter for the calculation. Theta values are accumulated with over samples and the obtained value is multiplied by a constant. The result is filtered with a LPF and the speed of the rotor is calculated. Related speed equation is given below,

$$\omega_r = \sum_{i=0}^{m} ((\theta_r)_n - (\theta_r)_{n-1}) * K \tag{5.38}$$

ω_r : angular velocity of the rotor [rad/s]

m : number of the accumulated value of the angular velocity of the rotor

$(\theta_r)_n$: current value of the displacement of the rotor [rad]

$(\theta_r)_{n-1}$: previous value of the displacement of the rotor [rad]

K : amplification factor for desired speed range

As above mentioned, the Back-EMF voltage is used to determine the position and the speed of the rotor in sensorless FOC operation. However, the FOC algorithm is unstable at low speed. Because the Back-EMF voltage is not sufficient to take measurement for the calculations. Hence, scalar control in another saying V/f control that is open loop is carried out from startup until the rotor reaches the predefined threshold speed value. After that point, the Back-EMF voltage is accurate enough to measure and the sensorless FOC algorithm which is closed loop can be conducted by taking into account the real rotor position. If desired operating speed is under the threshold speed value, the algorithm remains in open loop V/f control and does not pass to closed loop sensorless FOC algorithm. In the open loop V/f control, the rotor position is calculated as considering a linear and fixed relationship between voltage and frequency regardless of the real rotor position. V/f constant depends on the motor and load characteristics [72].

A PMSM reaches its maximum speed when the maximum phase voltage $\frac{V_{bus}}{\sqrt{3}}$ and zero load is applied to the motor. In this condition, the Back-EMF voltage almost reaches to the phase voltage. The rotor speed is linearly proportional with the Back-EMF voltage, so the rotor speed saturates. As described on previous pages, i_q current is responsible for the production of the torque and i_d current is also responsible for the building the field. i_d current is kept at zero because permanent magnets produce the required rotor flux. If i_d current has the negative value instead of zero, a reverse magnetic field against the rotor magnetic field is generated. In this way, the rotor flux is weakened by negative i_d current.

$$V_{bemf} = K_c * \lambda'_m * \omega_r \tag{5.39}$$

V_{bemf} : Back-EMF voltage

K_c : Back-EMF constant

λ'_m : magnitude of the flux linkage of the permanent magnet [Wb.t]

ω_r : angular velocity of the rotor [rad/s]

If the Back-EMF is considered to be constant at the phase voltage, decrease of the rotor flux linkage λ'_m allows increase of the rotor speed ω. By the weakening flux, the nominal speed of the rotor can be increased to 10 times for interior PMSM. However,

surface mounted PMSM has large airgap space. This situation causes a weak armature reaction that affects the flux linkage of the permanent magnets. Therefore, this type of a motor cannot spin faster more than double of the base speed. In addition to that, there is the risk of mechanical damage at high speed for surface mounted PMSM. Because the permanent magnets are embedded on the surface of the rotor and they may break due to high-speed stress. Secondly, demagnetization of the permanent magnets may occur if they are exposed to a high magnetic field due to exceeded i_{ds} current.

By adding i_d current to the stator current, the total power supply current may reach to a dangerous value. The stator current must not exceed the predetermined maximum value when flux weakening is applied. Above nominal speed, this current is kept constant at maximum value by decreasing i_q current in order to obtain the maximum torque. The dynamic d-q voltage equations which are used in the calculation of flux weakening parameters are shown as,

$$V_{ds} = r_s * i_{ds} - \omega_r * L_s * i_{qs} + L_s * \frac{di_{ds}}{dt} \tag{5.40}$$

$$V_{qs} = r_s * i_{qs} + \omega_r * L_s * i_{ds} + \omega_r * \lambda'_m + L_s * \frac{di_{qs}}{dt} \tag{5.41}$$

V_{ds} : direct component of the stator voltage [V]

r_s : resistance of the stator [Ohm]

i_{ds} : direct component of the stator current [A]

ω_r : angular velocity of the rotor [rad/s]

L_s : inductance of the stator [H]

i_{qs} : quadrature component of the stator current [A]

V_{qs} : quadrature component of the stator voltage [V]

i_{ds} and i_{qs} are DC parameters so derivative terms can be cancelled in steady state. If these two equations are rewritten as,

$$V_{ds} = r_s * i_{ds} - \omega_r * L_s * i_{qs} \tag{5.42}$$

$$V_{qs} = r_s * i_{qs} + \omega_r * L_s * i_{ds} + \omega_r * \lambda'_m \quad (5.43)$$

V_{ds} : direct component of the stator voltage [V]

r_s : resistance of the stator [Ohm]

i_{ds} : direct component of the stator current [A]

ω_r : angular velocity of the rotor [rad/s]

L_s : inductance of the stator [H]

i_{qs} : quadrature component of the stator current [A]

V_{qs} : quadrature component of the stator voltage [V]

λ'_m : magnitude of the flux linkage of the permanent magnet [Wb]

V_{qs} voltage needed i_d current for flux weakening and the maximum i_{qs} current that can be injected are calculated according to the following equation.

$$V_{q\_ref} = \sqrt{V_{s\_max}^2 - V_{ds}^2} \quad (5.44)$$

$$i_{ds\_flux\_weak} = \frac{V_{q\_ref} - r_s * i_{qs} - \omega_r * \lambda'_m}{\omega * L_s} \quad (5.45)$$

$$i_{qs\_ref\_max} = \sqrt{i_{s\_max}^2 - {i_{ds\_flux\_weak}}^2} \quad (5.46)$$

V_{qs_ref} : reference voltage of the quadrature axis [V]

V_{s_max} : maximum allowable stator voltage [V]

V_{ds} : direct component of the stator voltage [V]

$i_{ds\_flux\_weak}$: calculated reference current for flux weakening

r_s : resistance of the stator [Ohm]

i_{qs} : quadrature component of the stator current [A]

ω_r : angular velocity of the rotor [rad/s]

λ'_m : magnitude of the flux linkage of the permanent magnet [Wb]

$i_{qs\_ref\_max}$: maximum reference current of the quadrature axis [A]

i_{s_max} : maximum allowable stator current [A]

It is obvious that, torque is also decreased in this region because of a decrease in i_q current. These negative i_d current and positive i_q current are also controlled by PI controller as a nominal range. In addition to that, the resulting stator flux and the rotor flux is not perpendicular to each other anymore in the flux weakening situation [73].

6. HARDWARE DESIGN

Main hardware blocks are shown in Figure 6.1 as a chart. These blocks can be basically classified into two groups regarding to their functions. Power and control signals are generated with these hardware blocks.

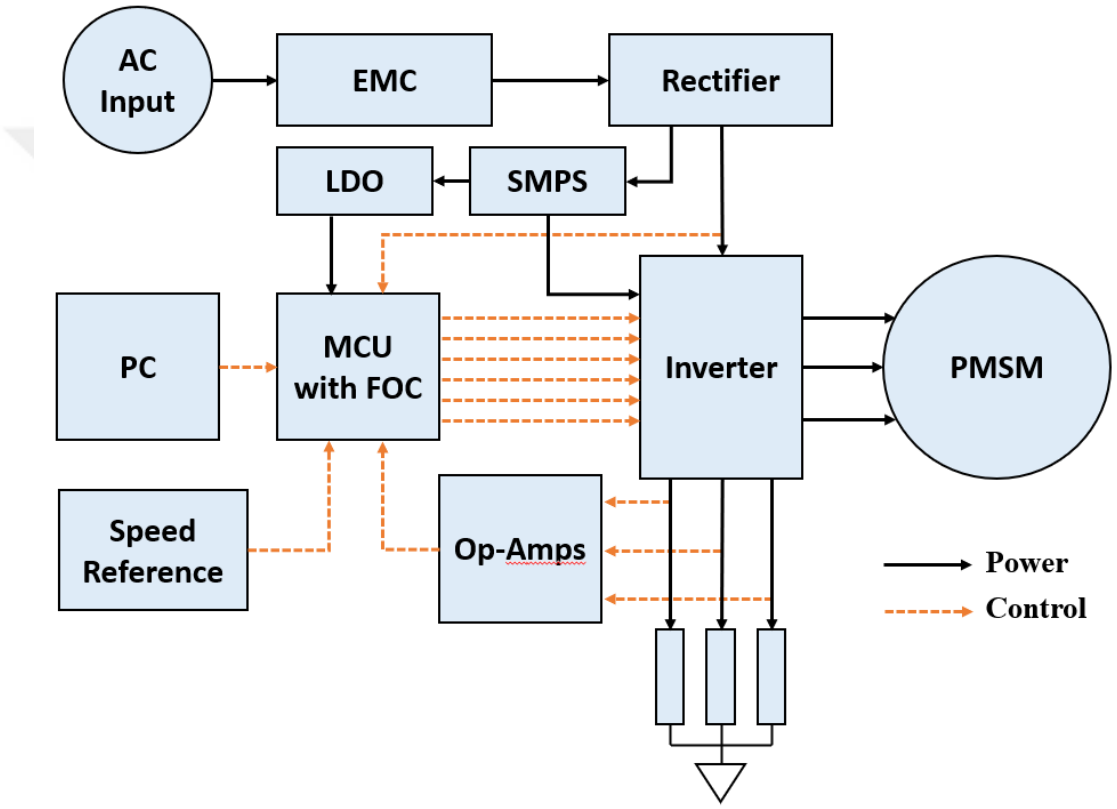

Figure 6.1: Hardware block diagram.

6.1 Schematic Design

Schematic design of the inverter board is performed in Altium Designer software. Before starting the design in detail, hardware block diagram that is shown in Figure 6.1 is constructed. After that, each block is designed component by component as will be explained in the following sections. The order of the blocks is given by considering the power flow.

6.1.1 EMI filter and rectification circuits

The designed input and rectification stage are shown in Figure 6.2. This circuit basically contains protection components, EMI filter components and rectification components.

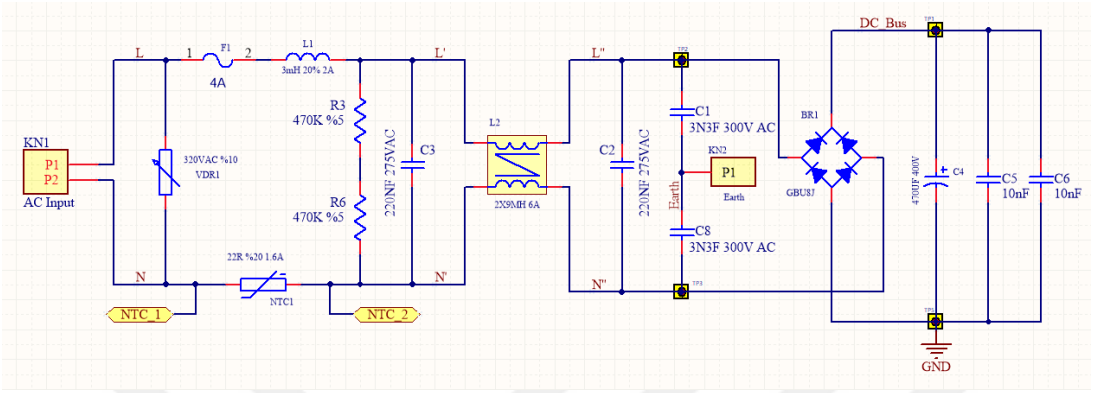

Figure 6.2: Input and rectification circuit.

First of all, AC input voltage is applied to KN1 connector. Input voltage is typically 230VAC; however, the motor could be driven without any problem between 120VAC and 265VAC input voltage. Although this maximum input voltage is mostly transient, components should be selected properly in order to withstand maximum voltage stress which is 265VAC and as explained before, nominal working voltage 230VAC. VCR1 component is a 14mm varistor and its rated value is 320VAC. In Figure 6.3, the voltage-current graph of the used varistor is shown. As seen in Figure 6.3, the varistor is not expected to clamp the input voltage to 320VAC directly.

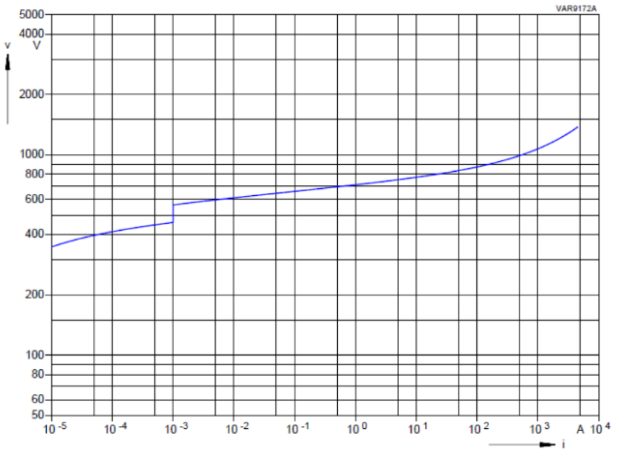

Figure 6.3: Voltage-current graph of the varistor [74].

It is actually used for transient condition in grid voltage which can be up to a few kV's. This type of the transient voltage can be caused by lightning. Varistor cannot protect

the circuit from abnormal steady state voltage which is above 265VAC and the circuit in this abnormal condition probably is damaged.

NTC1 is the negative temperature constant resistor. It is used to limit inrush current caused by electrolytic rectification capacitor which is 470uF in this circuit. When the circuit is energized, a high dV/dt value is applied to the electrolytic capacitor electrode. This causes an excessive current which can reach to hundreds of amps depending on capacitor value throught the electrolytic capacitor. This inrush current generates current stress in the capacitor and rectification bridge diode and the probability of failure of these components dramatically increase due to inrush current. When there is no current through NTC, it has high resistance and its value is 22R in this circuit. When the circuit is energized, the electrolytic capacitor tends to draw high current but NTC limits current depending on its value. As current increases, the temperature of NTC also increases so the resistance of the NTC dramatically decreases due to its negative temperature characteristics.

Table 6.1: Parameters of used NTC [75].

R_{25} Ω	I_{max} (0...25 °C) A	$B_{25/100}$ K	C_{test} [1)] 230 V µF	C_{test} [1)] 110 V µF	Param. for R(I)[1)] k	Param. for R(I)[1)] n
1	9.0	2700	700	2800	0.622	−1.27
2.2	7.0	2800	700	2800	0.806	−1.30
2.5	6.5	2800	700	2800	0.843	−1.30
4.7	5.1	2900	700	2800	1.03	−1.32
5	5.0	2900	700	2800	1.05	−1.32
7	4.2	3000	700	2800	1.16	−1.33
10	3.7	3060	700	2800	1.29	−1.34
15	3.0	3000	700	2800	1.49	−1.33
22	2.8	3300	700	2800	1.57	−1.37
33	2.5	3300	900	3600	1.78	−1.37
60	1.6	4000	400	1600	1.77	−1.44

Parameters which are used in calculations are given in Table 6.1. In addition to these parameters, its maximum power dissipation is 3.1W and its maximum working voltage is 265VAC. If a relay is not used to bypass NTC, this maximum power dissipation should be considered to avoid excessive temperature over NTC. Generally, this NTC is bypassed in order to increase the efficiency of the driver so it only operates in start-up condition. In this circuit, NTC is also bypassed. If it is not bypassed, equation (6.1) could be used to calculate the operating resistance of the 22R NTC,

$$R_{ntc} = k \times I_{rated}^{n} \tag{6.1}$$

R_{ntc} : NTC resistance [Ohm]

k : product coefficient

I_{rated} : rated RMS current [A]

n : exponent coefficient

Power dissipation could be calculated as below,

$$P_{loss\_ntc} = I_{rated}^2 \times R_{ntc} \quad (6.2)$$

P_{loss_ntc} : power loss of the NTC [W]

I_{rated} : rated RMS current [A]

R_{ntc} : NTC resistance [Ohm]

R_{ntc} and P_{loss_ntc} is calculated as 0.61 Ohms and 2.43 W respectively. If considering %10 tolerance of NTC resistance, the calculated 2.43W power loss could be higher or lower than this value. In order to eliminate this power dissipation, NTC is bypassed via relay.

F1 is the fuse that has 4A value for short circuit protection. This type of failure can be caused by the short circuit of the electrolytic capacitor used in a DC bus or a short circuit of the motor phases. Response of the fuse is slow especially in inductive load such as the motor. So, this feature could be a problem for semiconductor devices such as IGBT in the short circuit condition. Because IGBT can withstand to short circuit maximum 5-15 microseconds depending on its characteristics. Due to that, the fuse should be considered as backup protection for short circuits. Other hardware and software short circuit protections are much faster than a response time of the fuse.

L1 is used for two important purposes. First of all, this inductor can be thought as a passive PFC. Power factor (PF) is increased up to 0.65 thanks to this component. In addition to that, the harmonic content of the input current is also decreased. Compliance with international regulations is ensured in terms of both power factor and harmonic content.

Table 6.2: Classification of equipments [76].

Class A	• Balanced three-phase equipment • Household appliances, excluding equipment identified by Class D • Tools excluding portable tools • Dimmers for incandescent lamps • Audio equipment • Everything else that is not classified as B, C or D
Class B	• Portable tools • Arc welding equipment which is not professional equipment
Class C	• Lighting equipment
Class D	• Personal computers and monitors • Television receivers • Note: Equipment must have power level 75W up to and not exceeding 600W

Classification of equipment in terms of harmonic content is shown in Table 6.2. 270W motor driver circuit for compressor applications get involved to Class D group. For class D equipment, Table 6.3 is taken as a reference for the calculations. Odd harmonic frequencies from 3 to 39 are taken into an account. Applications in class D must follow both maximum permissible harmonic current per Watt and maximum permissible harmonic current for specified odd harmonics mentioned above.

Table 6.3: Harmonic limits for class D equipment [76].

Harmonic Order (n)	Maximum Permissible Harmonic Current per Watt (mA/W)	Maximum Permissible Harmonic Current (A)
3	3.4	2.30
5	1.9	1.14
7	1.0	0.77
9	0.5	0.40
11	0.35	0.33
$\mathbf{13 \leq n \leq 39}$ (odd harmonics only)	$\frac{3.85}{n}$	$0.15 \times \frac{15}{n}$

The second purpose of the usage of L1 is for EMI. This inductor attenuates the differential mode (DM) conducted noise with X capacitors which are C2 and C3 in this circuit. Conducted emission limits for class B application is shown in Figure 6.4. Industrial devices are part of class A and residential devices such as refrigerators, washing machines, dishwashers etc. are interpreted as class B devices.

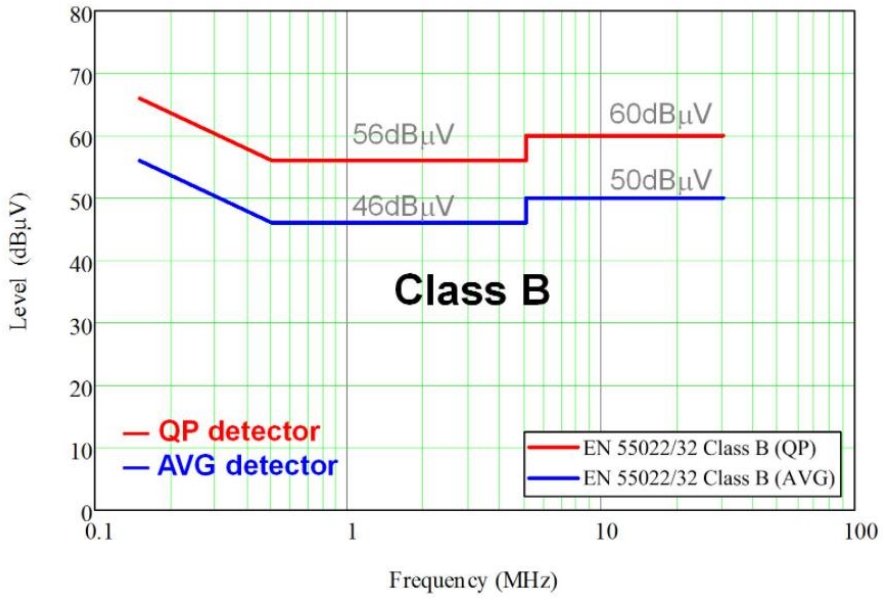

Figure 6.4: Conducted emission limits for class B applications [77].

L2 is used to attenuate the common mode (CM) conducted noise with Y capacitors that are C1 and C8 in the circuit. The fluxes that are generated by the currents with different directions cancel each other and these currents do not encounter with the inductance. However, the currents that flow through the same direction generate fluxes that support each other. Inductance is built, therefore; conducted common-mode noise is attenuated. The leakage inductance of the common mode filter behaves like differential-mode inductor like L1. The percentage of the leakage inductance of the common-mode inductor can be in the range of between 1% and %3 depending on the winding geometry. C2 and C3 are the X capacitors and used to attenuate the differential mode noise with L1. They can also smooth the effects of the electrical fast transient (EFT) signals with the varistor. These capacitors storage energy and when the consumer unplugs the device, this residual energy must be dissipated. Otherwise, the consumer may face the risk of the electric shock when they touch the plug of the device. According to the regulation, after unplugging the device, the voltage level must decrease under 34V which is peak voltage within 1 second. In order to dissipate this

residual energy, R3 and R6 resistors are used. These resistors are also called as bleeding resistors. Considering these two resistors and C2, C3 capacitors, a residual voltage is simulated using PSIM. As seen in Figure 6.5, approximately 29V remains at 1 second point after unplugging.

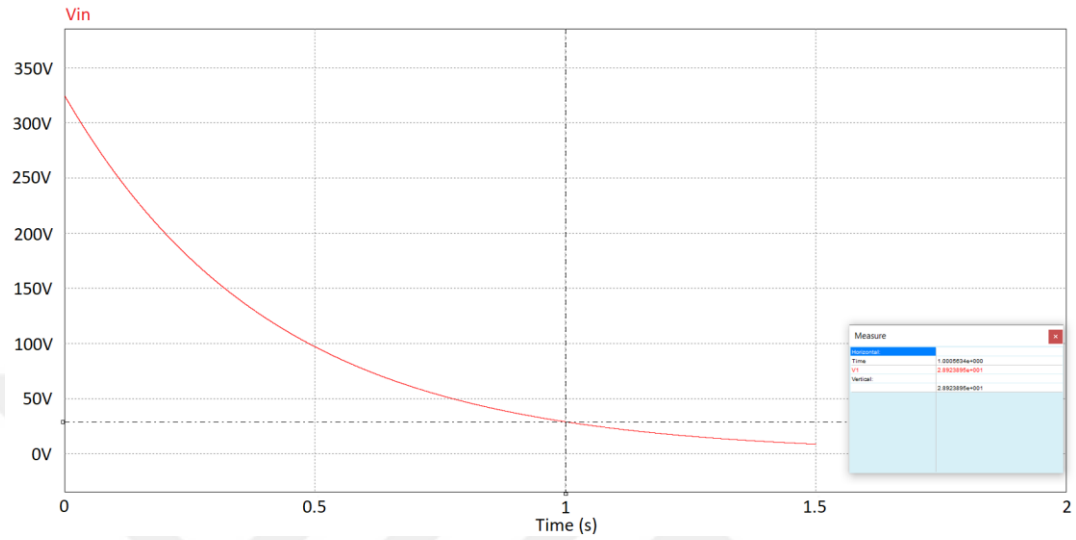

Figure 6.5: PSIM simulation result for residual voltage.

R3 and R6 are useful to dissipate residual energy; however, they keep consuming energy while the circuit is in a plug. Lost energy is calculated as 56 mW using equation (6.3).

$$P_{loss\_bleeding} = \frac{{V_{input}}^2}{R_{bleeding}} \tag{6.3}$$

$P_{loss\_bleeding}$: power loss of the bleeding resistor [W]

V_{input} : input RMS voltage [V]

$R_{bleeding}$: bleeding resistor [Ohm]

C1 and C8 are Y capacitors that are used to attenuate the common mode noise with L2. They also affect the differential mode noise; however, their effects are minor in the differential mode and can be omitted. These capacitors cause the leakage current that flows through the earth. The value of these capacitors is directly related to the leakage current. In case of disconnection of earth connection for class I equipment, these capacitors may cause a risk of electrical shock. Because class I equipment have earthed chassis and if a user touches the chassis which is unearthed, the leakage current

flows from the body of the user to the earth. This current has various effects that are described in Table 6.4.

Table 6.4: Effects of the current on the human body [78].

Current	Effect
1mA	Barely perceptible
1-3mA	Perception threshold (most cases)
3-9mA	Painful sensation
9-25mA	Muscular contraction (can't let go)
25-60mA	Respiratory paralysis (may be fatal)
60mA or more	Ventricular fibrillation (probably fatal)
4A or more	Heart paralysis (probably fatal)
5A or more	Tissue burning (fatal if vital organ)

Due to the effect of the leakage current, the value of the Y capacitor must be limited for class I equipment. The limit of the leakage current varies by region. The leakage current that is caused by the Y capacitor is calculated as 238 uA by using equation (6.4) [79].

$$I_{leakage} = V_{input} * 2 * \pi * f * C_y \tag{6.4}$$

$I_{leakage}$: leakage current [A]

V_{input} : input RMS voltage [V]

f : grid frequency [Hz]

C_y : value of the Y capacitor [F]

470uF DC bus capacitor is used in the rectification circuit. There is an also +-20% tolerance at capacitance value. Maximum DC voltage on DC bus, when 265V input voltage is applied, 377V so 400V is preferred in capacitor voltage value. As seen in

Figure 6.6, the capacitor can withstand 450V surge voltage without damage. Its working ambient voltage is between -25°C and 85°C. Tanδ is the dissipation factor that is used to calculate the ESR value in desired frequency. Leakage current is caused by equivalent parallel resistance to the capacitor. The most important parameter is the rated ripple current. It is ensured that 2510mA ripple current can be supplied to the load at 85°C and 120Hz frequency.

Capacitance (uF)	Tolerance on rated Capacitance (%)	Working Voltage (Vdc)	Surge Voltage (Vdc)	Category Temp. Range (℃)	Tanδ @25℃ (120Hz) (Max)	Leakage Current (uA) (5 min.)	Rated Ripple Current (mA rms) @85℃ 120Hz	Endurance @ 85℃ (Hours)	Dimensions (mm)		
									ΦD	L	F
470	±20	400	450	-25~+85	0.20	1300	2510	3000	30	40	10

Figure 6.6: Capacitor spesification [80].

However, it is needed to recalculate this ripple current value according to working conditions. If the ambient temperature is taken as 60°C, 1.4 coefficient is acquired. In addition to that, the frequency of the rectified voltage is 100Hz. If the linear correlation is done between 50Hz and 120Hz, 0.95 coefficient is calculated for 100Hz. The resulted ripple current is calculated as 3.33 A by using equation (6.5).

$$I_{ripple\_calculated} = I_{ripple} * n_{temp} * n_{freq} \quad (6.5)$$

$I_{ripple\_calculated}$: calculated ripple current [A]

I_{ripple} : ripple current [A]

n_{temp} : the temperature coefficient

n_{freq} : the frequency coefficient

Even the maximum input current is smaller than the capacitor current. So, this capacitor is suitable for usage in this study. Temperature and frequency coefficients of the capacitor are given in Table 6.5 and Table 6.6.

Table 6.5: Temperature coefficients of the capacitor [80].

Temperature	60 °C	70 °C	85 °C
Ripple Factor	1.40	1.23	1.00

Table 6.6: Frequency coefficients of the capacitor [80].

Frequency	50Hz	120Hz	300Hz	1kHz	10kHz
Ripple Factor	0.85	1.00	1.15	1.20	1.40

Maximum peak to peak voltage ripple on DC bus at different voltage levels of 120 V (minimum), 230 V (nominal), 265 V (maximum) can be calculated as 37V, 19V, 17V using the equation (6.6) respectively.

$$V_{p-p\_ripple} = \frac{P_{input\_max}}{2 \times f \times C_{bus} \times V_{input\_peak}} \tag{6.6}$$

V_{p-p_ripple} : peak to peak voltage ripple of the rectified side [V]
P_{input_max} : maximum input power [W]
f : grid frequency [Hz]
C_{bus} : capacitance of the DC bus capacitor [F]
V_{input_peak} : peak voltage of the input [V]

These peak-to-peak values is proper for motor control. 2x10nF 630V SMD ceramic capacitors are used for enhancing switching performance. High-frequency voltage oscillation on DC bus due to switching is decreased thanks to these capacitors. In addition to that, inrush current requirement in switching time is also provided from these capacitors. If the approximate power loss of the bridge diode at the full load which is 300W is calculated as 3.4 W by using equation (6.7).

$$P_{loss\_bridge} = 2 * V_f * I_{input\_max} \tag{6.7}$$

P_{loss_bridge} : power loss of the bridge diode [W]
V_f : forward voltage [V]
I_{rated} : rated RMS current [A]

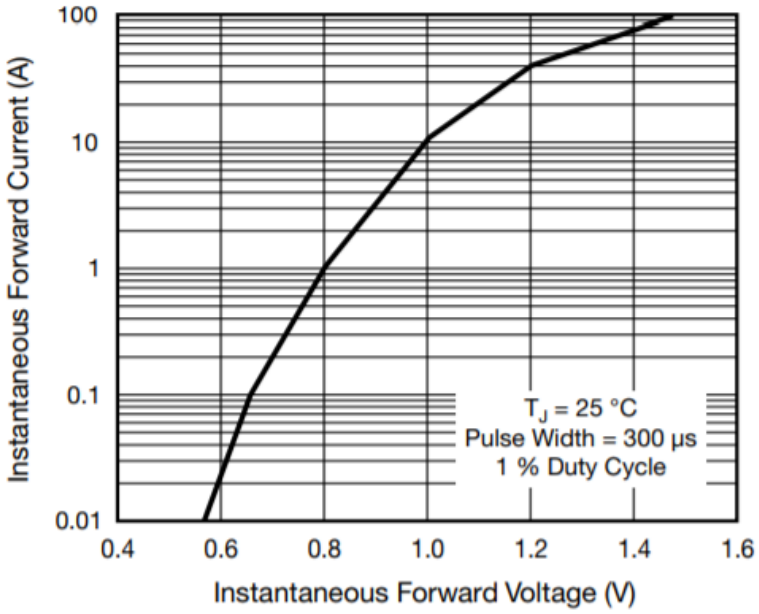

Figure 6.7: Forward voltage - forward current graph of the bridge diode [81].

If 2A is determined as a maximum input voltage, 0.85V is can be taken as a voltage drop on the bridge diode as seen Figure 6.7. The bridge diode will be connected to the heatsink with IPM. Thermal calculations will be done after calculating power loss on IPM. The thermal impedance of the heatsink will be also calculated.

6.1.2 15V SMPS design

Buck converter is chosen as a topology to supply voltage to the circuit. 15V output voltage is directly used to drive IGBT gates. In addition to that, a linear regulator which has a 5V output voltage is fed by 15V. Constructed buck converter circuit is shown in Figure 6.8.

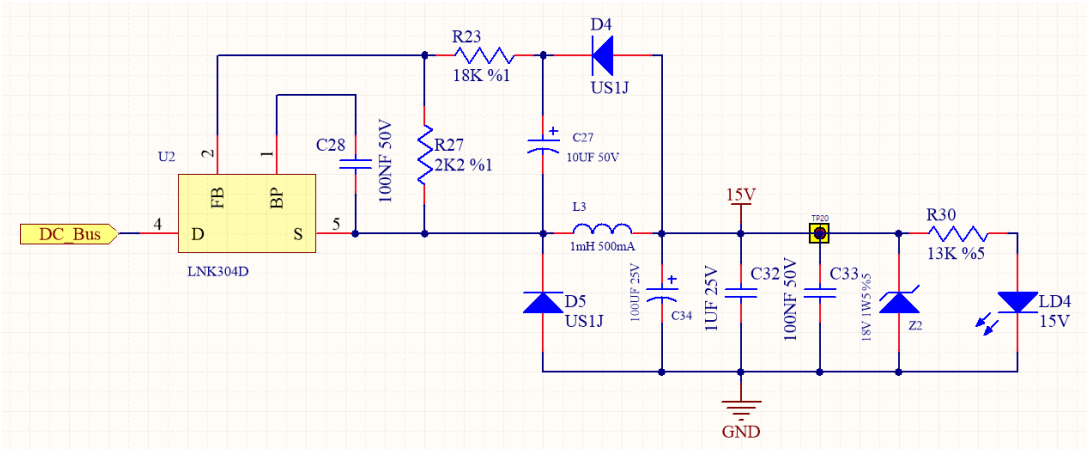

Figure 6.8: Buck converter with 15V output voltage.

LNK304D is used as a controller in the buck converter. This IC has fully integrated auto-restart for short circuit and open loop fault protection. It has 66 kHz switching frequency. Maximum 120mA current can be drawn from the output in discontinuous conduction mode. This value is enough to supply current for all components. Internal MOSFET can withstand up to 700VDC without any breakdown. When the maximum input voltage which is 265V is applied, it has 375VDC rectified voltage and this value is lower than the breakdown limit of the MOSFET. IC has a universal input voltage range (85VAC to 265VAC). The maximum 80mW is consumed in no-load condition. Maximum on state resistance of MOSFET is 44.2Ω and the typical efficiency value in full load is 75%.

LNK304D has high-side MOSFET due to buck converter topology. High voltage bus is converted to 15V. This means a very low duty cycle. It has a basic on/off control technique for regulation. A high voltage switched current source is used for start-up and operation conditions to provide power for IC. This feature eliminates bias supply. The frequency of the oscillator is 66kHz and it produces two signals which are the maximum duty signal and the starting clock signal of the PWM period. Oscillator frequency changes between 64kHz and 68kHz in order to spread EMI noise in a wide area and decrease peak value. Functional block diagram of LNK304D is given in Figure 6.9.

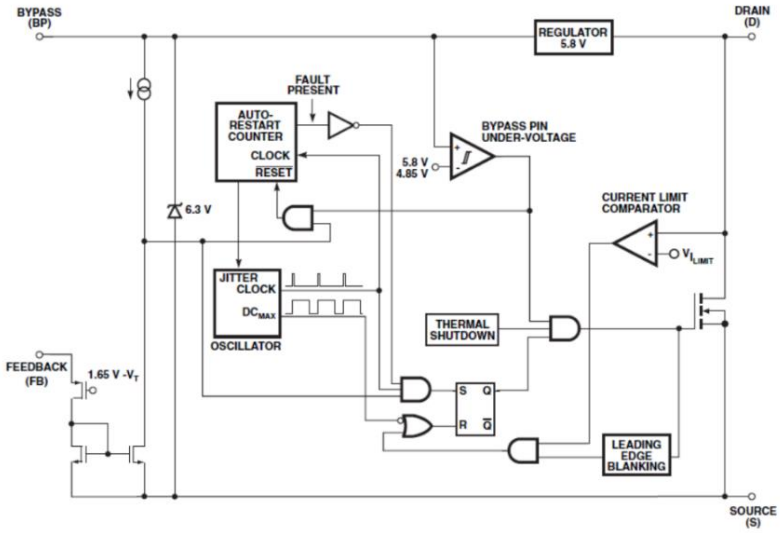

Figure 6.9: Functional block diagram of LNK304D [82].

The output voltage is regulated via voltage at the feedback pin. It has a low impedance source follower output. It is set to 1.65V. Voltage is sampled at the beginning of each cycle on the rising edge of the clock cycle. If the voltage at that pin is lower than the

threshold, MOSFET is opened for that switching period. On the other hand, in the light load condition, the voltage at that pin may be higher than the threshold voltage. In that condition, MOSFET is not open for that period. This is also called as cycle skipping mode. The effective switching frequency can be decreased to 16kHz in light load condition. Regulation is provided and switching loss is decreased in light load condition thanks to cycle skipping mode.

LNK304D has an internal regulator which is fed by a drain pin. This regulator has a 5.8V output voltage and charge capacitor connected to the bypass pin when MOSFET is off. When MOSFET is on, the needed power for the circuit in IC is provided by a charged capacitor. 100nF is enough to store energy. Bias supply with an external resistor can be used to provide energy to the capacitor. The internal zener diode clamps the voltage to 6.3V. In that way, the no-load power consumption of IC can be decreased to 50mW and efficiency is enhanced. A bypass pin also provides under-voltage protection. Whenever bypass pin voltage drops below 4.85, MOSFET is disabled until this voltage rises to 5.8V again.

LNK304D has over-temperature protection. If the temperature exceeds the threshold value which is 142 °C, MOSFET is disabled. MOSFET is not opened until the temperature decreases in IC 75 °C which is hysteresis value.

As mentioned before. LNK304D has a basic on-off control strategy. When the current flowing through MOSFET exceeds the threshold value, MOSFET is closed for this period. At the beginning of the period, the current flowing through MOSFET may exceed the threshold value due to reverse recovery of the freewheeling diode. This causes a false turn-off for MOSFET and regulation can be lost. In order to prevent this condition, the edge blanking circuit ignores the high current value at the beginning of each period and disables the current comparator. After removing this transient condition, the edge blanking circuit enables the current comparator again and false turn-off is avoided.

In case of overload, short circuit or open loop, LNK304D runs into the auto-start condition and MOSFET is disabled during 800ms. After this period, LNK304D tries to start again. If the fault does not disappear, IC again runs into fault condition until and this process continues until fault is removed.

In Figure 6.8, C27 capacitor is charged to the output voltage. It works as a sample and hold function. Value of C27 is recommended between 10uF and 22uF for regulation. In this circuit, 10uF is preferred. R23 and R27 are sense resistors and selected in order

to keep the voltage at feedback pin with 1.65V. In addition to that, approximately 0.8mA feedback current is recommended for regulation. With used resistors, the calculated output voltage is 15.15V. D5 diode is selected as a fast diode in order to reduce current stress in MOSFET. 1mH "I" core inductor is recommended to eliminate audible sound for discontinuous conduction mode. Continuous conduction mode is not needed due to low power demand. The output voltage ripple is closely related to the ESR of the output capacitor. In over-load condition, auto-start power is limited to 6% of the maximum over-load power. LD4 LED is used as both voltage indicator and pre-load. Regulation gets better by using small pre-load considering power consumption. Z2 is a 18V Zener diode and used for over-voltage protection at the output stage [83].

6.1.3 5V voltage source design

NCP1117 linear regulator with fixed 5V output voltage is shown in Figure 6.10. It is used to supply voltage to a microcontroller, Op-Amp and reference voltage in the circuit. NCP1117 has a low dropout voltage which is a maximum 1.2V. The output current can reach up to 1A but such a large current is not required for the driver circuit. The input voltage of the regulator is 15V that is provided by the SMPS circuit and it can operate with up to 20V input voltage.

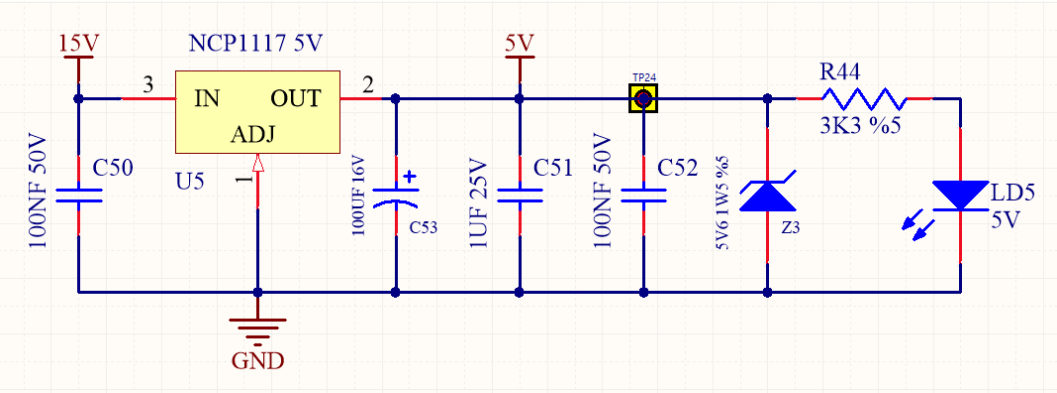

Figure 6.10: Linear regulator with 5V output.

IC has a 10mA quiescent current that causes an additional power loss. Ceramic capacitors at input and output are used to bypass high-frequency noise to the ground. The electrolytic capacitor at output storage energy and maintain the regulation. 5.6V zener diode is also used for over-voltage condition. LD5 is a 5V indicator and it consumes approximately 1mA current.

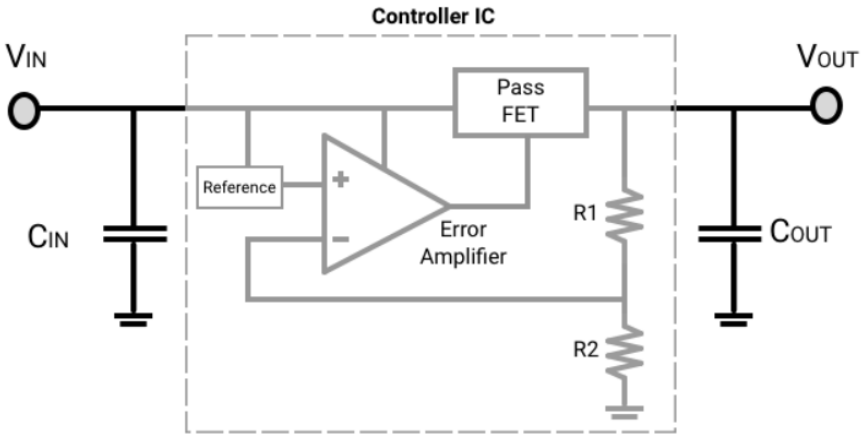

Figure 6.11: Typical series linear regulator structure [84].

A simplified circuit of a series linear regulator is shown in Figure 6.11. The main purpose of this kind of regulator is to compare reference voltage with output voltage divided by resistors and supply current to transistor connected series positive rail via op-amp in order to keep the output voltage constant at a desired level. It is obviously seen that, the voltage difference between input and output is on the series transistor that carries the main output current. This causes a high-power loss especially in the case of high input voltage. Therefore, this situation shows why switched power supplies have a higher efficiency value than the linear regulators [85].

6.1.4 2V5 reference voltage design

A voltage follower which is also called as a buffer amplifier is shown in Figure 6.12.

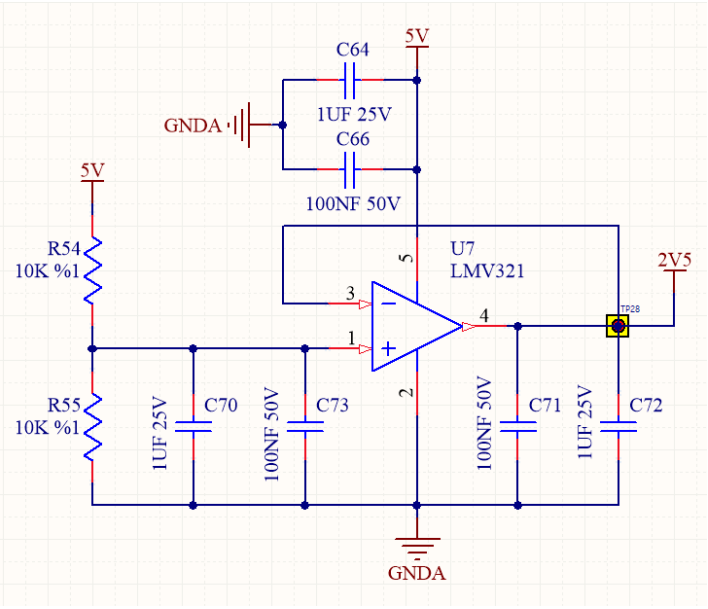

Figure 6.12: Reference voltage for Op-Amps.

It is used to generate reference voltage for current feedback op-amps. R54 and R55 are low tolerance resistors and 2.5V is generated in non-inverting input of the Op-Amp. This voltage is directly reflected to output voltage, so the voltage follower circuit has unit gain. The biggest advantage of using a voltage follower is that the output impedance is too low and it is also independent of the input impedance which is very high compared to output. Shunt voltages on the source of low side IGBTs are amplified with pre-defined gain value via current feedback op-amps and these voltages superpose with a reference voltage which is 2.5V. In this way, a swing of the shunt voltages spread over a full range of analog to digital converter. The utilization factor and resolution of analog to digital converter is maximized. In addition to that, reference voltage also allows the negative voltage on the shunt resistors to be read with analog to digital converter.

6.1.5 Current feedback Op-Amp design

The current feedback Op-Amp circuit is shown in Figure 6.13. Shunt voltages are amplified for a microcontroller. The reference voltage is also added as mentioned before. There is a three times amplification ratio that is adjusted by the feedback resistor.

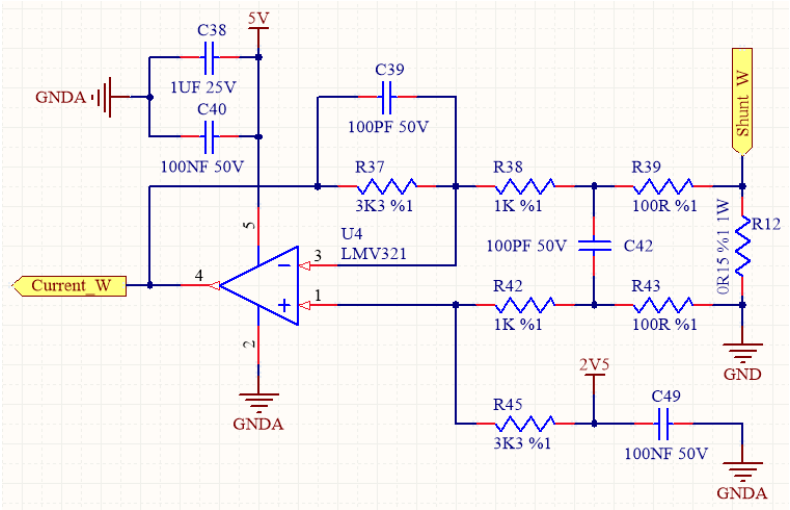

Figure 6.13: Current feedback Op-Amp circuit.

In addition to that, input and output have reserve polarity due to inverting Op-Amp structure. C38 and C40 are placed to eliminate the noise in the power input. There are three Op-Amp circuits for each shunt reading. Analog ground is placed in the power stage. C39 and C42 are placed to prevent amplification of high-frequency noise signal.

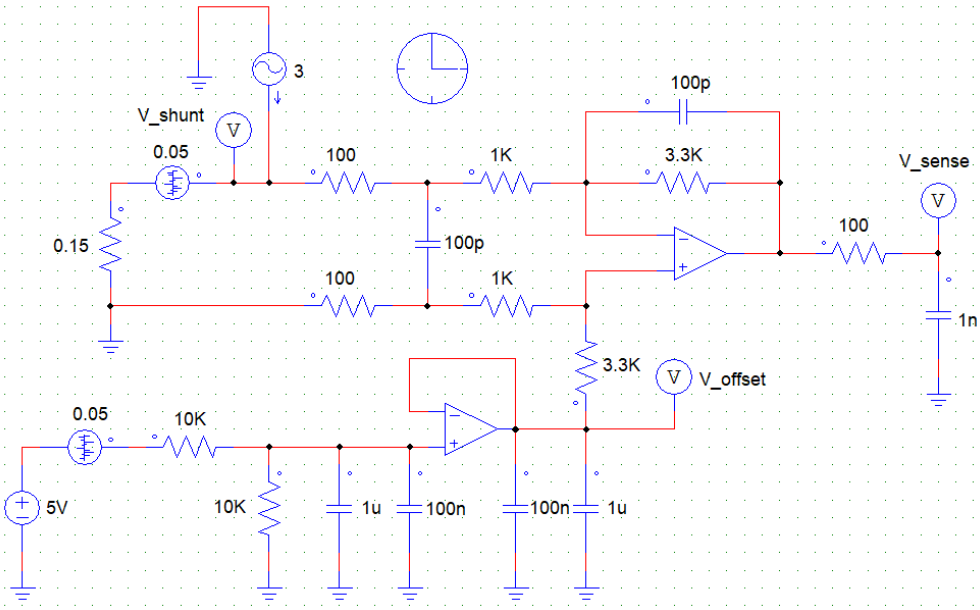

Figure 6.14: PSIM simulation circuit of current feedback Op-Amp.

This circuit is simulated in PSIM and it is given in Figure 6.14. The refence voltage circuit is also added to analyze all system. White noise which has 50mV peak to peak voltage is added to both the shunt resistor side and the input of the reference voltage circuit to get closer to real circuit behaviour. In order to bypass this noise, bypass capacitors are added to critical points. Three amps flow through the shunt resistor and a current source is used for that. 3A is the maximum allowed peak current in one phase.

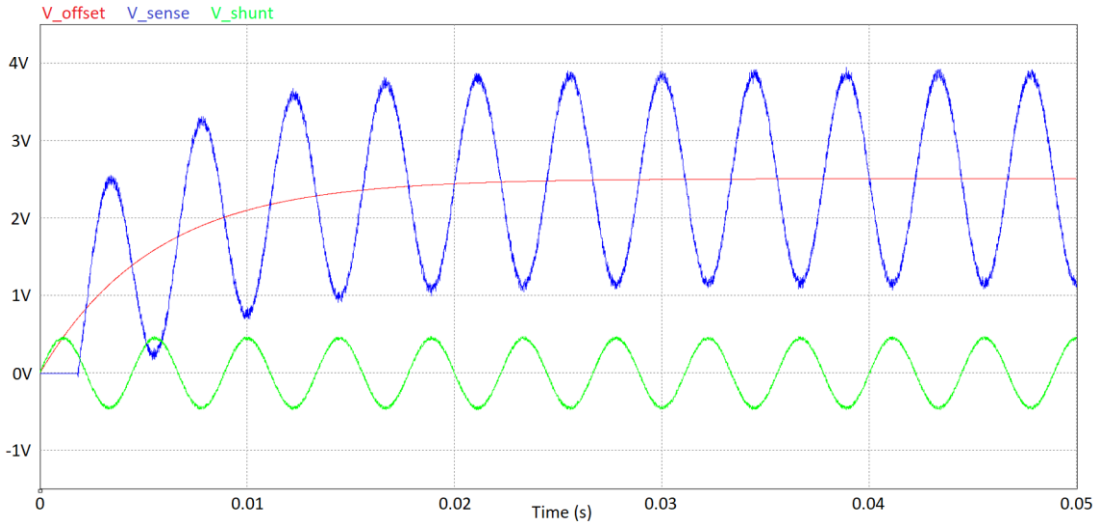

Figure 6.15: PSIM simulation result of Op-Amp circuit.

The simulation result is given in Figure 6.15. Red line represents the reference voltage which is 2.5V. The green one shows the shunt voltage and blue one shows amplified and filtered shunt voltage with offset. As seen in the graph, after the transient

condition, amplified voltage has a 2.5V average voltage as expected. There times amplification ratio and reverse polarity are also seen. Noise effect can be observed in three signals especially in amplified voltage. Because noise is also amplified with op-amp. This is the main drawback of these kinds of circuits. By taking the average value of the current with software, this condition can be solved [86].

6.1.6 IPM stage design

An intelligent power module which is called as IPM is shown in Figure 6.16.

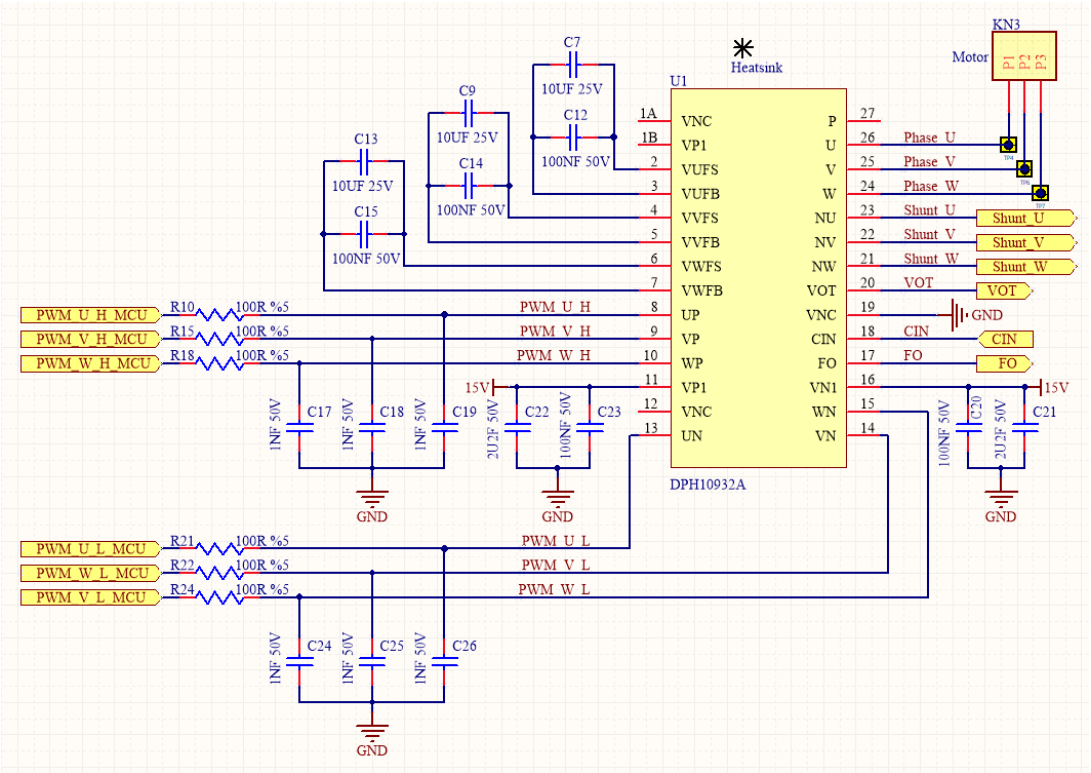

Figure 6.16: IPM circuit.

PWM signals coming from the microcontroller are filtered before corresponding pins of IPM. On threshold voltage of these pins is 2.1V and the off-threshold voltage is also 1.3V. In addition to that, the allowable minimum input pulse width is 0.7us. The time constant of these filters is small enough not to affect the shape of the square wave. 2.2uF and 100nF bypass capacitors are recommended in the 15V input side for the best performance. KN3 is a motor connector. Shunt_U, Shunt_V and Shunt_W are the input of the shunt resistors. VOT is analog output of the temperature signal. CIN is input for over-current detection. FO is the fault signal. These inputs and outputs will be explained in the next sections.

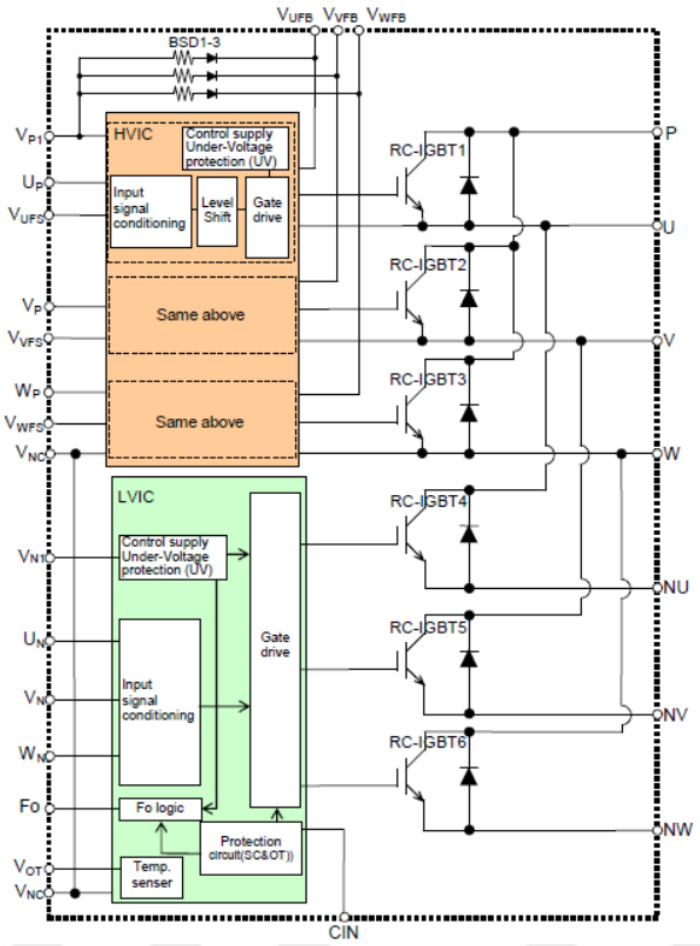

Figure 6.17: Internal block diagram of IPM [87].

The internal block diagram of IPM is shown in Figure Figure 6.17. This module includes six IGBTs that are used for three-phase inverter stage to drive the motor. It is suitable for up to 1.5kW motor power which is common on consumer appliances such as air-conditioners, washing machines, refrigerators and so on. The maximum collector-emitter voltage of the IGBTs is 600V. It is recommended to consider a safety margin for this maximum voltage. Each IGBT has a 15A maximum current value under the 25°C case temperature. This maximum value should be calculated for each special design considering ambient temperature, power factor, switching frequency and so on. There are built-in bootstrap diodes with current limiter resistors as series configuration for each phase. The typical forward voltage of this bootstrap diode is 1.7V and the typical built-in limiting resistance value is 100Ω. Arm-shoot-through blocking time is determined as 1us in the chip. The maximum junction temperature of the chip is 150°C. Junction to the case thermal resistance of each IGBT in the module is 4K/W at steady state condition. The maximum PWM input frequency is 20kHz; however, a 6kHz switching frequency will be used in this thesis.

Bootstrap capacitor value plays an important role for the driving stage. If the value is chosen too low, gate voltage on the high side can decrease especially when the high duty cycle is applied to the high side. This causes additional heating on high side IGBTs and permanent damage may occur if there is an insufficient cooling condition. If the capacitor value is too high, the charging time is too long and this causes the capacitor to not be charged enough. 10uF 25V is chosen as a generic value for the bootstrap capacitor. This capacitor value can decrease by 80% of the nominal value under DC bias voltage. With 100nF is placed parallel with the bootstrap capacitor in order to eliminate high-frequency noise on the gate voltage.

Before starting to calculate power loss on the IPM, some assumptions should be made in order to make the calculation easier. These assumptions are,

- Output currents of the IPM are sinusoidal that do not include ripple.
- PWM signals are generated by the comparison of sine waveform and triangular waveform.
- PWM signals are sinusoidal and vary between 0% and 100% duty ratio.
- Load is an ideal inductive load.

Conduction losses on IPM are caused by two components that are IGBT and internal diode. The conduction power loss of one IGBT (without diode) can be calculated, by using the equation (6.8).

$$P_{loss\_cond\_IGBT} = V_{CE0} * I_{phase\_peak} * \left(\frac{1}{2\pi} + \frac{m_{index} * cos\,\varphi}{8}\right) + r_{IGBT} * I_{phase\_peak}^2 * \left(\frac{1}{8} + \frac{m_{index} * cos\,\varphi}{3\pi}\right) \quad (6.8)$$

$P_{loss\_cond\_IGBT}$	: conduction power loss on IGBT [W]
V_{CE0}	: V_{CE} that is found by tangenting to operation point [V]
I_{phase_peak}	: peak of the motor phase current [A]
m_{index}	: modulation index
$cos\,\varphi$	: power factor of the motor
r_{IGBT}	: dynamic IGBT resistance [Ohm]

In order to determine the V_{CE0} a tangent is drawn to the curve (the blue one) at the operation point as Figure 6.18. The operation point will be taken as 1.36A that is

expected to be the peak of the motor phase current. So, 0.625V is determined as the V_{CE0}. On the other hand, the cotangent value of the angle x gives dynamic resistance of the IGBT that is called as r_{IGBT}. This value can be found as 0.14Ω. The modulation index will be determined as 0.972 on the software. Power factor will be taken as a 1 for worst-case conditions. The conduction power loss of one IGBT (without diode) is equal to 0.3 W with these values.

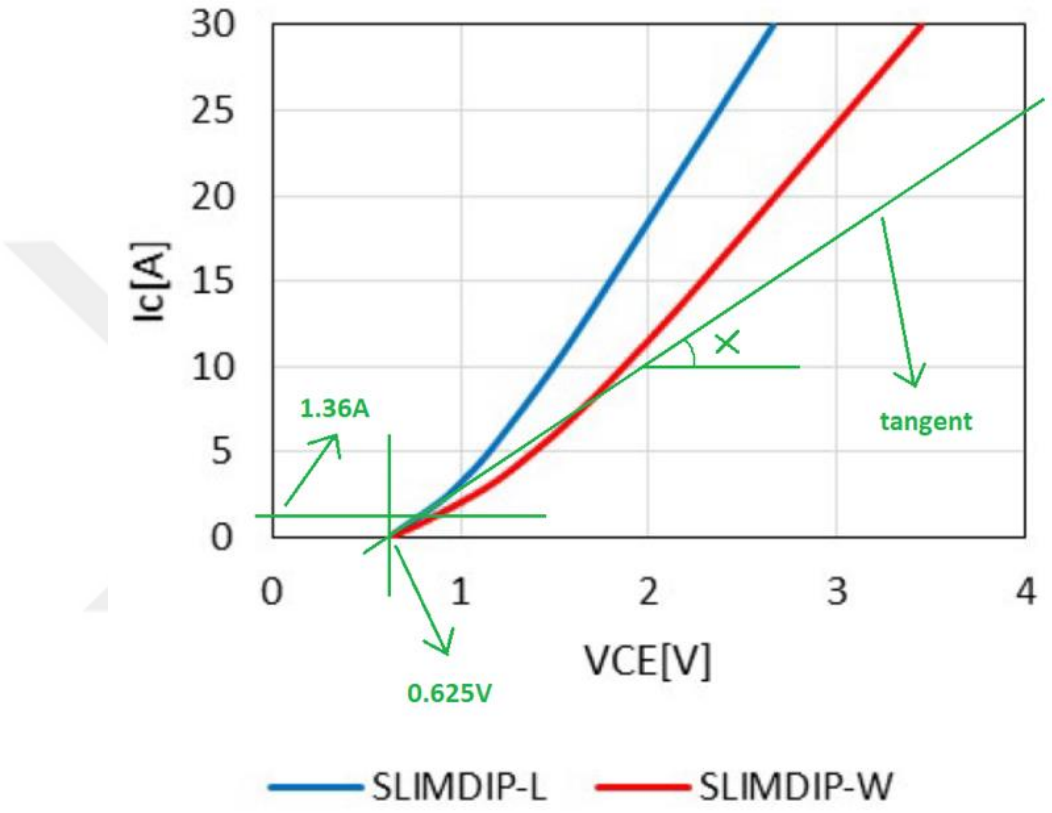

Figure 6.18: Collector-emitter voltage and collector current graph of the IPM [87].

In order to find the conduction loss on diode (in IGBT package), equation (6.9) can be used.

$$P_{loss\_cond\_diode} = V_{d0} * I_{phase\_peak} * \left(\frac{1}{2\pi} - \frac{m_{index} * cos\,\varphi}{8}\right) + r_d * I_{phase\_peak}^2 * \left(\frac{1}{8} - \frac{m_{index} * cos\,\varphi}{3\pi}\right) \quad (6.9)$$

$P_{loss\_cond\_diode}$: conduction power loss on the diode [W]

V_{d0} : V_d that is found by tangenting to operation point [V]

I_{phase_peak} : peak of the motor phase current [A]

m_{index} : modulation index

$cos\,\varphi$: power factor of the motor

r_d : dynamic diode resistance [Ohm]

Forward voltage-current graph of the diode is not given in the datasheet. Due to that, the value of the diode parameters will be taken as the same as IGBT parameters. As a result, the conduction loss on diode (in IGBT package) is calculated as 0.04 W.
Sum of the conduction loss on IGBT and the diode which are results in as 0.34 W for one switch 2.04 W for the six switches by using the equation (6.10).

$$P_{loss\_cond\_pack} = P_{loss\_cond\_IGBT} + P_{loss\_cond\_diode} \quad (6.10)$$

$P_{loss\_cond\_pack}$: conduction power loss on the package [W]

$P_{loss\_cond\_IGBT}$: conduction power loss on IGBT [W]

$P_{loss\_cond\_diode}$: conduction power loss on the diode [W]

After calculating all conduction losses on IPM, switching losses are needed to calculate in order to find total IPM losses. Switching losses consists of turn-on IGBT loss, turn-off IGBT loss and turn-off diode loss. Turn-on diode loss is so small and it does not worth calculating.
In order to find the switching losses on IGBT; firstly, the average current of IGBT over half period is calculated as 0.866 A with equation (6.11).

$$I_{IGBT\_ave\_half} = \frac{2 * I_{phase\_peak}}{\pi} \quad (6.11)$$

$I_{IGBT\_ave\_half}$: average current of IGBT over half period [A]

I_{phase_peak} : peak of the motor phase current [A]

After calculating this value, switching losses can be found by using triangle approach. The switching times that are given in Figure 6.19 are used for calculations. Values are given for 15A current; however, they can be taken as worst-case values.

Symbol	Parameter	Condition		Limits			Unit
				Min.	Typ.	Max.	
$V_{CE(sat)}$	Collector-emitter saturation voltage	V_D=V_{DB} = 15V, V_{IN}= 5V	I_C= 15A , T_j= 25°C	-	1.60	1.95	V
			I_C= 15A , T_j= 125°C	-	1.80	2.15	
V_{EC}	FWDi forward voltage	V_{IN}= 0V, -I_C= 15A		-	1.40	1.90	V
t_{on}	Switching times	V_{CC}= 300V, V_D= V_{DB}= 15V I_C= 15A, T_j= 125°C, V_{IN}= 0↔5V Inductive Load (upper-lower arm)		0.65	1.05	1.45	µs
$t_{C(on)}$				-	0.40	0.65	µs
t_{off}				-	1.15	1.60	µs
$t_{C(off)}$				-	0.15	0.30	µs
t_{rr}				-	0.30	-	µs
I_{CES}	Collector-emitter cut-off current	V_{CE}=V_{CES}	T_j= 25°C	-	-	1	mA
			T_j= 125°C	-	-	10	

Figure 6.19: Switching time of the IPM [87].

Switching times are defined in Figure 6.20.

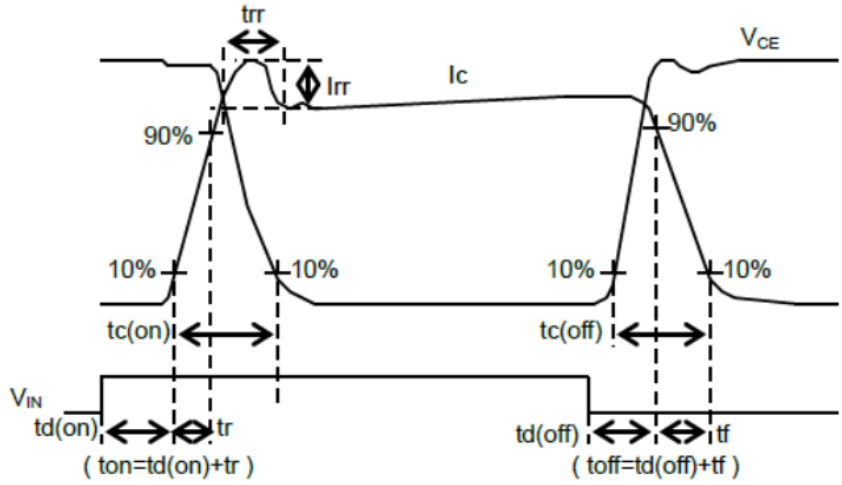

Figure 6.20: Switching time definition [87].

Turn-on IGBT loss is found by using equation (6.12).

$$P_{loss\_on\_IGBT} = \frac{1}{2} * V_{DC} * I_{IGBT\_ave\_half} * t_{c(on)} * \frac{f_{switching}}{2} \qquad (6.12)$$

$P_{loss\_on\_IGBT}$: turn-on IGBT loss [W]

V_{DC} : DC bus voltage [V]

$I_{IGBT\_ave\_half}$: average current of IGBT over half period [A]

$t_{c(on)}$: turn-on time [s]

$f_{switching}$: switching frequency [Hz]

In the 180° commutation type, an IGBT is only in conduction over half period. Therefore, switching loss on an IGBT only occurs over half period. Due to that, the switching frequency in equation (6.12) is divided by two.

$$P_{loss\_off\_IGBT} = \frac{1}{2} * V_{DC} * I_{IGBT\_ave\_half} * t_{c(off)} * \frac{f_{switching}}{2} \qquad (6.13)$$

$P_{loss\_off\_IGBT}$: turn-off IGBT loss [W]

V_{DC} : DC bus voltage [V]

$I_{IGBT\_ave\_half}$: average current of IGBT over half period [A]

$t_{c(off)}$: turn-off time [s]

If values are inserted in the equation (6.12) and (6.13) for the turn on and turn off IGBT losses, they are calculated as 0.274 W and 0.127 W respectively.

In order to find the turn-off diode loss which is caused by the reverse recovery characteristic of the diode, the average peak current of the reverse recovery over a half period should be estimated. Figure 6.21 can be used for this estimation. As seen in Figure 6.21, there is a reverse recovery current about two-thirds of the main IGBT current.

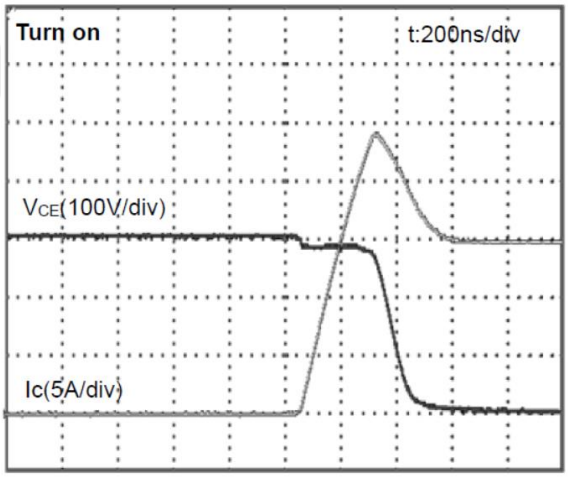

Figure 6.21: Typical turn-on switching waveform [87].

The average peak current of the reverse recovery over half period is calculated as 0.58 A using equation (6.14),

$$I_{rev\_ave\_half} = \frac{2}{3} * I_{IGBT\_ave\_half} \qquad (6.14)$$

$I_{rev\_ave\_half}$: average peak current of the reverse recovery over half period [A]

$I_{IGBT\_ave\_half}$: average current of IGBT over half period [A]

The turn-off diode loss can be calculated using equation (6.15) and it is found as 0.021 W.

$$P_{loss\_off\_diode} = \frac{I_{rev\_ave\_half} * t_{rr} * V_{DC}}{8} * \frac{f_{switching}}{2} \quad (6.15)$$

$P_{loss\_off\_diode}$: turn-off diode loss [W]
$I_{rev\_ave\_half}$: average peak current of the reverse recovery over half period [A]
t_{rr} : reverse recovery time [s]
V_{DC} : DC bus voltage [V]
$f_{switching}$: switching frequency [Hz]

The turn-off diode loss also occurs over half of the period due to 180° commutation. If all values are put in equation (6.15),
If all the switching losses should be added as given in equation (6.16) and equal to 0.422 W for one IGBT, 2.532 W for six IGBTs,

$$P_{loss\_sw\_pack} = P_{loss\_on\_IGBT} + P_{loss\_off\_IGBT} + P_{loss\_off\_diode} \quad (6.16)$$

$P_{loss\_sw\_pack}$: switching loss in package [W]
$P_{loss\_on\_IGBT}$: turn-on IGBT loss [W]
$P_{loss\_off\_IGBT}$: turn-off IGBT loss [W]
$P_{loss\_off\_diode}$: turn-off diode loss [W]

The total power loss that is consisted of conduction loss and switching loss is calculated for the inverter as 4.572 W by using the equation (6.17),

$$P_{loss\_tot\_inv} = P_{loss\_cond\_inv} + P_{loss\_sw\_inv} \quad (6.17)$$

$P_{loss\_tot\_inv}$: total power loss on the inverter [W]
$P_{loss\_cond\_inv}$: conduction power loss on the inverter [W]
$P_{loss\_sw\_inv}$: switching power loss on the inverter [W]

In order to find the temperature value of the bridge diode and the IPM which are connected to the heatsink, the thermal model of these two circuits are generated as seen in Figure 6.22.

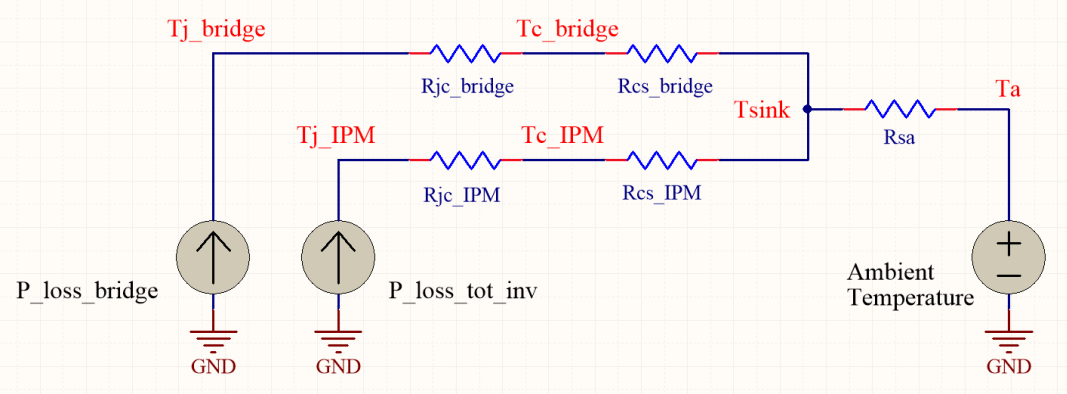

Figure 6.22: Thermal model of the bridge and the IPM circuits.

P_{loss_bridge} : power loss of the bridge diode [W]

$P_{loss\_tot\_inv}$: total power loss on the inverter [W]

T_{j_bridge} : junction temperature of the bridge diode [°C]

T_{j_IPM} : junction temperature of the IPM [°C]

T_{c_bridge} : case temperature of the bridge diode [°C]

T_{c_IPM} : case temperature of the IPM [°C]

T_{sink} : heatsink temperature [°C]

T_a : ambient temperature [°C]

R_{jc_bridge} : junction to case thermal resistance of the bridge diode [°C/W]

R_{jc_IPM} : junction to case thermal resistance of the IPM [°C/W]

R_{cs_bridge} : case to the heatsink thermal resistance of the bridge diode [°C/W]

R_{cs_IPM} : case to the heatsink thermal resistance of the IPM [°C/W]

R_{sa} : sink to the ambient thermal resistance of the heatsink [°C/W]

In order to find the junction temperature of the bridge diode, equation (6.18) can be used according to Figure 6.22.

$$T_{j\_bridge} = P_{loss\_bridge} * \left(R_{jc\_bridge} + R_{cs\_bridge}\right) + \left(P_{loss\_bridge} + P_{loss\_tot\_inv}\right) * R_{sa} + T_a \quad (6.18)$$

$T_a$will be taken as a maximum ambient temperature which is 55°C. Case to sink thermal resistances of the bridge diode and the IPM will be taken as 1°C/W for worst-case condition. Junction to case thermal resistances of them will be taken from its datasheets. The junction temperature is calculated as 77.8°C. This value is less than the maximum junction temperature of the bridge diode which is 150°C. The junction temperature of the IPM is calculated AS 74.6 °C using the equation (6.19).

$$T_{j\_IPM} = P_{loss\_tot\_inv} * \left(R_{jc\_IPM} + R_{cs\_IPM}\right) + \left(P_{loss\_tot\_inv} + P_{loss\_bridge}\right) * R_{sa} + T_a \quad (6.19)$$

The recommended maximum junction temperature of the IPM is 125°C. Therefore, 74.6°C is lower than this value [88].

6.1.7 Microcontroller design

The microcontroller circuit for the motor control is shown in Figure 6.23.

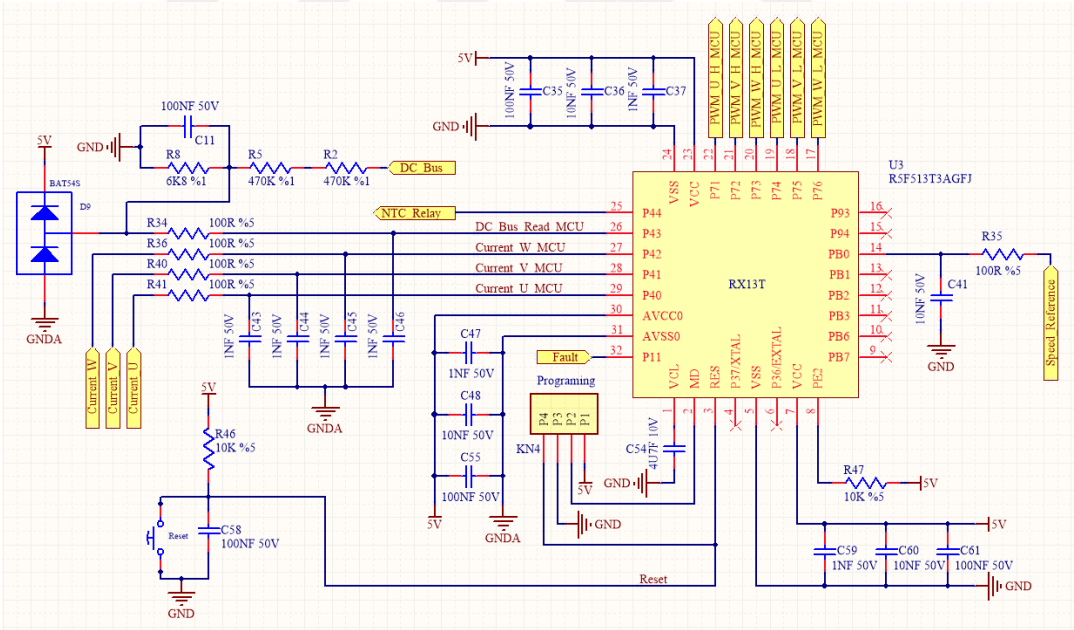

Figure 6.23: Microcontroller circuit.

Renesas RX13T group 32-Bit microcontroller is used. Its maximum clock frequency is 32MHz. There is a CISC Harvard architecture with 5-stage pipeline. On-chip code flash memory capacity is 128 Kbytes and on-chip data flash memory capacity is 4 Kbytes. In addition to that, this microcontroller includes 12 Kbytes of SRAM. All memories have no wait states to execute. It also has an independent watchdog timer

clocked by an on-chip oscillator for reset. There are seven types of reset sources such as power-on reset and low voltage detection reset. and I^2C, SPI, USART and UART can be used as communication protocols. It has 8 channel 12-Bit analog to digital converter (ADC). 3 channel has an amplifier as internal for shunt reading. However, in this thesis, an external op-amp circuit is preferred to amplify shunt voltage. 16-Bit timer is used to generate PWM signals. Three of these six signals are complementary signals. Dead time should be inserted between complementary signals in order to avoid cross conduction. Sleep mode can be used to decrease IDLE power of the driver circuit. A microcontroller has two digital power inputs and one analog power input. The voltage level of these inputs is 5V. This voltage comes from a linear regulator. 100nF, 10nF and 1nF capacitors are placed at each three power inputs to bypass noise to the ground. These capacitors should be as close as possible to pins in order not to lose their effects. It is recommended to connect VCL pin to the VSS pin via 4.7uF smoothing capacitor used to stabilize the internal power supply. This capacitor should be also as close as to the pin. KN4 is a programming connector. The reset pin is pulled up to 5V and a button is placed for external reset by users. Current_U, Current_V and Current_W are amplified and offset added signals. These signals pass through RC filter and reach ADC pins. The time constant should not be so large to disrupt the signals. PWM signals are generated considering these current signals so, these signals must be read correctly. Analog and digital ground are also separated to enhance current reading accuracy. Grounds are connected from one point via ferrite bead. There is a fault pin that comes from IPM. In case of fault condition which will explain below in detail, IPM disables the PWM signals as hardware protection. After then, fault signal becomes low logic and the microcontroller interprets that as a fault. All PWM signals are also disabled as software protection. NTC relay signal is generated after the transient current condition is disappeared in the first energized. DC bus voltage is sensed regularly by the microcontroller. If voltage dividers are considered, there is 2.34V on DC bus voltage sense pin when 230VAC voltage is applied to the input. When the maximum input voltage which is 265VAC is applied, the voltage on that pin becomes 2.69V. In case of voltage transient on DC bus, diode pair D9 is placed on DC bus sense pin. Because this voltage transient reflects to sense pin and microcontroller may be damaged. Diode pair clamps both negative and positive transient voltage on the pin to a certain value. The signals pass through the RC filter before it reaches the pin.

6.1.8 Protection and indicator circuits design

The fault circuit is shown in Figure 6.24.

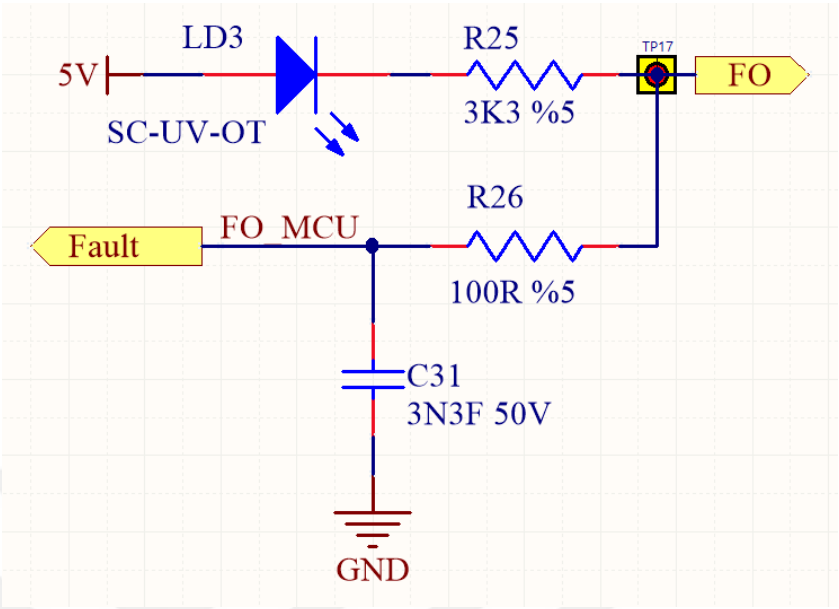

Figure 6.24: Fault circuit.

FO label is directly connected to the related pin of IPM. This pin has an open collector structure so it should be pulled up to 5V with the resistor. LED is also connected series to the resistor for the indication. The maximum source current of this pin is 1mA and R23 resistor is chosen considering this value. When there is no fault condition, the voltage on FO pin is 5V. Whenever a fault occurs, the voltage on that pin decreases to 0V. This voltage is continuously sensed from the Fault label via the microcontroller. All gate signals are disabled immediately when the fault is perceived by the microcontroller. R26 and C31 are filter for fault signal. They are selected to detect fault within 2us. Three abnormal conditions affect the output of the fault pin. These are short circuit which means an over-current condition, an under-voltage condition in supply voltage and over-temperature condition. These failures which can pull down fault voltage to 0V are only valid for low side IGBTs. However, if there is under-voltage on the high side supply, all gate signals are disabled. On the other hand, the fault state does not change which means the voltage on that pin remains at a high state. Trip level of the under-voltage varies between 10.3V and 12.5V. Gate driving with low voltage can be dangerous for IGBTs. High temperature can occur and if temperature rise becomes excessive, this may damage the module.

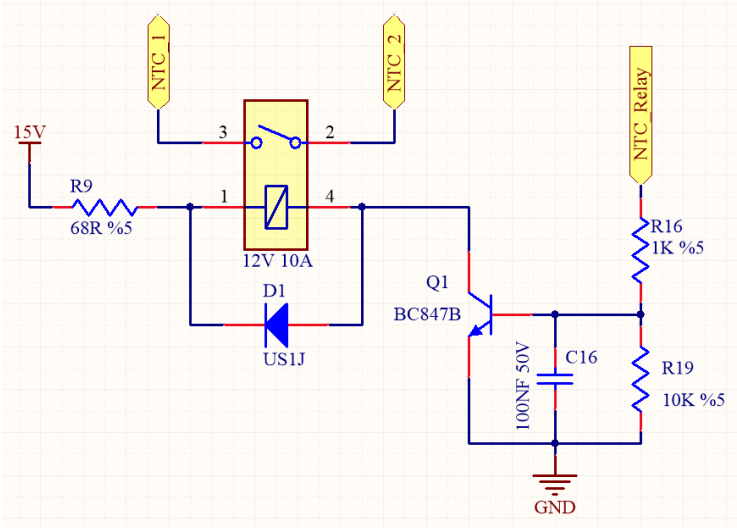

Figure 6.25: Relay circuit.

In Figure 6.25, the relay circuit for bypassing for the NTC is shown. As mentioned before, inrush current occurs due to charging of the capacitor when the circuit is first energized. In order to overcome this situation, NTC is used to limit input current. However, NTC causes additional power losses and the efficiency of the circuit decreases. The relay bypasses the NTC after the current transient disappears. Duration of the current transient can last a few hundred milliseconds.

The relay has a 12V working voltage and there are only 5V and 15V sources in the circuit so R9 should be connected to the bobbin of the relay to keep current at rated value. When the transistor is closed, the bobbin of the relay gets reverse polarity and voltage stress on the collector of the transistor may exceed the breakdown voltage. D1 should be also connected between terminals of the bobbin to clamp this inductive kick to 15V.

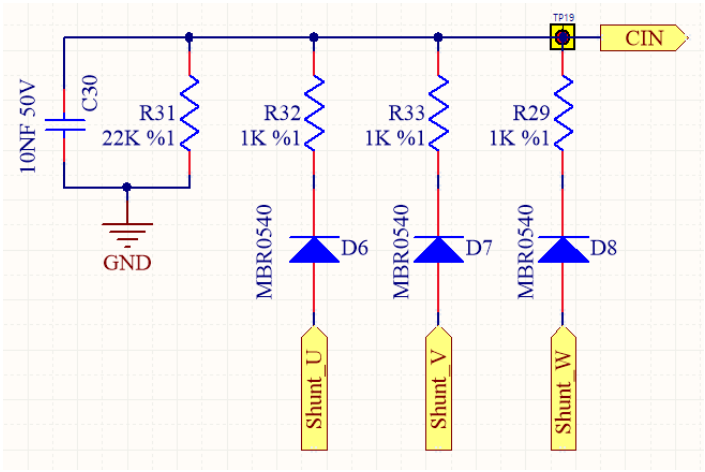

Figure 6.26: Over-current protection circuit.

The driver has hardware over-current protection as shown in Figure 6.26. CIN is an over-current input for IPM. When the voltage on that pin exceeds the threshold voltage which is 0.48V, a trip signal is generated. According to the datasheet, the threshold voltage can change between 0.455 and 0.505V. When the trip occurs, all N-side IGBTs gates are hard interrupted and the FAULT output of IPM is pulled down to 0V. It is recommended to set the RC time constant of filter 1.5-2us so that IGBT shut down within 2us when short circuit condition. If this time is exceeded in over-current condition, permanent and irreversible damage can occur in IPM. Phase currents are sensed through Shunt_U, Shunt_V and Shunt_W. These inputs come from the terminal of shunt resistors. MBR0540 is a schottky diode and it has approximately 0.3V forward voltage at a very low current. If considered voltage divider on the above circuit and the minimum-maximum threshold voltage of trip level on CIN pin, the minimum voltage is 0.776V and maximum voltage is 0.828V on shunt side for generating trip signal. The value of the shunt resistors is 0.15Ω so this corresponds to an over-current value that varies between 5.17A and 5.52A. C30 is placed to avoid false over-current alarm due to the circuit noise.

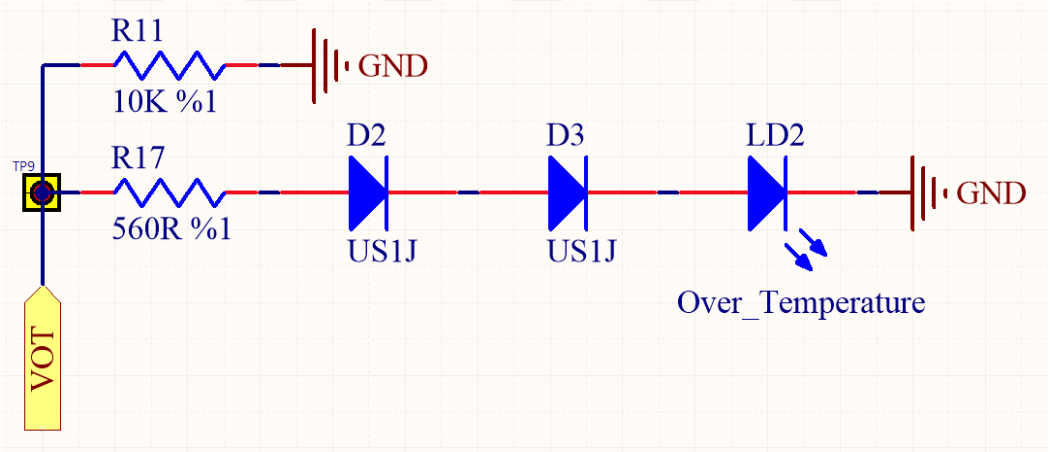

Figure 6.27: Over-temperature indicator.

The over-voltage indicator is shown in Figure 6.27. Input VOT comes from the pin of the IPM. This is the analog signal. The temperature signal in IPM is amplified by the internal op-amp. In Figure 6.28, VOT voltage versus LVIC temperature is shown.

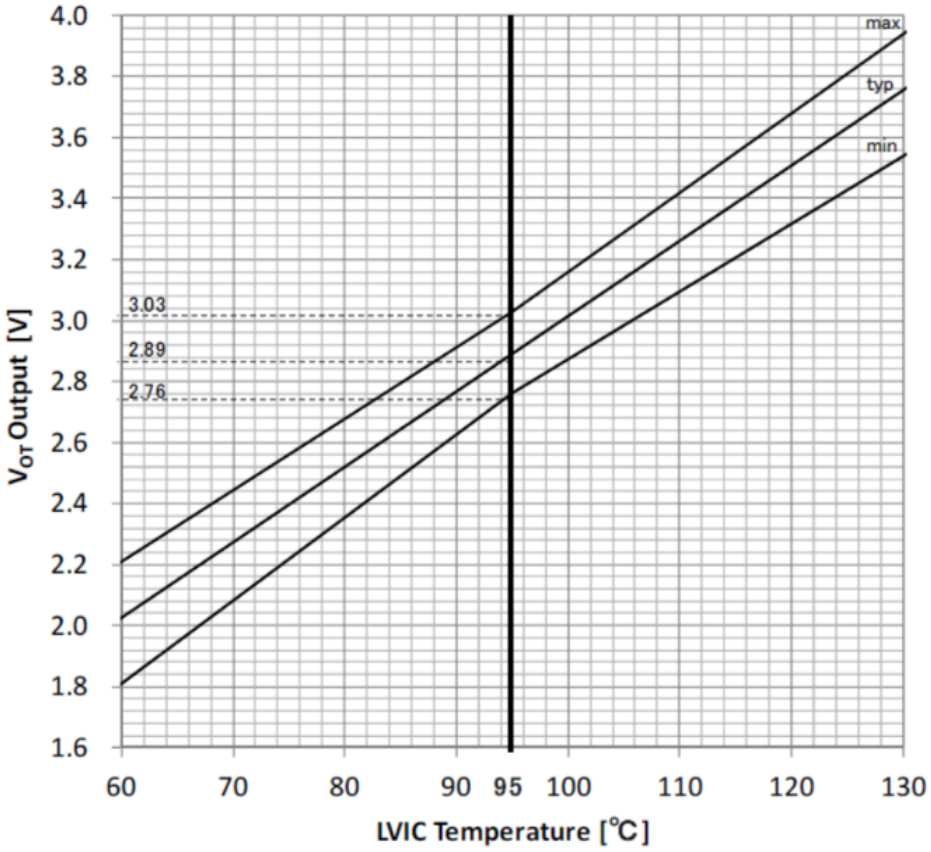

Figure 6.28: VOT voltage versus LVIC voltage [87].

As seen in Figure 6.28, there is a linear characteristic between these two parameters. If considered forward voltage of US1J which is 0.7V and forward voltage of LD2 (red colour) which is 1.7V, LED starts to light approximately 95 °C. The tolerance of the components may change the threshold value. As temperature increases in LVIC, the brightness of LED also increases. R11 is used to enhance linear characteristic between two parameters. The maximum source current of this pin is 1.7mA and care should be taken not to exceed this current. IPM has its own over-temperature protection. The nominal trip level is 130 °C and this level can change between 115 °C and 145 °C. There is a 10 °C hysteresis temperature. In case of exceeding this threshold, all N-side IGBTs turn-off despite control input condition and the FAULT output of IPM is pulled down to 0V.

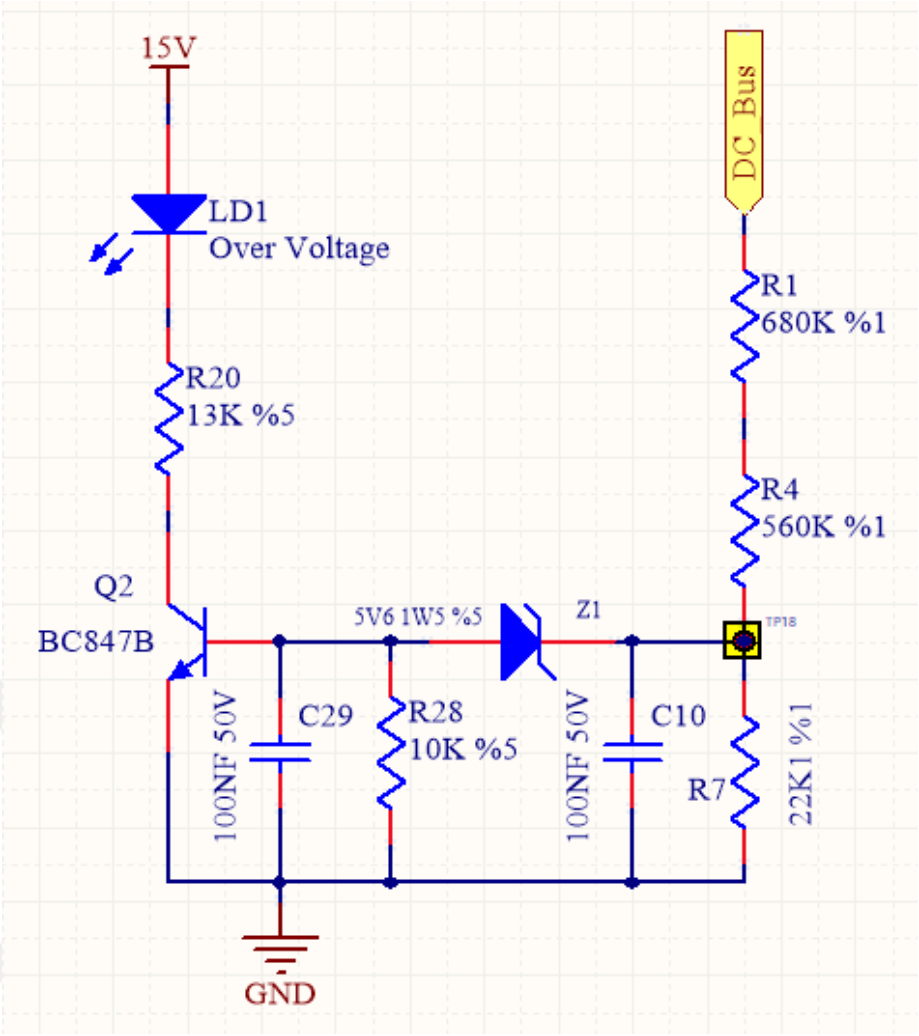

Figure 6.29: Over-voltage indicator.

In Figure 6.29, the over-voltage indicator is given. In case of pre-determined over-voltage is occurred, the indicator LED is open to alert. In order to open the transistor, voltage on TP18 must be the sum of zener voltage and V_{BE}. Considering V_{BE} as 0.7V and zener voltage as 5.6V, the voltage on TP18 must be approximately 6.3V. If voltage divider resistors that are R1, R4 and R7 are taken into account, DC Bus threshold voltage for over-voltage is calculated as 360V. This value can be adjusted by changing the value of voltage divider resistors. This threshold value is just an indicator. Main over-voltage protection is provided by the software to decide the driving situation. C29 and C10 are used to eliminate high-frequency noise to avoid false over-voltage alarm. It is set to pass 1mA through each LED in the circuit.

6.1.9 Reference speed circuit design

The reference circuit used for rotor speed calculation is shown in Figure 6.30.

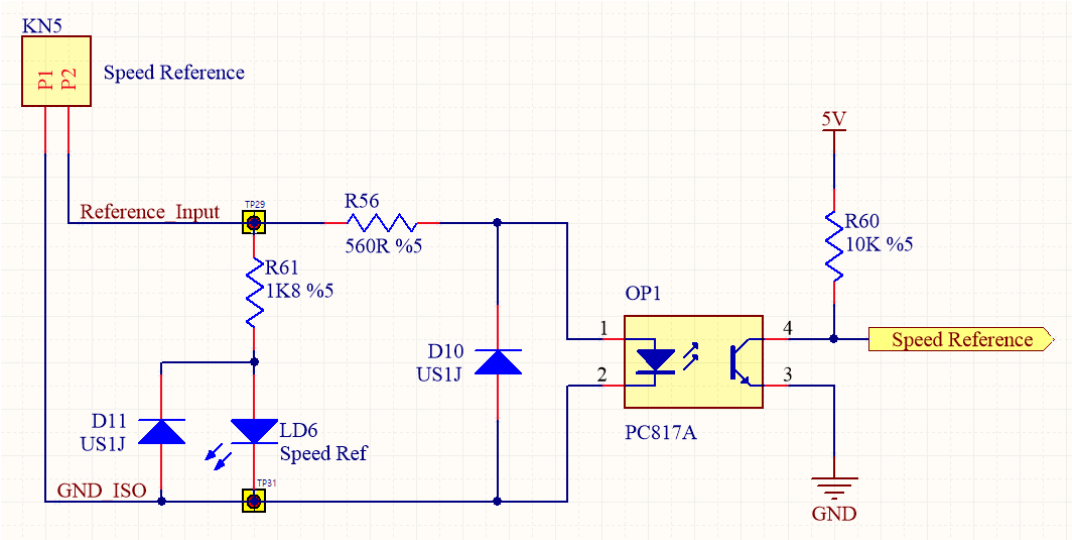

Figure 6.30: Speed reference circuit.

PC817A photocoupler is used for reinforced isolation between driver and signal generator. There is 5kV isolation guaranteed by PC817A. A signal generator sends a square wave with 50% duty cycle. The frequency of this signal varies between 50Hz and 150Hz depending on desired speed value. Rotor speed which is from 1000 rpm to 3000 rpm is linearly adjusted by changing the frequency of the signal generator. The most important parameter of a photocoupler is the current transfer ratio. The forward current of the photocoupler should be large enough to saturate the transistor of the photocoupler.

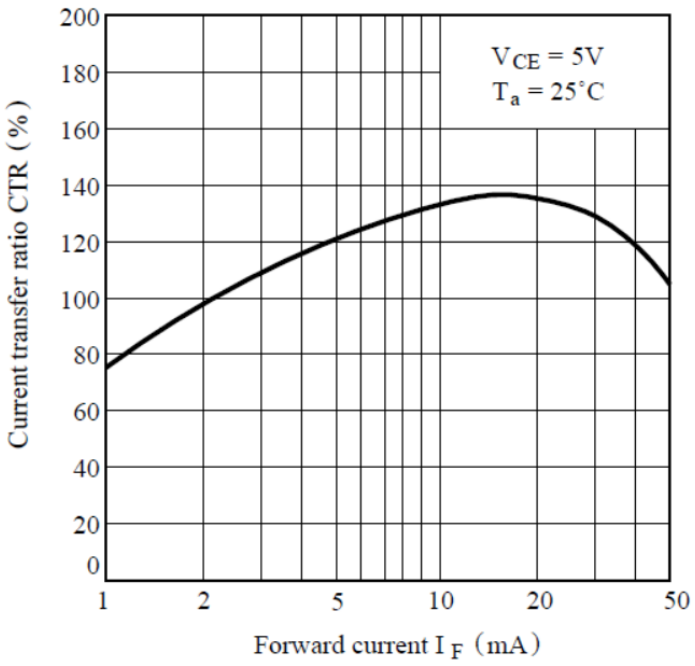

Figure 6.31: Forward current versus current transfer ratio of the photocoupler [89].

As seen in Figure 6.31, the current transfer ratio approximately varies between 75% and 135%. The magnitude of signal generator voltage is 5V and maximum forward voltage is 1.4V. If the value of R56 is also considered, the forward current is approximately 6.5mA. And even if the lowest value of the current transfer ratio which is 75% is taken, it is obvious that the transistor goes into saturation. In the case of the reverse connection of the signal generator, D10 protects the photocoupler from any damage. LD6 is an indicator of the speed reference and D11 is also protects the LD6.

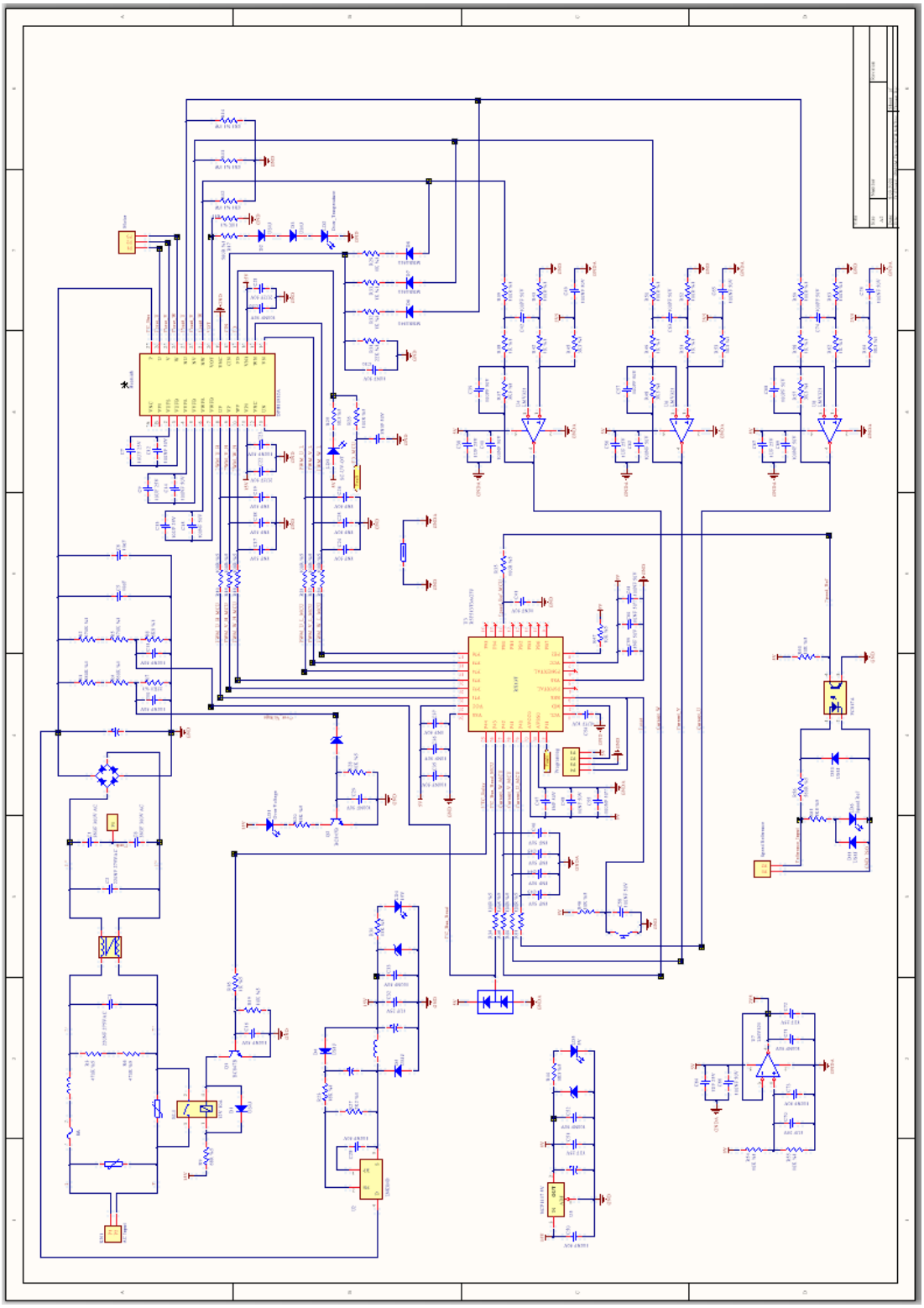

Figure 6.32: Overall schematic of the driver circuit.

6.2 PCB Design

Main PCB information is given in Table 6.7.

Table 6.7: PCB information.

PCB size	155mm x 150mm
PCB material	FR4
PCB thickness	1.6mm
Number of layers	2
Copper thickness	35um
Number of SMD components	161
Number of THD components	25
Number of total components	186
Number of tracks	1746
Minimum track thickness	0.4mm
Number of via	315
Minimum via size	0.35 hole size, 0.7 diameter
HASL colour	green

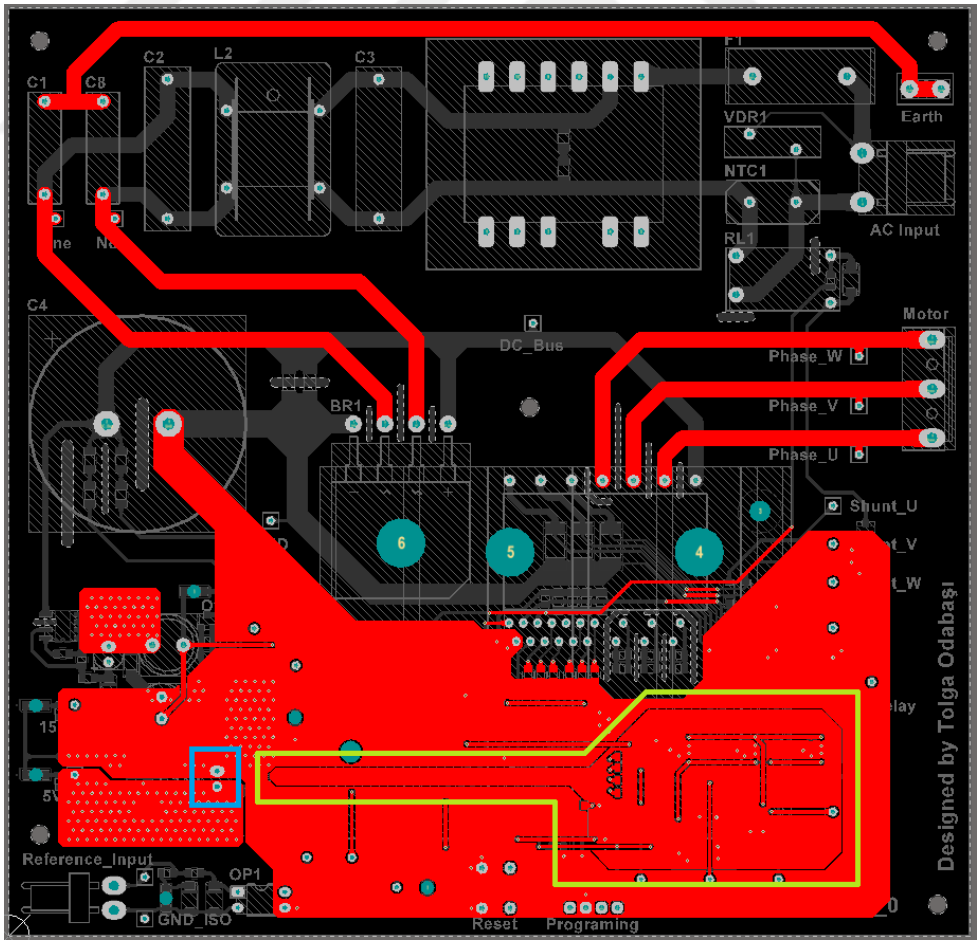

Figure 6.33: Top layer of the PCB in Altium Designer.

In Figure 6.33, the top layer of the PCB is shown. Analog ground is indicated by enclosing with the green line. There is a digital ground at outside of that. Analog ground is separated from the digital ground and they are connected to each other via ferrite bead on the ground pin of the 5V side electrolytic capacitor shown by the blue rectangle. In this way, the mixing of the noises of these two grounds is prevented. A ground plane is directly connected to DC bus electrolytic capacitor.

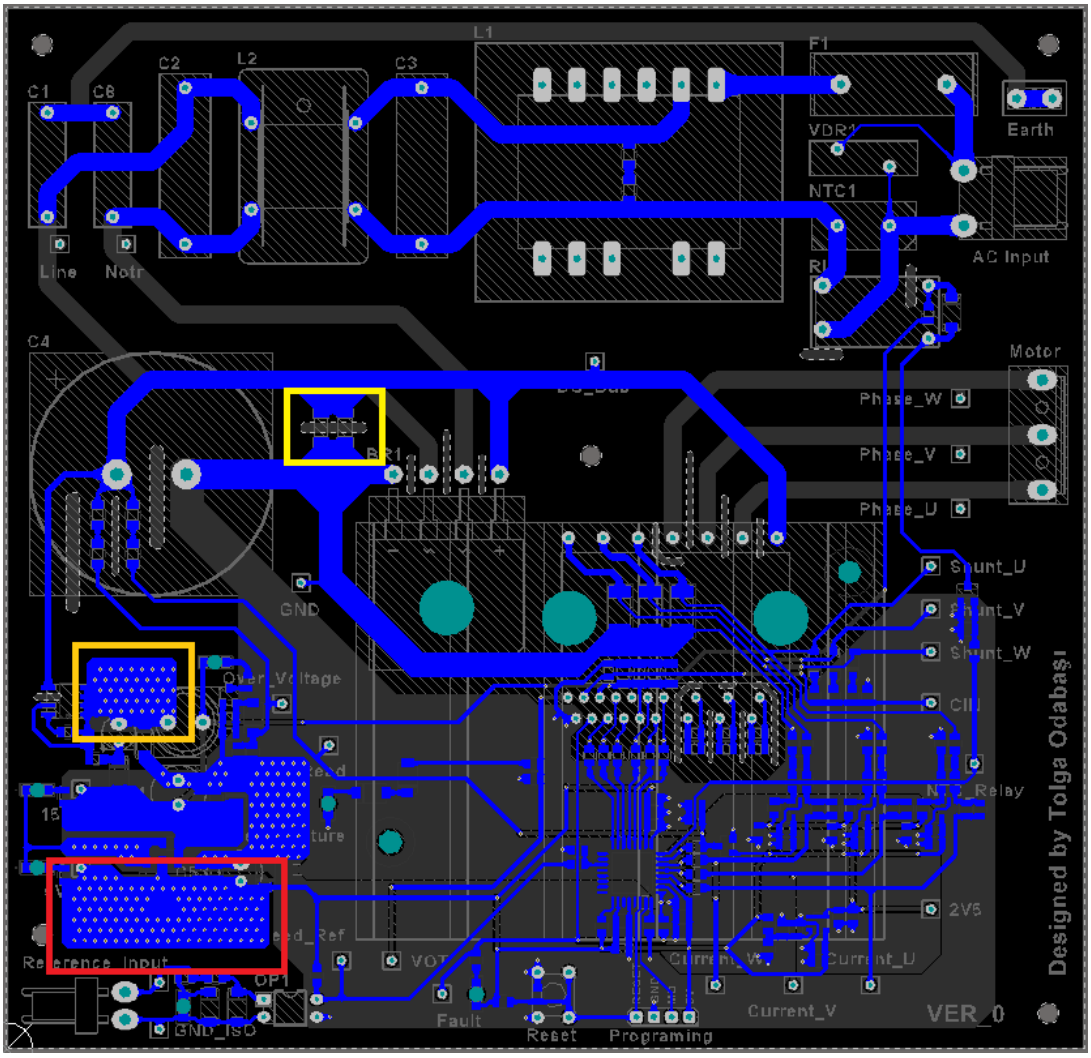

Figure 6.34: Bottom layer of the PCB in Altium Designer.

A bottom layer of the PCB is shown in Figure 6.34. This layer is used as a signal and power signal layer. Ground signals of the components are directly connected to the top layer using via. The main power ground is first connected to SMD high voltage ceramic capacitors shown by the yellow rectangle. This prevents a DC bus from a high voltage spike. After that, this ground is connected to the DC bus electrolytic capacitor. An orange rectangle shows the drain polygon plane of the LNK304D. And this polygon is connected to the top layer with a lot of via. In this way, thermal properties

are improved. LDO thermal pad is shown with re rectangle. With the same method, thermal properties are improved by using a large copper area and connecting to the top layer with a lot of via.

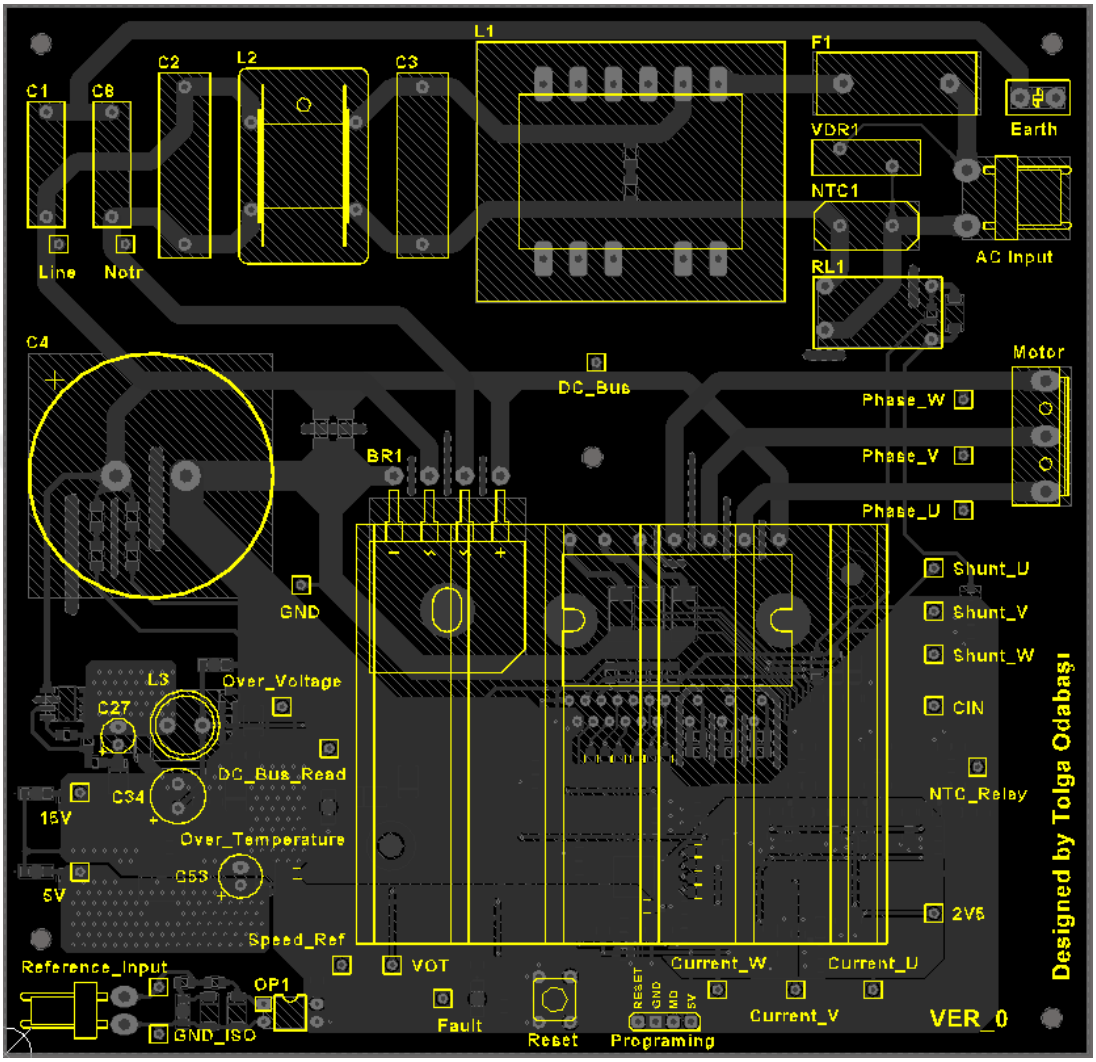

Figure 6.35: Top overlay of the PCB in Altium Designer.

Top side component places, names, indicator texts and test points are placed on top overlay as shown in Figure 6.35. This layer is used to improve the visuality of the circuit.

Top view of the PCB in Altium Designer is shown in Figure 6.36.

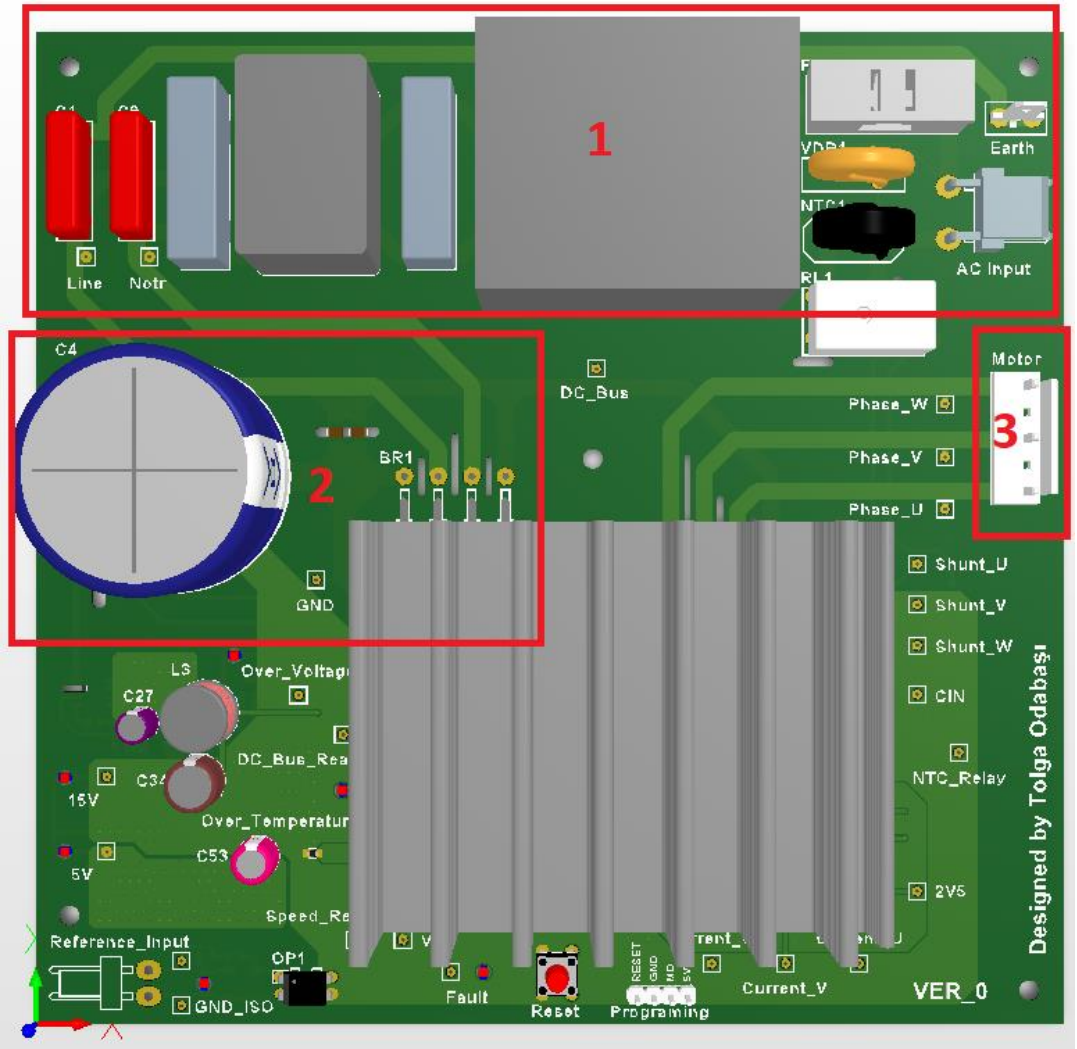

Figure 6.36: Top view of the PCB in Altium Designer.

The red rectangles placed in Figure 6.36 shows below sections.

1: Input stage and EMI filter

2: Rectification stage

3: Motor output connector

Bottom view of the PCB in Altium Designer is given in Figure 6.37.

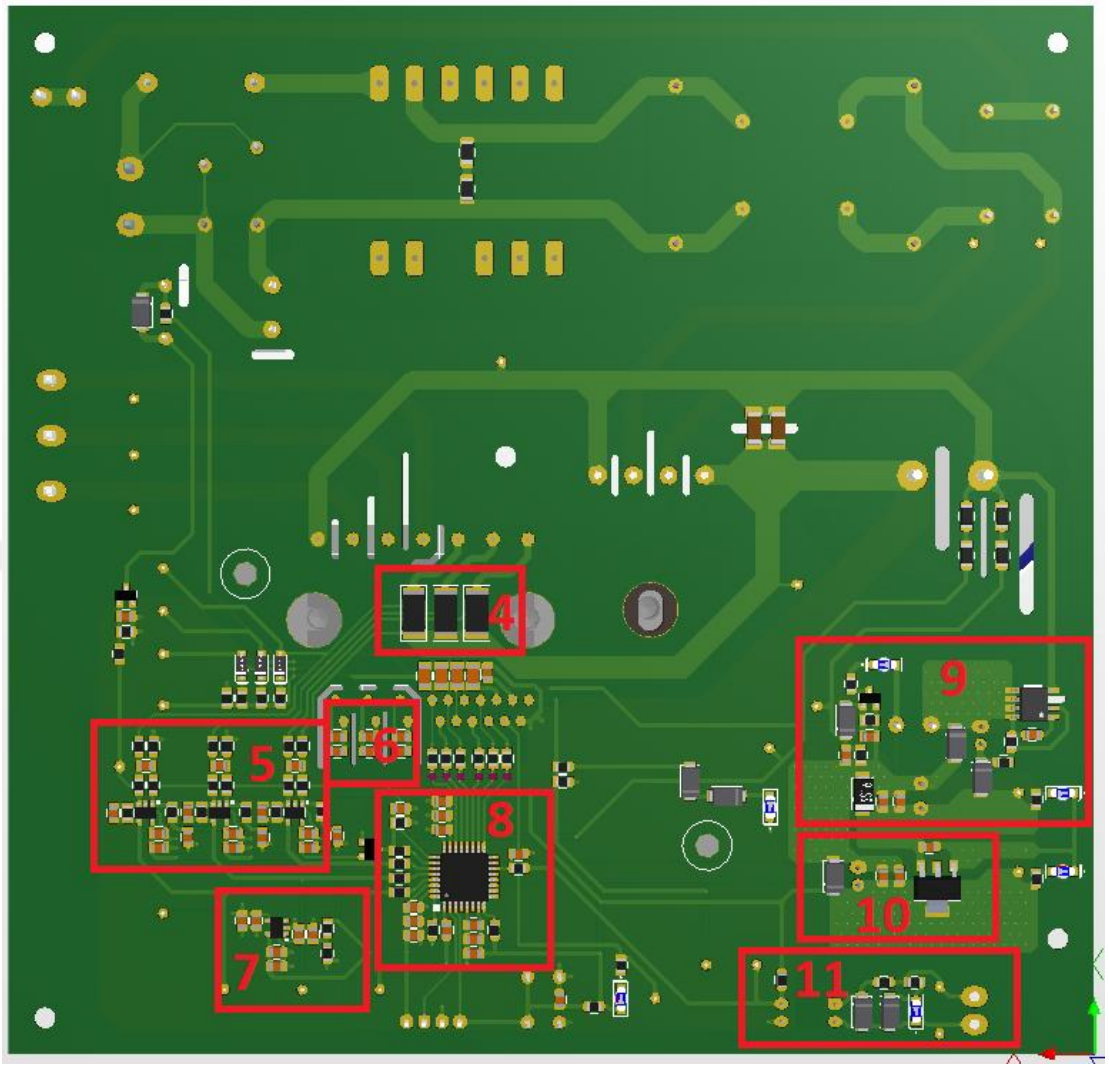

Figure 6.37: Bottom view of the PCB in Altium Designer.

The red rectangles placed in Figure 6.37 shows below sections.

4: Shunt resistors

5: Current sense op-amp circuits

6: Bootstrap capacitors

7: Reference voltage circuit

8: Microcontroller

9: 15V circuit

10: 5V circuit

11: Speed reference circuit.

Side view of the PCB in Altium Designer is shown in Figure 6.38.

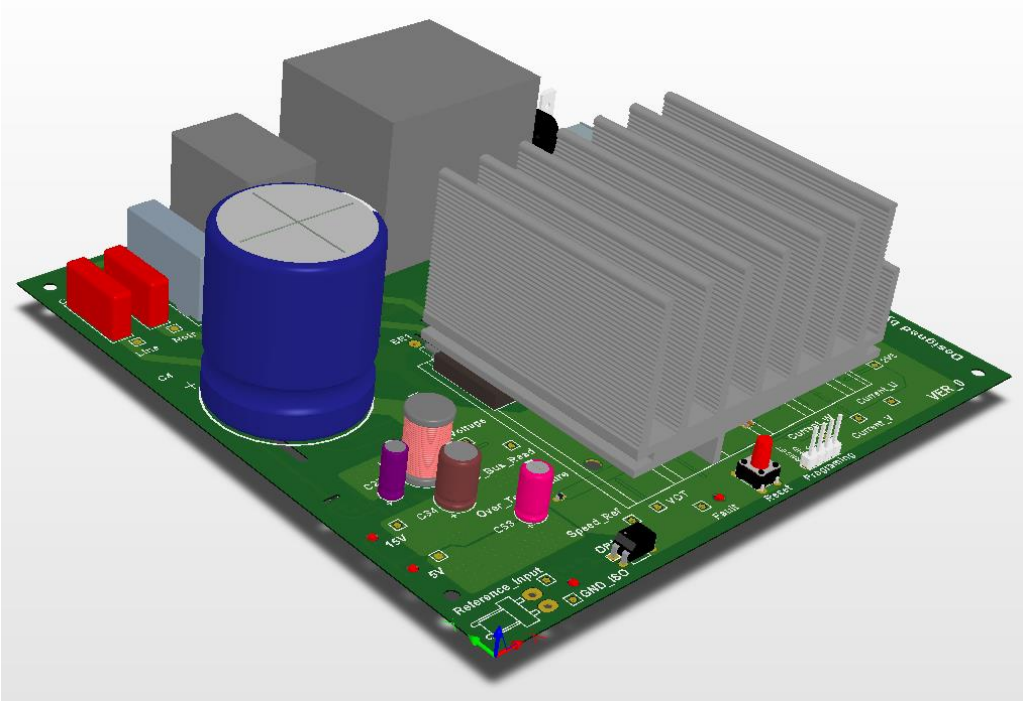

Figure 6.38: Side view of the PCB in Altium Designer.

Top side of the not assembled PCB is given in Figure 6.39.

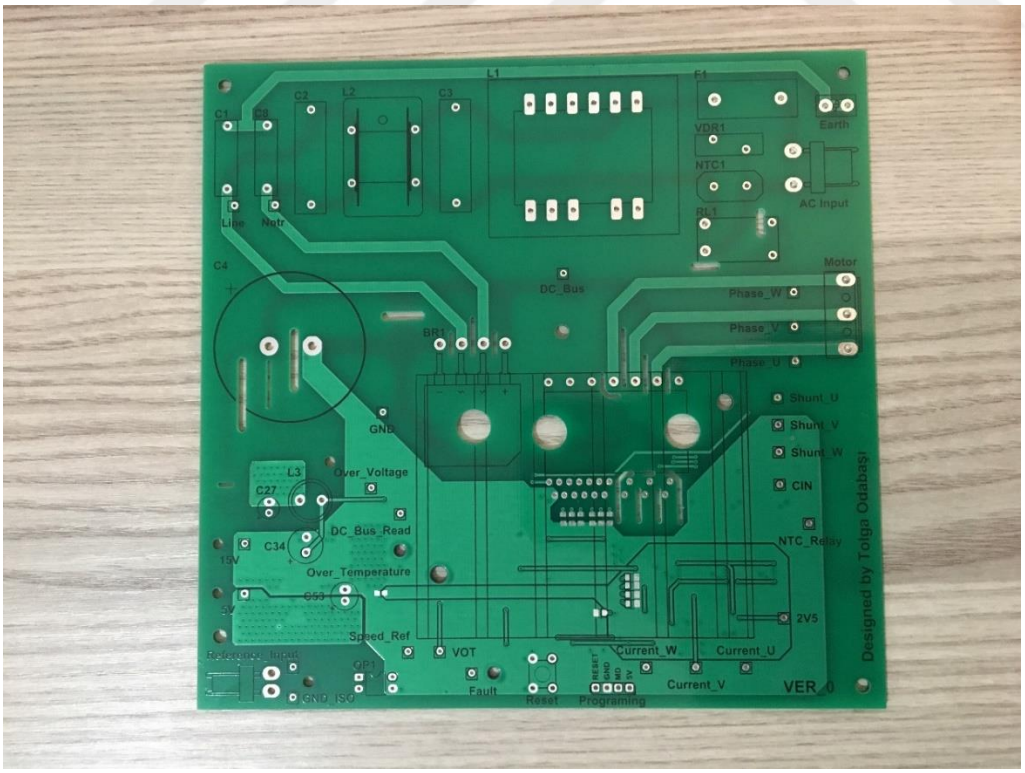

Figure 6.39: Top side of the not assembled PCB.

Bottom side of the not assembled PCB is seen in Figure 6.40.

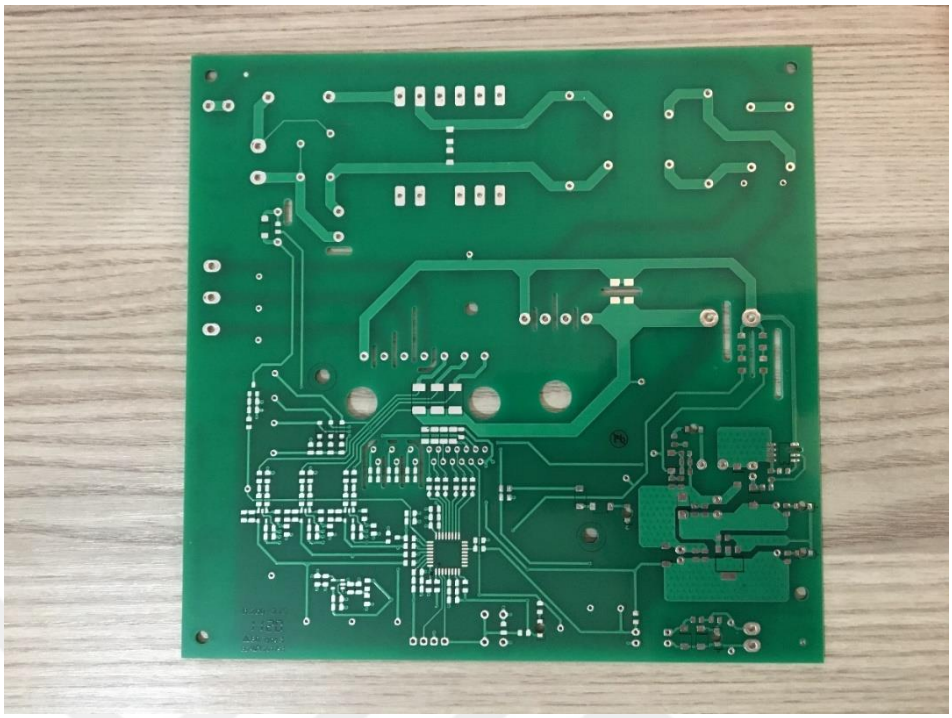

Figure 6.40: Bottom side of the not assembled PCB.

Top side of the assembled PCB is shown in Figure 6.41.

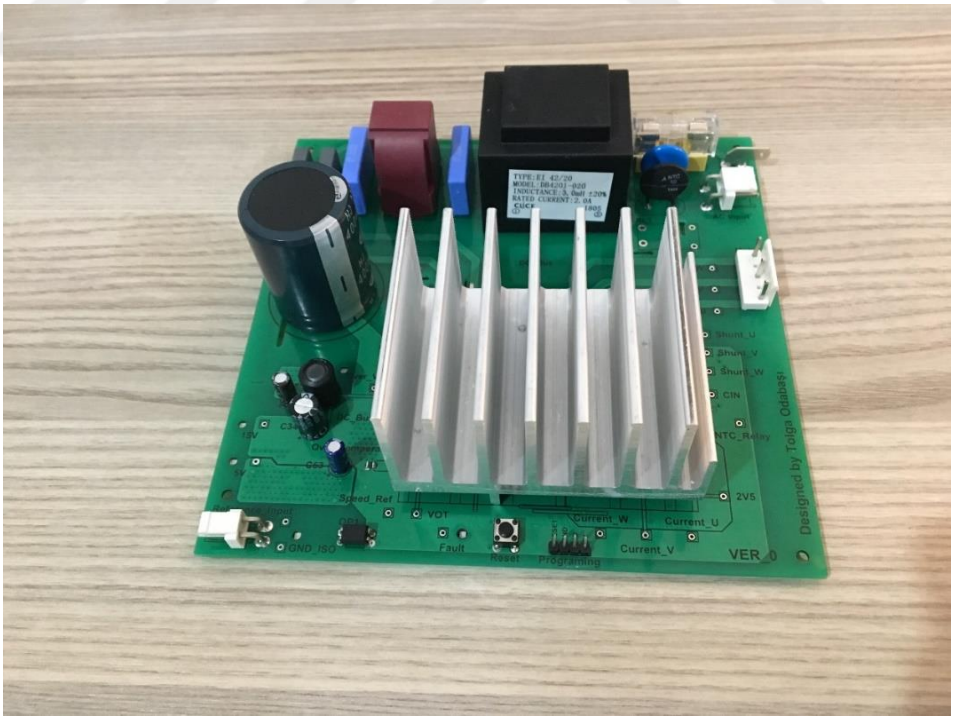

Figure 6.41: Top side of the assembled PCB.

Two boards are assembled for the thesis study.

Bottom side of the assembled PCB is given in Figure 6.42.

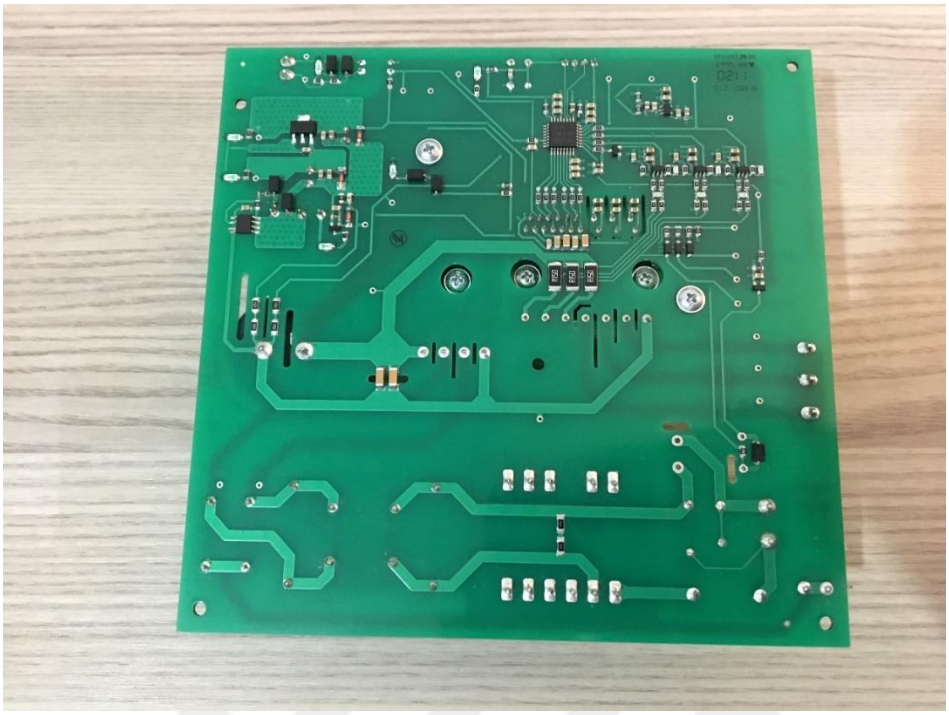

Figure 6.42: Bottom side of the assembled PCB.

7. SIMULATION

PMSM driver with field oriented control is simulated by using PSIM for three different reference speeds: 1300 rpm, 2000 rpm and 3000 rpm. In the simulation, a sensored control technique is used. Information of rotor position directly comes from the sensor placed in the rotor shaft. In a real application, Back-EMF based sensorless algorithm will be executed. PSIM schematic of driver circuit is shown in Figure 7.1.

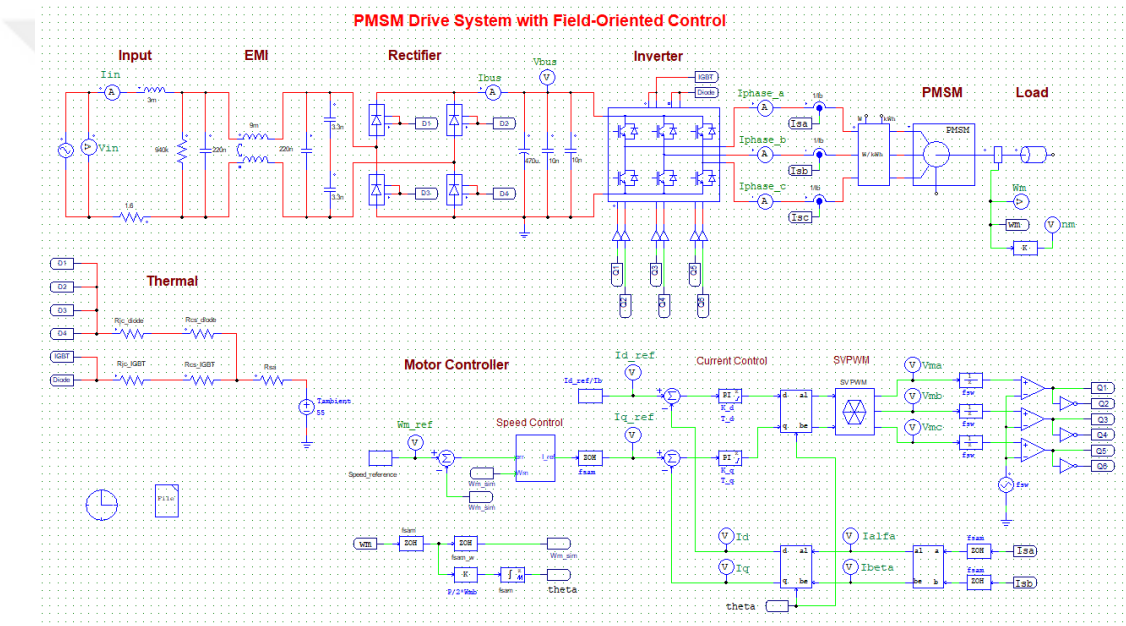

Figure 7.1: PSIM schematic of the driver circuit.

Parameters of a PMSM with compressor is given in Table 7.1

Table 7.1: Motor parameters.

Phase to neutral stator resistance [Ohm]	7.05
Phase to phase stator resistance [Ohm]	14.1
Phase to neutral stator inductance [mH]	21.4
Phase to phase stator inductance [mH]	57.8
L_d at 50Hz [mH]	81.0
L_q at 50Hz [mH]	38.7
Phase to phase Back-EMF voltage at 2000 rpm [V]	193
Phase to phase Back-EMF voltage at 3000 rpm [V]	288
K_e [V/rad.s]	0.92
Maksimum power [W]	270

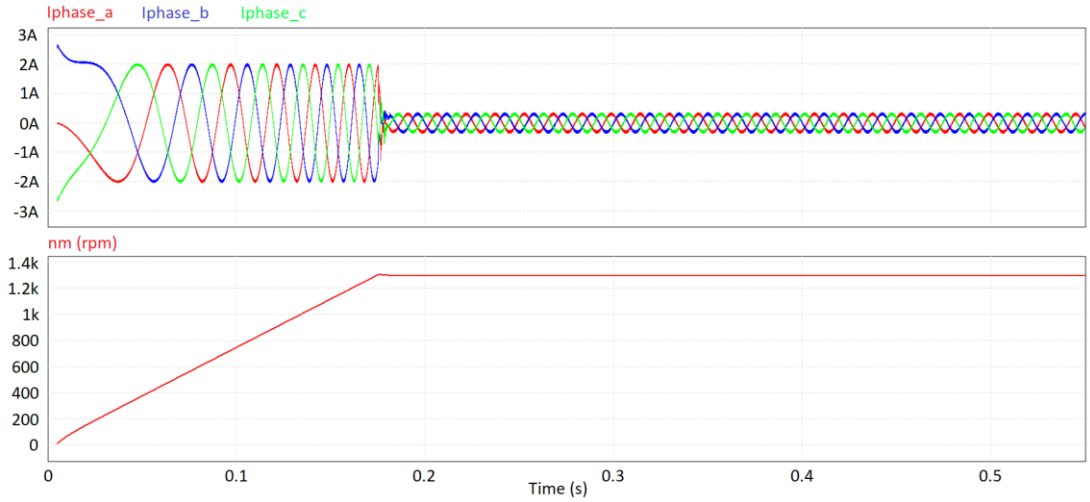

Figure 7.2: Phase currents and rotor speed @1300 rpm reference speed.

Phase currents and rotor speed at 1300 rpm reference speed is shown in Figure 7.2. The current value is fixed to 2A peak at the maximum torque algorithm region. Rotor speed reaches to reference speed from zero speed in 175ms. RMS value of the phase current after reaching reference speed is 0.22A.

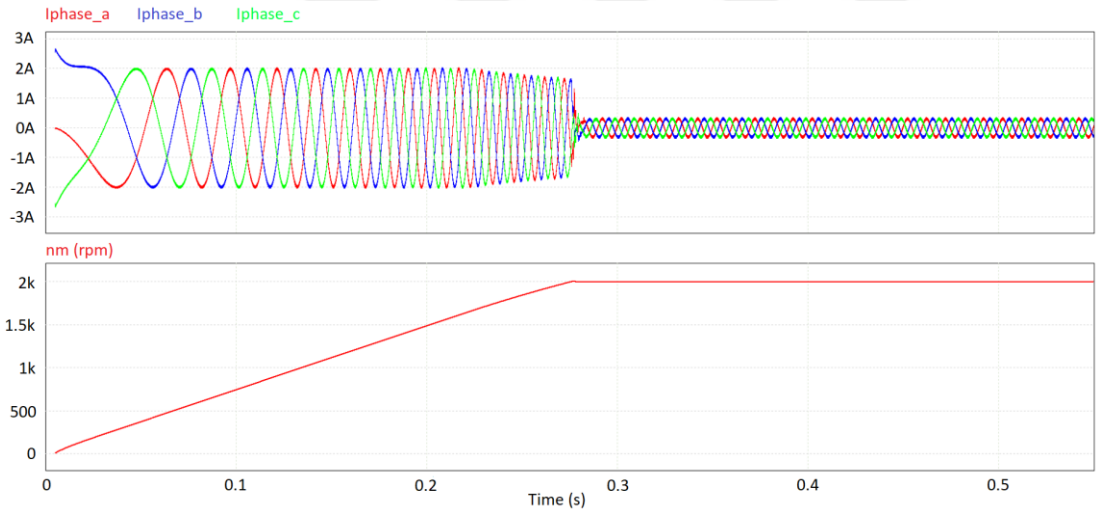

Figure 7.3: Phase currents and rotor speed @2000 rpm reference speed.

Phase currents and rotor speed at 2000 rpm reference speed is shown in Figure 7.3. The current value is fixed to 2A peak at the maximum torque algorithm region. Rotor speed reaches to reference speed from zero speed in 275ms. RMS value of the phase current after reaching reference speed is 0.22A.

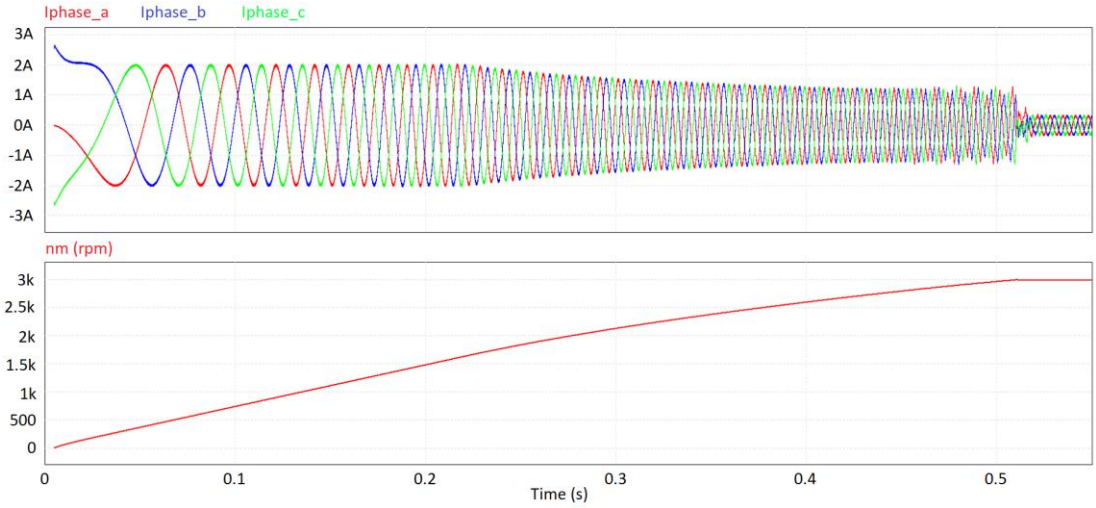

Figure 7.4: Phase currents and rotor speed @3000 rpm reference speed.

Phase currents and rotor speed at 2000 rpm reference speed is shown in Figure 7.4. The current value is fixed to 2A peak at the maximum torque algorithm region. Rotor speed reaches to reference speed from zero speed in 515ms. RMS value of the phase current after reaching reference speed is 0.22A.

If Figure 7.2, Figure 7.3 and Figure 7.4 are investigated, time duration of reaching reference speed increases as rotor speed increases. In addition to that, RMS values of the current when motor is running at reference speed are the same regardless of the rotor speed.

8. SOFTWARE DESIGN

A flowchart of sensorless field oriented control that is used in the driver is shown in Figure 8.1.

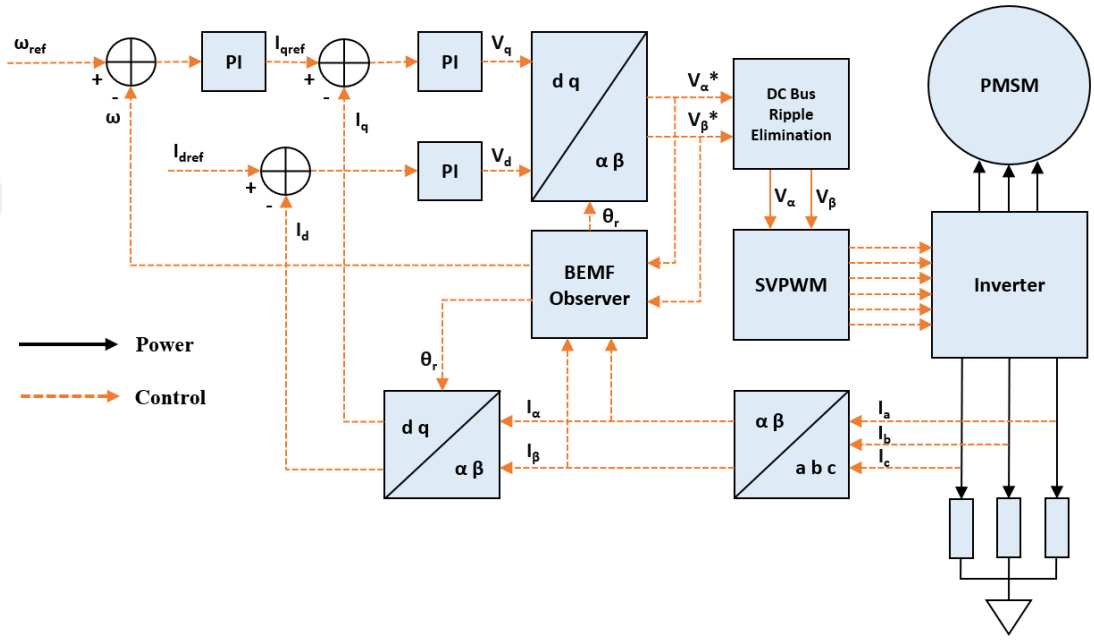

Figure 8.1: Flow chart of sensorless FOC.

Main control functions are listed below,

1) Clarke Transform
2) Park Transform
3) Back-EMF Observer
4) Inverse Park Transform
5) Inverse Clarke Transform
6) DC Ripple Elimination
7) SVPWM Generator
8) PI Regulator

Main functions of FOC which are vector transformations and SVPWM generator are explained in fifth chapter in detail. Inverter drive systems that use field oriented control algorithm have the same calculation methods for these type of functions. However, there may also be some special algorithms specific to drive systems. In this

thesis, DC bus ripple elimination and Back-EMF observer functions can be given as an example of these explanation.

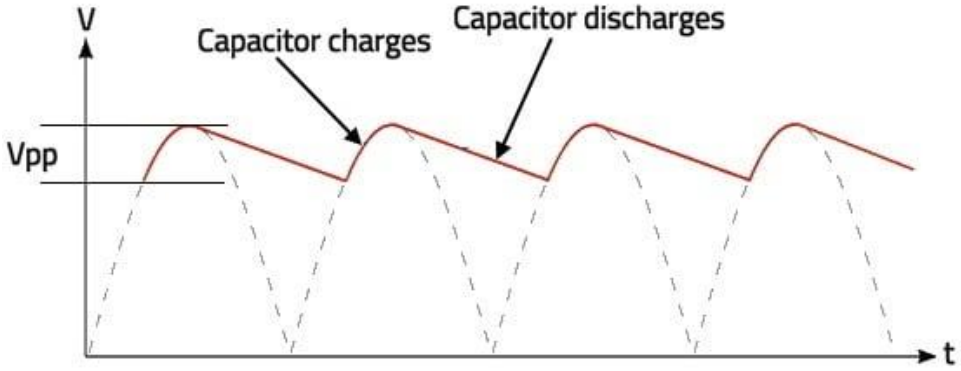

Figure 8.2: Bus voltage fluctuation [93].

Bus voltage fluctuation in any inverter drive system that has electrolytic capacitor is shown in Figure 8.2. The magnitute of this fluctuation changes according to the load. When load increases, this value also increases and visa versa. Aim of the DC bus ripple elimination function is to reduce the effect of this phenomen on the control system. In general, the peak output voltage value strictly depends on the bus voltage. Fluctuation on the bus voltage reflects to the output voltage and this may cause unexpected torque and speed ripple on the system. Output voltage reference is clamped to the minimum value of the bus voltage in order to avoid these consequences. The minimum value of the bus voltage can be determined with a low-pass filter, in which the rising time constant is much higher than the falling time constant.

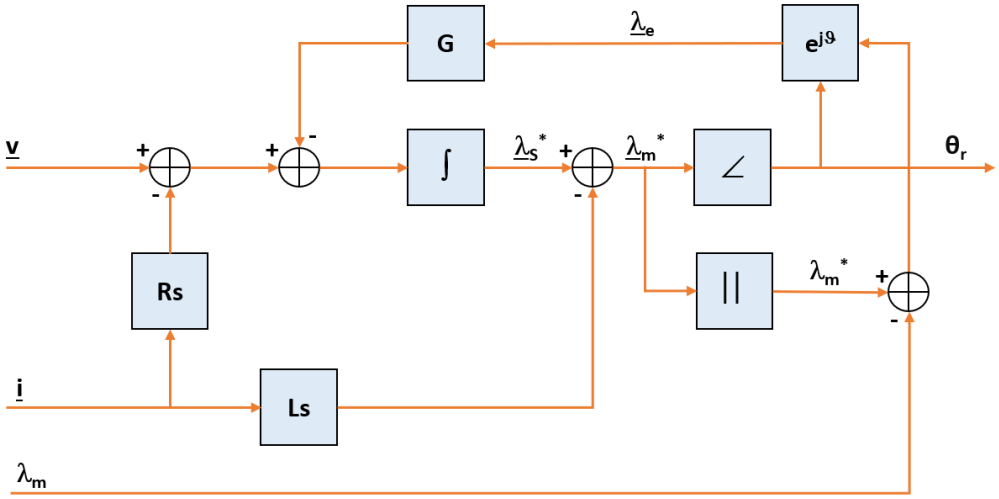

Figure 8.3: Flow chart of Back-EMF exact integration method.

Flow chart of Back-EMF exact integration method which is used in the thesis is given in Figure 8.3. There is an integration operation in this control technique. It may

difficult to execute an integration operation for a microcontroller. There are a lot of reasons for this difficulty. Firstly, initial conditions of integration are not exactly known. Moreover, it could be totally unknown. Secondly, noise is induced due to measurement circuit and quantization and so on. Although filters are used in the hardware, some noise always exists in the measurement and this unwanted signal is superposed with the Back-EMF signal. Thirdly, there is some offset in the measurement and it could cause integral to grow up over the numeric limits. Lastly, non-linearity of inverter system causes some error in the calculation. In order to overcome or weaken these problems, the integral operation is corrected with a signal obtained modulating accordingly with the estimated phase the error between the estimated flux amplitude and the amplitude of the permanent magnets flux, known as a motor parameter; also stator resistance and synchronous inductance are considered known. Output of the function in Figure 8.3 is angular rotor position denoted by θ_r. If derivative of this value is taken, velocity value of the rotor is obtained.

One of the advantages of this method is to model the system easier than other type of the methods. Another advantage is that mathematical calculations need less effort in this method. There are some drawbacks also. Calculations are sensitive to motor parameters such as resistance and inductance. It is significant to consider changes in the motor parameters in order to predict position and velocity of the rotor more accurate. Another one is that there is not enough Back-EMF signal in the low speed to execute sensorless algorithm based on Back-EMF. This is the reason why open loop algorithm is implemented at the starting [90].

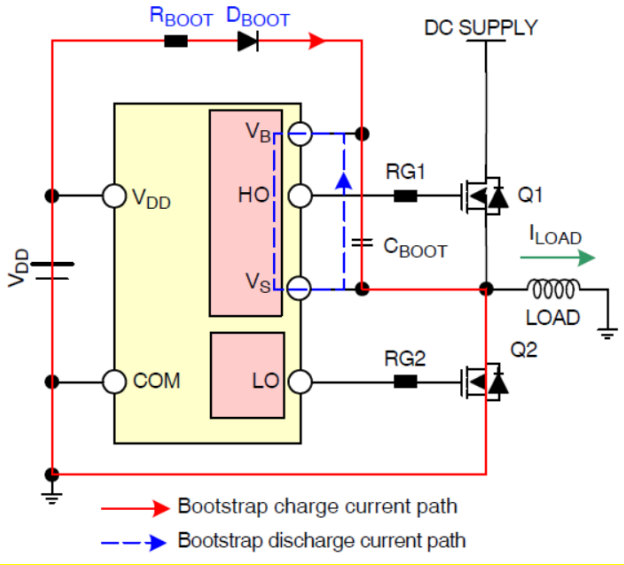

Figure 8.4: Bootstrap capacitor charge and discharge paths [91].

Bootstrap capacitor charge and discharge paths are shown in Figure 8.4. Although this figure belongs to discrete solution, it is also valid for IPM type switch that is used in the thesis. Only difference is that these current circulations occur in the IPM. This topic seems to belong to hardware section; however, there is software side of the issue. At the beginning which means motor does not start to rotate, bootstrap capacitors are not charged. Before starting, these three capacitors are needed to be charged. Otherwise, high side IGBT's could not be driven due to low bootstrap voltage and driver goes into under voltage lock out failure mode and IPM is shut down. Avoid this condition, low side IGBT's are switch on enough time to charge before starting. Enough time depends on the bootstrap capacitor value and the bootstrap resistor. 10uF ceramic capacitor is used as bootstrap capacitor. Maximum value of bootstrap resistor that is inside of IPM is 120Ω. Electrical time constant is equal to 1.2ms. Five times of this value is enough to charge fully for this capacitor and this value is 6ms. In the algorithm, three low side IGBT's are switched on at the same time during 10ms with 100% duty cycle for charging before starting. In normal operating condition, this capacitor is charged while low side IGBT is on and discharged while high side IGBT is on. Therefore, this capacitor is always charged in operating condition thanks to complementary switching technique.

9. EXPERIMENT AND RESULTS

Driver circuit is tested with compressor setup and measurement equipment shown in Figure 9.1.

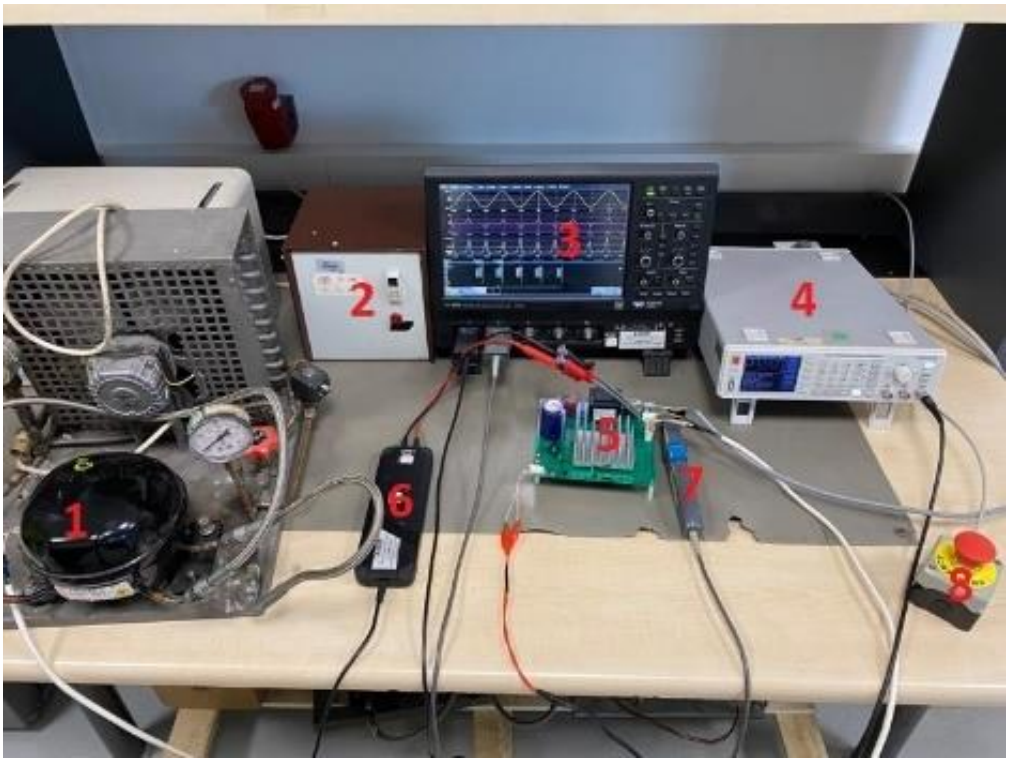

Figure 9.1: Experimental setup.

Test setup is consisted of below parts,

1) Compressor setup
2) Isolation transformer
3) Oscilloscope
4) Signal generator
5) Driver circuit
6) Differential probe
7) Current probe
8) Emergency button

Table 9.1: Input measurements.

Motor Speed [rpm]	Input Voltage [V_{rms}]	Input Current [A_{rms}]	Input Power [W]	Power Factor
1300	226.76	0.72	91.43	0.56
2000	225.94	1.52	195.21	0.57
3000	225.10	1.90	270.57	0.63

Input measurements regarding the rotor speed are given in Table 9.1. This concludes voltage, current, power and power factor. As motor speed increases, current, power and power factor also increase as expected. At full speed, input power has reached to 270W.

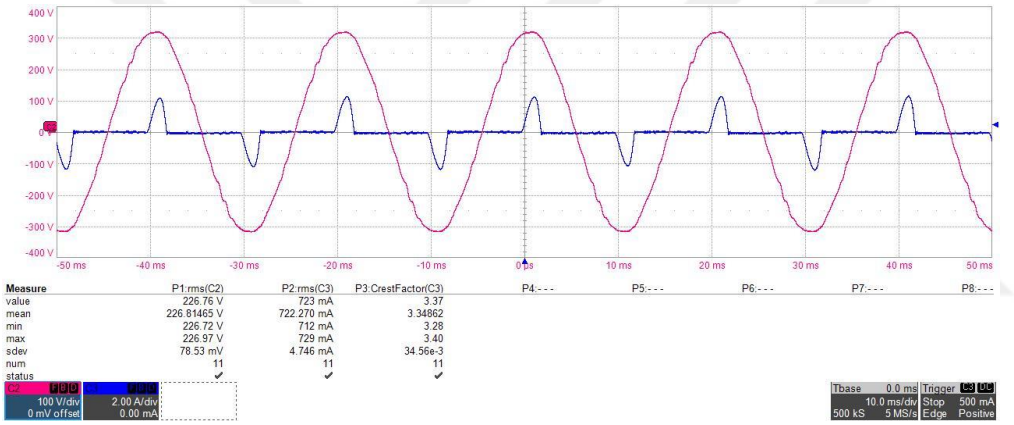

Figure 9.2: Input voltage and input current @1300 rpm.

Input voltage and input current at 1300 rpm is given in Figure 9.2. RMS value of input voltage is 226.76V and RMS value of input current is also 0.72A. Crest factor of the current is also 3.37.

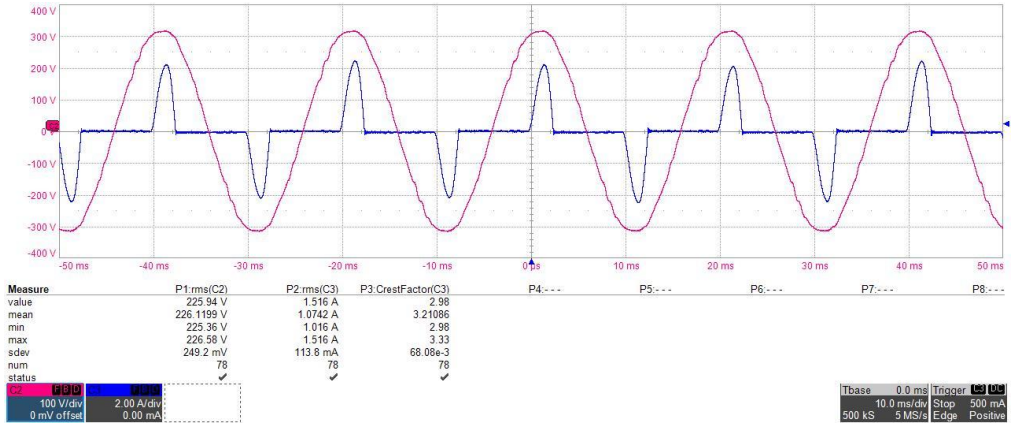

Figure 9.3: Input voltage and input current @2000 rpm.

Input voltage and input current at 2000 rpm is given in Figure 9.3. RMS value of input voltage is 225.94V and RMS value of input current is also 1.52A. Crest factor of the current is also 2.98.

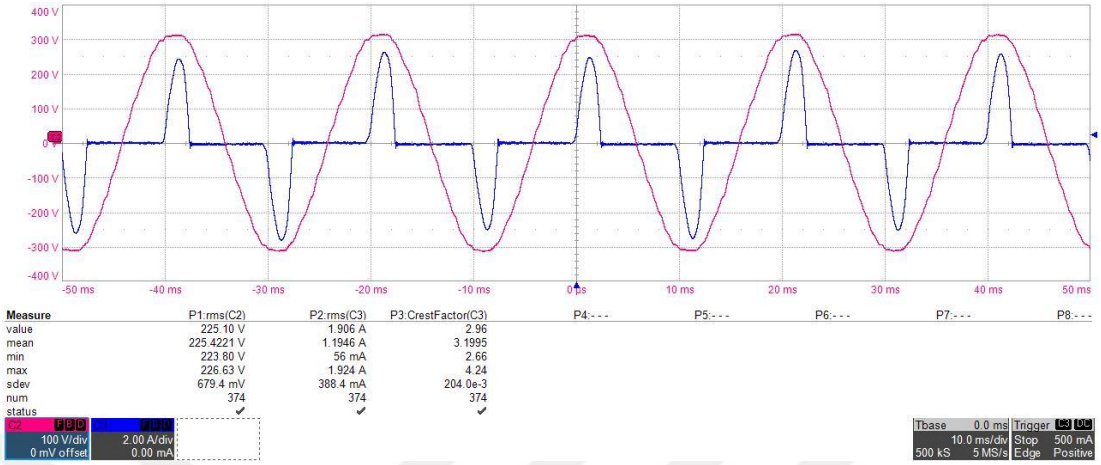

Figure 9.4: Input voltage and input current @3000 rpm.

Input voltage and input current at 3000 rpm is given in Figure 9.4. RMS value of input voltage is 225.10V and RMS value of input current is also 1.90A. High crest factor due to electrolytic bus capacitor can be seen in Figure 9.2, Figure 9.3 and Figure 9.4.

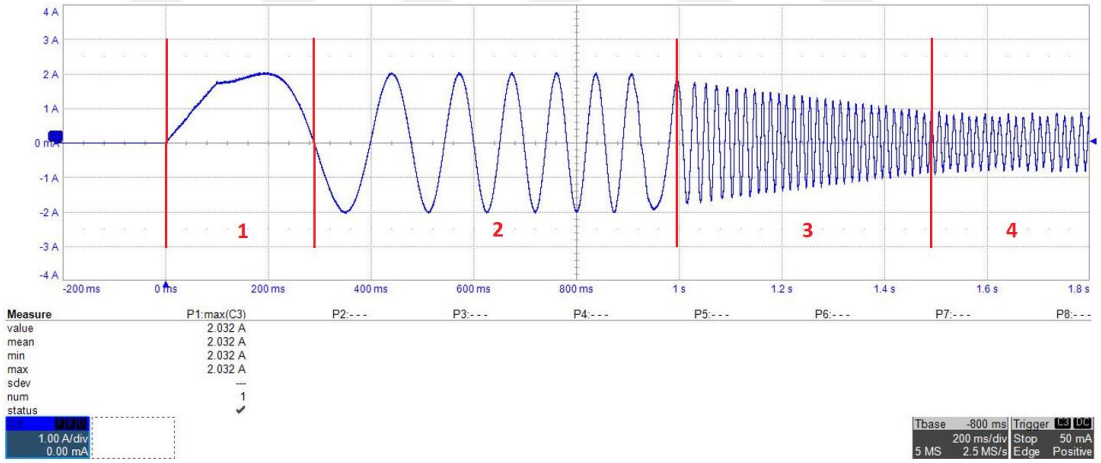

Figure 9.5: Start-up phase current.

The start-up sequence of the phase current is given in Figure 9.5. As seen, this sequence consists of four parts. The first part is aligning also called as parking. Half period sinus wave with 280ms duration is applied to the stator windings. The rotor is aligned to the pre-determined position while the transition to the open loop to keep the motor in control. If aligning is not applied properly, control can be lost. Peak current is 2A for this period. The second part is the open loop part. The voltage vector of the stator is rotated with a ramp speed until the Back-EMF signal is enough to close the

speed loop. Sin wave with 6-7 period is applied in this part. The peak current is fixed to 2A. The third part and the fourth part are the closed loop parts. The position of the rotor is extracted from fedback currents from the shunt resistors via Back-EMF observer. An algorithm is switched to closed loop from open loop at approximately 700 rpm. At the third part, direct axis current is gradually decreased to the zero value. At the end of the third part, this current reaches to zero. Direct axis current plays vital role in the open loop stage that is shown at the second part in order to synchronize the flux of the rotor with rotating stator flux. At the fourth part, startup issue is completed and classical FOC algorithm is conducted.

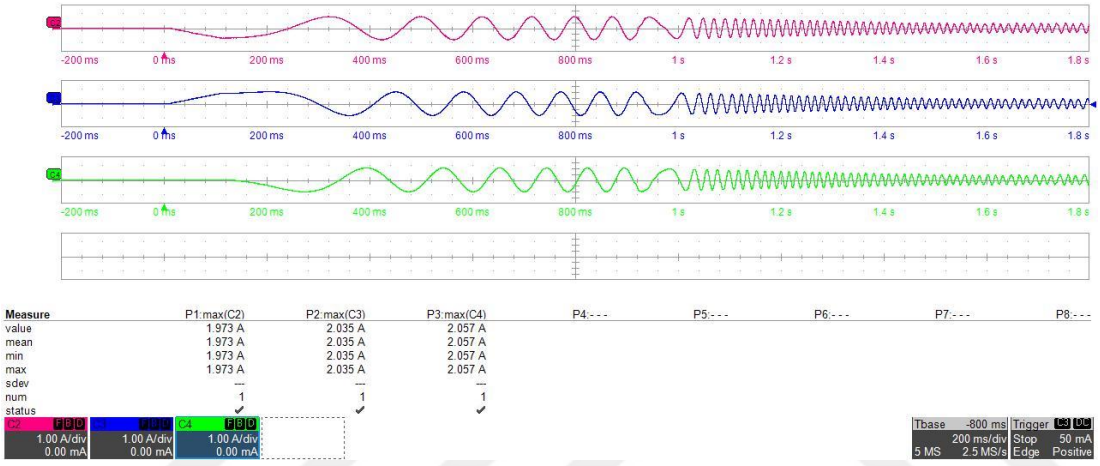

Figure 9.6: Startup of three phase currents.

Startup of three phase currents are shown in Figure 9.6. The similar startup waveforms are seen both three phases.

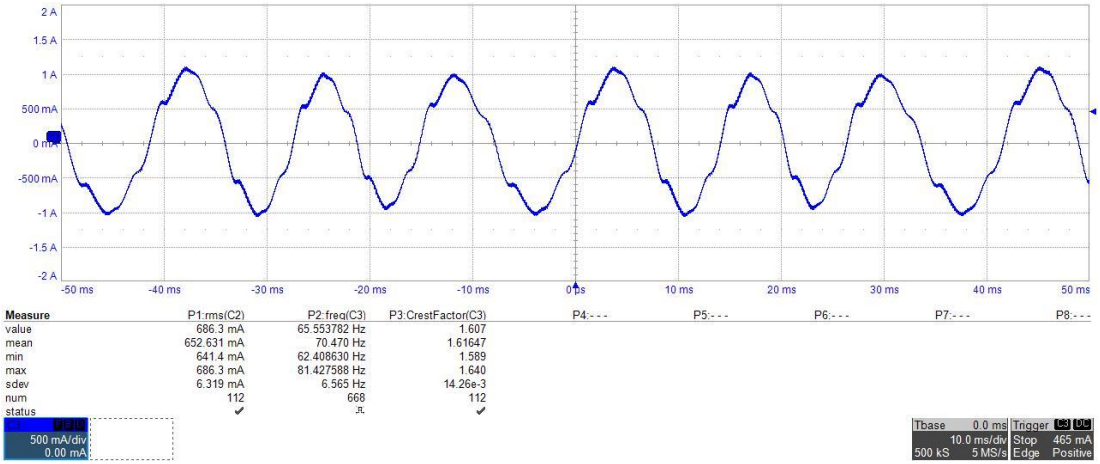

Figure 9.7: Phase current @1300 rpm.

Phase current at 1300 rpm is shown in Figure 9.7. RMS value of current is 0.69A.

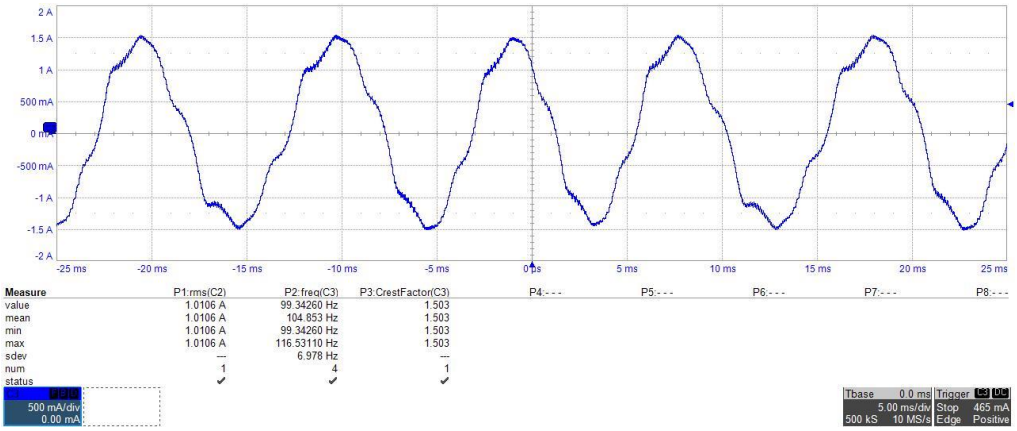

Figure 9.8: Phase current @2000 rpm.

Phase current at 2000 rpm is shown in Figure 9.8. RMS value of current is 1.01.

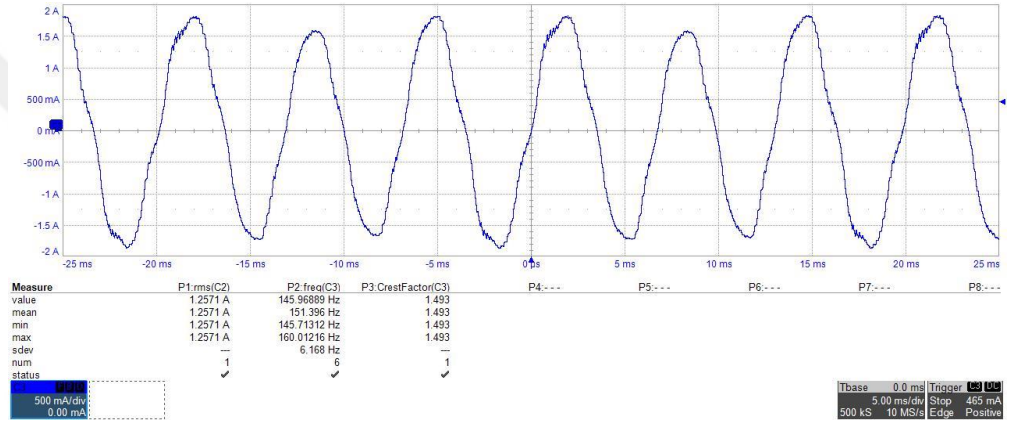

Figure 9.9: Phase current @3000 rpm.

Phase current at 3000 rpm is shown in Figure 9.9. RMS value of current is 1.26A. If currents are shown in Figure 9.7, Figure 9.8 and Figure 9.9 are analyzed, at 3000 rpm, the imbalance of the current seems to have increased. Peak value of the current is not the same for adjacent periods. This may cause acoustic noise for compressor systems. This is the possible enhacement area for control algorithm side.

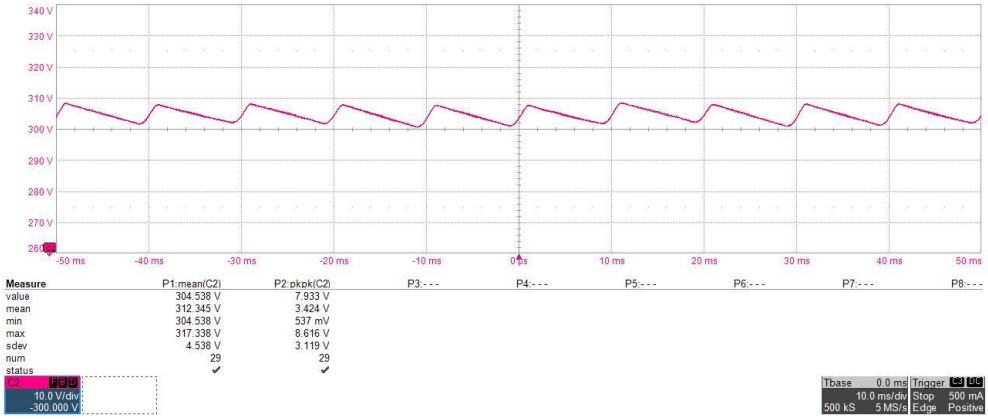

Figure 9.10: DC bus voltage @1300 rpm.

DC bus voltage at 1300 rpm is shown in Figure 9.10. Peak to peak voltage is 7.93V.

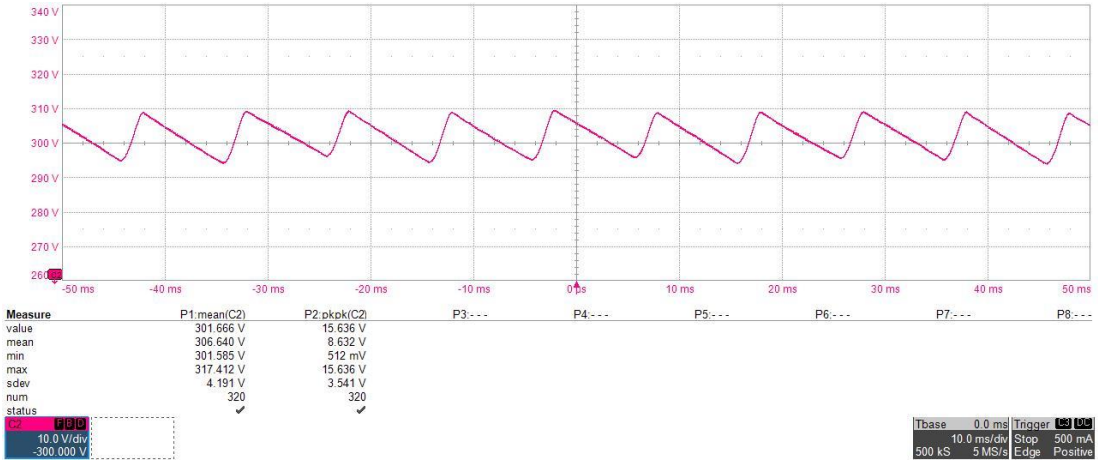

Figure 9.11: DC bus voltage @2000 rpm.

DC bus voltage at 2000 rpm is shown in Figure 9.11. Peak to peak voltage is 15.64V.

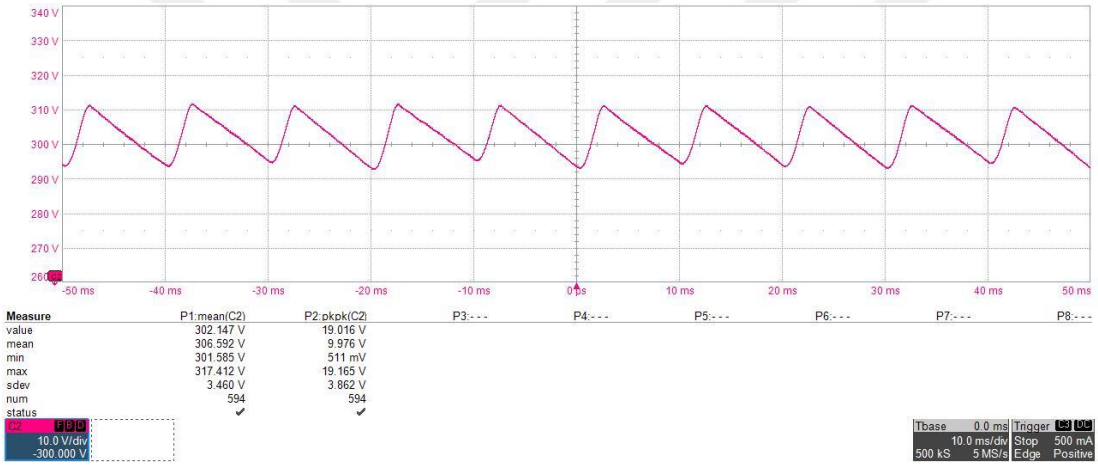

Figure 9.12: DC bus voltage @3000 rpm.

DC bus voltage at 3000 rpm is shown in Figure 9.12. Peak to peak voltage is 19.02. Peak to peak voltage increases as rotor speed and power increase.

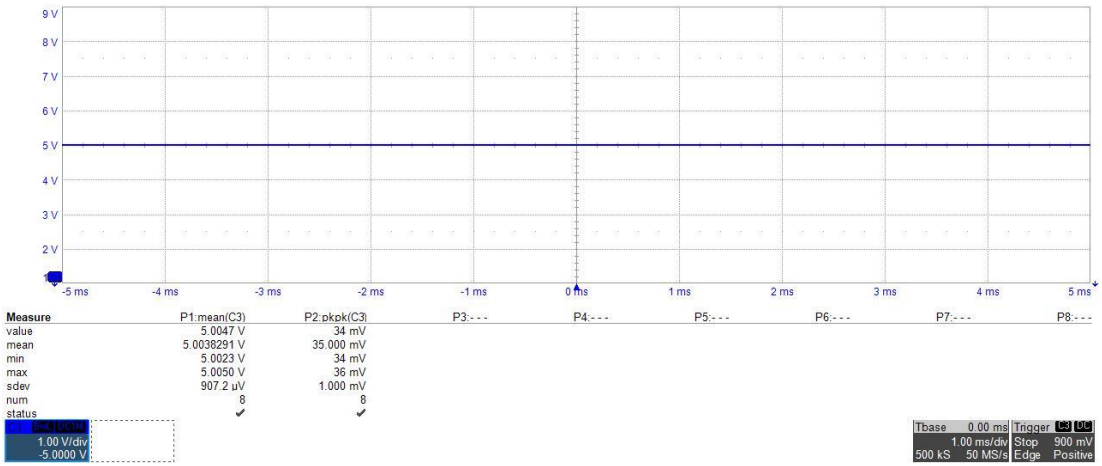

Figure 9.13: LDO voltage @not rotating.

LDO voltage that is measured when the rotor is not rotating is given in Figure 9.13. The mean value of this voltage is 5.00V. The peak to peak value is also 34mV.

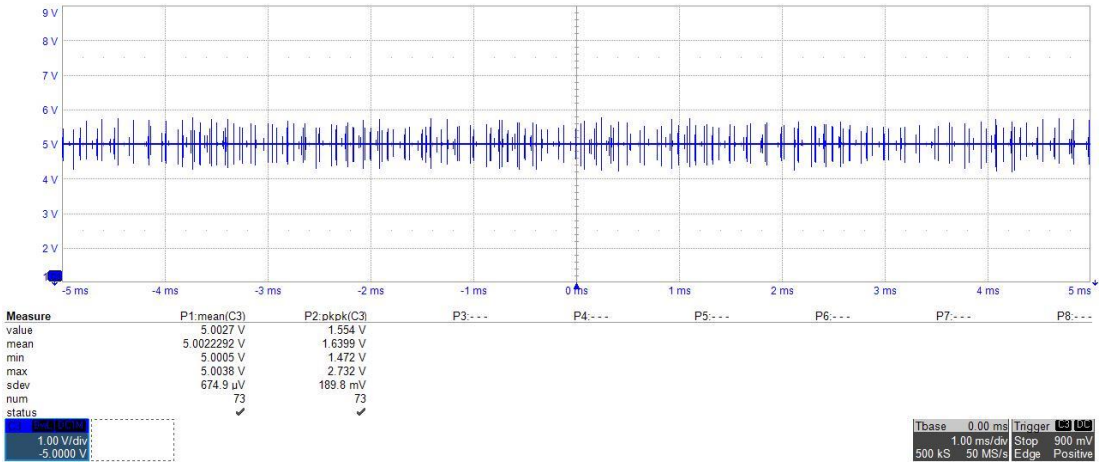

Figure 9.14: LDO voltage @2000 rpm.

LDO voltage that is measured when the rotor is rotating is given in Figure 9.14. The mean value of this voltage is 5.00V. As seen, peak to peak noise value reaches 1.55V. The main reason for this noise is the strong noise coming from the inverter stage. Switching noise can be obviously seen in Figure 9.13. Although there is filter circuit on the output, this noise can not be eliminated. It can just be reduced in value.

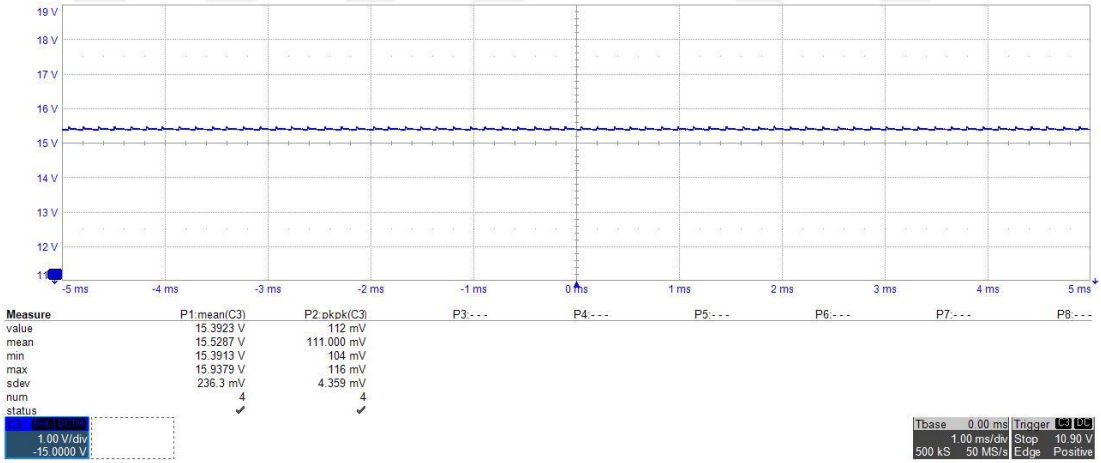

Figure 9.15: SMPS voltage @not rotating.

SMPS voltage that is measured when the rotor is not rotating is shown in Figure 9.15. The mean value of this voltage is 15.39V. The peak to peak value is also 112mV.

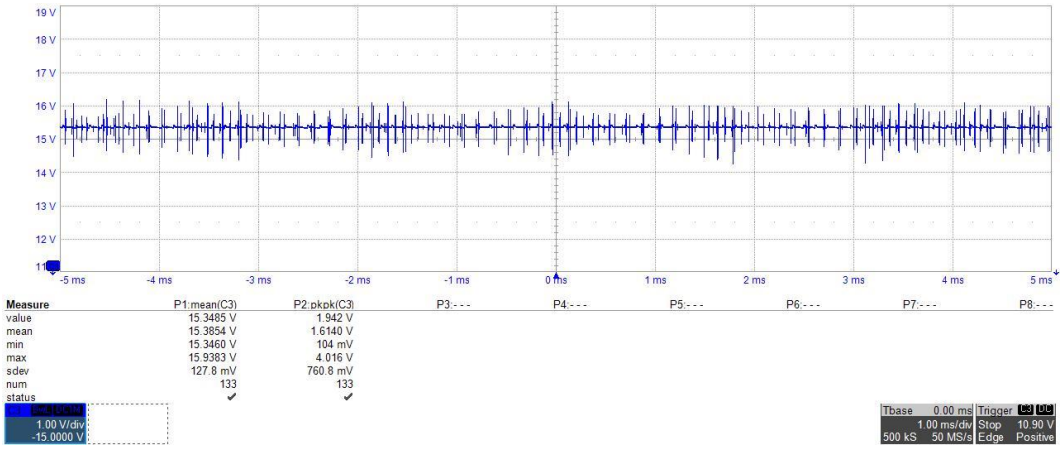

Figure 9.16: SMPS voltage @2000 rpm.

SMPS voltage that is measured when the rotor is rotating is given in Figure 9.16. The mean value of this voltage is 15.35V. Peak to peak noise value is measured as 1.94V. Like LDO voltage, SMPS output voltage is also noisy due to the inverter stage.

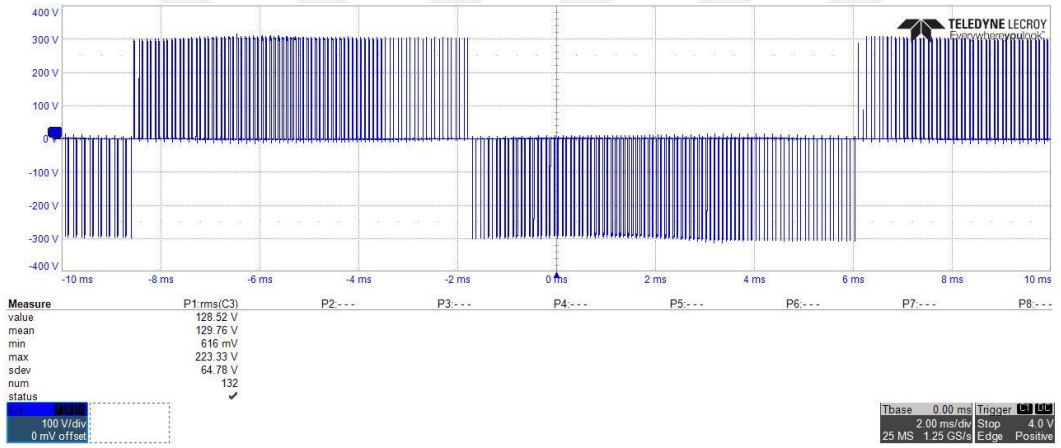

Figure 9.17: Phase to phase voltage of the motor @1300 rpm.

Phase to phase voltage of the motor at 1300 rpm is shown in Figure 9.17. RMS value of the voltage is 128.52V.

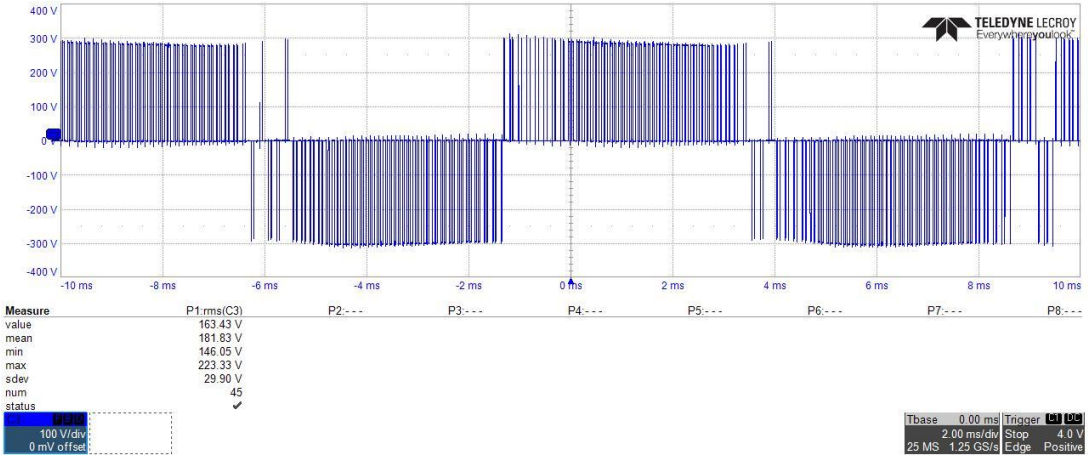

Figure 9.18: Phase to phase voltage of the motor @2000 rpm.

Phase to phase voltage of the motor at 2000 rpm is shown in Figure 9.18. RMS value of the voltage is 163.43V.

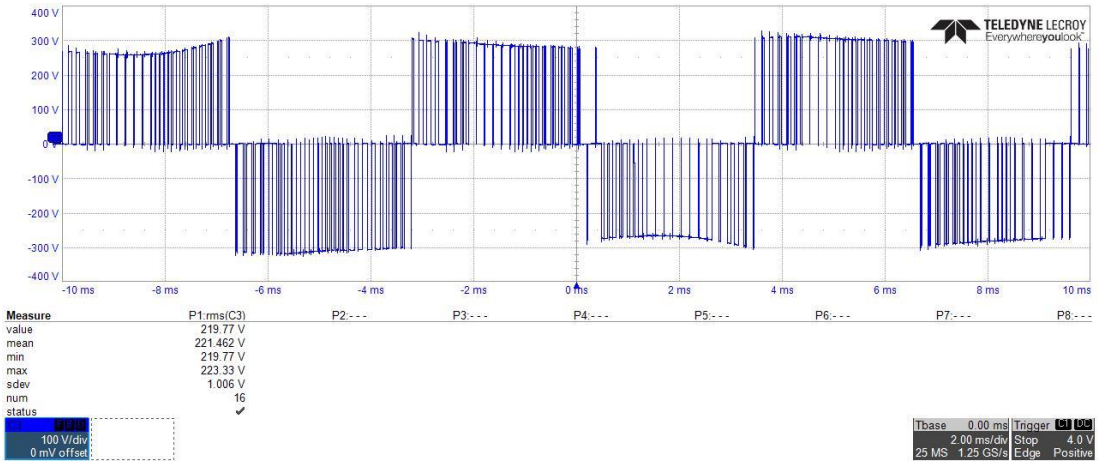

Figure 9.19: Phase to phase voltage of the motor @3000 rpm.

Phase to phase voltage of the motor at 3000 rpm is shown in Figure 9.19. RMS value of the voltage is 219.77V. If Figure 9.17, Figure 9.18 and Figure 9.19 are investigated, RMS value of this voltage and its frequency increase as the rotor speed increases. In addition to that, the ratio of the voltage and frequency is tried to be kept constant so that the flux remains the same. This is one of the main ideas of the motor control technique.

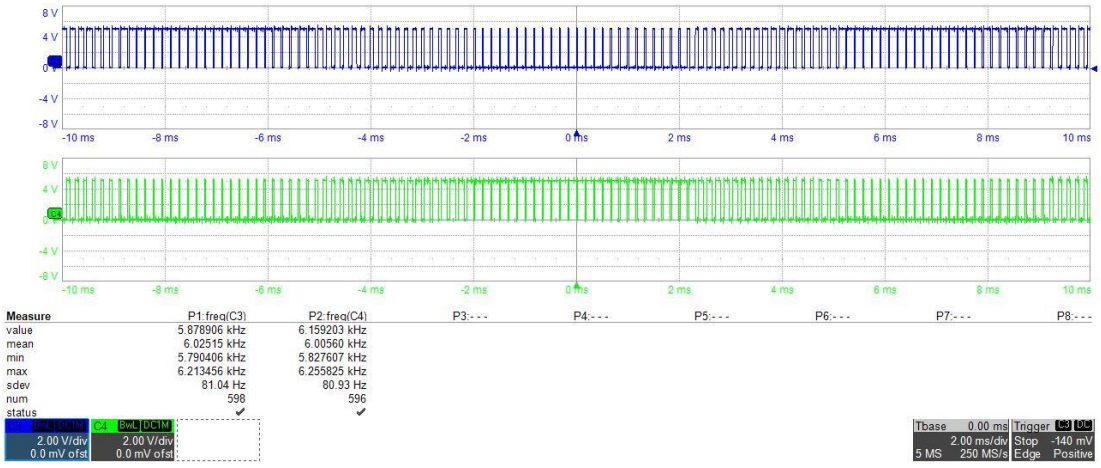

Figure 9.20: High side and low side PWM signals for half bridge.

High side and low side PWM signals for half bridge are shown in Figure 9.20. These are complementary PWM signals. Although frequency of the PWM signals are exactly 6kHz, it is not seen like this in the measurement shown in Figure 9.21 due measurement error. And also, 1us dead time is inserted between these complementary signals in order to avoid cross-conduction.

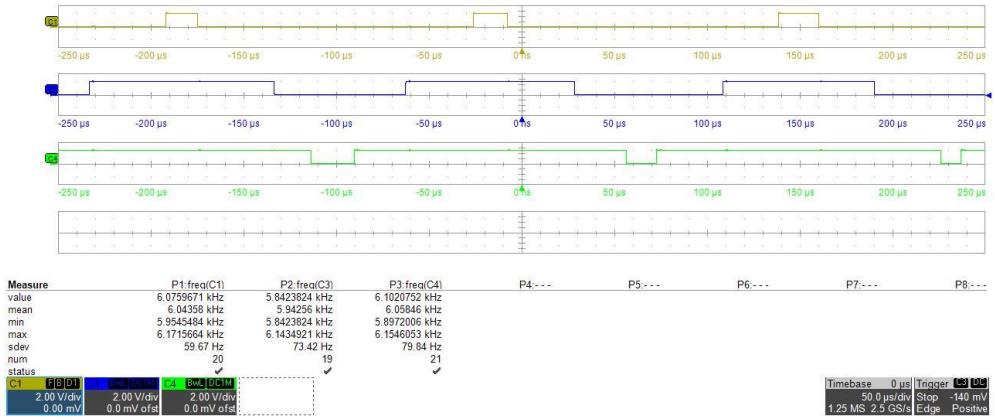

Figure 9.21: Centre aligned high side PWM signals.

Centre aligned high side PWM signals are obviously seen in Figure 9.21. Centre aligned mode is valid not only high side signals but also low side signals. Edge aligned PWM signals are not preffered in the motor control applications. Because edge aligned PWM cause more current distortion than centre aligned mode. In addition to that, dead time control is easily implemented to the centre align mode PWM signals.

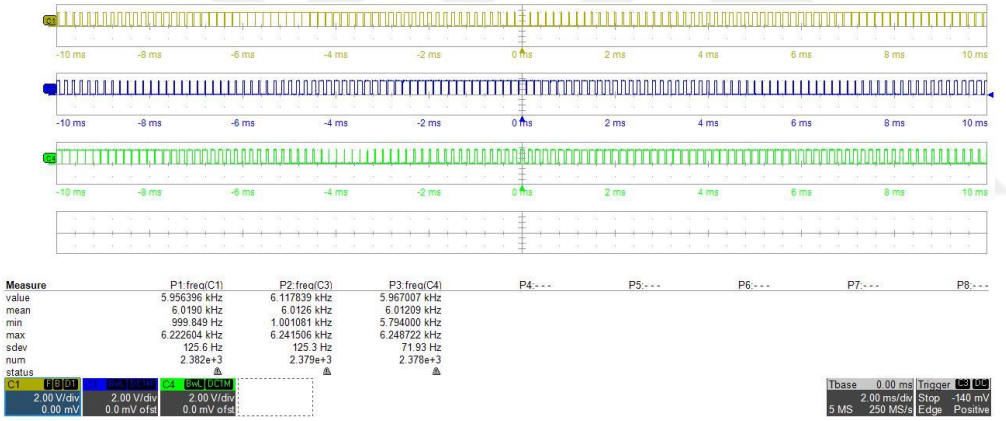

Figure 9.22: High side PWM signals @1300 rpm.

High side PWM signals at 1300 rpm are shown in Figure 9.22.

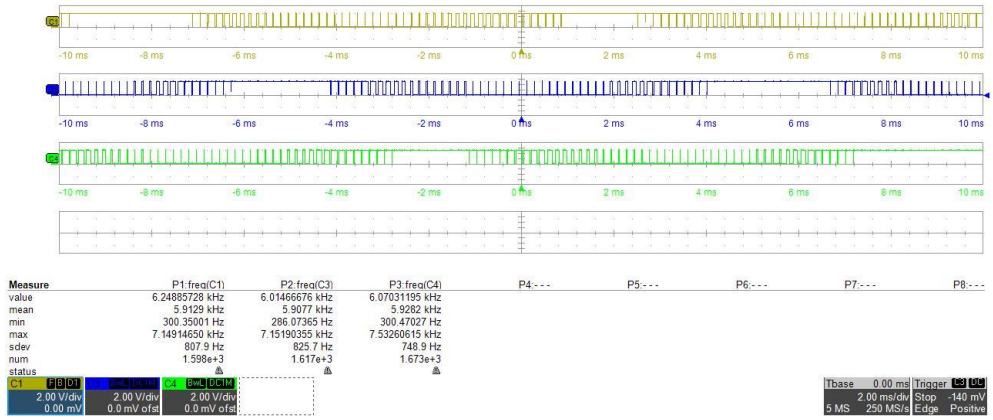

Figure 9.23: High side PWM signals @2000 rpm.

High side PWM signals at 2000 rpm are shown in Figure 9.23.

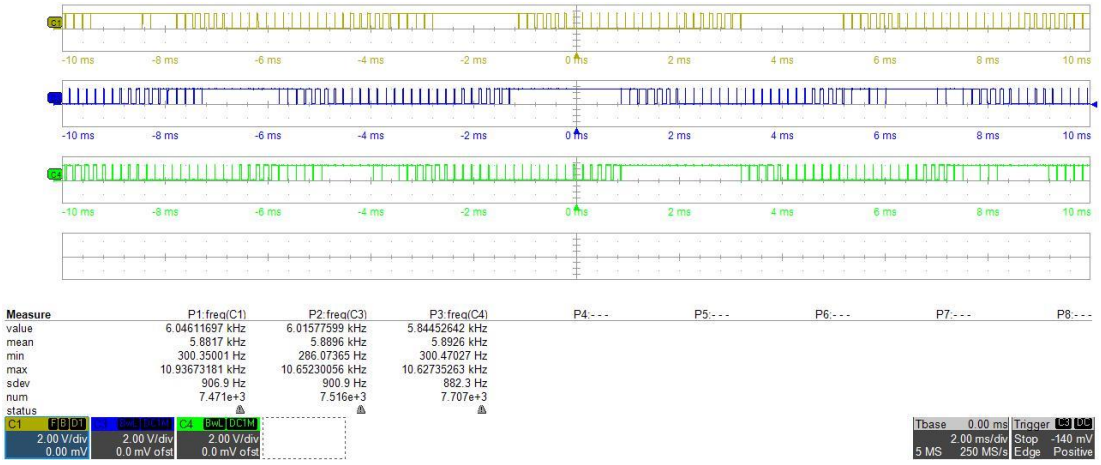

Figure 9.24: High side PWM signals @3000 rpm.

High side PWM signals at 3000 rpm are shown in Figure 9.24. If Figure 9.22, Figure 9.23 and Figure 9.24 are investigated, duty cycle of PWM signals are increased as rotor speed and motor power increase. This is also the nature of the motor control applications.

Figure 9.25: The input and the output signals of the optocoupler.

The input and the output signals of the optocoupler are shown in Figure 9.25. These signals are complementary to each other due to the circuit configuration. The input signal shown with green trace is an external signal that comes from the signal generator. It has 50% duty cycle and 3.3V magnitude. The frequency value is changed between 50Hz and 150Hz. The output signal that shown with blue trace has 5V magnitude. The output signal goes to the microcontroller to adjust the rotor speed linearly.

Efficiency values of the inverter board are measured with a power analyzer at different speeds and shown in Figure 9.26.

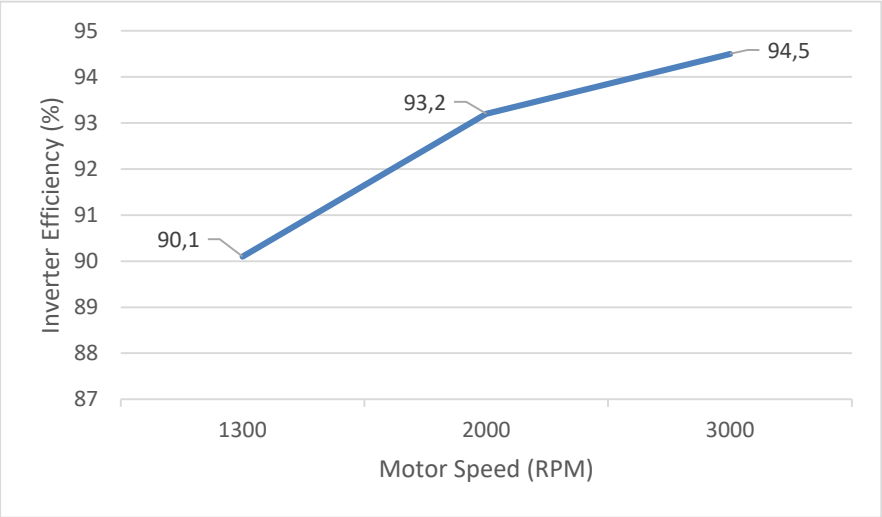

Figure 9.26: Inverter efficiency @different speeds.

As seen, efficiency value has the tendency to increase as rotor speed increases. Efficiency value reaches 94.5% at full load. Generally, power electronic circuits such as inverter boards have higher efficiency value at higher power values. Because base power losses in the board affect the efficiency more especially at low speed or low power.

Total harmonic distortion (THD) values of the phase current at different speeds are shown in Figure 9.27.

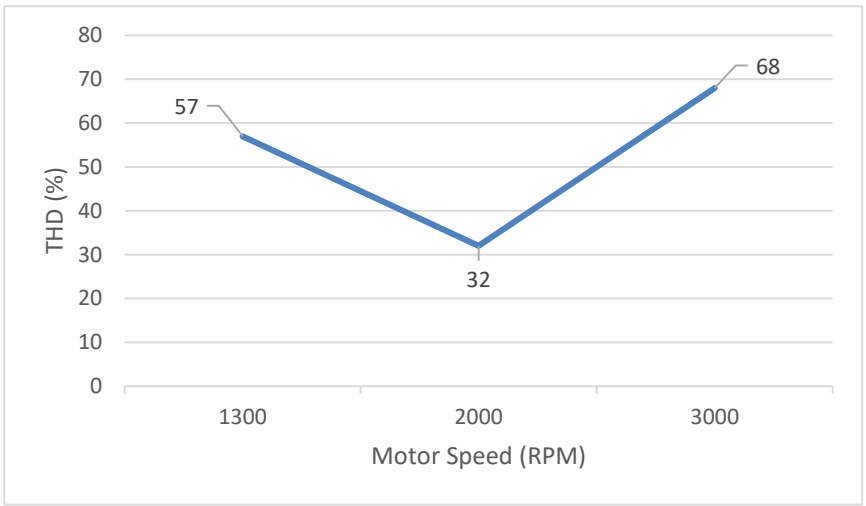

Figure 9.27: THD of the phase current @different speeds.

Distortion of phase currents can be seen even without spectrum analysis. Phase currents have not a perfect sinusoidal shape and they are shown at different speeds in Figure 9.7, Figure 9.8 and Figure 9.9 .

Compressor systems may have such a distorted current shape. One of the main reasons of that, the load torque pattern of the system is not constant regarding the angular position. The maximum torque value can reach 6-7 times higher than the average torque value. It can even be negative in a short range. These are illustrated in an example torque graph shown in Figure 9.28. The dynamic of the load torque distorts the shape of the phase currents. Negative torque condition can cause the motor to start audible, especially by showing itself at the starting.

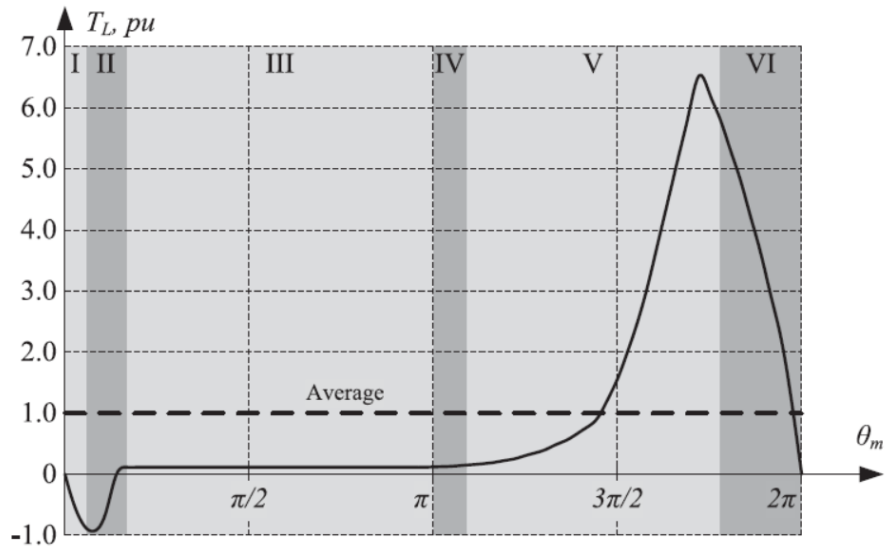

Figure 9.28: Load torque – angular position characteristic of the compressor system [92].

In addition to the nature of the compressor system, there may also be other factors causing this distortion. Incorrect position estimation of the observer can also cause this. Since it is difficult for compressor systems to observe the actual position of the rotor, this subject will not be studied. Another reason may be a low switching frequency of the inverter board. The motor is driven with 6kHz switching frequency. This value is tried to be kept as small as possible. Because the higher switching frequency, the higher switching losses. However, there is a trade-off in this issue. Low switching frequency means low control frequency and this means a system that responds slowly to torque changes. In addition to that, low switching frequency may cause an acoustic noise in inverter board and the motor. This can be critical for noise sensitive applications.

In order to observe the effect of the switching frequency in current distortion, this frequency is increased from 6kHz to 12kHz. After this implementation, THD values the phase current at 12kHz switching frequency is measured as shown in Figure 9.29.

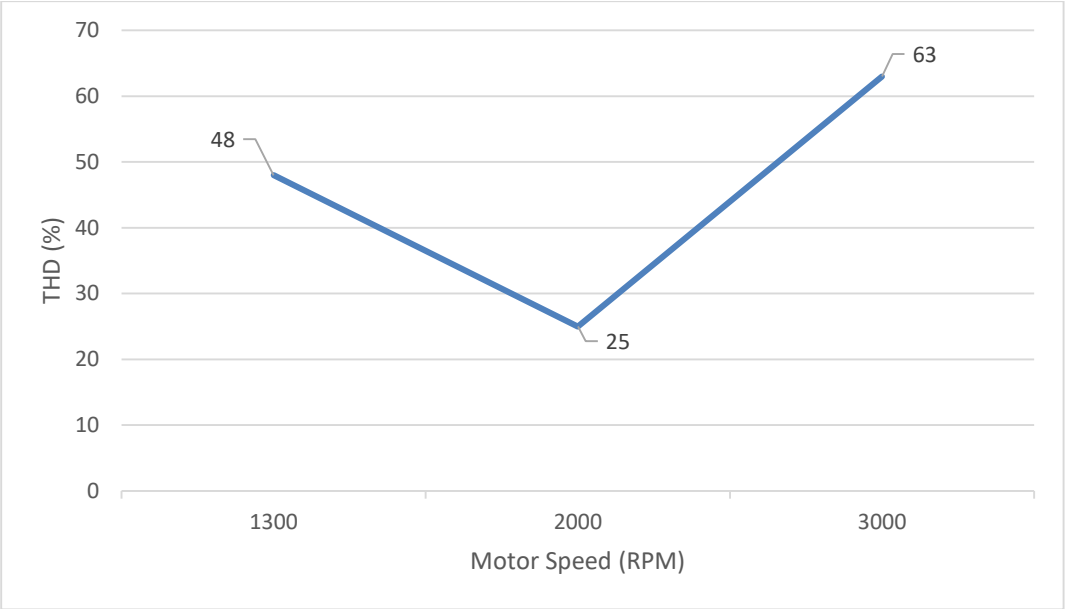

Figure 9.29: THD of the phase currents @12kHz switching frequency @different speeds.

The comparison of THD of the phase currents between 6kHz and 12kHz at different speeds is given in Figure 9.30.

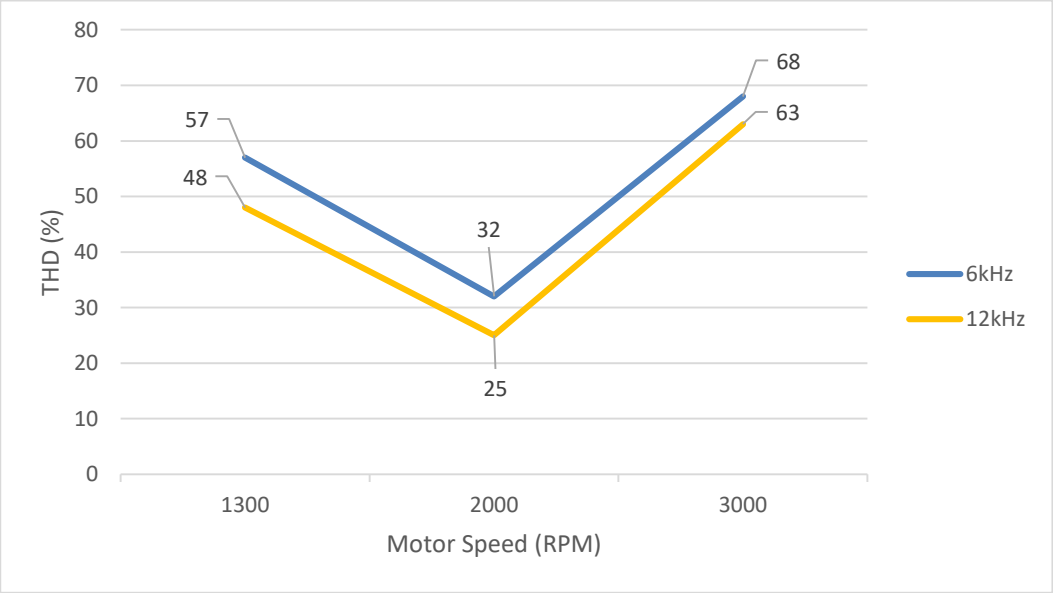

Figure 9.30: Comparison of THD of the phase currents between 6kHz and 12kHz @different speeds.

It can be seen, total harmonic distortion values of the phase currents are improved at all speed values by increasing switching frequency from 6kHz to 12kHz.

In addition to that, the efficiency aspect of this implementation should be observed. Although overall system efficiency that consists of the inverter board, the motor and compressor system may be increased due to improvement of THD value of the phase

currents, the efficiency of the inverter is expected to decrease due to higher switching frequency. Inverter efficiency at 12kHz switching frequency and different speeds are obtained as shown in Figure 9.31.

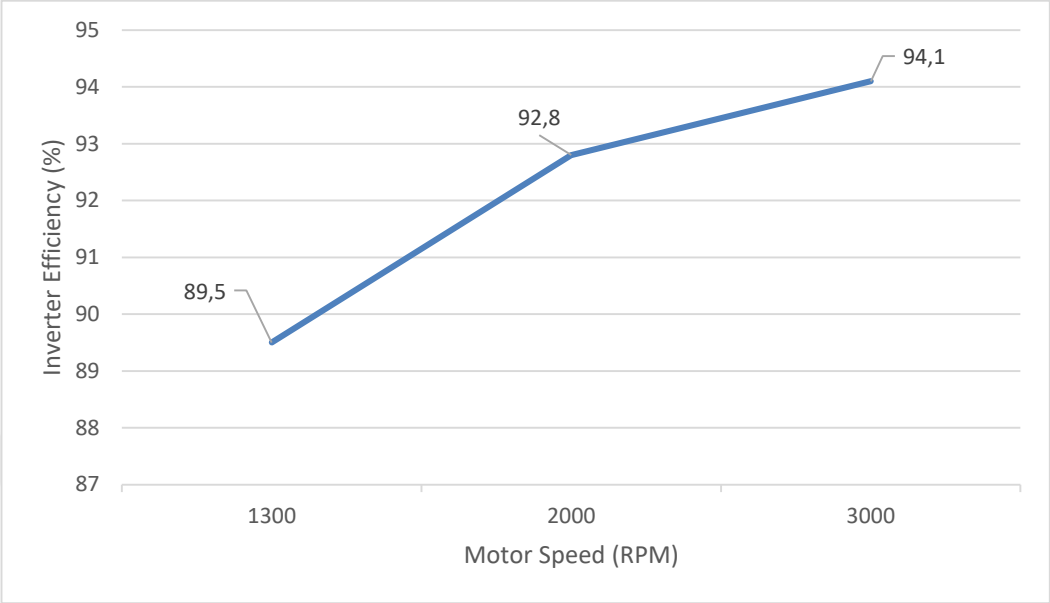

Figure 9.31: Inverter efficiency @12kHz switching frequency @different speeds.

The comparison of the efficiency between 6kHz and 12kHz at different speeds is given in Figure 9.32. As expected, there is some decrease in inverter efficiency at all speeds especially at low speed. However, system efficiency should be analyzed in order to determine the benefit of an increase of switching frequency. These may be a future study as a continuation of the thesis.

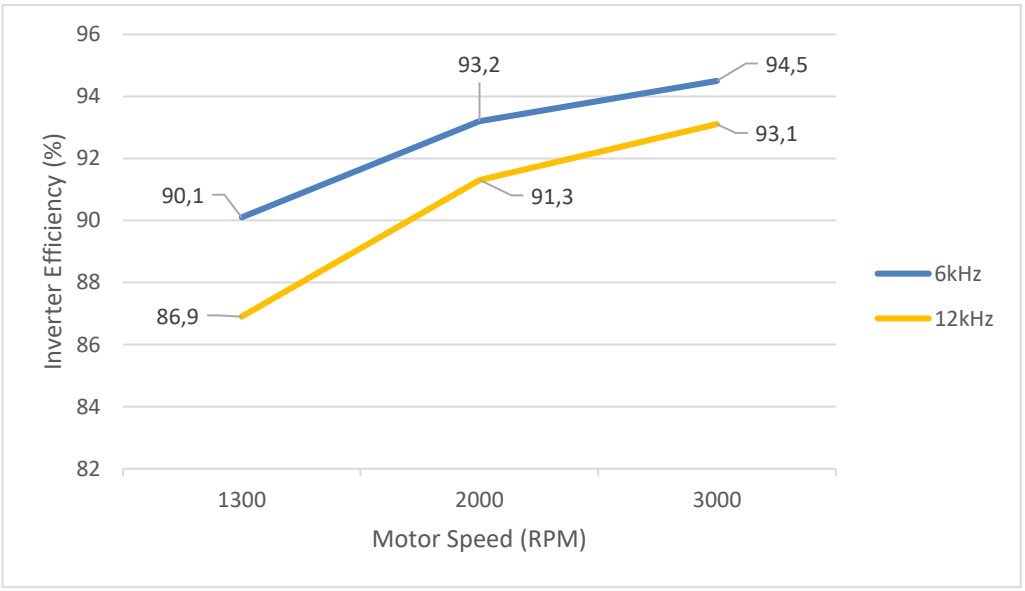

Figure 9.32: Comparison of the efficiency between 6kHz and 12kHz @different speeds.

10. CONCLUSION

In this thesis, the inverter driver board for a PMSM which is used in refrigerator compressor system is designed and carried out with sensorless field oriented control algorithm. Before starting the inverter board design, literature review, PMSM, dynamic model of a motor and sensorless field oriented control are studied in detail to collect useful information as the design inputs. Hardware is divided into subcircuit blocks to build the system architecture. After construction, each circuit block is designed component by component considering electrical requirements. Simulation is also given in the PSIM simulation tool. In the simulation, motor phase currents are directly derived from the phases and the sensored starting algorithm is applied. Aligning sequence at the starting is not required for the simulation. However, in the real case, starting should include the aligning sequence in order to obtain a smooth starting and not lose control. In the simulation, the maximum torque is applied during the starting until the real speed is equal to the reference speed. After that, the algorithm is switched to the conventional FOC algorithm. On the other hand, in the implementation, the open loop control is applied after the aligning sequence since there is no sufficient Back-EMF signal for the sensorless algorithm. When a pre-determined speed which is approximately 700 rpm in this inverter board is reached, the algorithm is switched to the closed loop control. Sensorless field oriented control algorithm is implemented to the inverter board and the board is successfully operated. Important voltage, current and control signal measurements are taken from the inverter board connected to the compressor setup. Efficiency values at different speeds are also measured. It is seen that this value has the tendency to increase as rotor speed increases and efficiency value reaches 94.5% at full load. Due to the nature of the compressor, the load torque pattern of the system is not constant regarding the angular position. The maximum torque value can reach 6-7 times higher than the average torque value. It can even be negative in a short range. This condition may cause phase current distortion in the system. In addition to that, compressor setup also causes phase current distortion, especially at high speed. Because this setup has an open loop environment

that exhibits uncontrolled gas flow in the compressor system. In order to evaluate phase current distortion, the switching frequency is increased from 6kHz to 12kHz. Spectrum analysis is conducted to compare the results and it is seen that increase of the switching frequency decreases the total harmonic distortion of the phase current for all operating speeds. The reason of the improvement is that, the torque producing current which is the quadrature current is more tightly controlled due to the doubling of the switching frequency. Doubling of the switching frequency means control frequency is also doubled. On the other hand, this also causes additional switching losses in the IPM and the overall efficiency of the inverter board decreases at each speed especially at low speed due to these losses. However, system efficiency consisting of inverter board, a PMSM and compressor parts should be analyzed in order to determine the benefit of an increase of switching frequency. The human sense of hearing is higher at lower frequencies. Therefore, acoustic noise reduction on the inverter driver board and the motor can be also investigated due to the doubling of the switching frequency. Torque and dead time compensations for reduction of the distortion can also be a future study on the software side. Usage of the wide band gap devices in the inverter stage and their benefit on the efficiency can be given as an example on the hardware side as a continuation of the thesis.

REFERENCES

[1] **Cahill, D. P. M., and Adkins, B.** (1962). The Permanent Magnet Synchronous Motor, *IEEE,* vol. 109, no. 48, pp. 483-491.

[2] **Slemon, G. R.** (1971). Analytical Models for Saturated Synchronous Machines, *IEEE,* vol. 90, no. 2, pp. 409-417.

[3] **Rahman, M. A.** (1979). High Efficiency Permanent Magnet Synchronous Motors, in *IAS Annual Meeting.*

[4] **Richter, E. (1979).** Power Density Considerations for Permanent Magnet Machines, *Electric Machines & Power Systems,* vol. 4, no. 1, pp. 21-32.

[5] **Honsinger, V. B.** (1980). Performance of Polyphase Permanent Magnet Machines, *IEEE,* vol. 99, no. 4, pp. 1510-1518.

[6] **Miller, T. J. E.** (1981). Transient Performance of Permanent Magnet Machines, in *IAS Annual Meeting*.

[7] **Rahman, M. A., Little, T. A., and Dash, P. K.** (1981). Computer Simulation of the Dynamic Performance of Permanent Magnet Synchronous Motors, in *IAS Annual Meeting.*

[8] **Slemon, G. R., and Gumaste, A. V.** (1981). Steady State Analysis of a Permanent Magnet Synchronous Motor Drive with Current Source Inverter, in *IAS Annual Meeting.*

[9] **Weschta, A.** (1982). Design Considerations and Performance of Brushless Permanent Magnet Servo Motors, in *IAS Annual Meeting.*

[10] **Pfaff, G., Weschta, A., and Wick, A.** (1982). Design and Experimental Results of a Brushless AC Servo Drive, in *IAS Annual Meeting.*

[11] **Takeda, Y., Morimoto, S., and Hirasi, T.** (1983). Generalized Analysis of Steady State Characteristics of DC Commutatorless Motors, *IEEE,* vol. 130, no. 6, pp. 373-380.

[12] **Binns, K. J., and Wong, T. M.** (1984). Analysis and Performance of a High-Field Permanent Magnet Synchronous Machine, *IEEE,* vol. 131, no. 6, pp. 252-257.

[13] **Richter, E., Miller, T. J. E., and Neumann, T. W.** (1984). The Ferrite Permanent Magnet AC Motor – A Technical and Economic Assessment, in *IAS Annual Meeting*.

[14] **Chalmers, B. J., Hamed, S. A., and Baines, G. D.** (1985). Parameters and Performance of a High Field Permanent Magnet Synchronous Motor for Variable Frequency Operation, *IEEE,* vol. 132, no. 3, pp. 117-124.

[15] **Neumann, T. W., and Tompkins, R. E.** (1985). Line Start Motor Designed With Ne-Fe-B Permanent Magnets, in *8th Intl. Workshop on Rare Earth Magnets and Their Applications*, Ohio.

[16] **Enjeti, P., Lindsay, J. F., and Rashid, M. H.** (1985). Parameter Estimation and Dynamic Performance of Permanent Magnet Synchronous Motors, in *IAS Annual Meeting*.

[17] **Lajoie-Mazenc, M., Villaneuva, C., and Hector, J.** (1985). Study and Implementation of Hysteresis Controlled Inverter on a Permanent Magnet Synchronous Machine, *IEEE, Transactions on Energy Conversion*, vol. 21, no. 2, pp. 408-413.

[18] **Rahman, M. A., and Osheiba, A. M.** (1986). Effect of Parameter Variations on the Performance of Permanent Magnet Motors, in *IAS Annual Meeting*.

[19] **Sebastian, T., Slemon, G. R., and Rahman, M. A.** (1986). Modelling of Permanent Magnet Synchronous Motors, *IEEE*, vol. 22, no. 9, pp. 1069-1086.

[20] **Pillay, P., and Krishnan, R.** (1987). Application Characteristics of Permanent Magnet Synchronous and Brushless DC motors for Servo Drives, in *IAS Annual Meeting*, Atlanta.

[21] **Krause, P., Nucera, R., Krefta, R., and Waynczuk, O.** (1987). Analysis of a Permanent Magnet Synchronous Machine Supplied from a 180 Degrees Inverter with Phase Control, *IEEE, Transactions on Energy Conversion*, vol. 2, no. 3, pp. 423-431.

[22] **Pillay, P., and Krishnan, R.** (1987). Modeling Analysis and Simulation of a High Performance, Vector Controlled Permanent Magnet Synchronous Motor Drive, in *IAS Annual Meeting*, Atlanta.

[23] **Bose, B. K.** (1987). A High Performance Inverter-Fed Drive System of an Interior Permanent Magnet Synchronous Machine, in *IAS Annual Meeting*, Atlanta.

[24] **Demerdash, N. A., Hijazi, T. M., and Arkadan, A. A.** (1988). Computation of Winding Inductance of Permanent Magnet Brushless DC Motors with Damper Windings by Energy Perturbation, *IEEE, Transactions on Energy Conversion*, vol. 3, no. 3, pp. 705-713.

[25] **Hijazi, T. M., and Demerdash, N. A.** (1988). The Impact of the Addition of a Rotor-Mounted Damper Bar Cage on the Performance of a Samarium-Cobalt Permanent Magnet Brushless DC Motor System, *IEEE, Transactions on Energy Conversion*, vol. 3, no. 4, pp. 890-898.

[26] **Pillay, P., and Krishnan, R.** (1988). Development of Digital Models for a Vector Controlled Permanent Magnet Synchronous Motor Drive, in *IAS Annual Meeting*.

[27] **Colby, R.** (1988). Classification of Inverter Driven Permanent Magnet Synchronous Motors, in *IAS Annual Meeting*.

[28] **Schiferl, R., and Lipo, T. A.** (1988). Power Capability of Salient Pole Permanent Magnet Synchronous Motors in Variable Speed Drive Applications, in *IAS Annual Meeting*.

[29] **Zeid, S. M.** (1998). An Analysis of Permanent Magnet Synchronous Motor Drive.

[30] **Bolognani, S., Oboe, R., and Ziglitto, M.** (1999). Sensorless Full-Digital PMSM Drive with EKF Estimation of Speed and Rotor Position, *IEEE, Transactions on Energy Conversion*, vol. 46, no. 1.

[31] **Jin, K. C., Yong, H. W., and Goo, L. C.** (2001). Speed Control of PMSM Using a Robust Adaptive Controller, *IEEE, Proceedings of the 40th SICE Annual Conference, International Session Papers*.

[32] **Hwang, J. S., Kim, K. H., Kim, Y. T., and Baek, S. M.** (2001). Parameter Optimization of Field Oriented Control with 6 Sigma Tool, *IEEE, International Symposium on Industrial Electronics Proceedings, Conference Paper,* vol. 3.

[33] **Perera, P. D. C., Petersen, J. K., Blaabjerg, F., and Thøgersen, P.** (2003). A Sensorless, Stable V=f Control Method for Permanent Magnet Synchronous Motor Drives, *IEEE, Transactions on Industry Applications,* vol. 39.

[34] **Sun, P., Shi, X., Wang, A., and Wang, Y.** (2005). DSP and CPLD Based Field Oriented Control of PMSM Using Application Specific IPM, *IEEE, International Conference on Electrical Machines and Systems,* vol. 1.

[35] **Jiang, F., Zhang, W., Liang, W., and Liu, X. (2005).** A MC56F8357 Based Permanent Magnet Synchronous Motor (PMSM) Servo System, *IEEE, International Conference on Electrical Machines and Systems,* vol. 2.

[36] **Zhou, F., Li, B., Yang, J., and Yan, R.** (2007). A Sliding Model Speed/Position Observer Integrated with a PI Controller for PM Synchronous Motors, *IEEE, International Conference on Robotics and Biomimetics (ROBIO), Conference Paper*.

[37] **Song, K., Liu, W., and Luo, G.** (2008). Permanent Magnet Synchronous Motor Field Oriented Control and HIL Simulation, *IEEE, Vehicle Power and Propulsion Conference, Conference Paper*.

[38] **Simanek, J., Novak, J., Cerny, O., and Dolecek, R.** (2008). FOC and Flux Weakening for Traction Drive with Permanent Magnet Synchronous Motor, *IEEE, International Symposium on Industrial Electronics, Conference Paper*.

[39] **Zhang, Z., and Feng, J.** (2008). Sensorless Control of Salient PMSM with EKF of Speed and Rotor Position, *IEEE, International Conference on Electrical Machines and Systems, Conference Paper*.

[40] **Accetta, A., Cirrincione, M., Pucci, M., and Vitale, G.** (2009). PMSM Drives Sensorless Position Control with Signal Injection and Neural Filtering, *IEEE, International Electric Machines and Drives Conference, Conference Paper*.

[41] **El-Sousy, F. F. M.** (2010). Hybrid H∞-Based Wavelet-Neural-Network Tracking Control for Permanent-Magnet Synchronous Motor Servo Drives, *IEEE, Transactions on Industrial Electronics, Journal Article,* vol. 57.

[42] **Rahimi, M., Abbaszadeh, K., and Radan, A.** (2010). Torque Ripple Suppression of Surface Mounted Permanent Magnet Synchronous Motor Using Harmonic Injected Currents, *IEEE, 1st Power Electronic & Drive Systems & Technologies Conference (PEDSTC), Conference Paper*.

[43] **Kangkang, Z., Jianqiu, L., Minggao, O., Jing, G., and Yan, M.** (2011). Electric Braking Performance Analysis of PMSM for Electric Vehicle Applications, *IEEE, Proceedings of International Conference on Electronic & Mechanical Engineering and Information Technology, Conference Paper,* vol. 5.

[44] **Wang, T., Guo, Y., Zhu, J., and Zhang, Y.** (2012). An Assessment of the Influence of Sampling Frequency on Steady-State Performance of PMSM Drive System, *IEEE, 22nd Australasian Universities Power Engineering Conference (AUPEC), Conference Paper*.

[45] **Wang, W., Li, Z., and Xu, X.** (2014). A Novel Smooth Transition Strategy for BEMF-Based Sensorless Drive Startup of PMSM, *IEEE, Proceeding of the 11th World Congress on Intelligent Control and Automation, Conference Paper*.

[46] **Savadkoohi, H. K., Khaburi, D. A., and Sadr, S.** (2015). A New Switching Method for PWM Inverter with Uniform Distribution of Output Current's Spectrum, *IEEE, The 6th Power Electronics, Drive Systems & Technologies Conference (PEDSTC), Conference Paper*.

[47] **Kung, Y. S., and Risfendra.** (2016). ModelSim/Simulink Co-Simulation of a Sensorless Control for PMSM Drives Based on I-F Startup and EKF, *International Conference on Applied System Innovation (ICASI), Conference Paper*.

[48] **Tau, J. H., and Tzou, Y. Y.** (2017). PFC Control of Electrolytic Capacitor-less PMSM Drives for Home Appliances, *IEEE, 26th International Symposium on Industrial Electronics (ISIE), Conference Paper*.

[49] **Li, Y., Zhang, P., Hang, J., Ding, S., Liu, L., and Wang, Q.** (2018). Comparison of Dynamic Characteristics of Field Oriented Control and Model Predictive Control for Permanent Magnet Synchronous Motor, *IEEE, 13th Conference on Industrial Electronics and Applications (ICIEA), Conference Paper*.

[50] **Chethan, G. N., and Kumaran, G. K.** (2019). Performance Analysis of PMSM Drive with SpaceVector PWM and Sinusoidal PWM fed VSI, in *International Conference on Power Electronics Applications and Technology in Present Energy Scenario (PETPES)*.

[51] **Nicola, M., Nicola, C. I., and Duta, M.** (2020). Sensorless Control of PMSM using FOC Strategy Based on Multiple ANN and Load Torque Observer, in *International Conference on Development and Application Systems (DAS)*, Suceava.

[52] **Zuluaga, C. C., Riba, J. R., and Garcia, A.** (2021). PMSM Parameter Estimation for Sensorless FOC Based on Differential Power Factor, *IEEE Transactions on Instrumentation and Measurement*, vol. 70, pp. 1-12.

[53] **Tian, B., Molinas, M., An, Q., Zhou, B., and Wei, J.** (2022). Freewheeling Current-Based Sensorless Field-Oriented Control of Five-Phase Permanent Magnet Synchronous Motors Under Insulated Gate Bipolar Transistor Failures of a Single Phase, *IEEE Transactions on Industrial Electronics*, vol. 69, no. 1, pp. 213-224, Jan.

[54] **Wilamowski, B. M., and Irwin, J. D.** (2017). Power Electronics and Motor Drives, 2nd ed., R. C. Dorf, Ed., London: CRC Press, pp. 162-164.

[55] **Cirrincione, M., Pucci, M., and Vitale, G.** (2012). Power Converters and AC Electrical Drives with Linear Neural Networks, 1st ed., A. Emadi, Ed., London: CRC Press, pp. 322-323.

[56] **Gieras, J. F.** (2010). Permanent Magnet Motor Technology, Design and Applications, 3rd ed., London: CRC Press, pp. 170-198.

[57] **Krishnan, R.** (2010). Permanent Magnet Synchronous and Brushless DC Motor Drives, 1st ed., London: CRC Press, pp. 31-276.

[58] **Krause, P., Wasynczuk, O., Sudhoff, S., and Pekarek, S.** (2013). Analysis of Electric Machinery and Drive Systems, 3rd ed., New Jersey: Wiley, pp. 121-140.

[59] **Nam, K. H.** (2010). AC Motor Control and Electric Vehicle Applications, 1st ed., London: CRC Press, pp. 133-157.

[60] **Abad, G.** (2017). Power Electronics and Electric Drives for Traction Applications, 1st ed., Wiley, pp. 100-146.

[61] **Url-1** <*https://www.infineon.com/dgdl/ap0809010_Sensorless_FOC_XC878.pdf?fileId=db3a304320896aa20120d245735250c3*>, date retrieved 14.12.2020.

[62] **Url-2**<*https://ww1.microchip.com/downloads/en/appnotes/01078b.pdf*>, date retrieved 14.12.2020.

[63] **Url-3**<*https://www.microchip.com/content/dam/mchp/documents/parked-documents/BLDC%20MC%2000957a.pdf*>, date retrieved 14.12.2020.

[64] Hayes, J. G., and Goodarzi, G. A. (2018). Electric Powertrain, 1st ed., Wiley, pp. 276-295.

[65] **Url-4**<*http://ww1.microchip.com/downloads/en/DeviceDoc/TB3220-Sensorless-Field-Oriented-Control-of-PMSM-for-Appliances-DS90003220A.pdf*>, date retrieved 14.12.2020.

[66] **Manias, S. N.** (2017). Power Electronics and Motor Drive Systems, L. Reading, Ed., London: Academic Press, pp. 938-956.

[67] **Url-5**<*https://www.cypress.com/file/157806/download*>, date retrieved 14.12.2020.

[68] **Glumineau, A., and Morales, J. L.** (2015). Sensorless AC Electric Motor Control, 1st ed., M. J. Grimble and M. A. Johnson, Eds., Springer, pp. 1-44.

[69] **Url-6** <*https://www.ti.com/lit/an/spra494/spra494.pdf?ts=1635862166046&ref_url=https%253A%252F%252Fwww.google.com%252F*>, date retrieved 14.12.2020.

[70] **Vodovozov, V., and Vinnikov, D.** (2008). Electric Sysyems of Motor Drive, M. A. Laane, Ed., Tallinn: RAK, pp. 137-142.

[71] **Url-7**<*http://ww1.microchip.com/downloads/en/appnotes/01017a.pdf*>, date retrieved 14.12.2020.

[72] **Xia, C. L.** (2012). Permanent Magnet Brushless DC Motor Drives and Controls, 1st ed., Wiley, pp. 167-206.

[73] **Bose, B.** (2006). Power Electronics and Motor Drives, 1st ed., Tennessee: Academic Press, pp. 477-579.

[74] **Url-8**<*https://www.tdk-electronics.tdk.com/inf/70/db/var/SIOV_Leaded_StandarD.pdf?ref_disty=digikey*>, date retrieved 14.12.2020.

[75] **Url-9** <*https://media.digikey.com/pdf/Data%20Sheets/Epcos%20PDFs/B57234S0xxxM000.pdf*>, date retrieved 14.12.2020.

[76] **Url-10**<*http://www.powerint.cn/sites/default/files/documents/an53.pdf*>, date retrieved 14.12.2020.

[77] **Url-11**<*https://e2e.ti.com/blogs_/b/powerhouse/posts/a-review-of-emi-standards-part-1-conducted-emissions*>, date retrieved 14.12.2020.

[78] **Url-12**<*https://www.electricaltechnology.org/2018/08/electrical-shock-hazards-its-effects-on-human-body.html*>, date retrieved 14.12.2020.

[79] **Rashid, M. H.** (2018). Power Electronics Handbook, 4th ed., L. Reading, Ed., Florida: Butterworth-Heinemann, pp. 1381-1397.

[80] **Url-13**<*https://cdn.ozdisan.com/ETicaret_Dosya/39288_9207465.pdf*>, date retrieved 14.12.2020.

[81] **Url-14**<*https://www.vishay.com/docs/88616/gbu8a.pdf*>, date retrieved 20.10.2021.

[82] **Url-15**<*https://www.power.com/sites/default/files/product-docs/lnk302_304-306.pdf*>, date retrieved 14.12.2020.

[83] **Emadi, A., Khaligh, A., Nie, Z., and Lee, Y. J.** (2009). Integrated Power Electronic Converters and Digital Control, 1st ed., M. H. Rashid, Ed., Florida: CRC Press, pp. 1-8.

[84] **Url-16**<*https://octopart.com/blog/archives/2017/08/how-to-select-voltage-regulator*>, date retrieved 14.12.2020.

[85] **Brown, M.** (2007). Power Sources and Supplies: World Class Designs, 1st ed., Newnes, pp. 1-13.

[86] **Cordell, B.** (2011). Designing Audio Power Amplifiers, 1st ed., The McGraw-Hill, pp. 79-95.

[87] **Url-17** <*https://www.mitsubishielectric.com/semiconductors/content/product/powermodule/dipipm/slimdip/slimdip-l_e.pdf*>, date retrieved 20.10.2021.

[88] **Perret, R.** (2009). Power Electronics Semiconductor Devices, 1st ed., London: Wiley, pp. 57-130.

[89] **Url-18**<*https://www.farnell.com/datasheets/73758.pdf*>, date retrieved 14.12.2020.

[90] **Url-19**<*https://www.renesas.com/eu/en/document/apn/sensorless-vector-control-three-phase-permanent-magnet-synchronous-motors?language=en*>, date retrieved 12.02.2022.

[91] **Url-20**<*https://www.eeweb.com/wp-content/uploads/articles-app-notes-files-design-and-application-guide-of-bootstrap-circuit-for-high-voltage-gate-drive-ic.pdf*>, date retrieved 12.02.2022.

[92] **Dianov, A.** (2020). Estimation of the Mechanical Position of Reciprocating Compressor for Silent Stoppage, *IEEE Open Journal of Power Electronics*, vol. 1, pp. 64-73.

[93] **Url-21**<*https://blog.programmablepower.com/blog/know-your-power-supply-jargon-ripple*>, date retrieved 12.02.2022.

APPENDICES

APPENDIX A: GBU8J - Bridge Diode Datasheet

APPENDIX B: 470uF 400V - Bus Capacitor Datasheet

APPENDIX C: SLIMDIP-L - IPM Datasheet

APPENDIX D: LNK304 - SMPS IC Datasheet

APPENDIX E: NCP1117 - LDO Datasheet

APPENDIX F: LMV321 - Op-Amp Datasheet

APPENDIX G: RX13T - MCU Datasheet

APPENDIX H: PC817A - Optocoupler Datasheet

APPENDIX A

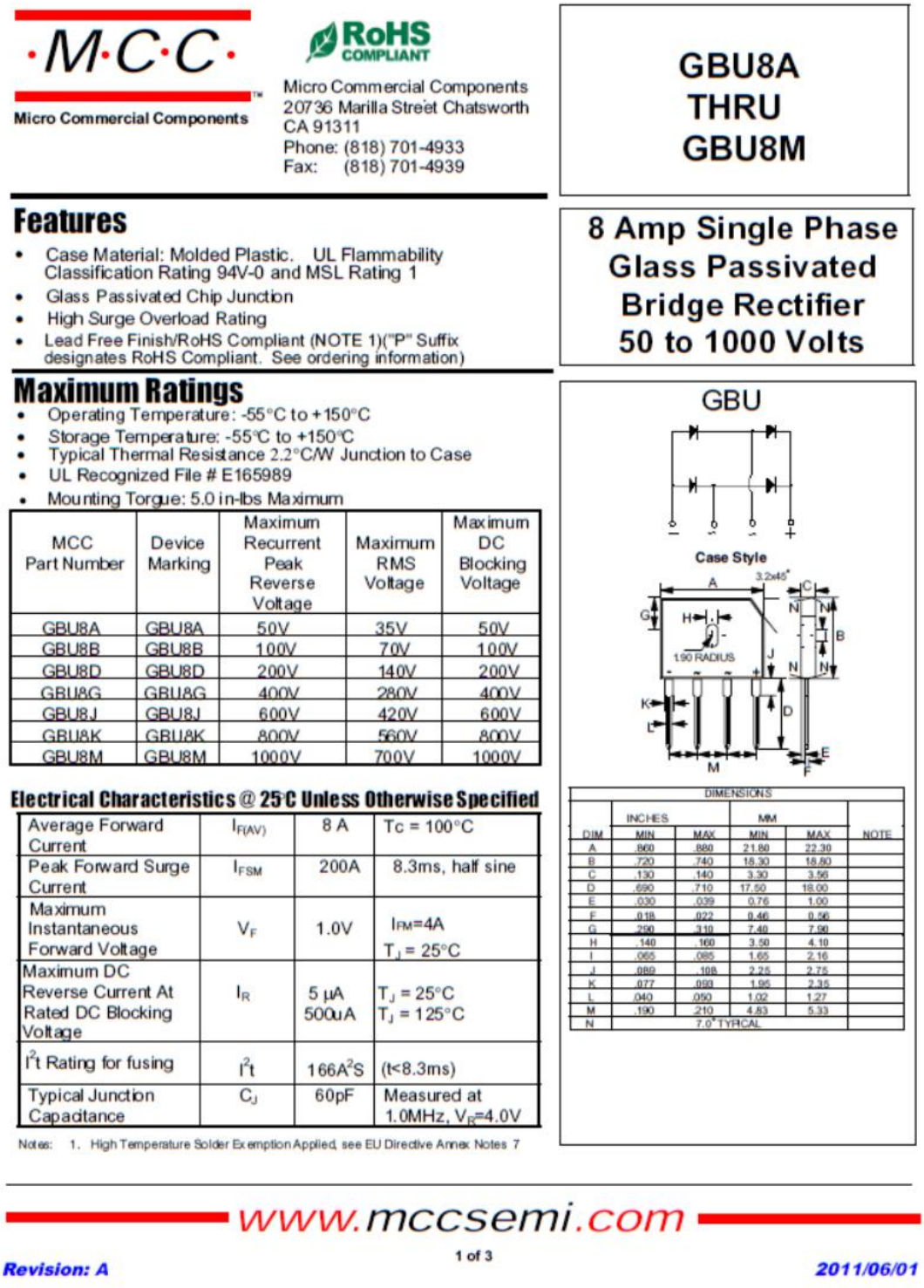

·M·C·C·

Micro Commercial Components

RoHS COMPLIANT

Micro Commercial Components
20736 Marilla Street Chatsworth
CA 91311
Phone: (818) 701-4933
Fax: (818) 701-4939

GBU8A THRU GBU8M

8 Amp Single Phase Glass Passivated Bridge Rectifier 50 to 1000 Volts

Features

- Case Material: Molded Plastic. UL Flammability Classification Rating 94V-0 and MSL Rating 1
- Glass Passivated Chip Junction
- High Surge Overload Rating
- Lead Free Finish/RoHS Compliant (NOTE 1)("P" Suffix designates RoHS Compliant. See ordering information)

Maximum Ratings

- Operating Temperature: -55°C to +150°C
- Storage Temperature: -55°C to +150°C
- Typical Thermal Resistance 2.2°C/W Junction to Case
- UL Recognized File # E165989
- Mounting Torque: 5.0 in-lbs Maximum

MCC Part Number	Device Marking	Maximum Recurrent Peak Reverse Voltage	Maximum RMS Voltage	Maximum DC Blocking Voltage
GBU8A	GBU8A	50V	35V	50V
GBU8B	GBU8B	100V	70V	100V
GBU8D	GBU8D	200V	140V	200V
GBU8G	GBU8G	400V	280V	400V
GBU8J	GBU8J	600V	420V	600V
GBU8K	GBU8K	800V	560V	800V
GBU8M	GBU8M	1000V	700V	1000V

Electrical Characteristics @ 25°C Unless Otherwise Specified

Average Forward Current	$I_{F(AV)}$	8 A	Tc = 100°C
Peak Forward Surge Current	I_{FSM}	200A	8.3ms, half sine
Maximum Instantaneous Forward Voltage	V_F	1.0V	I_{FM}=4A T_J = 25°C
Maximum DC Reverse Current At Rated DC Blocking Voltage	I_R	5 µA 500uA	T_J = 25°C T_J = 125°C
I^2t Rating for fusing	I^2t	166A^2S	(t<8.3ms)
Typical Junction Capacitance	C_J	60pF	Measured at 1.0MHz, V_R=4.0V

Notes: 1. High Temperature Solder Exemption Applied, see EU Directive Annex Notes 7

GBU

Case Style

DIM	INCHES MIN	INCHES MAX	MM MIN	MM MAX	NOTE
A	.860	.880	21.80	22.30	
B	.720	.740	18.30	18.80	
C	.130	.140	3.30	3.56	
D	.690	.710	17.50	18.00	
E	.030	.039	0.76	1.00	
F	.018	.022	0.46	0.56	
G	.290	.310	7.40	7.90	
H	.140	.160	3.50	4.10	
I	.065	.085	1.65	2.16	
J	.089	.108	2.25	2.75	
K	.077	.093	1.95	2.35	
L	.040	.050	1.02	1.27	
M	.190	.210	4.83	5.33	
N	7.0° TYPICAL				

www.mccsemi.com

Revision: A

2011/06/01

Figure A. 1: GBU8J - Bridge Diode Datasheet – 1.

GBU8A thru GBU8M

Micro Commercial Components

FIG.1 - FORWARD CURRENT DERATING CURVE

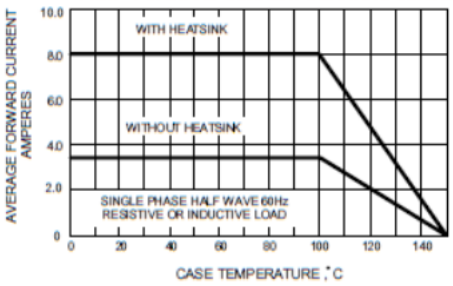

FIG.2 - MAXIMUM NON-REPETITIVE SURGE CURRENT

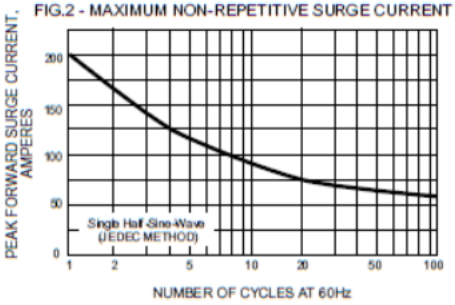

FIG.3 - TYPICAL JUNCTION CAPACITANCE

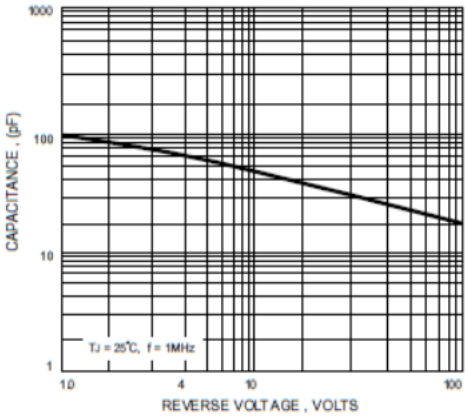

FIG.4 - TYPICAL FORWARD CHARACTERISTICS

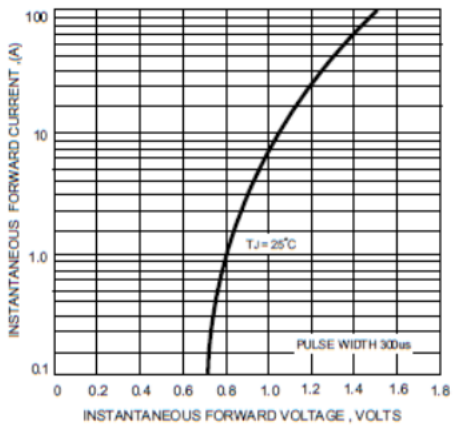

FIG.5 - TYPICAL REVERSE CHARACTERISTICS

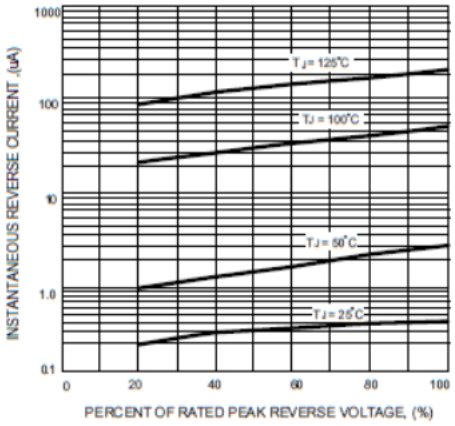

Figure A. 2: GBU8J - Bridge Diode Datasheet – 2.

APPENDIX B

1. Scope

This specification is for aluminum electrolytic capacitors.

2. Applicable standards

KS C IEC 60384-4, except as specified in this specification

3. Operating temperature range

Rated voltage (VDC)	WV< 350	WV ≥ 350
Temperature range (℃)	-40~+85	-25~+85

4. Dimensions

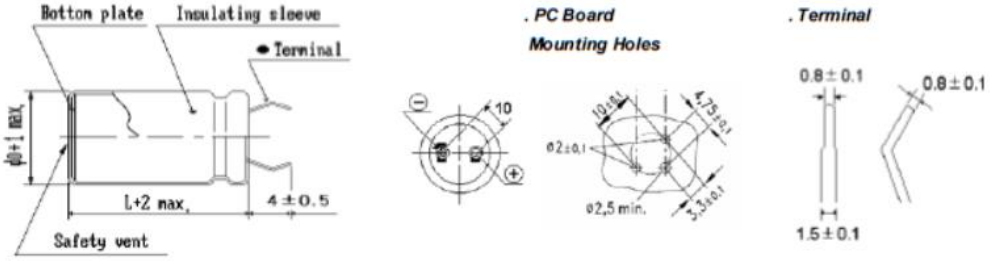

For dimensions of ΦD & L, refer to the table 1.

5. Marking

. SAMWHA trade mark
. Series identification
. Rated voltage . Capacitance
. Maximum operating Temperature
. Capacitance tolerance
. Polarity & date code
. Sleeve color : Dark green
. Print color : Silver

Table 1.

6.1 Rated Voltage (VDC)	6.2 Cap. (μF)	4. Dimensions ΦD (mm)	4. Dimensions L (mm)	6.3 tanδ	6.4 ESR (Ω)	6.5 Leakage Current (μA)	6.6 Ripple Current (A rms)	6.7 Surge Voltage (VDC)	SAMWHA PART No.
400	470	30	40	0.20	0.56	1300.8	2.51	450	HJ 2G 477 M 30040 HR

Figure B. 1: 470uF 400V - Bus Capacitor Datasheet - 1.

6. Performance

Test environmental conditions

- Ambient temperature : 25±2℃ / Relative humidity : 60~70% / Air pressure : 86~106kPa

No.	Item	Test condition	Specification
6.1	Rated voltage		**See table 1**
6.2	Capacitance (Tolerance)	. Measuring frequency : 120Hz±20% . Measuring voltage : 0.5Vrms or less . DC bias voltage : +1.5~2.0VDC . Measurement circuit : Equivalent series circuit	**See table 1** (M : ±20%)
6.3	tanδ	. Measurement shall be made under the same conditions as those given for the measurement of capacitance.	**See table 1**
6.4	ESR	. ESR can be obtained from the following formula. $ESR = \frac{\tan\delta}{2\pi fC}$ f : 120Hz C: capacitance (F)	**See table 1**
6.5	Leakage Current	The rated voltage shall be applied across the capacitor through a 1000±10Ω protective resistor. The leakage current shall be measured after an electrification period of 5 minutes.	**See table 1**
6.6	Maximum Permissible Ripple current	. Temperature : 85℃ . Ripple : rms value of 120Hz sine wave AC (The sum of DC voltage and peak voltage shall not exceed the rated voltage.)	**See table 1**

● RIPPLE GUARANTEE COEFFICIENT BY TEMPERATURE

TEMP(℃)	60℃	70℃	85℃
Ripple Factor	1.40	1.23	1.00

● FREQUENCY COEFFICIENT OF PERMISSIBLE RIPPLE CURRENT

WV \ Frequency(Hz)	50Hz	120Hz	300Hz	1kHz	10kHz~
400	0.85	1.00	1.15	1.20	1.40

6.7	Surge voltage	. Applied voltage : **See table 1** . Temperature : 15~35℃ . Duration of charge : 30±5 seconds . Duration of discharge: 5 minutes 30 seconds . Cycles : 1000 times	. No visible damage . Leakage current ≤ initial specified value . Capacitance change within ±15% of initial value . tanδ≤initial specified value
6.8	Solderability	. Solder : HSE-02 SR-34 . Flux : 25% by weight of rosin in ethanol . Solder temperature : 250±5℃ . Immersion depth : 2.0mm . Immersion time : 10±0.5 sec. . Immersion speed : 25±2.5 mm/sec.	. 3/4 of the circumference of the surface up to the immersed shall be covered with new solder.

Figure B. 2: 470uF 400V - Bus Capacitor Datasheet - 2.

APPENDIX C

MITSUBISHI ELECTRIC

< DIPIPM >

SLIMDIP-L

TRANSFER MOLDING TYPE
INSULATED TYPE

OUTLINE

Normal terminal type

MAIN FUNCTION AND RATINGS

- RC-IGBT inverter bridge for three phase DC-to-AC power conversion
- Built-in bootstrap diodes with current limiting resistor
- Open emitter type

APPLICATION

- AC 100~240V (DC voltage:400V or below) three phase low power motor inverter drive

TERMINAL LINE UP

Terminal	Part number	Suffix
Normal terminal	SLIMDIP-L	500
Short terminal	SLIMDIP-L	505

INTEGRATED DRIVE, PROTECTION AND SYSTEM CONTROL FUNCTIONS

- For P-side : Drive circuit, High voltage high-speed level shifting, Control supply under-voltage protection (UV)
- For N-side : Drive circuit, Control supply under-voltage protection (UV), Short circuit protection (SC), Over temperature protection (OT)
- Fault signaling : Corresponding to SC fault (N-side IGBT), UV fault (N-side supply) and OT fault
- Temperature monitoring : Outputting LVIC temperature by analog signal
- Input interface : Schmitt-triggered 3V, 5V input compatible, high active logic.
- UL Recognized : UL1557 File E323585

INTERNAL CIRCUIT

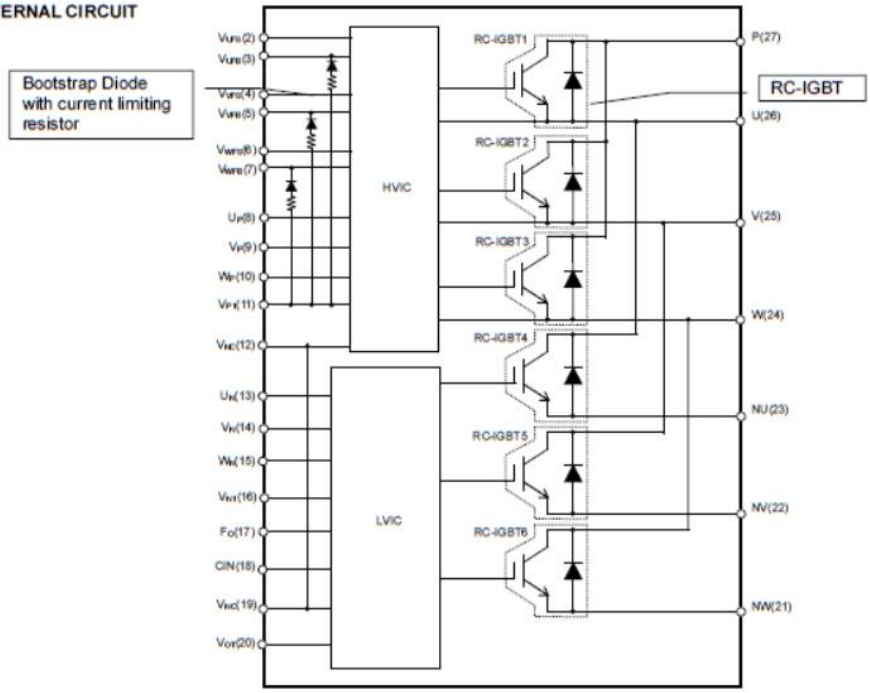

Publication Date : January 2021

MITSUBISHI ELECTRIC CORPORATION

1

Figure C. 1: SLIMDIP-L - IPM Datasheet - 1.

< DIPIPM >

SLIMDIP-L

TRANSFER MOLDING TYPE
INSULATED TYPE

MAXIMUM RATINGS (T_j = 25°C, unless otherwise noted)

INVERTER PART

Symbol	Parameter	Condition	Ratings	Unit
V_{CC}	Supply voltage	Applied between P-NU,NV,NW	450	V
$V_{CC(surge)}$	Supply voltage (surge)	Applied between P-NU,NV,NW	500	V
V_{CES}	Collector-emitter voltage		600	V
$\pm I_C$	Each IGBT collector current	T_C= 25°C (Note 1)	15	A
$\pm I_{CP}$	Each IGBT collector current (peak)	T_C= 25°C, less than 1ms	30	A
T_j	Junction temperature	(Note 2)	-30~+150	°C

Note1: Pulse width and period are limited due to junction temperature.

CONTROL (PROTECTION) PART

Symbol	Parameter	Condition	Ratings	Unit
V_D	Control supply voltage	Applied between V_{P1}-V_{NC}, V_{N1}-V_{NC}	20	V
V_{DB}	Control supply voltage	Applied between V_{UFB}-V_{UFS}, V_{VFB}-V_{VFS}, V_{WFB}-V_{WFS}	20	V
V_{IN}	Input voltage	Applied between U_P, V_P, W_P, U_N, V_N, W_N-V_{NC}	-0.5~V_D+0.5	V
V_{FO}	Fault output supply voltage	Applied between F_O-V_{NC}	-0.5~V_D+0.5	V
I_{FO}	Fault output current	Sink current at F_O terminal	1	mA
V_{SC}	Current sensing input voltage	Applied between CIN-V_{NC}	-0.5~V_D+0.5	V

TOTAL SYSTEM

Symbol	Parameter	Condition	Ratings	Unit
$V_{CC(PROT)}$	Self protection supply voltage limit (Short circuit protection capability)	V_D = 13.5~16.5V, Inverter Part T_j = 125°C, non-repetitive, less than 2μs	400	V
T_C	Module case operation temperature	Measurement point of Tc is described in Fig.1 (Note2)	-30~+115	°C
T_{stg}	Storage temperature		-40~+125	°C
V_{iso}	Isolation voltage	60Hz, Sinusoidal, AC 1min, between connected all pins and heat sink plate	2000	V_{rms}

Note2 T_C MEASUREMENT POINT

Fig. 1

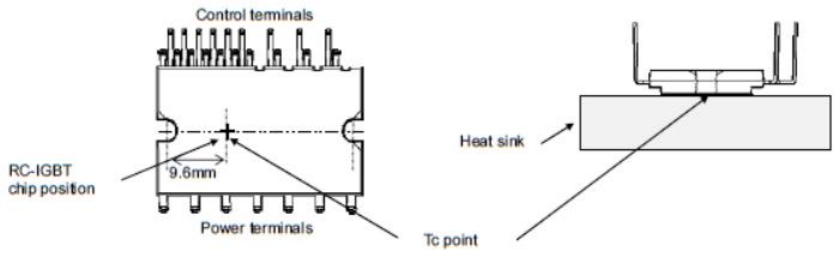

THERMAL RESISTANCE

Symbol	Parameter	Condition	Limits			Unit
			Min.	Typ.	Max.	
$R_{th(j-c)Q}$	Junction to case thermal resistance (Note 3)	Inverter RC-IGBT part (per 1/6 module)	-	-	4.0	K/W

Note 3: Grease with good thermal conductivity and long-term endurance should be applied evenly with about +100μm~+200μm on the contacting surface of DIPIPM and heat sink. The contacting thermal resistance between DIPIPM case and heat sink Rth(c-f) is determined by the thickness and the thermal conductivity of the applied grease. For reference, Rth(c-f) is about 0.4K/W (per 1/6 module, grease thickness: 20μm, thermal conductivity: 1.0W/m•K).

Figure C. 2: SLIMDIP-L - IPM Datasheet - 2.

< DIPIPM >
SLIMDIP-L
TRANSFER MOLDING TYPE
INSULATED TYPE

ELECTRICAL CHARACTERISTICS (T_j = 25°C, unless otherwise noted)
INVERTER PART

Symbol	Parameter	Condition		Limits Min.	Limits Typ.	Limits Max.	Unit
$V_{CE(sat)}$	Collector-emitter saturation voltage	V_D=V_{DB} = 15V, V_{IN}= 5V	I_C= 15A, T_j= 25°C	-	1.60	1.95	V
			I_C= 15A, T_j= 125°C	-	1.80	2.15	
V_{EC}	FWDi forward voltage	V_{IN}= 0V, -I_C= 15A		-	1.40	1.90	V
t_{on}	Switching times	V_{CC}= 300V, V_D= V_{DB}= 15V I_C= 15A, T_j= 125°C, V_{IN}= 0↔5V Inductive Load (upper-lower arm)		0.65	1.05	1.45	µs
$t_{C(on)}$				-	0.40	0.65	µs
t_{off}				-	1.15	1.60	µs
$t_{C(off)}$				-	0.15	0.30	µs
t_{rr}				-	0.30	-	µs
I_{CES}	Collector-emitter cut-off current	V_{CE}=V_{CES}	T_j= 25°C	-	-	1	mA
			T_j= 125°C	-	-	10	

CONTROL (PROTECTION) PART

Symbol	Parameter	Condition		Limits Min.	Limits Typ.	Limits Max.	Unit
I_D	Circuit current	Total of V_{P1}-V_{NC}, V_{N1}-V_{NC}	V_D=15V, V_{IN}=0V	-	-	3.10	mA
			V_D=15V, V_{IN}=3.3V	-	-	4.20	
			V_D=15V, V_{IN}=5V	-	-	3.10	
I_{DB}		Each part of V_{UFB}-V_{UFS}, V_{VFB}-V_{VFS}, V_{WFB}-V_{WFS}	V_D=V_{DB}=15V, V_{IN}=0V	-	-	0.10	
			V_D=V_{DB}=15V, V_{IN}=5V	-	-	0.10	
$V_{SC(ref)}$	Short circuit trip level	V_D = 15V (Note 4)		0.455	0.480	0.505	V
UV_{DBt}	P-side Control supply under-voltage protection(UV)	T_j ≤125°C	Trip level	7.0	10.0	12.0	V
UV_{DBr}			Reset level	7.0	10.0	12.0	V
UV_{Dt}	N-side Control supply under-voltage protection(UV)		Trip level	10.3	-	12.5	V
UV_{Dr}			Reset level	10.8	-	13.0	V
V_{OT}	Temperature Output	Pull down R=5.1kΩ (Note 5)	LVIC Temperature=95°C	2.76	2.89	3.03	V
			LVIC Temperature=25°C	0.86	1.16	1.39	V
OT_t	Over temperature protection (Note6)	V_D = 15V	Trip level	115	130	145	°C
OT_{th}		Detect LVIC temperature	Hysteresis of trip-reset	-	10	-	°C
V_{FOH}	Fault output voltage	V_{SC} = 0V, F_O terminal pulled up to 5V by 10kΩ		4.9	-	-	V
V_{FOL}		V_{SC} = 1V, I_{FO} = 1mA		-	-	0.95	V
t_{FO}	Fault output pulse width	(Note 7)		20	-	-	µs
I_{IN}	Input current	V_{IN} = 5V		0.70	1.00	1.50	mA
$V_{th(on)}$	ON threshold voltage	Applied between U_P, V_P, W_P, U_N, V_N, W_N-V_{NC}		-	1.70	2.35	V
$V_{th(off)}$	OFF threshold voltage			0.70	1.30	-	
$V_{th(hys)}$	ON/OFF threshold hysteresis voltage			0.25	0.40	-	
V_F	Bootstrap Di forward voltage	I_F=10mA including voltage drop by limiting resistor (Note 8)		1.1	1.7	2.3	V
R	Built-in limiting resistance	Included in bootstrap Di		80	100	120	Ω

Note 4 : SC protection works only for N-side IGBT. Please select the external shunt resistance such that the SC trip-level is less than 1.7 times of the current rating.
5 : Temperature of LVIC vs. V_{OT} output characteristics is described in Fig.3.
6 : When the LVIC temperature exceeds OT trip temperature level(OT_t), OT protection works and Fo outputs. In that case if the heat sink dropped off or fixed loosely, don't reuse that DIPIPM. (There is a possibility that junction temperature of power chips exceeded maximum Tj(150°C).
7 : Fault signal Fo outputs when SC, UV or OT protection works. Fo pulse width is different for each protection modes. At SC failure, Fo pulse width is a fixed width (=minimum 20µs), but at UV or OT failure, Fo outputs continuously until recovering from UV or OT state. (But minimum Fo pulse width is 20µs.)
8 : The characteristics of bootstrap Di is described in Fig.2.

Fig. 2 Characteristics of Bootstrap Di V_F-I_F curve (@Ta=25°C) Including Voltage Drop by Limiting Resistor (Right chart is enlarged chart.)

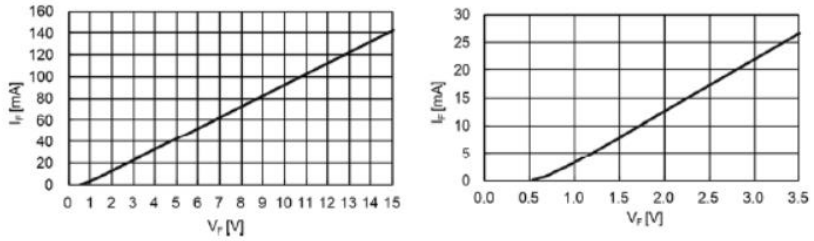

Figure C. 3: SLIMDIP-L - IPM Datasheet - 3.

APPENDIX D

LNK302/304-306
LinkSwitch™-TN Family

POWER INTEGRATIONS

Lowest Component Count, Energy-Efficient
Off-Line Switcher IC

Product Highlights

Cost Effective Linear/Cap Dropper Replacement

- Lowest cost and component count buck converter solution
- Fully integrated auto-restart for short-circuit and open loop fault protection – saves external component costs
- LNK302 uses a simplified controller without auto-restart for very low system cost
- 66 kHz operation with accurate current limit – allows low cost off-the-shelf 1 mH inductor for up to 120 mA output current
- Tight tolerances and negligible temperature variation
- High breakdown voltage of 700 V provides excellent input surge withstand
- Frequency jittering dramatically reduces EMI (~10 dB)
  - Minimizes EMI filter cost
- High thermal shutdown temperature (+135 °C minimum)

Much Higher Performance Over Discrete Buck and Passive Solutions

- Supports buck, buck-boost and flyback topologies
- System level thermal overload, output short-circuit and open control loop protection
- Excellent line and load regulation even with typical configuration
- High bandwidth provides fast turn-on with no overshoot
- Current limit operation rejects line ripple
- Universal input voltage range (85 VAC to 265 VAC)
- Built-in current limit and hysteretic thermal protection
- Higher efficiency than passive solutions
- Higher power factor than capacitor-fed solutions
- Entirely manufacturable in SMD

EcoSmart™– Extremely Energy Efficient

- Consumes typically only 50/80 mW in self-powered buck topology at 115/230 VAC input with no-load (opto feedback)
- Consumes typically only 7/12 mW in flyback topology with external bias at 115/230 VAC input with no-load
- Meets California Energy Commission (CEC), Energy Star, and EU requirements

Applications

- Appliances and timers
- LED drivers and industrial controls

Description

LinkSwitch-TN is specifically designed to replace all linear and capacitor-fed (cap dropper) non-isolated power supplies in the under 360 mA output current range at equal system cost while offering much higher performance and energy efficiency. LinkSwitch-TN devices integrate a 700 V power MOSFET, oscillator, simple On/Off control scheme, a high-voltage switched current source, frequency jittering, cycle-by-cycle current limit and thermal shutdown circuitry onto a monolithic IC. The start-up and operating power are derived directly from the voltage on the DRAIN pin, eliminating the need for a bias supply and associated circuitry in buck or flyback converters. The fully integrated auto-restart circuit in the LNK304-306 safely limits output power during fault conditions such as short-circuit or open loop, reducing component count and system-level load protection cost. A local supply provided by the IC allows use of a non-safety graded optocoupler acting as a level shifter to further enhance line and load regulation performance in buck and buck-boost converters, if required.

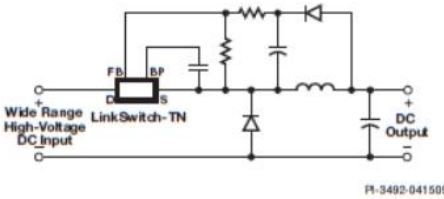

Figure 1. Typical Buck Converter Application (See Application Examples Section for Other Circuit Configurations).

Output Current Table[1]

Product[4]	230 VAC ±15%		85-265 VAC	
	MDCM[2]	CCM[3]	MDCM[2]	CCM[3]
LNK302P/G/D	63 mA	80 mA	63 mA	80 mA
LNK304P/G/D	120 mA	170 mA	120 mA	170 mA
LNK305P/G/D	175 mA	280 mA	175 mA	280 mA
LNK306P/G/D	225 mA	360 mA	225 mA	360 mA

Table 1. Output Current Table.

Notes:
1. Typical output current in a non-isolated buck converter. Output power capability depends on respective output voltage. See Key Applications Considerations Section for complete description of assumptions, including fully discontinuous conduction mode (DCM) operation.
2. Mostly discontinuous conduction mode.
3. Continuous conduction mode.
4. Packages: P: DIP-8B, G: SMD-8B, D: SO-8C.

Figure D. 1: LNK304 - SMPS IC Datasheet – 1.

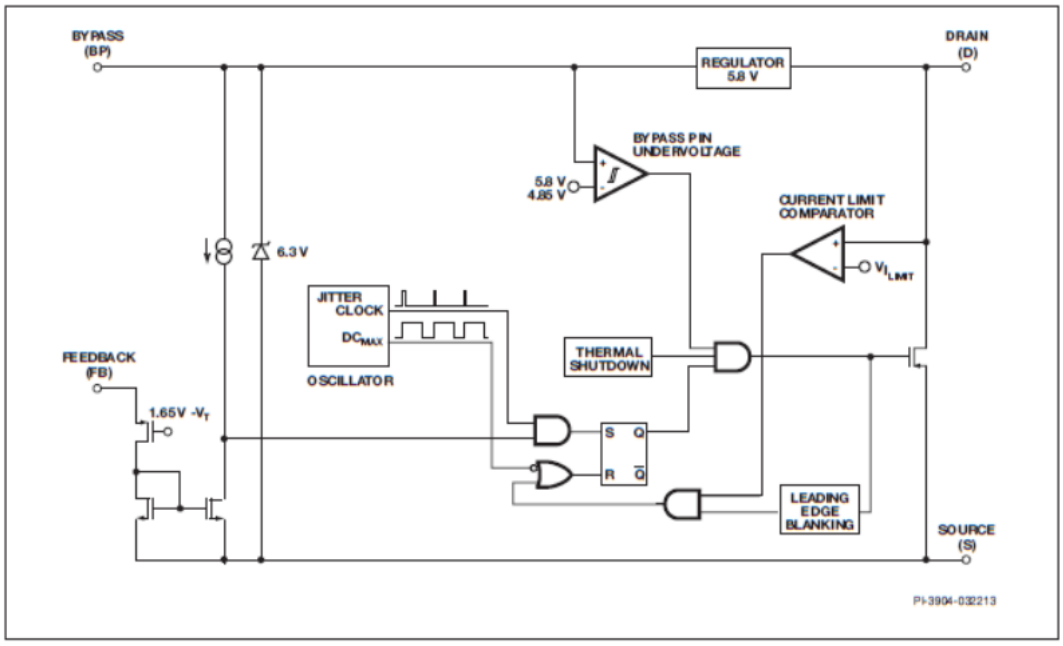

Figure 2a. Functional Block Diagram (LNK302).

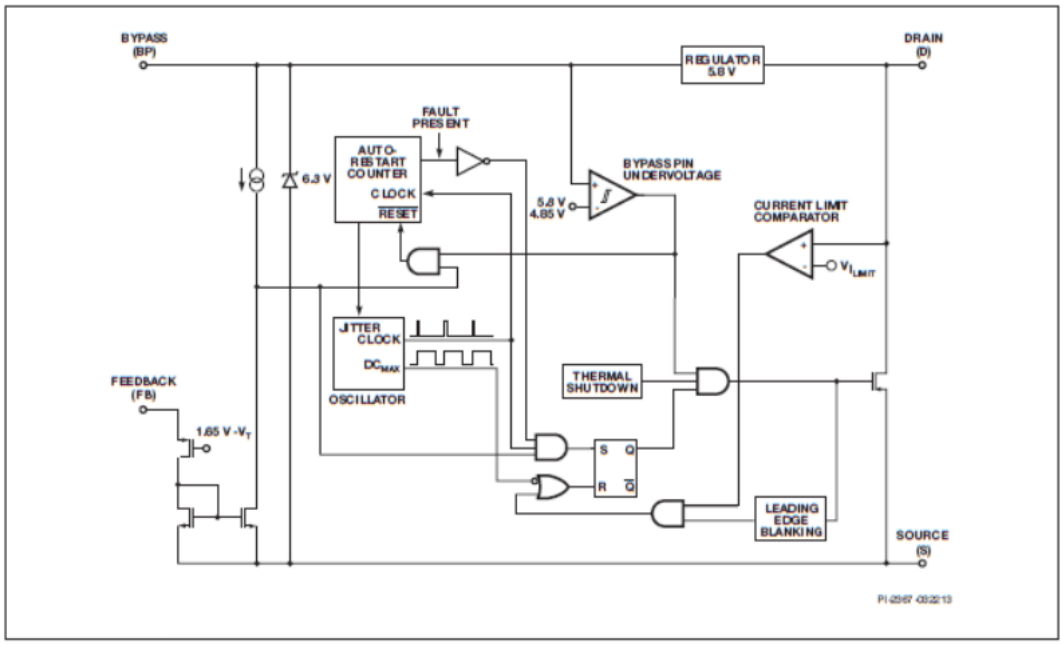

Figure 2b. Functional Block Diagram (LNK304-306).

Figure D. 2: LNK304 - SMPS IC Datasheet – 2.

Pin Functional Description

DRAIN (D) Pin:
Power MOSFET drain connection. Provides internal operating current for both start-up and steady-state operation.

BYPASS (BP) Pin:
Connection point for a 0.1 µF external bypass capacitor for the internally generated 5.8 V supply.

FEEDBACK (FB) Pin:
During normal operation, switching of the power MOSFET is controlled by this pin. MOSFET switching is terminated when a current greater than 49 µA is delivered into this pin.

SOURCE (S) Pin:
This pin is the power MOSFET source connection. It is also the ground reference for the BYPASS and FEEDBACK pins.

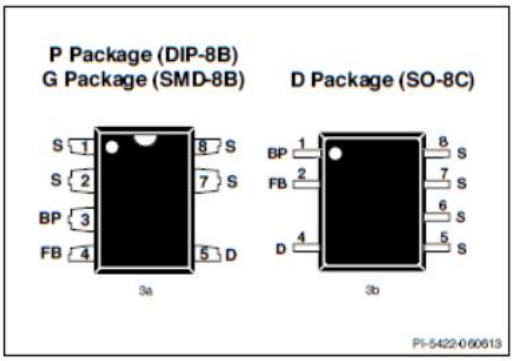

Figure 3. Pin Configuration.

LinkSwitch-TN Functional Description

LinkSwitch-TN combines a high-voltage power MOSFET switch with a power supply controller in one device. Unlike conventional PWM (pulse width modulator) controllers, LinkSwitch-TN uses a simple ON/OFF control to regulate the output voltage. The LinkSwitch-TN controller consists of an oscillator, feedback (sense and logic) circuit, 5.8 V regulator, BYPASS pin undervoltage circuit, over-temperature protection, frequency jittering, current limit circuit, leading edge blanking and a 700 V power MOSFET. The LinkSwitch-TN incorporates additional circuitry for auto-restart.

Oscillator

The typical oscillator frequency is internally set to an average of 66 kHz. Two signals are generated from the oscillator: the maximum duty cycle signal (DC_{MAX}) and the clock signal that indicates the beginning of each cycle.

The LinkSwitch-TN oscillator incorporates circuitry that introduces a small amount of frequency jitter, typically 4 kHz peak-to-peak, to minimize EMI emission. The modulation rate of the frequency jitter is set to 1 kHz to optimize EMI reduction for both average and quasi-peak emissions. The frequency jitter should be measured with the oscilloscope triggered at the falling edge of the DRAIN waveform. The waveform in Figure 4 illustrates the frequency jitter of the LinkSwitch-TN.

Feedback Input Circuit

The feedback input circuit at the FEEDBACK pin consists of a low impedance source follower output set at 1.65 V. When the current delivered into this pin exceeds 49 µA, a low logic level (disable) is generated at the output of the feedback circuit. This output is sampled at the beginning of each cycle on the rising edge of the clock signal. If high, the power MOSFET is turned on for that cycle (enabled), otherwise the power MOSFET remains off (disabled). Since the sampling is done only at the beginning of each cycle, subsequent changes in the FEEDBACK pin voltage or current during the remainder of the cycle are ignored.

5.8 V Regulator and 6.3 V Shunt Voltage Clamp

The 5.8 V regulator charges the bypass capacitor connected to the BYPASS pin to 5.8 V by drawing a current from the voltage on the DRAIN, whenever the MOSFET is off. The BYPASS pin is the internal supply voltage node for the LinkSwitch-TN. When the MOSFET is on, the LinkSwitch-TN runs off of the energy stored in the bypass capacitor. Extremely low power consumption of the internal circuitry allows the LinkSwitch-TN to operate continuously from the current drawn from the DRAIN pin. A bypass capacitor value of 0.1 µF is sufficient for both high frequency decoupling and energy storage.

In addition, there is a 6.3 V shunt regulator clamping the BYPASS pin at 6.3 V when current is provided to the BYPASS pin through an external resistor. This facilitates powering of LinkSwitch-TN externally through a bias winding to decrease the no-load consumption to about 50 mW.

BYPASS Pin Undervoltage

The BYPASS pin undervoltage circuitry disables the power MOSFET when the BYPASS pin voltage drops below 4.85 V. Once the BYPASS pin voltage drops below 4.85 V, it must rise back to 5.8 V to enable (turn-on) the power MOSFET.

Over-Temperature Protection

The thermal shutdown circuitry senses the die temperature. The threshold is set at 142 °C typical with a 75 °C hysteresis. When the die temperature rises above this threshold (142 °C) the power MOSFET is disabled and remains disabled until the die temperature falls by 75 °C, at which point it is re-enabled.

Current Limit

The current limit circuit senses the current in the power MOSFET. When this current exceeds the internal threshold (I_{LIMIT}), the power MOSFET is turned off for the remainder of that cycle. The leading edge blanking circuit inhibits the current limit comparator for a short time (t_{LEB}) after the power MOSFET is turned on. This leading edge blanking time has been set so that current spikes caused by capacitance and rectifier reverse recovery time will not cause premature termination of the switching pulse.

Figure D. 3: LNK304 - SMPS IC Datasheet – 3.

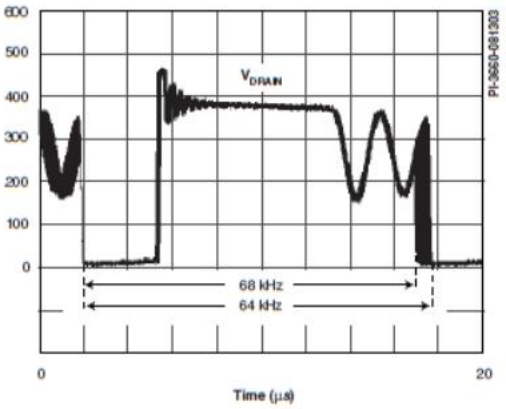

Figure 4. Frequency Jitter.

Auto-Restart (LNK304-306 Only)

In the event of a fault condition such as output overload, output short, or an open-loop condition, LinkSwitch-TN enters into auto-restart operation. An internal counter clocked by the oscillator gets reset every time the FEEDBACK pin is pulled high. If the FEEDBACK pin is not pulled high for 50 ms, the power MOSFET switching is disabled for 800 ms. The auto-restart alternately enables and disables the switching of the power MOSFET until the fault condition is removed.

Applications Example

A 1.44 W Universal Input Buck Converter

The circuit shown in Figure 5 is a typical implementation of a 12 V, 120 mA non-isolated power supply used in appliance control such as rice cookers, dishwashers or other white goods. This circuit may also be applicable to other applications such as night-lights, LED drivers, electricity meters, and residential heating controllers, where a non-isolated supply is acceptable.

The input stage comprises fusible resistor RF1, diodes D3 and D4, capacitors C4 and C5, and inductor L2. Resistor RF1 is a flame proof, fusible, wire wound resistor. It accomplishes several functions: a) Inrush current limitation to safe levels for rectifiers D3 and D4; b) Differential mode noise attenuation; c) Input fuse should any other component fail short-circuit (component fails safely open-circuit without emitting smoke, fire or incandescent material).

The power processing stage is formed by the LinkSwitch-TN, freewheeling diode D1, output choke L1, and the output capacitor C2. The LNK304 was selected such that the power supply operates in the mostly discontinuous-mode (MDCM). Diode D1 is an ultrafast diode with a reverse recovery time (t_{RR}) of approximately 75 ns, acceptable for MDCM operation. For continuous conduction mode (CCM) designs, a diode with a t_{rr} of ≤35 ns is recommended. Inductor L1 is a standard off-the-shelf inductor with appropriate RMS current rating (and acceptable temperature rise). Capacitor C2 is the output filter capacitor; its primary function is to limit the output voltage ripple. The output voltage ripple is a stronger function of the ESR of the output capacitor than the value of the capacitor itself.

To a first order, the forward voltage drops of D1 and D2 are identical. Therefore, the voltage across C3 tracks the output voltage. The voltage developed across C3 is sensed and regulated via the resistor divider R1 and R3 connected to U1's FEEDBACK pin. The values of R1 and R3 are selected such that, at the desired output voltage, the voltage at the FEEDBACK pin is 1.65 V.

Regulation is maintained by skipping switching cycles. As the output voltage rises, the current into the FEEDBACK pin will rise. If this exceeds I_{FB} then subsequent cycles will be skipped until the current reduces below I_{FB}. Thus, as the output load is reduced, more cycles will be skipped and if the load increases, fewer cycles are skipped. To provide overload protection if no cycles are skipped during a 50 ms period, LinkSwitch-TN will enter auto-restart (LNK304-306), limiting the average output power to approximately 6% of the maximum overload power. Due to tracking errors between the output voltage and the voltage across C3 at light load or no-load, a small pre-load may be required (R4). For the design in Figure 5, if regulation to zero load is required, then this value should be reduced to 2.4 kΩ.

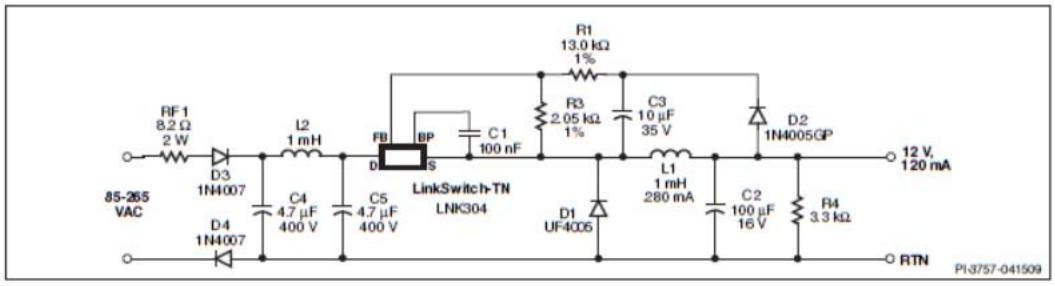

Figure 5. Universal Input, 12 V, 120 mA Constant Voltage Power Supply Using LinkSwitch-TN.

Figure D. 4: LNK304 - SMPS IC Datasheet – 4.

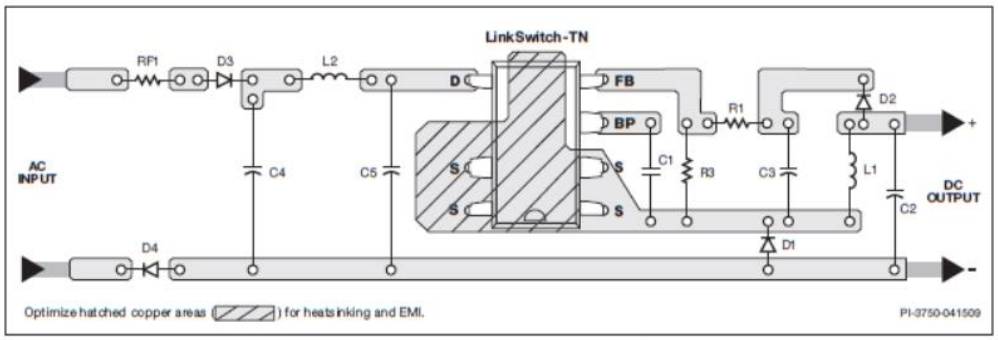

Figure 6a. Recommended Printed Circuit Layout for LinkSwitch-TN in a Buck Converter Configuration using P or G Package.

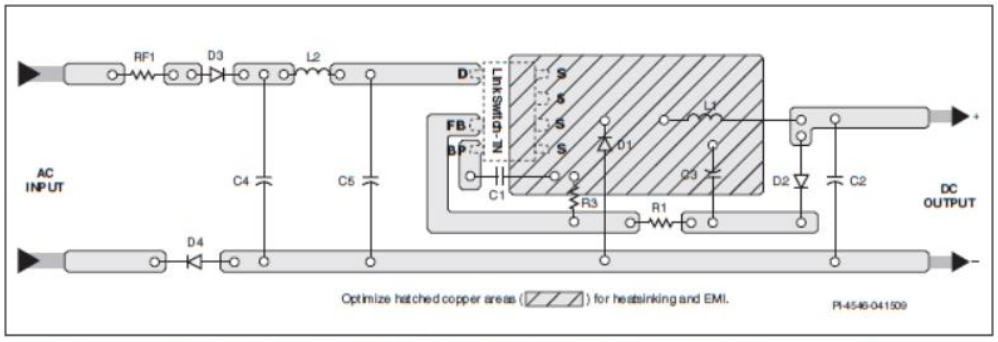

Figure 6b. Recommended Printed Circuit Layout for LinkSwitch-TN in a Buck Converter Configuration using D Package to Bottom Side of the Board.

Key Application Considerations

LinkSwitch-TN Design Considerations

Output Current Table

Data sheet maximum output current table (Table 1) represents the maximum practical continuous output current for both mostly discontinuous conduction mode (MDCM) and continuous conduction mode (CCM) of operation that can be delivered from a given LinkSwitch-TN device under the following assumed conditions:

1. Buck converter topology.
2. The minimum DC input voltage is ≥70 V. The value of input capacitance should be large enough to meet this criterion.
3. For CCM operation a KRP* of 0.4.
4. Output voltage of 12 VDC.
5. Efficiency of 75%.
6. A catch/freewheeling diode with t_{RR} ≤75 ns is used for MDCM operation and for CCM operation, a diode with t_{RR} ≤35 ns is used.
7. The part is board mounted with SOURCE pins soldered to a sufficient area of copper to keep the SOURCE pin temperature at or below 100 °C.

*KRP is the ratio of ripple to peak inductor current.

LinkSwitch-TN Selection and Selection Between MDCM and CCM Operation

Select the LinkSwitch-TN device, freewheeling diode and output inductor that gives the lowest overall cost. In general, MDCM provides the lowest cost and highest efficiency converter. CCM designs require a larger inductor and ultrafast (t_{RR} ≤ 35 ns) freewheeling diode in all cases. It is lower cost to use a larger LinkSwitch-TN in MDCM than a smaller LinkSwitch-TN in CCM because of the additional external component costs of a CCM design. However, if the highest output current is required, CCM should be employed following the guidelines below.

Topology Options

LinkSwitch-TN can be used in all common topologies, with or without an optocoupler and reference to improve output voltage tolerance and regulation. Table 2 provide a summary of these configurations. For more information see the Application Note – LinkSwitch-TN Design Guide.

Figure D. 5: LNK304 - SMPS IC Datasheet – 5.

Topology	Basic Circuit Schematic	Key Features
Low-Side Buck-Boost – Optocoupler Feedback	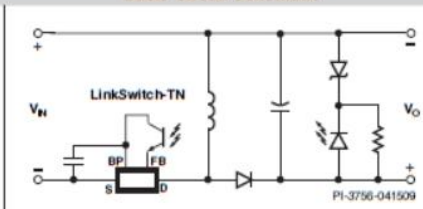	1. Output referenced to input 2. Positive output (V_O) with respect to $+V_{IN}$ 3. Step up/down – $V_O > V_{IN}$ or $V_O < V_{IN}$ 4. Optocoupler feedback - Accuracy only limited by reference choice - Low cost non-safety rated optocoupler - No pre-load required 5. Fail-safe – output is not subjected to input voltage if the internal power MOSFET fails 6. Minimum no-load consumption

Table 2 (cont). Common Circuit Configurations Using LinkSwitch-TN.

Component Selection

Referring to Figure 5, the following considerations may be helpful in selecting components for a LinkSwitch-TN design.

Freewheeling Diode D1

Diode D1 should be an ultrafast type. For MDCM, reverse recovery time t_{RR} ≤75 ns should be used at a temperature of 70 °C or below. Slower diodes are not acceptable, as continuous mode operation will always occur during startup, causing high leading edge current spikes, terminating the switching cycle prematurely, and preventing the output from reaching regulation. If the ambient temperature is above 70 °C then a diode with t_{RR} ≤35 ns should be used.

For CCM an ultrafast diode with reverse recovery time t_{RR} ≤35 ns should be used. A slower diode may cause excessive leading edge current spikes, terminating the switching cycle prematurely and preventing full power delivery.

Fast and slow diodes should never be used as the large reverse recovery currents can cause excessive power dissipation in the diode and/or exceed the maximum drain current specification of LinkSwitch-TN.

Feedback Diode D2

Diode D2 can be a low-cost slow diode such as the 1N400X series, however it should be specified as a glass passivated type to guarantee a specified reverse recovery time. To a first order, the forward drops of D1 and D2 should match.

Inductor L1

Choose any standard off-the-shelf inductor that meets the design requirements. A "drum" or "dog bone" "I" core inductor is recommended with a single ferrite element due to its low cost and very low audible noise properties. The typical inductance value and RMS current rating can be obtained from the LinkSwitch-TN design spreadsheet available within the PI Expert design suite from Power Integrations. Choose L1 greater than or equal to the typical calculated inductance with RMS current rating greater than or equal to calculated RMS inductor current.

Capacitor C2

The primary function of capacitor C2 is to smooth the inductor current. The actual output ripple voltage is a function of this capacitor's ESR. To a first order, the ESR of this capacitor should not exceed the rated ripple voltage divided by the typical current limit of the chosen LinkSwitch-TN.

Feedback Resistors R1 and R3

The values of the resistors in the resistor divider formed by R1 and R3 are selected to maintain 1.65 V at the FEEDBACK pin. It is recommended that R3 be chosen as a standard 1% resistor of 2 kΩ. This ensures good noise immunity by biasing the feedback network with a current of approximately 0.8 mA.

Feedback Capacitor C3

Capacitor C3 can be a low cost general purpose capacitor. It provides a "sample and hold" function, charging to the output voltage during the off time of LinkSwitch-TN. Its value should be 10 µF to 22 µF; smaller values cause poorer regulation at light load conditions.

Pre-Load Resistor R4

In high-side, direct feedback designs where the minimum load is <3 mA, a pre-load resistor is required to maintain output regulation. This ensures sufficient inductor energy to pull the inductor side of the feedback capacitor C3 to input return via D2. The value of R4 should be selected to give a minimum output load of 3 mA.

In designs with an optocoupler the Zener or reference bias current provides a 1 mA to 2 mA minimum load, preventing "pulse bunching" and increased output ripple at zero load.

LinkSwitch-TN Layout Considerations

In the buck or buck-boost converter configuration, since the SOURCE pins in LinkSwitch-TN are switching nodes, the copper area connected to SOURCE should be minimized to minimize EMI within the thermal constraints of the design.

In the boost configuration, since the SOURCE pins are tied to DC return, the copper area connected to SOURCE can be maximized to improve heat sinking.

The loop formed between the LinkSwitch-TN, inductor (L1), freewheeling diode (D1), and output capacitor (C2) should be kept as small as possible. The BYPASS pin capacitor C1 (Figure 6) should be located physically close to the SOURCE (S) and BYPASS (BP) pins. To minimize direct coupling from switching nodes, the LinkSwitch-TN should be placed away

Figure D. 6: LNK304 - SMPS IC Datasheet – 6.

from AC input lines. It may be advantageous to place capacitors C4 and C5 in-between LinkSwitch-TN and the AC input. The second rectifier diode D4 is optional, but may be included for better EMI performance and higher line surge withstand capability.

Quick Design Checklist

As with any power supply design, all LinkSwitch-TN designs should be verified for proper functionality on the bench. The following minimum tests are recommended:

1. Adequate DC rail voltage – check that the minimum DC input voltage does not fall below 70 VDC at maximum load, minimum input voltage.
2. Correct Diode Selection – UF400x series diodes are recommended only for designs that operate in MDCM at an ambient of 70 °C or below. For designs operating in continuous conduction mode (CCM) and/or higher ambients, then a diode with a reverse recovery time of 35 ns or better, such as the BYV26C, is recommended.
3. Maximum drain current – verify that the peak drain current is below the data sheet peak drain specification under worst-case conditions of highest line voltage, maximum overload (just prior to auto-restart) and highest ambient temperature.
4. Thermal check – at maximum output power, minimum input voltage and maximum ambient temperature, verify that the LinkSwitch-TN SOURCE pin temperature is 100 °C or below. This figure ensures adequate margin due to variations in $R_{DS(ON)}$ from part to part. A battery powered thermocouple meter is recommended to make measurements when the SOURCE pins are a switching node. Alternatively, the ambient temperature may be raised to indicate margin to thermal shutdown.

In a LinkSwitch-TN design using a buck or buck-boost converter topology, the SOURCE pin is a switching node. Oscilloscope measurements should therefore be made with probe grounded to a DC voltage, such as primary return or DC input rail, and not to the SOURCE pins. The power supply input must always be supplied from an isolated source (e.g. via an isolation transformer).

Figure D. 7: LNK304 - SMPS IC Datasheet – 7.

APPENDIX E

NCP1117LP

1.0 A Low-Dropout Positive Fixed and Adjustable Voltage Regulators

The NCP1117LP is the low power version of the popular NCP1117 family of low dropout voltage regulators, with reduced quiescent current. It is intended primarily for high volume consumer applications over the 0 to 125 degree temperature range. Capable of providing an output current in excess of 1 A, with a dropout voltage of 1.3 V at 1 A full current load, the series consists of an adjustable and five fixed voltage versions of 1.5 V, 1.8 V, 2.5 V, 3.3 V and 5.0 V.

Internal protection features consist of output current limiting and built−in thermal shutdown. The NCP1117LP series can operate up to 18 V max input voltage. The device is available in the popular SOT−223 and DPAK packages.

Features

- Output Current in Excess of 1.0 A
- 1.4 V Maximum Dropout Voltage at 1 A
- Quiescent Current over 10 times Lower than Traditional 1117
- Fixed Output Voltages of 1.5 V, 1.8 V, 2.5 V, 3.3 V and 5.0 V
- Adjustable Output Voltage Option
- No Minimum Load Requirement for Fixed Voltage Output Devices
- Good Noise Rejection
- Current Limit and Thermal Shutdown Protection
- Operation up to 18 V Input
- These are Pb−Free Devices

Applications

- TV and Monitors
- Set Top Boxes and Entertainment Devices
- Switching Power Supply Post Regulation
- Game Consoles and Consumer Applications
- Hard Drive Controllers

ON Semiconductor®

www.onsemi.com

SOT−223
ST SUFFIX
CASE 318H

Pin: 1. Adjust/Ground
2. Output
3. Input

MARKING DIAGRAM

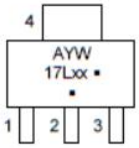

Heatsink tab is connected to Pin 2.

xx	= 15, 18, 25, 33, 50, AD
A	= Assembly Location
Y	= Year
W	= Work Week
▪	= Pb−Free Package

(Note: Microdot may be in either location)

DPAK
DT SUFFIX
CASE 369C

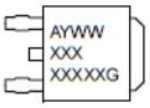

ORDERING INFORMATION

See detailed ordering and shipping information in the package dimensions section on page 12 of this data sheet.

TYPICAL APPLICATIONS

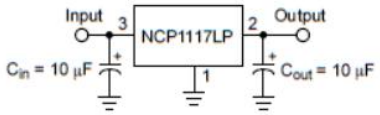

Figure 1. Fixed Output Regulator

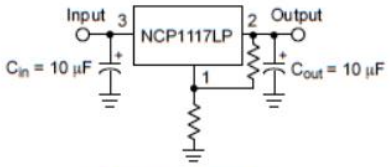

Figure 2. Adjustable Output Regulator

Figure E. 1: NCP1117 - LDO Datasheet – 1.

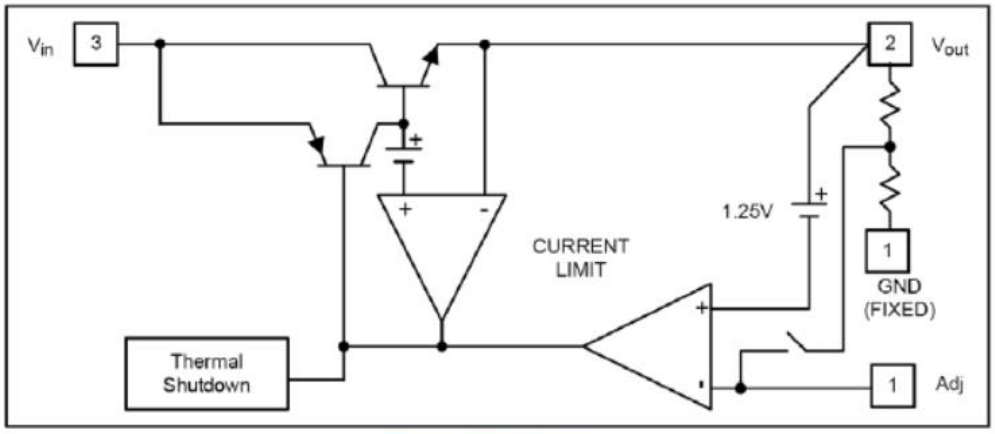

Figure 3. Block Diagram

Table 1. PIN FUNCTION DESCRIPTION

Pin No.	Pin Name	Description
1	Adj (GND)	A resistor divider from this pin to the Vout pin and ground sets the output voltage (Ground only for Fixed−Mode).
2	Vout	The output of the regulator. A minimum of 10 μF capacitor (20 mΩ ≤ ESR ≤ 20 Ω) must be connected from this pin to ground to insure stability.
3	Vin	The input pin of regulator. Typically a large storage capacitor (20 mΩ ≤ ESR ≤ 20 Ω) is connected from this pin to ground to insure that the input voltage does not sag below the minimum dropout voltage during the load transient response. This pin must always be 1.3 V (typ.) higher than Vout in order for the device to regulate properly.

Table 2. MAXIMUM RATINGS

Rating		Symbol	Value	Unit
DC Input Voltage		V_{in}	−0.3 to 18	V
Operating Junction Temperature Range		T_{OP}	0 to 125	°C
Operating Ambient Temperature Range		T_A	0 to 125	°C
Maximum Junction Temperature Range		$T_{J(max)}$	−55 to 150	°C
Power Dissipation and Thermal Characteristics − Power Dissipation (Note 1) − Thermal Resistance, Junction−to−Ambient (Note 2) − Thermal Resistance, Junction−to−Case		P_D $R_{\theta JA}$ $R_{\theta JC}$	Internally Limited 108 15	W °C/W °C/W
Electrostatic Discharge	Human Body Model	ESD	2000	V
	Machine Model		200	
Storage Temperature Range		T_{STG}	−65 to 150	°C
NOTE: This device series contains ESD protection and exceeds the following tests: ESD HBM tested per AEC−Q100−002 (EIA/JESD22−A114) ESD MM tested per AEC−Q100−003 (EIA/JESD22−A115) Latch−up Current Maximum Rating: ≤ 150mA per JEDEC standard: JESD78				

Stresses exceeding those listed in the Maximum Ratings table may damage the device. If any of these limits are exceeded, device functionality should not be assumed, damage may occur and reliability may be affected.

NOTE: All voltages are referenced to GND pin.

1. The maximum package power dissipation is:

$$P_D = \frac{T_{J(max)} - T_A}{R_{\theta JA}}$$

2. $R_{\theta JA}$ on a 100 x 100 mm PCB Cu thickness 1 oz; T_A = 25°C

Figure E. 2: NCP1117 - LDO Datasheet – 2.

Table 3. ELECTRICAL CHARACTERISTICS (C_{in} = 10 µF, C_{out} = 10 µF, for typical value T_A = 25°C, for min and max values T_A is the operating ambient temperature range that applies unless otherwise noted.)

Parameter	Conditions		Symbol	Min	Typ	Max	Unit
Reference Voltage, Adjustable Output Devices	NCP1117−ADJ	T_J = 25°C (Vin − Vout) = 1.5 V, Io = 10 mA	V_{ref}	1.225	1.250	1.275	V
Output Voltage, Fixed Output Devices	NCP1117−1.5	T_J = 25°C 3 V ≤ Vin ≤ 12 V, Io = 10 mA	V_{out}	1.470	1.5	1.530	V
	NCP1117−1.8	T_J = 25°C 3.3 V ≤ Vin ≤ 12 V, Io = 10 mA		1.760	1.8	1.840	V
	NCP1117−2.5	T_J = 25°C 4 V ≤ Vin ≤ 12 V, Io = 10 mA		2.450	2.5	2.550	V
	NCP1117−3.3	T_J = 25°C 4.8 V ≤ Vin ≤ 12 V, Io = 10 mA		3.235	3.3	3.365	V
	NCP1117−5.0	T_J = 25°C 6.5 V ≤ Vin ≤ 12 V, Io = 10 mA		4.900	5	5.100	V
Line Regulation, Adjustable & Fixed (Note 3)	NCP1117−XXX	T_J = 25°C Vout + 1.5 V < Vin < 12 V, Io = 10 mA	Reg_{line}			0.2	%
Load Regulation (Note 3)	NCP1117−ADJ	T_J = 25°C 10 mA < Io < 1 A, Vin = 3.3 V	Reg_{load}			1	%
	NCP1117−1.5	T_J = 25°C 10 mA < Io < 1 A, Vin = 3 V			12	15	mV
	NCP1117−1.8	T_J = 25°C 10 mA < Io < 1 A, Vin = 3.3 V			15	18	mV
	NCP1117−2.5	T_J = 25°C 10 mA < Io < 1 A, Vin = 4 V			20	25	mV
	NCP1117−3.3	T_J = 25°C 10 mA < Io < 1 A, Vin = 4.7 V			26	33	mV
	NCP1117−5.0	T_J = 25°C 10 mA < Io < 1 A, Vin = 6.5 V			40	50	mV
Dropout Voltage (Vin – Vout), Adjustable & Fixed	NCP1117−XXX	Iout = 1 A, T_A = 25°C ΔVout = Vout − 100 mV			1.3	1.4	V
Current Limit, Adjustable & Fixed	NCP1117−XXX	Vin = 7 V, T_A = 25°C	Iout	1.1			A
Minimum Load Current (Note 4)	NCP1117−XXX	0°C ≤ Tj ≤ 125°C	I_{Lmin}		1	5	mA
Quiescent Current	NCP1117−fixed	Vin = 12 V Io = 10 mA	I_{QFIX}		550	700	µA
	NCP1117−ADJ		I_{QADJ}		30	50	µA
Thermal Regulation (Note 5)		T_A = 25°C, T = 30 ms pulse			0.008	0.04	%W
Ripple Rejection	NCP1117−XXX	F = 120 Hz, Cout = 25 µF tantalum, Iout = 1 A, Vin = Vout + 3 V	RR		60		dB
Thermal Shutdown	NCP1117−XXX		T_{shdn}		165		°C
Thermal Hysteresis	NCP1117−XXX		T_{hyst}		10		°C

Product parametric performance is indicated in the Electrical Characteristics for the listed test conditions, unless otherwise noted. Product performance may not be indicated by the Electrical Characteristics if operated under different conditions.

3. Low duty cycle pulse techniques are used during testing to maintain the junction temperature as close to ambient as possible.
4. Guaranteed by design.
5. Thermal Regulation is defined as the change in output voltage at a time after a change in power dissipation is applied, excluding load or line regulation effects. Specifications are for a current pulse equal to Io_{max} at VIN = VIN + 1.5 V for T = 30 msec. Guaranteed by characterization.

Figure E. 3: NCP1117 - LDO Datasheet – 3.

APPENDIX F

Single, Dual, Quad Low-Voltage, Rail-to-Rail Operational Amplifiers

LMV321, NCV321, LMV358, LMV324

The LMV321, LMV321I, NCV321, LMV358/LMV358I and LMV324 are CMOS single, dual, and quad low voltage operational amplifiers with rail−to−rail output swing. These amplifiers are a cost−effective solution for applications where low power consumption and space saving packages are critical. Specification tables are provided for operation from power supply voltages at 2.7 V and 5 V. Rail−to−Rail operation provides improved signal−to−noise preformance. Ultra low quiescent current makes this series of amplifiers ideal for portable, battery operated equipment. The common mode input range includes ground making the device useful for low−side current−shunt measurements. The ultra small packages allow for placement on the PCB in close proximity to the signal source thereby reducing noise pickup.

Features

- Operation from 2.7 V to 5.0 V Single−Sided Power Supply
- LMV321 Single Available in Ultra Small 5 Pin SC70 Package
- No Output Crossover Distortion
- Rail−to−Rail Output
- Low Quiescent Current: LMV358 Dual − 220 μA, Max per Channel
- No Output Phase−Reversal from Overdriven Input
- NCV Prefix for Automotive and Other Applications Requiring Unique Site and Control Change Requirements; AEC−Q100 Qualified and PPAP Capable
- These Devices are Pb−Free, Halogen Free/BFR Free and are RoHS Compliant

Typical Applications

- Notebook Computers and PDA's
- Portable Battery−Operated Instruments
- Active Filters

ON Semiconductor®

www.onsemi.com

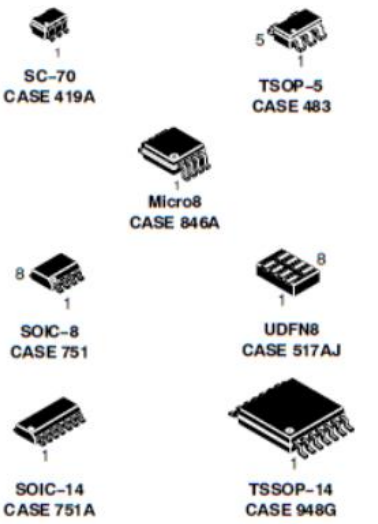

ORDERING AND MARKING INFORMATION

See detailed ordering and shipping information in the package dimensions section on page 12 of this data sheet.

Figure F. 1: LMV321 - Op-Amp Datasheet - 1.

MAXIMUM RATINGS

Symbol	Rating	Value	Unit
V_S	Supply Voltage (Operating Range V_S = 2.7 V to 5.5 V)	5.5	V
V_{IDR}	Input Differential Voltage	± Supply Voltage	V
V_{ICR}	Input Common Mode Voltage Range	−0.5 to (V+) + 0.5	V
	Maximum Input Current	10	mA
t_{So}	Output Short Circuit (Note 1)	Continuous	
T_J	Maximum Junction Temperature	150	°C
T_A	Operating Ambient Temperature Range LMV321, LMV358, LMV324 LMV321I, LMV358I NCV321 (Note 2)	 −40 to 85 −40 to 125 −40 to 125	 °C °C °C
θ_{JA}	Thermal Resistance:		°C/W
	SC−70	280	
	Micro8	238	
	TSOP−5	333	
	UDFN8 (1.2 mm x 1.8 mm x 0.5 mm)	350	
	SOIC−8	212	
	SOIC−14	156	
	TSSOP−14	190	
T_{stg}	Storage Temperature	−65 to 150	°C
	Mounting Temperature (Infrared or Convection −20 sec)	260	°C
V_{ESD}	ESD Tolerance (Note 3) LMV321, LMV321I, NCV321 Machine Model Human Body Model LMV358/358I/324 Machine Model Human Body Mode	 100 1000 100 2000	V

Stresses exceeding those listed in the Maximum Ratings table may damage the device. If any of these limits are exceeded, device functionality should not be assumed, damage may occur and reliability may be affected.

1. Continuous short−circuit operation to ground at elevated ambient temperature can result in exceeding the maximum allowed junction temperature of 150°C. Output currents in excess of 45 mA over long term may adversely affect reliability. Shorting output to either V+ or V− will adversely affect reliability.
2. NCV prefix is qualified for automotive usage.
3. Human Body Model, applicable std. MIL−STD−883, Method 3015.7
   Machine Model, applicable std. JESD22−A115−A (ESD MM std. of JEDEC)
   Field−Induced Charge−Device Model, applicable std. JESD22−C101−C (ESD FICDM std. of JEDEC).

Figure F. 2: LMV321 - Op-Amp Datasheet - 2.

5.0 V DC ELECTRICAL CHARACTERISTICS (Unless otherwise specified, all limits are guaranteed for T_A = 25°C, V+ = 5.0 V, R_L = 1 MΩ, V− = 0 V, V_O = V+/2)

Parameter	Symbol	Condition	Min	Typ	Max	Unit
Input Offset Voltage	V_{IO}	$T_A = T_{Low}$ to T_{High} (Note 6)		1.7	9	mV
Input Offset Voltage Average Drift	T_CV_{IO}	$T_A = T_{Low}$ to T_{High} (Note 6)		5		μV/°C
Input Bias Current (Note 7)	I_B	$T_A = T_{Low}$ to T_{High} (Note 6)		< 1		nA
Input Offset Current (Note 7)	I_{IO}	$T_A = T_{Low}$ to T_{High} (Note 6)		< 1		nA
Common Mode Rejection Ratio	CMRR	0 V ≤ V_{CM} ≤ 4 V	50	65		dB
Power Supply Rejection Ratio	PSRR	2.7 V ≤ V+ ≤ 5 V, V_O = 1 V, V_{CM} = 1 V	50	60		dB
Input Common−Mode Voltage Range	V_{CM}	For CMRR ≥ 50 dB	0 to 4	−0.2 to 4.2		V
Large Signal Voltage Gain (Note 7)	A_V	R_L = 2 kΩ	15	100		V/mV
		$T_A = T_{Low}$ to T_{High} (Note 6)	10			
Output Swing	V_{OH}	R_L = 2 kΩ to 2.5 V $T_A = T_{Low}$ to T_{High} (Note 6)	V_{CC} − 300 V_{CC} − 400	V_{CC} − 40		mV
	V_{OL}	R_L = 2 kΩ to 2.5 V (Note 7) $T_A = T_{Low}$ to T_{High} (Note 6)		120	300 400	mV
	V_{OH}	R_L = 10 kΩ to 2.5 V (Note 7) $T_A = T_{Low}$ to T_{High} (Note 6)	V_{CC} − 100 V_{CC} − 200			mV
	V_{OL}	R_L = 10 kΩ to 2.5 V $T_A = T_{Low}$ to T_{High} (Note 6)		65	180 280	mV
Output Short Circuit Current	I_O	Sourcing = V_O = 0 V (Note 7) Sinking = V_O = 5 V (Note 7)	10 10	60 160		mA
Supply Current	I_{CC}	LMV321 $T_A = T_{Low}$ to T_{High} (Note 6)		130	250 350	μA
		NCV321 $T_A = T_{Low}$ to T_{High} (Note 6)		130	250 350	
		LMV358/358I Both Amplifiers $T_A = T_{Low}$ to T_{High} (Note 6)		210	440 615	
		LMV324 All Four Amplifiers $T_A = T_{Low}$ to T_{High} (Note 6)		410	830 1160	

5.0 V AC ELECTRICAL CHARACTERISTICS (Unless otherwise specified, all limits are guaranteed for T_A = 25°C, V+ = 5.0 V, R_L = 1 MΩ, V− = 0 V, V_O = V+/2)

Parameter	Symbol	Condition	Min	Typ	Max	Unit
Slew Rate	S_R			1		V/μs
Gain Bandwidth Product	GBWP	C_L = 200 pF		1		MHz
Phase Margin	Θ_m			60		°
Gain Margin	G_m			10		dB
Input−Referred Voltage Noise	e_n	f = 50 kHz		50		nV/$\sqrt{Hz}$

Product parametric performance is indicated in the Electrical Characteristics for the listed test conditions, unless otherwise noted. Product performance may not be indicated by the Electrical Characteristics if operated under different conditions.

6. For LMV321, LMV358, LMV324: T_A = −40°C to +85°C
   For LMV321I, LMV358I, NCV321: T_A = −40°C to +125°C.
7. Guaranteed by design and/or characterization.

Figure F. 3: LMV321 - Op-Amp Datasheet - 3.

APPENDIX G

RENESAS

Datasheet

RX13T Group
Renesas MCUs

R01DS0341EJ0110
Rev.1.10
Mar 16, 2021

32-MHz 32-bit RX MCUs, built-in FPU, 50 DMIPS, power supply 5 V
12-bit ADC (equipped with 3-channel synchronous S/H circuits, programmable gain amplifier × 3 ch, and comparator)
32-MHz PWM (three-phase complementary output × 1 ch), On-chip data flash memory

Features

■ 32-bit RX CPU core
- Max. operating frequency: 32 MHz
  Capable of 50 DMIPS in operation at 32 MHz
- Accumulator handles 64-bit results (for a single instruction) from 32-bit × 32-bit operations
- Multiplication and division unit handles 32-bit × 32-bit operations (multiplication instructions take one CPU clock cycle)
- Built-in FPU: 32-bit single-precision floating point (compliant to IEEE754)
- Fast interrupt
- CISC Harvard architecture with 5-stage pipeline
- Variable-length instructions, ultra-compact code
- On-chip debugging circuit

■ Low power design and architecture
- Operation from a single 2.7-V to 5.5-V supply
- Three low power consumption modes

■ On-chip code flash memory, no wait states
- 128-/64-Kbyte capacities
- On-board or off-board user programming
- For instructions and operands

■ On-chip data flash memory
- 4 Kbytes (1,000,000 program/erase cycles (typ.))
- BGO (Background Operation)

■ On-chip SRAM, no wait states
- 12 Kbytes of SRAM

■ DMA
- DTC: Five transfer modes

■ Reset and supply management
- Seven types of reset, including the power-on reset (POR)
- Low voltage detection (LVD) with voltage settings

■ Clock functions
- Main clock oscillator frequency: 1 to 20 MHz
- External clock input frequency: Up to 20 MHz
- PLL circuit input: 4 MHz to 8 MHz
- Low-speed on-chip oscillator: 4 MHz
- High-speed on-chip oscillator: 32 MHz ±1%
- IWDT-dedicated on-chip oscillator: 15 kHz
- On-chip clock frequency accuracy measurement circuit (CAC)

■ Independent watchdog timer
- 15-kHz on-chip oscillator produces a dedicated clock signal to drive IWDT operation.

■ Useful functions for IEC60730 compliance
- Self-diagnostic and disconnection-detection assistance functions for the A/D converter, clock frequency accuracy measurement circuit, independent watchdog timer, RAM test assistance functions using the DOC, etc.

■ MPC
- Multiple locations are selectable for I/O pins of peripheral functions

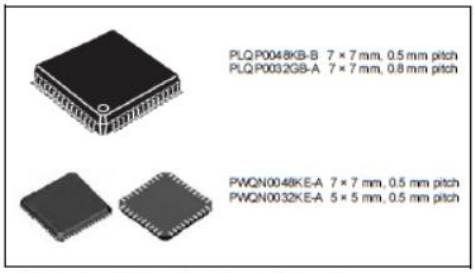

■ Up to 4 communications channels
- SCI with many useful functions (3 channels)
  Asynchronous mode, clock synchronous mode, smart card interface mode, simplified SPI, simplified I²C, and extended serial mode.
- I²C bus interface: Transfer at up to 400 kbps (one channel)

■ Up to 8 extended-function timers
- 16-bit MTU3 (six channels): 32 MHz operation, input capture, output compare, three-phase complementary PWM × 1 channel-output, CPU-efficient complementary PWM, phase counting mode (2 channels)
- 16-bit compare-match timers (2 channels)

■ 12-bit A/D converter: 8 ch
- On-chip sample-and-hold circuit: 12-bit × up to 3 channels
- Sampling time can be set for each channel
- Group scan priority control mode (3 levels)
- Self-diagnostic function and analog input disconnection detection assistance function (compliant to IEC60730)
- Input signal amplitude by the programmable gain amplifier (3 channels)
- ADC: 3-channel simultaneous sample-and-hold circuit (3 shunt method), double data register (1 shunt method), amplifier (3 channels), comparator (3 channels)

■ Register write protection function can protect values in important registers against overwriting.

■ Up to 39 pins for general I/O ports
- 5-V tolerant, open drain, input pull-up

■ Operating temperature range
- –40 to +85°C
- –40 to +105°C

■ Applications
- General industrial and consumer equipment

Figure G. 1: RX13T - MCU Datasheet - 1.

1. Overview

1.1 Outline of Specifications

Table 1.1 lists the specifications, and Table 1.2 gives a comparison of the functions of the products in different packages.
Table 1.1 is for products with the greatest number of functions, so the number of peripheral modules and channels will differ in accordance with the package type. For details, see Table 1.2, Comparison of Functions for Different Packages.

Table 1.1 Outline of Specifications (1/3)

Classification	Module/Function	Description
CPU	CPU	• Maximum operating frequency: 32 MHz • 32-bit RX CPU • Minimum instruction execution time: One instruction per clock cycle • Address space: 4-Gbyte linear • Register set General purpose: Sixteen 32-bit registers Control: Nine 32-bit registers Accumulator: One 64-bit registers • Basic instructions: 73 Variable-length instruction format • DSP instructions: 9 • Addressing modes: 10 • Data arrangement Instructions: Little endian Data: Selectable as little endian or big endian • On-chip 32-bit multiplier: 32-bit × 32-bit → 64-bit • On-chip divider: 32-bit ÷ 32-bit → 32 bits • Barrel shifter: 32 bits
	FPU	• Single precision (32-bit) floating point • Data types and floating-point exceptions in conformance with the IEEE754 standard
Memory	ROM	• Capacity: 64 K/128 Kbytes • 32 MHz, no-wait memory access • Programming/erasing method: Serial programming (asynchronous serial communication), self-programming
	RAM	• Capacity: 12 Kbytes • 32 MHz, no-wait memory access
	E2 DataFlash	• Capacity: 4 Kbytes • Number of erase/write cycles: 1,000,000 (typ)
MCU operating mode		Single-chip mode
Clock	Clock generation circuit	• Main clock oscillator, low-speed and high-speed on-chip oscillator, PLL frequency synthesizer, and IWDT-dedicated on-chip oscillator • Oscillation stop detection: Available • Clock frequency accuracy measurement circuit (CAC): Available • Independent settings for the system clock (ICLK), peripheral module clock (PCLK), and FlashIF clock (FCLK) The CPU and system sections such as other bus masters run in synchronization with the system clock (ICLK): 32 MHz (at max.) Peripheral modules run in synchronization with the PCLKB: 32 MHz (at max.) The flash peripheral circuit runs in synchronization with the FCLK: 32 MHz (at max.) The ICLK frequency can only be set to FCLK, PCLKB, or PCLKD multiplied by n (n: 1, 2, 4, 8, 16, 32, 64)
Resets		RES# pin reset, power-on reset, voltage monitoring reset, independent watchdog timer reset, and software reset
Voltage detection	Voltage detection circuit (LVDAb)	• When the voltage on VCC falls below the voltage detection level, an internal reset or internal interrupt is generated. Voltage detection circuit 0 is capable of selecting the detection voltage from 3 levels Voltage detection circuit 1 is capable of selecting the detection voltage from 9 levels Voltage detection circuit 2 is capable of selecting the detection voltage from 4 levels
Low power consumption	Low power consumption functions	• Module stop function • Three low power consumption modes Sleep mode, deep sleep mode, and software standby mode
	Function for lower operating power consumption	• Operating power control modes High-speed operating mode and middle-speed operating mode

Figure G. 2: RX13T - MCU Datasheet - 2.

Table 1.1 Outline of Specifications (2/3)

Classification	Module/Function	Description
Interrupt	Interrupt controller (ICUb)	• Interrupt vectors: 256 • External interrupts: 7 (NMI, IRQ0 to IRQ5 pins) • Non-maskable interrupts: 5 (NMI pin, oscillation stop detection interrupt, voltage monitoring 1 interrupt, voltage monitoring 2 interrupt, and IWDT interrupt) • 16 levels specifiable for the order of priority
DMA	Data transfer controller (DTCb)	• Transfer modes: Normal transfer, repeat transfer, and block transfer • Activation sources: External interrupts and interrupt requests from peripheral functions • Sequence transfer
I/O ports	General I/O ports	48-/32-pin • I/O: 38/22 • Input: 1/1 • Pull-up resistors: 38/22 • Open-drain outputs: 30/18 • 5-V tolerance: 2/2
Multi-function pin controller (MPC)		Capable of selecting the input/output function from multiple pins
Timers	Multi-function timer pulse unit 3 (MTU3c)	• 6 units (16 bis × 6 channels) • Provides up to 16 pulse-input/output lines and three pulse-input lines • Select from among fourteen counter-input clock signals for each channel (PCLK/1, PCLK/2, PCLK/4, PCLK/8, PCLK/16, PCLK/32, PCLK/64, PCLK/256, PCLK/1024, MTCLKA, MTCLKB, MTCLKC, MTCLKD, MTIOC1A) other than channel 1/3/4, for which only eleven signals are available, channel 2 for 12, channel 5 for 10 • 26 output compare/input capture registers • Counter clear operation (with compare match- or input capture-sourced simultaneous counter clear capability) • Simultaneous writing to multiple timer counters (TCNT) • Simultaneous register input/output by synchronous counter operation • Buffer operation • Cascaded operation • 28 interrupt sources • Automatic transfer of register data • Pulse output modes: Toggle/PWM/complementary PWM/reset-synchronized PWM • Complementary PWM output mode 3-phase non-overlapping waveform output for inverter control Automatic dead time setting Adjustable PWM duty cycle: from 0 to 100% A/D conversion request delaying function Interrupt at crest/trough can be skipped Double buffer function • Reset-synchronized PWM mode Outputs three phases each for positive and negative PWM waveforms in user-specified duty cycle • Phase counting modes: 16-bit mode (channel 1 and 2)/32-bit mode (channel 1 and 2) • Dead time compensation counter function • A/D converter start trigger can be generated • A/D converter start triggers can be skipped • Signals from the input capture and external counter clock pins are input via a digital filter
	Port output enable 3 (POE3C)	Controls the high-impedance state of the MTU's waveform output pins
	Compare match timer (CMT)	• (16 bits × 2 channels) × 1 units • Select from among four clock signals (PCLK/8, PCLK/32, PCLK/128, PCLK/512)
	Independent watchdog timer (IWDTa)	• 14 bits × 1 channel • Count clock: Dedicated low-speed on-chip oscillator for the IWDT Frequency divided by 1, 16, 32, 64, 128, or 256

Figure G. 3: RX13T - MCU Datasheet - 3.

Table 1.1 Outline of Specifications (3/3)

Classification	Module/Function	Description
Communication functions	Serial communications interfaces (SCIg, SCIh)	• 3 channels (channel 1 and 5: SCIg, channel 12: SCIh) • SCIg Serial communications modes: Asynchronous, clock synchronous, and smart-card interface Multi-processor function On-chip baud rate generator allows selection of the desired bit rate Choice of LSB-first or MSB-first transfer Average transfer rate clock can be input from MTU timers Start-bit detection: Level or edge detection is selectable. Simple I^2C Simple SPI 9-bit transfer mode Bit rate modulation • SCIh (The following functions are added to SCIg) Supports the serial communications protocol, which contains the start frame and information frame Supports the LIN format
	I^2C bus interface (RIICa)	• 1 channel • Communications formats: I^2C bus format/SMBus format • Master mode or slave mode selectable • Supports fast mode
12-bit A/D converter (S12ADF)		• 12 bits (8 channels × 1 unit) • 12-bit resolution • Minimum conversion time: 1.4 µs per channel when the ADCLK is operating at 32 MHz • Operating modes Scan mode (single scan mode, continuous scan mode, and 3 group scan mode) Group A priority control (only for 3 group scan mode) • Sampling variable Sampling time can be set up for each channel • Self-diagnostic function • Double trigger mode (A/D conversion data duplicated) • Assist on analog input disconnection detection • A/D conversion start conditions A software trigger, a trigger from a timer (MTU), or an external trigger signal • Sample-and-hold function Sample-and-hold circuit included (3 channels) • Amplification of input signals by a programmable gain amplifier (3 channels) Amplification rate: 2.000 times, 2.500 times, 3.077 times, 5.000 times, 8.000 times, 10.000 times (total of 6 steps)
Comparator C (CMPC)		• 3 channels • Function to compare the reference voltage and the analog input voltage • Reference voltage: Select from among two voltages • Analog input voltage: Select from among four voltages
D/A converter (DA) for generating comparator C reference voltage		• 1 channel • 8-bit resolution • Output voltage: 0 to AVCC0 • Reference voltage generation circuit for comparator C
CRC calculator (CRC)		• CRC code generation for arbitrary amounts of data in 8-bit units • Select any of three generating polynomials: $X^8 + X^2 + X + 1$, $X^{16} + X^{15} + X^2 + 1$, or $X^{16} + X^{12} + X^5 + 1$ • Generation of CRC codes for use with LSB-first or MSB-first communications is selectable.
Data operation circuit (DOC)		Comparison, addition, and subtraction of 16-bit data
Power supply voltages/Operating frequencies		VCC = 2.7 to 5.5V: 32 MHz
Supply current		11 mA at 32 MHz (typ.)
Operating temperature range		D version: –40 to +85°C, G version: –40 to +105°C
Packages		48-pin LFQFP (PLQP0048KB-B) 7 × 7 mm, 0.5 mm pitch 32-pin LQFP (PLQP0032GB-A) 7 × 7 mm, 0.8 mm pitch 48-pin HWQFN (PWQN0048KE-A) 7 × 7 mm, 0.5 mm pitch 32-pin HWQFN (PWQN0032KE-A) 5 × 5 mm, 0.5 mm pitch
Debugging interface		FINE interface

Figure G. 4: RX13T - MCU Datasheet - 4.

APPENDIX H

■ Absolute Maximum Ratings (Ta= 25°C)

Parameter		Symbol	Rating	Unit
Input	Forward current	I_F	50	mA
	*1Peak forward current	I_{FM}	1	A
	Reverse voltage	V_R	6	V
	Power dissipation	P	70	mW
Output	Collector-emitter voltage	V_{CEO}	35	V
	Emitter-collector voltage	V_{ECO}	6	V
	Collector current	I_C	50	mA
	Collector power dissipation	P_C	150	mW
Total power dissipation		P_{tot}	200	mW
*2Isolation voltage		V_{iso}	5 000	V_{rms}
Operating temperature		T_{opr}	- 30 to + 100	°C
Storage temperature		T_{stg}	- 55 to + 125	°C
*3Soldering temperature		T_{sol}	260	°C

*1 Pulse width<=100μs, Duty ratio : 0.001
*2 40 to 60% RH, AC for 1 minute
*3 For 10 seconds

■ Electro-optical Characteristics (Ta= 25°C)

Parameter			Symbol	Conditions	MIN.	TYP.	MAX.	Unit
Input	Forward voltage		V_F	I_F = 20mA	-	1.2	1.4	V
	Peak forward voltage		V_{FM}	I_{FM} = 0.5A	-	-	3.0	V
	Reverse current		I_R	V_R = 4V	-	-	10	μA
	Terminal capacitance		C_t	V= 0, f= 1kHz	-	30	250	pF
Output	Collector dark current		I_{CEO}	V_{CE} = 20V	-	-	10^{-7}	A
Transfer characteristics	*4Current transfer ratio		CTR	I_F = 5mA, V_{CE} = 5V	50	-	600	%
	Collector-emitter saturation voltage		$V_{CE(sat)}$	I_F = 20mA, I_C = 1mA	-	0.1	0.2	V
	Isolation resistance		R_{ISO}	DC500V, 40 to 60% RH	5×10^{10}	10^{11}	-	Ω
	Floating capacitance		C_f	V= 0, f= 1MHz	-	0.6	1.0	pF
	Cut-off frequency		f_c	V_{CE} = 5V, I_C = 2mA, R_L = 100Ω, -3dB	-	80	-	kHz
	Response time	Rise time	t_r	V_{CE} = 2V, I_C = 2mA, R_L = 100Ω	-	4	18	μs
		Fall time	t_f		-	3	18	μs

*4 Classification table of current transfer ratio is shown below.

Model No.	Rank mark	CTR (%)
PC817A	A	80 to 160
PC817B	B	130 to 260
PC817C	C	200 to 400
PC817D	D	300 to 600
PC8✱7AB	A or B	80 to 260
PC8✱7BC	B or C	130 to 400
PC8✱7CD	C or D	200 to 600
PC8✱7AC	A, B or C	80 to 400
PC8✱7BD	B, C or D	130 to 600
PC8✱7AD	A, B, C or D	80 to 600
PC8✱7	A, B, C, D or No mark	50 to 600

✱ : 1 or 2 or 3 or 4

Fig. 1 Forward Current vs. Ambient Temperature

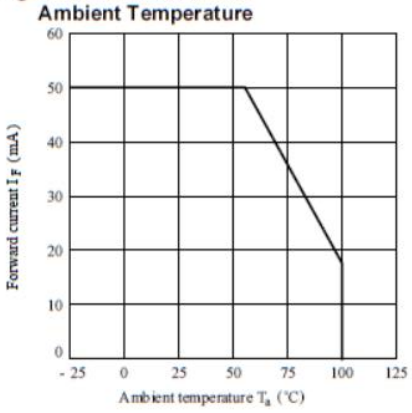

Figure H. 1: PC817A - Optocoupler Datasheet - 1.

CURRICULUM VITAE

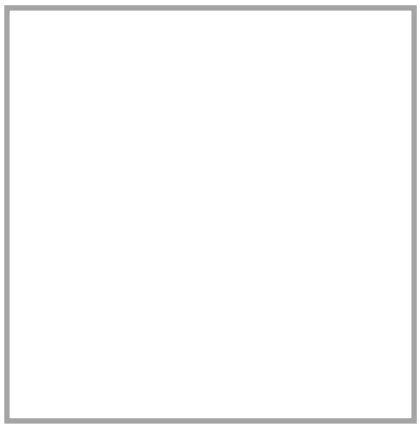

Name-Surname: Tolga Odabaşı

EDUCATION

- Bachelor's degree in Electrical Engineering, Istanbul Technical University, 2017

PROFESSIONAL EXPERIENCES

- Arçelik Global
  - R&D Specialist, October 2021 – present
  - R&D Engineer, November 2020 – October 2021
  - Project Engineer, December 2019 – November 2020
- Penta Electronic
  - R&D Engineer, March 2018 – October 2019

PUBLICATIONS, PRESENTATIONS AND PATENTS ON THE THESIS:

- **Odabaşı T., Tap A.** , **Ergene L. T.** 2021: (Certificate of Outstanding Paper Award), IEEE 3rd Global Power, Energy and Communication Conference, GPECOM 2021, October 5-8, Online Conference, Turkey.